The Dissertation Committee for Timothy Daniel Siegler
Certifies that this is the approved version of the following dissertation:

Hybrid Organic-Inorganic Perovskites: Humidity Stability and CdTe Tandem Photovoltaics

APPROVED BY
SUPERVISING COMMITTEE:

Brian A Korgel, Supervisor

Delia J Milliron

David Vanden Bout

Benjamin (Keith) Keitz

Hybrid Organic-Inorganic Perovskites: Humidity Stability and CdTe Tandem Photovoltaics

by

Timothy Daniel Siegler

Dissertation

Presented to the Faculty of the Graduate School of

The University of Texas at Austin

in Partial Fulfillment

of the Requirements

for the Degree of

Doctor of Philosophy

The University of Texas at Austin

August 2019

Dedication

Für Ernst & Helma Brenner. Ohne Ihren Mut wäre diese Dissertation nicht möglich.

Acknowledgements

There are so many people to whom I owe a fantastic debt of gratitude for this Ph.D. Without the support and help of so many friends and family seeing me through this experience, who knows where I am today. To do this properly, I decided not to cut any words. Apologies, but each and every person here mentioned deserves it. First and foremost, I would like to thank my adviser Dr. Korgel, who gave me the freedom to pursue my own project idea coming into my Ph.D. Allowing me the great creative research freedom you did throughout my Ph.D., even when I was failing and faltering, allowed me to become a great independent researcher. Thanks in particular for liking my work even when I didn't like my work; the nickel iodide paper in Chapter 3 would have never been completed without your enthusiasm, and it may be the best work of my first four years at UT. Also thanks for teaching me how to write. Editing each paper was a painful process-it still is, in truth-but I am truly a much better technical writer for having gone through the pain. Even though we may have not always understood each other, I appreciate all the support and trust you showed in me through this process, and am better for having received it. Thanks for believing in me. Also thank you to my committee, Drs. Milliron, Keitz, and Vanden Bout, for their support during these 5 years. Dr. Milliron, you in particular deserve my deepest thanks. Thanks for being a great collaborator who was able to toe the line of challenging and supportive expertly. Being next door, I learned many things by observing you and your group at work, and I owe a lot of my current research philosophy to watching you and your students work.

During my time at the Korgel Group, I had the pleasure to work with a countless number of inspiring and helpful people who have made my time that much less of a burden.

Mokshin, thank you for being the best undergraduate researcher I could have asked for. Once of the few harebrained ideas I had coming into my Ph.D. that had merit was the idea that I would take an undergraduate freshman in my second year such that we could work together for our entire time at UT, learning and growing together. This worked extremely well, but not because of my mentorship, rather on account of your work ethic and determination. Little did I expect when you came to visit as a high school senior with your dad that you would learn circles around me, becoming an intelligent, thoughtful, ambitious researcher in four short years working part-time. Nor did I expect that you would submit your first author paper to a journal way more prestigious than the journals of my publications. But looking back, it's unsurprising. You're a rising star that through your own merit and hard work will be able to do anything you want to do in engineering or chemistry. Always remember that, and don't let the next five years of your Ph.D. journey take away your light and ambition. You're an awesome scientist, and Cornell is lucky to have you. Oh, and keep telling jokes at prestigious national conferences.

Dan, thank you for being my buddy throughout this experience. Starting in the group with you made this whole process so much easier. Having our own little subgroup in the corner of 6.352 where we could talk about our science at any time for any length of time was such a blessing. We dealt with colleagues together, managed struggles together, celebrated success together, and helped each other write papers countless times through these last 5 years. You were the best co-worker someone could ask for, and the best ally to have in the lab. I'm super proud of how I feel we made our impact on the Korgel Group culture (particularly challenging the idea that a grad student should never challenge another grad student's science at group meeting) and of all the things we accomplished together. Thanks for everything.

Lauren, thanks for helping me see how cool the nickel iodide paper was. You were an ideal co-author, and it was a pleasure working with you. Your quick response times, rigor, and creative thinking helped teach me how to be a good scientist and made an odd throwaway paper an impactful, interesting, thorough study. I don't know how many grad students can say they learned as much from a junior colleague as I've learned from you. Thanks for helping me, and hopefully our collaboration is the first of many between our groups. Yangning, thanks for teaching me how to do X-Ray scattering. Your assistance was a cornerstone of much of this Ph.D. work, and I'm indebted to you for all the work and teaching you've helped me with these 3-odd years. I really am excited by your new work, and hope you continue to pursue really interesting perovskite work through your Ph.D. Michael, thanks for keeping up the perovskite work. Your work on TRPL is really neat and interesting, and will hopefully keep the perovskite work up for a long time. Also thanks for pitching in at a moments notice several times throughout my Ph.D. to help finish various projects. Shin, speaking of pitching in at a moment's notice, you've always been there to help me with whatever I need help working on something. Thanks for teaching me all about FTIR and your DRA instrument. Never lose that enthusiasm for everything. Hope your second career as a geologist goes great.

Jackson, thanks for teaching me everything I know about solar and PV. Thanks for being the true founding member of the perovskite subgroup (I'm still going to take credit for it, hope you don't mind) and setting up the testing equipment. Sorry we couldn't keep the paper writing tutorial going; in truth, it's hard to host until you write a paper, and it took me a while to publish my first. Yixuan, thanks for being a model grad student. Coming in as a first year, I saw your accomplishments and was awed immediately. I knew from day 1 I wanted to be like you. I wasn't quite as prolific in the end, but thank you for being my answer to every question for my first two years. Doug, thanks for being my lead blocker,

coming from ND to UT before I did and showing me how it's done. Tushti, thanks for helping me do HRTEM and make my Japan trip less lonely. TJ, you were there with me from the beginning and being supported through these last five years; thanks for being kind and empathetic through it all. You'll love Memphis, I know it. Kim, thanks for being a happy smiling face even when things weren't so happy. Gang, thanks for being there for the first couple years. Sorry it didn't work out in our group, but it looks like you're doing great things. Wei, thanks for being around during those first couple of years to show me how the world of academia worked. Sorry we couldn't get that paper together, but I was kind of an idiot back then, and didn't really know what I was doing. Vikas, thanks for being a really "cool dude" through my time, and not overreacting to my semi-meltdowns during my stressful third year. I feel you got the brunt of those; sorry. Arun, Melody, and Carolyn: thanks for your hard work in my first year. Also thanks to all the other Korgel group members who I didn't have quite as much interaction with these last 5 years, but were nonetheless important to getting my Ph.D.: Xiaotang, Chris Bosoy, Emily, Cherrelle, Adrien, Dorothy, Phil, Tim Bogart, Will, Wen, and Jungchul. Thank you all for everything. To the younger members of the group mentioned here: be genuinely curious and worry less about the successes on paper. Solving some mystery of the universe-however obscure- is more rewarding than a litany of empty papers could ever be.

Outside of the group, I also had some great collaborators helping me to succeed. Tushar and Dr. Sampath, thanks for bringing me into the CdTe project and remining enthusiastic despite the many, many setbacks I encountered along the way. Hopefully we can still get another paper out before I leave here for good. Geir, thanks for being there for me throughout my Ph.D. You were a fantastic mentor, and really helped me to get excited about my own project. It's rare that a funding source is so supportive and appreciative of the hard work you do, and I really needed that confidence boost and support when you

offered it. Thanks for being a great supporter during my time at Statoil/Equinor in Oslo. I really enjoyed that experience, and it was professionally formative in a substantial way. I truly owe you a debt of gratitude for all the support you showed to me and my projects. Thomas, we've just met, but I think we're going to get along great. Your attitude towards science as an industrial funding source is as refreshing as Geir's. I look forward to continue working together going forward. Gary, thanks for being the resident expert for the entirety of my Ph.D. Your enthusiasm for your work and the level of detail and completeness you pursue in lab every day is truly aspirational. If I'm lucky, hopefully I can be that level of detailed and thoughtful one day. Amy, thanks for helping me while I was still so young in my Ph.D. You really pushed me to pursue cool stuff early on. I really appreciate what you did for me in 2015, more than you probably expect.

Prashant, thanks for bringing me into this whole research thing. Without you being exceedingly generous and forgiving to a dumb young kid, all of this doesn't happen and I'm working on an oil rig or at a bank somewhere. I can't thank you enough for saving me from that path. Jeff Christians and Joe Manser, thanks for being the "cool kids" putting me in my place in undergrad and then teaching me how to make perovskite solar cells in grad school. Couldn't exactly replicate what you taught me at UT, but you still helped me a ton. James, thanks for being my first real peer mentor for research. You were truly an inspiration.

Taylor, thanks for the SEM help and showing me how a startup should be run. You taught me an important lesson: don't start a startup (unless your technology is REALLY great). Aida, thanks for the help with the SEM. Marlene, thanks for teaching me how to do collaborations well. Sorry my solar cells sucked, but you taught me a lot. Simin, thanks for bringing me in on your paper the way you did. You didn't have to do that, and it means a lot that you'd include me. Thanks to all the others who helped me to finish my papers:

Gabe, Junho, Elaine Li, and the countless others not listed here. Thanks also to all the technical people who made my life that much easier: Andrei, Vince, Dwight, Hugo, Yichen, Raluca, Mark, and Damon. I owe particular thanks to Andrei for all his help with Chapter 5, Raluca for all the help with instrument repair and getting new stuff for TMI, and Mark for going above and beyond the call of duty to help me with all those old instruments in the clean room that kept breaking.

To the reader: thanks for hanging in there. This is the home stretch. You can blame Evan Runnerstrom, who I thank for giving me the idea/leeway to write such an extensive acknowledgment.

To all my friends from before graduate school who helped me get through, thank you for keeping me sane and away from my work from time to time. Laura, thanks for being my best friend. Even though we don't always talk as frequently as either of us would like, your support is immeasurably important to me. Thanks for keeping me sane my first two years, and thanks for being my friend for so long. Mat, thanks for being the perfect roommate. We had a rocky start, but eventually we figured each other out, and I couldn't have asked for a better compatriot to accompany me along this journey. Enjoy the good life in the mid-Atlantic; you deserve it. Alon, thanks for being a good friend through this experience. Without Sunday ball, I'd probably be 245 lb right now. Grad school isn't great on the diet. Outside of that, thanks for being a good friend who was always open for a talk and a beer. And to all the basketball gang: thank you for being a great support group/stress relief society, making my Sundays that much better. Kristen, thanks for being there for all my trips to Colorado. You took a depressing and stressful trip and made me start to look forward to it. Sarah, thanks for being a great friend so close. I appreciated all the couch crashing I was able to do whenever I needed to visit Houston thanks to you (even if the house was horribly scarred from flood damage part of the time). Kevan, Mike, and Kyle:

thanks for being my oldest friends and supporting what I am doing whenever I go back home. And to all my friends who I still talk to: Hollyn, Jen Z., Mary, Garima, Dea, Jen J., and all the others. Thank you. Without you, none of this is possible.

I suppose the biggest "thank you"s always come last, whether it be in life or in practical writing. With that in mind, I have some final big "thank you"s to acknowledge. First, thanks and glory to God, through Whom all is possible, and the intercession of the Blessed Virgin, who helped give me the virtues (patience and humility in particular) to continue the entire way down the road to my Ph.D. and not leave the program prematurely. Thank you to my extended family for being abundantly supportive. Even if you had no idea what I was doing, your lessons in perseverance and your sympathy helped root me to my identity and inspired me to just finish this damn thing no matter what. To my grandparents, thanks for being a great example of good people who can think independently and demonstrate great integrity no matter what. I love you all and appreciate your example.

Thank you to my brother Erik, who always reminded me that industry is always worse (debatable) and who I could always count on to distract me in difficult times. I still don't think you believe me when I say I work in lab full-time like a normal job, but you were still supportive in your own way. It was also fun playing GM games with you constructing the Bucks rosters when life sucked. Hopefully it will still be fun to do this in 18 months when our roster is truly screwed. Dad, thanks for being a role model in science for me. You paved the way for me to do this and supported me pursuing an engineering degree, even when I didn't really want one. But you were never (too) pushy. Thanks for letting me go to ND as well; I know you thought it was a mistake at the time. But I've now spent extended periods at ND and at a large state school, and let me tell you, without ND, I am (as I said earlier) working at a bank or in an oil field. So thanks for letting me find my own way. Also stop talking to me about Ham radio and rf inverters and wiring and java;

I'm not that kind of engineer. Mom, thank you for being my academic rock from day 1. While your drilling was extensive, it taught me how to study and do well in school. You taught me how to learn and also how to play the game of school well-two entirely separate things that have nothing to do with each other but nonetheless are crucial for my present success. You always supported me throughout my PhD and really tried to make me realize finishing was the only option. You were right, even when I was in the dark night of the Ph.D. Thanks for always being my emotional rock and someone I can turn to no matter what. I appreciate that no matter what, I know we will never fall out or stop speaking. I love you and Dad tremendously.

Finally, Camila, thank you so so so much for everything you do for me every single day. Meeting you was the best thing to happen in my Ph.D.; it's hardly close, and I'm proud of so many things that I've done these past 5 years. Having both of us in the program means we both are experiencing awful stress day in and day out, it's hard to expend the emotional energy needed to be caring, and I love you for putting that effort into me every single day. I hope you can say the same from me. Thank you for showing me where all the best food is, for cooking for me, for drinking beer with me, for exploring with me, for traveling with me, and for just hanging out with me. You're my best friend, my emotional rock, and my number one fan. Without you these last five years would have been a disaster. I love you, so very much, and can't wait for out next adventure.

Abstract

Hybrid Organic-Inorganic Perovskites: Humidity Stability and CdTe Tandem Photovoltaics

Timothy Daniel Siegler, Ph.D.

The University of Texas at Austin, 2019

Supervisor: Brian A. Korgel

Solution-processed hybrid organic-inorganic perovskites (HOIPs) have garnered significant interest for tandem photovoltaics (PVs)-solar cell architectures that employ two absorber layers to overcome the PV thermodynamic efficiency limit. Perovskites have been coupled in tandem with silicon, CIGS, and other perovskites to boost PV efficiency. However, they have not been employed in tandem with popular PV material CdTe. Additionally, HOIPs suffer from rapid humidity-induced degradation, which limits their commercial application in general. Here, compositional engineering of the B-site is used to tune humidity stability of model HOIP semiconductors, and HOIP materials for tandem CdTe-HOIP PV are developed.

Substituting Pb^{2+} 5% with Bi^{3+} in model HOIP $CH_3NH_3PbI_3$ (MAPI) is seen to stabilize MAPI at 90% humidity, but destabilize MAPI at 60% humidity, making bismuth the first HOIP additive observed to have a stabilizing and destabilizing effect at different humidity conditions. From mechanistic insight and kinetic modeling, this stabilizing and

destabilizing effect is shown to be due to Bi^{3+} impacting the kinetics of different steps of the degradation reaction mechanism distinctly. The related humidity-induced degradation/deliquescence of transition metal halide thin films is then made use of in thin films of NiI_2. Water vapor uptake is seen to rapidly modulate light transmittance uniformly across the visible spectra, making NiI_2 films candidates for color-neutral smart windows.

HOIP-CdTe tandem cells are then studied. Traditional iodide-based HOIPs have band gaps that are too similar to CdTe for efficient tandem PV; therefore, CdTe is coupled with wide band gap $CH_3NH_3PbBr_3$ (MAPBr). MAPBr films exhibit a significant amount of haze due to optical loss in the MAPBr layer, which correlates with poor tandem PV performance. The Semiconductor Capacitance Simulator (SCAPS) software package is then utilized to determine the degree of haze that can be tolerated in a MAPBr-CdTe tandem before MAPBr begins to worsen CdTe PV efficiency. Inclusion of Ag^+ is seen to produce MAPBr films with uniform crystallographic orientation due to surface segregation of Ag and respective lowering of the surface energy of (100) MAPBr facets. Finally, initial steps towards Tl-based low band gap HOIP nanostructures for CdTe-HOIP tandem PV with ideally matched band gaps are undertaken.

Table of Contents

List of Tables

List of Figures

Chapter 1: Introduction

1.1 The Need for and Opportunity of a Cleantech Revolution

Human-induced climate change caused by the emission of greenhouse gasses is an existential threat to our way of life and the health of our planet. The story of human development-it has been said- can be told as the story of energy availability. Indeed, global historical estimates of gross domestic product (GDP) and global energy demand are well correlated,[1] and the Industrial Revolution that kickstarted the modern era is attributable in large part to the development of cheap sources of portable energy and the inventions of engines and thermodynamic cycles that could harvest this portable energy ever more efficiently. We refer today to these cheap sources of power as "fossil fuels".[2,3]

Fossil fuels were implemented widely not merely because they were cheap and easy for early industrial era manufacturing to utilize, but also for their ease of transport and flexibility in usage.[2,3] To take an example, coal can be used as a thermal heat source for manufacturing, as a transportation fuel for trains, and as a source of electricity. Not only that, but one truck of coal can be transported easily from the manufacturing plant to the railway to the power plant in a matter of minutes, delivering much higher energy densities than traditional fuels of the time (wood, peat) along the way. Truly, coal was seen as a one-size-fits-all energy solution.

While the combustion of these fossil fuels advanced society and brought about the modern era, the emission they produced created the environmental catastrophe in which the world finds itself today. Pollutant CO_2, accumulating from almost a century and a half of the industrialized economy, has tripled the CO_2 concentration in the atmosphere over the last century,[4] raised global surface temperatures by ~1^{o}C,[4] and is being treated as a national security threat by the US government.[5] In spite of this, global emissions continue

to increase at a troubling rate[4] as growing/emerging economies still rely on increased fuel consumption to promote GDP growth.[1,3,4] Therefore, there is a tremendous need for electricity/energy generation that is (a) emission-free, (b) inexpensive enough to be accessible by all strata of society, and (c) reliable enough to promote economic development in low income countries.

This need lays the framework for what many analysts call "the largest wealth-creation opportunity of our lifetime"[6]-the emergence of greentech and the green economy. The economic incentives for providing consistent clean energy are massive; the Paris Climate Accord and goals laid out therein demonstrate the tremendous demand for clean energy among nearly all nations in the world. Many have recognized that the clean economy is not just a charity case-that the economic potential is tremendous. Solar and wind have become increasingly significant energy generation infrastructure; wind today provides 2.5% of electricity in the United States, (https://www.llnl.gov/sites/default/files/field/image/article/2019/04/energyflowchart875x500.jpg) and the US has recently achieved 2 million solar installations nationwide.[7] With growth in implementation, the economic opportunity is also growing. Battery storage, as well, is rapidly decreasing in cost, prompting rapid growth in this field as well.[8] However, cleantech technologies are still far from ubiquitous. There is still a lot of opportunity for technology-driven growth to promote continual reduction of our carbon footprint; even with the tremendous growth we see in the sector today, fossil fuels still power 80% of the US economy. (https://www.llnl.gov/sites/default/files/field/image/article/2019/04/energyflowchart875x500.jpg) Technological improvements must continue to drive growth in the cleantech industry, helping accelerate this green energy transition.

1.2 SOLAR PV IN THE NEW GREEN ECONOMY

Generally, policymakers and professionals in the industry believe that the best roadmap for developing an emissions-free economy is to (1) make the electricity sector free of emissions and (2) "electrify everything", where as much energy demand is electrified as possible.[9] The second half of this plan is not relevant for this thesis, but will rely on the development of new batteries, electrical heating elements, and pump-driven membrane separations development for effective implementation. Much work is to be done on all these fronts, including significant research advancements in these areas at the University of Texas at Austin. Deep decarbonization of the electricity sector will rely on the replacement of fossil fuel generation with nuclear and renewable energy generation sources, with preferably more renewable generation as safe nuclear plants become more costly to build.[4,9]

Within the renewable sector, there are several players that are fairly well established yet have not experienced significant growth in the last decade. Hydro power and biofuels have been around for centuries, with the latter being the primary form of energy generation for the large majority of human history (wood, peat, etc.).[1,3] Unfortunately, biofuels are very inefficient for electricity generation, and hydropower has local environmental and political issues associated with the technology[10] that have stalled many recent projects.[11] In recent years, two new emissions-free technologies have exponentially grown: wind and solar. Wind power has been growing in interest as wind producers make new turbines that are larger, more efficient, better located (i.e. offshore), and kill fewer birds.[12] Solar, however, has seen the most growth, as costs have come down exponentially[13] and efficiencies continue to increase (www.nrel.gov/pv/cell-efficiency) driving unprecedented growth in the solar energy sector.[13]

The growth of this sector- which is dominated currently by silicon and CdTe generation technologies- has shown the potential opportunity for solar PV in new applications. Outside of rigid panels, ubiquitous PV that can be used in flexible of bendable substrates, or in buildings, has started to realize its enormous potential. Even within the rigid panel industry, use of new transformative technologies will soon be needed to continue to improve panel efficiency. There is still a lot of potential for technology-driven growth in the solar PV industry to fill the tremendous need for green energy generation in the new energy economy.

1.3 Basic Solar Cell Physics

The simplest solar photovoltaic (PV) system is a solid-state semiconductor device that absorbs light at an interface and uses the electrochemical potential difference between the two sides of the interface to drive separation of positive and negative charge. Take as an example a silicon homojunction solar cell. Such a cell only uses one semiconductor material-silicon, with a band gap of 1.1 eV. The chemical potential of the two silicon layers-henceforth referred to as the Fermi level of the layers- is then tuned via heterovalent doping. In a typical system, boron dopants are used to lower the Fermi level, and phosphorous dopants are used to raise the Fermi level. This occurs via either electron donation (in the case of P) or occupation (in the case of B), which changes the free charge carrier concentration in the layer, which in turn tunes the semiconductor's chemical potential. The layers in isolation look as in Figure 1.1a. We refer to the material with the raised potential as n-type and to the material with the lowered potential as p-type. We also do not conceptually refer to p-type doping as the acceptance of free electrons, but the donation of solid state "holes", which are semiclassical quasiparticles that represent the absence of an electron in an energy band that is mostly occupied by electrons.

Once p-type and n-type layers are brought together, seen in Figure 1.1b, band bending occurs between p-type and n-type layers. This occurs due to the requirements that (a) the Fermi level at equilibrium needs to be equal across the entire film, and (b) the phenomenon of band "pinning" at solid state interfaces. This pinning occurs during the act of equilibration; as the two layers are brought into contact, free electrons and free holes fly into each other at the interface, recombining. This means that at the interface, there are no more excess free electrons or holes (assuming the dopant concentration on each side of the interface is equal) and the Fermi level is an intermediate position (whose exact value is determined by dopant concentration in each silicon layer). As the Fermi level changes, however, an energy barrier for electrons and holes forms at this same interface, preventing their rapid recombination. This barrier forms because electrons wish to be lower in energy, while holes wish to be higher, and the interface begins to exhibit a conduction band energy that raises at the interface on the electron-rich side and a valence band energy that lowers at the interface on the hole-rich side during equilibration. Therefore, further recombination of electrons and holes from deeper into the layer is limited by diffusion; electrons and holes must feel a strong enough concentration gradient to overcome the chemical potential barrier of that interface. This creates a gradual leveling off of the bands to their bulk positions far away from the interface, and continuous (in the case of homojunctions) bands that bend at interfaces, seen in Figure 1.1b. The volume which exhibits band bending is referred to as the "depletion region"

Solar energy is created from light that is absorbed in the depletion region, seen in Figure 1.1c. Light is absorbed, creating an electron-hole pair. Electrons and holes are then separated from each other due to the potential gradients in the depletion region, which allows for the extraction of current. In this thesis, PVs will not adopt a "p-n" junction, as in silicon, but a "p-i-n" heterojunction architecture, seen in Figure 1.1d. In this

configuration, an intrinsic absorber is sandwiched between two p- and n-type layers of different composition than the absorber to create a PV with a depletion region that extends through the entire film.

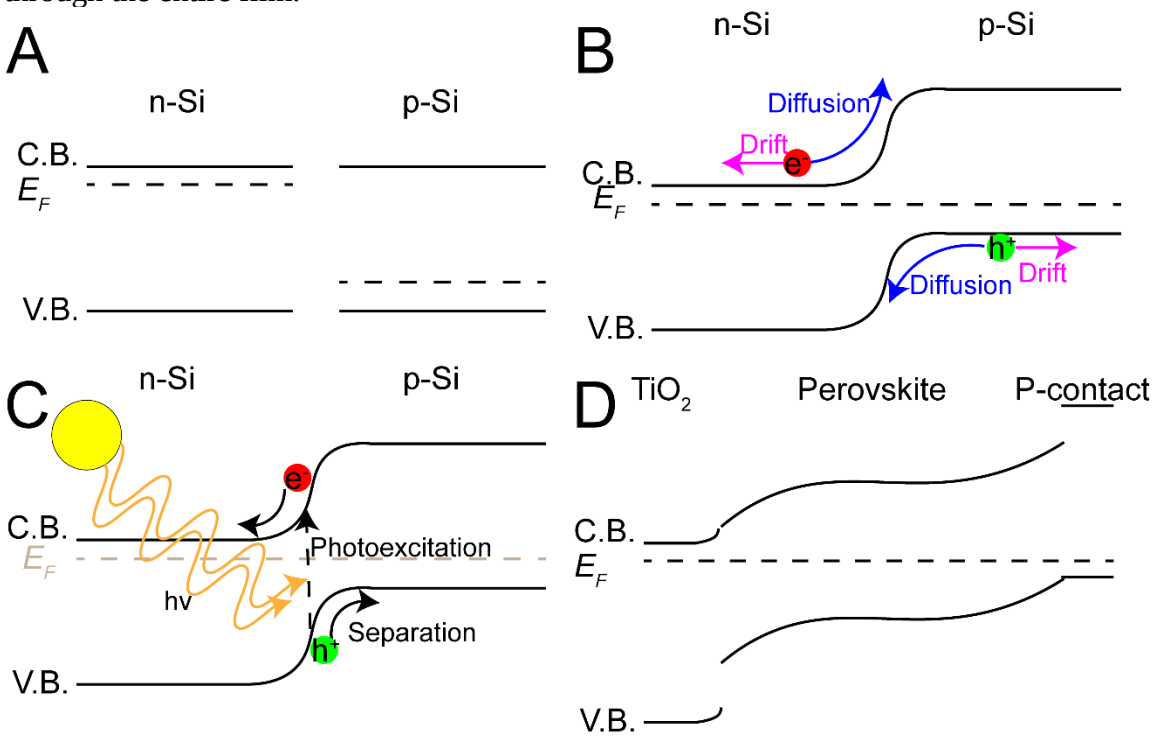

Figure 1.1 (A-C) P-and n-type silicon layers (A) in isolation, (B) in equilibrium contact with each other, and (C) absorbing light without applied bias. (D) A generic p-i-n perovskite band diagram with an organic hole transporter.

Power is extracted from the cell by applying bias to the system to extract "negative" current. The point at which the power of the electricity extracted P=-IV is at its the maximum (P_{MPP}) is called power point. Efficiency in the case of PVs is defined as Power Conversion Efficiency (PCE), which is $PCE=\frac{P_{MPP}}{100\ mW\ cm^{-2}}$, where 100 mW cm^{-2} is the power of incident light. A cartoon of an example J-V curve is seen in Figure 1.2. Other metrics that can be extracted from the curve include short circuit current (J_{SC}), open circuit voltage

(V_{OC}) and fill factor (FF). J_{SC} and V_{OC} are labeled in Figure 1.2, and fill factor is defined as $FF=\frac{P_{MPP}}{J_{SC}V_{OC}}$.

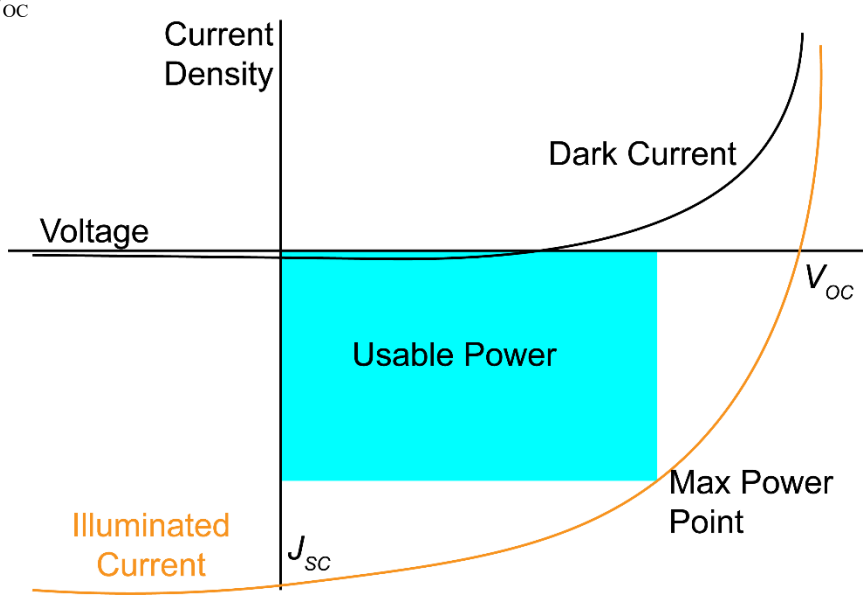

Figure 1.2 Example J-V curve used for analyzing PV performance.

1.4 The Shockley-Queisser Limit and How to Beat It

Solar cell PCE is limited by two competing factors: light absorption and output voltage. The maximum possible V_{OC} of a solar cell cannot be larger than its band gap; therefore, the band gap is an upper bound on the voltage of extracted power. However, semiconductors cannot absorb light with an energy lower than the band gap energy. Therefore, as you increase band gap to increase the V_{OC} of the device, you decrease the number of photons you can absorb, lowering current extraction. Shockley and Queisser considered this and came up with a maximum theoretical efficiency for each band gap energy.[14,15] In the ideal case, with a band gap of 1.3 eV, they determined that the maximum possible PCE was 34%. Modern day PVs are rapidly approaching this limit; there are a half dozen technologies with certified PCE of 22% or higher, and other PVs that are nearly at the Shockley-Queisser limit for their specific band gap.[16] Therefore, creative strategies will

need to be employed moving forward to further increase PV PCE without significantly increasing cost.

There are several established methods to overcome the Shockley-Queisser limit. Emissive materials that upconvert and downconvert are currently being employed in light management schemes to change the thermodynamic efficiency limit by changing the spectra of incident light.[17] In upconversion schemes, two photons of low-energy light are simultaneously absorbed by one electron, which excites this electron to a high energy state that would be inaccessible to it given single-photon absorbance. Once excited, the high energy electron then emits directly to its ground state, creating one photon of higher energy from two low-energy photons. Such a scheme is used to improve the J_{SC} of wide band gap PVs without sacrificing voltage.[18–20] Likewise, in a downconversion process, sometimes called a singlet fission process, one high energy electron absorbed with at least twice the energy of the host material band gap is absorbed and, through some Auger process and radiative recombination, generates two photons of lower energy light. This is used in lower band gap materials and in concentrated solar power systems to increase incident light intensity and short circuit current. A similar process exclusive to nanocrystal photovoltaic systems is multiple electron generation (MEG), where two electrons are generated in a semiconductor quantum dot from one high-energy photon in an Auger process.[21] Instead of emission in the quantum dot and re-absorbance elsewhere, the quantum dot also acts as the active PV material, meaning these extra electrons can be directly extracted after they are generated.

However, the most direct and potentially the most effective way of eclipsing the Shockley-Queisser limit is through use of tandem cell architectures. Tandem photovoltaics employ two absorbing layers of different band gaps stacked on top of each other. Using this strategy, once can absorb more of the solar spectrum with fewer thermal losses. Unlike

other strategies mentioned, tandems are a voltage-additive strategy which is already being implemented commercially.[22] Tandems have two general designs: 2-terminal (or monolithic) tandems, and 4-terminal tandems. Figure 1.3 shows examples of each design. While 4-terminal tandems are easier to design, 2-terminal tandems are desirable due to their lower balance of system costs.[23] In any event, there is a need in the tandem PV industry for new PV technology that has a widely tunable band gap, can be processed at mild temperatures so that 2-terminal PVs can be fabricated without damaging underlying layers, and can be made cheaply. Hybrid organic-ingorganic perovskites have recently emerged to meet this need.

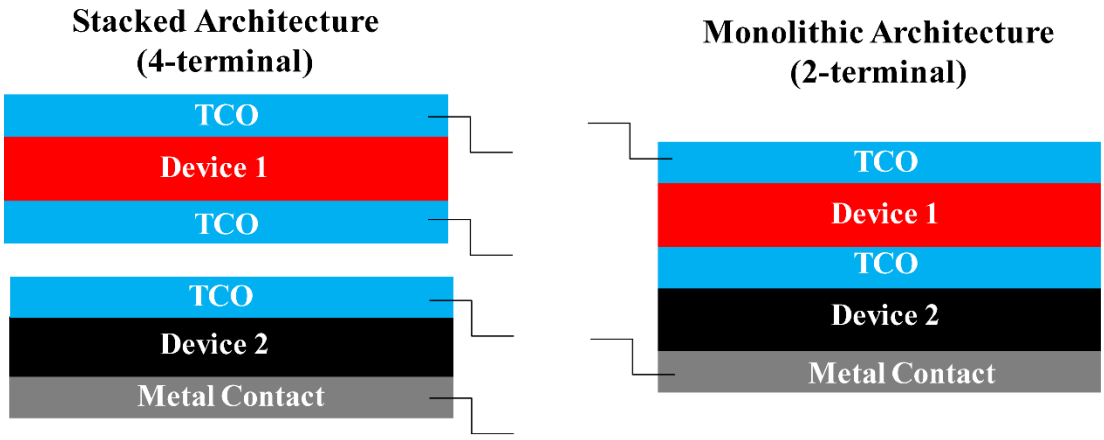

Figure 1.3 Comparison of 2-terminal and 4-terminal tandem PVs

1.5 Hybrid Organic-Inorganic Perovskites

Hybrid Organic-Inorganic Perovskites (HOIPs) are a relatively new field of solution-processed optoelectronic semiconductors which demonstrate long carrier diffusion lengths and very high defect tolerance. These favorable properties have contributed to their meteoric rise in the PV field, with perovskites achieving 24% PCE in and unprecedently short ten years of research (www.nrel.gov/pv/cell-efficiency). A brief

look into the history of HOIPs is warranted before discussion on their limitations and tandem cell applications thus far.

1.5.1 Early discovery

Hybrid organic-inorganic perovskites are semiconductors with an ABX_3 formula that have cubic perovskite crystal structure, an organic cation A site, and (usually) a halide X-site. The crystal can be easily visualized as octahedral BX_3 forming a hollow cubic cage which is filled by the large A-site cation. Often, the geometric factor, called the Goldschmidt Tolerance Factor[24] in perovskites, is slightly off due to an undersized or oversized A-site cation. This induces tilting in the inorganic cage, lowering the symmetry of the crystal to tetragonal or orthorhombic perovskite analogues.[24–26] In cases with subtle tilting, there is a negligible change in band gap when this tilting occurs.[24,25] Therefore, these non-cubic semiconductors are also called "perovskites" out of convenience.

Perovskites of this type were first discovered in 1893, where $CsPbX_3$ perovskites were synthesized in a powder form.[27] Later, in 1958, Møller characterized the crystal structure of these compounds and recorded their photoconductivity in the first report of their potential in optoelectronics.[28] The first truly hybrid HOIP-methylammonium lead and tin halides- were discovered in 1978 by Weber et al.[29,30] Then, in the mid-1990s, Dr. David Mitzi-at IBM at the time- began exploring Sn-based HOIPs for use in thin film transistors.[31,32] These Sn-based perovskites were later shown to have good hole conductivity, and HOIPs found their first PV application: as solid state electrolytes for dye-sensitized solar cells (DSSCs), replacing the traditional liquid phase redox couple.[33] Soon after, however, a more promising application for this material was discovered, with a much greater potential for innovative transformation.

1.5.2 The Invention of the Perovskite Solar Cell

In 2009, Tsutomu Miyasaka of the Toin University of Yokohama and colleagues decided to flip the conventional wisdom of using HOIPs in DSSCs. Instead of using HOIPs as the hole shuttle, they employed a HOIP sensitizer in a DSSC, using methylammonium lead iodide (MAPI) and methylammonium lead bromide (MAPBr) to make solar cells with ~1-3% PCE.[34] The authors employed these absorbers in a traditional DSSC architecture, using a very thick mesoporous TiO_2 layer as the n-type contact, and shuttling away holes using a liquid iodide redox couple that competed the circuit via electrolyte reduction at a counter electrode.[34] The authors also noted that devices tended to degrade rapidly, as the HOIP layer would readily dissolve in the electrolyte solution.

It was this last observation that inspired the groups of Nam-Gyu Park and Henry Snaith to pursue replacement of this liquid electrolyte with an organic solid-state hole conducting material. Both groups published reports in 2012 detailing the use of HOIP PVs around 10% PCE[35,36] utilizing spiro-OMeTAD, a common solid-state electrolyte for DSSCs, as the hole transporting material (HTM). This performance-impressive for a new PV material- inspired a flurry of research, which in turn lead to an unprecedented rate of performance improvement. (www.nrel.gov/pv/cell-efficiency) Very rapidly thereafter, cells with 15% PCE[37] and then 20% PCE[38] were being reported. Additionally, PVs were being fabricated with a variety of different architectures and with new materials,[38,39] showing the wide range of tunable properties this material could possess.

1.5.3 Current State of Research

Today, top performing cells have achieved upwards of 24% PCE (www.nrel.gov/pv/cell-efficiency). PVs today usually employ simultaneous A-site and X-site alloying in HOIP absorbers with very complex compositions. Additionally, HOIPs are

finding applications in a variety of other fields as well, including in high efficiency LEDs,[40,41] radiation detectors,[42] and photodetection schemes.[43]

Researchers are also going beyond traditional perovskite structures, utilizing the soft bonding of HOIPs to make new interesting bulk materials. Of particular interest are new lower dimensional perovskites, which employ A-site cations that are too large to fit into 3D perovskites. As a result, the inorganic components of these perovskites crystallize into plate-like structures (2D HOIPs) or wires (1D HOIPs) separated from each other by the A-site spacer ion. Since the local dielectric constant of the inorganic and organic components are significantly different, lower-dimensional HOIPs behave like self-assembled quantum wells or wires with long-range uniform ordering. This intriguing structure results in semiconductors with interesting properties not present in 3D analogues including efficient white light emission and large luminescence quantum yields in bulk films and crystals.[44–46] The large hydrophobic organic component of 2D HOIPs also significantly improve humidity stability compared to 3D counterparts.[47]

Other work focusing on lead- and tin- free HOIP materials discovery has opened up a new field of "double perovskites". Double perovskites, also called elpasolites, have a chemical formula of $A_2B'B'''X_6$, where heterovalent alternating B' and B''' sites replace the traditional B-site of regular perovskites.[48,49] For halogen perovskites, these B' and B''' sites are in the 1+ and 3+ oxidation state, respectively. For example, traditional 3D perovskite $CsPbBr_3$ employs Cs in the 1+ oxidation state, Pb in the 2+ state, and Br in the 1- state. Analogous double perovskite $Cs_2AgBiBr_6$, however, employs alternating Ag^+ and Bi^{3+} cations in the B-site in lieu of lead.[48] Such double perovskites are attracting much attention as white light emitters, as low band gap HOIPs, and for lead-free optoelectronics.[46,48,49]

1.5.4 Companies and the Commercial Future

Currently, there are several companies who have attempted to utilize HOIP technology for PV applications. Oxford PV is the first and most successful perovskite startup created thus far, raising $100 million in capital and reporting a world-record 28% silicon-HOIP tandem PV.[50] (www.nrel.gov/pv/cell-efficiency) Saule technoliges, a Polish company, is working on flexible or flexed HOIP PVs for building-integrated designs, and has installed a demonstration plant recently in Warsaw.[51] There are also several other companies working towards perovskite commercialization, including Microquanta, Solar-tectic, and Frontier Energy Solutions. (https://www.perovskite-info.com/companies) While much work still needs to be done, HOIP technology is showing that it has the potential to truly contribute to the cleantech industry in earnest.

1.6 Humidity Instability in Perovskites

One of the major limitations impeding the commercialization of HOIP PVs is the humidity-induced instability exhibited by most HOIPs. Some of the earliest reports of HOIP PVs-including the very first report by Miyasaka et. al.-report rapid degradation of HOIP materials exposed to polar solvents[34] and water vapor.[52] This rapid degradation has dampened the pace of scale up for commercial development of HOIP PVs. Recently, this degradation has been dramatically slowed via compositional tuning; by alloying two or more A-sites and X-sites in a single HOIP, one can create extremely stable HOIP thin films and PVs.[52–54] Additionally, recent advances in overlayer coating/surface passivation have dramatically improved HOIP stability as well,[55] leading to perovskite PVs that can pass preliminary IEC accelerated aging tests.[56] However, to fully reach the stability goals laid out in the DOE SunShot report for next-generation PV,[13] HOIPs will require one more order of magnitude in stability lifetime improvement. To achieve this, fundamental

understanding of the degradation processes must be further developed and studied in depth to determine the root cause of the improved stability in HOIP alloys and to develop representative aging tests for this next generation technology.

1.7 PEROVSKITE TANDEM CELLS

Once these issues are overcome, one of the major applications for perovskite PV is in tandem cells. While perovskites can be used to make flexible devices on low melting point substrates, the field of tandem cells remains the largest market opportunity for perovskite PV technology. As mentioned earlier, perovskites are uniquely suited for tandem PV due to their low temperature manufacturing, wide band gap tunability, and solution processability. Additionally, high defect tolerance and carrier mobility of these materials across a wide compositional space allow for a large degree of flexibility in tandem cell processing. These advantages have been used widely in literature to make a variety of tandem cells. A full citation list of all tandem cell work pre-October 2018 is in Chapter 4; here are the highlights of what has been done thus far.

1.7.1 HOIP-Silicon Tandem Cells

The first HOIP-silicon tandem cell was made in 2014 and achieved an efficiency of 17% by mechanically stacking a HOIP cell on top of a high performing silicon device.[57] Soon after, two terminal devices were established, achieving efficiencies in excess of 20% when employing an antireflective coating in a large-area device.[58] Further progress was unfortunately delayed by the revelation that, in traditional HOIP thin films, mixed iodide-bromide HOIPs undergo photoinduced phase segregation under illumination.[59] This was troubling for the tandem community, since ideal band gap top cells could only be realized by mixing the bromide and iodide in a HOIP film. Further research was then focused on

created idealized band gap pairings by using simultaneous A- and X-site alloying to increase the amount of bromide that could be incorporated into the HOIP before the onset of this phase segregation.[60] The development of these wider band gap perovskites allowed for rapid development of silicon-HOIP tandems with ideally matched band gaps.[61–63] Recently, tandem cell efforts have focused on using textured bottom cells, as simulations have shown these are theoretically better at trapping light in the silicon bottom layer.[64,65] Ballif et al have made great progress in this area, first developing a process to deposit smooth, uniform layers on a patterned silicon substrate,[64] then using said process to fabricate 25% efficient tandem cells,[64] and then finally fabricating the first triple junction HOIP device: a HOIP-HOIP-Si monolithic triple junction cell with 14% PCE.[65] The current silicon-HOIP tandem record is held by Oxford PV, a startup out of the UK. (www.nrel.gov/pv/cell-efficiency)

1.7.2 HOIP-CIGS Tandem Cells

HOIP-CIGS tandem cells have also been developed to a more limited extent. This architecture is interesting as both top and bottom cells have band gap tunability, which allows for more easily realized ideal band gap tandems. The first report of Si-HOIP tandem PV also reported a CIGS-HOIP PV with 18% PCE.[57] Likewise, 2-terminal cells were developed soon after with similar efficiency.[66] Recently, HOIP-CIGS tandem cells have achieved upwards of 21% PCE using similar strategies to that of HOIP-Si tandem cells, whereby a process was developed to deposit HOIPs monolithically on the nonuniform surface of a CIGS device.[67]

1.7.3 HOIP-HOIP Tandem Cells

One of the more interesting developments to recently come about is the development of all-perovskite (or HOIP-HOIP) tandem PVs. Such devices were first developed as monolithic cells in 2015,[68] and have recently become a very popular research topic. HOIP-HOIP PVs have the same band gap tunability advantages as HOIP-CIGS tandem cells, but with the additional potential application in flexible tandem PVs.[69] Top HOIP-HOIP tandem PVs employ a tin-lead alloy bottom layer to sufficiently lower the band gap of the bottom cell for effective tandem performance. This was first implemented effectively in 2016, where a HOIP-HOIP tandem device with 20% PCE was achieved using ideally matched band gaps.[70] The record HOIP-HOIP tandem in literature presently employs a 4-terminal architecture and 2D additive guadinium thiocyanate to achieve a PCE of 25%.[71]

1.7.4 What's next for Tandem HOIP PV?

Recently, HOIP architectures have been expanding further to incorporate other PV technologies such as nanocrystal solar cells.[72,73] However, HOIP PVs have yet to be coupled with some high efficiency PV devices such as GaAs and CdTe. CdTe-HOIP tandems are particularly interesting, as CdTe technology has the second largest market cap of any PV technology in 2019.[74] Furthermore, while HOIP-HOIP PVs with reasonable band gap pairing have achieved high efficiency tandem PV to date, ideal HOIP-HOIP PVs would utilize a bottom cell with a bandgap lower than the lowest band gap HOIP known to date.[75] Groundbreaking work towards tandem PV will be achieved via (1) exploration of new tandem architectures and (2) new materials exploration to find low band gap HOIPs more well-suited for certain tandem applications.

1.8 Dissertation Overview

This dissertation tackles these two issues hindering the commercialization of HOIPs: humidity stability and limit applicability in tandem architectures. Book 1 details the interactions between water vapor and HOIP/metal halide thin films, while Book 2 explores tandem cell applications. Chapter 2 demonstrates that bismuth doping into methylammonium lead iodide (MAPI) impacts humidity stability differently at different humidity conditions, the first such report of an additive having a disparate effect at different humidity. This not only has implications for compositional design, but also for reliability testing, showing that accelerated aging tests performed at high humidity may not accurately represent the real-world degradation behavior of perovskite PVs. Chapter 3 shows how this humidity-induced degradation could be utilized effectively for different applications, showing how deliquescent chromism in nickel (II) iodide films can be used as a switchable smart window material. Chapter 4 details the challenges of making HOIP-CdTe thin films, identifying wide band gap $CH_3NH_3PbBr_3$ as the best material currently known in literature to match with CdTe in a tandem cell. In chapter 5, control of crystal orientation is demonstrated in thin films of $CH_3NH_3PbBr_3$ with the addition of a small amount of Ag^+. Chapter 6 initiates development of lower band gap HOIPs for CdTe tandem cells by exploring thallium bromide nanoparticle chemistry. Finally, Chapter 7 summarizes all work and provides a roadmap for continuing progress in these areas.

1.9 References

(1) Mattick, C.; Williams, E.; Allenby, B. Historical Trends in Global Energy Consumption. *IEEE Technol. Soc. Mag.* **2010**, 29, 22–30.

(2) Wrigley, E. A. Energy and the English Industrial Revolution. *Philos. Trans. R. Soc. Math. Phys. Eng. Sci.* **2013**, 371, 20110568–20110568.

(3) Smil, V. *Energy Transitions: History, Requirements, Prospects*; Praeger: Santa Barbara, 2010.

(4) IPCC. *Summary for Policymakers.*; Global Warming of 1.5 ^{o}C. An IPCC Special Report on the impacts of Global Warming of 1.5 ^{o}C Above Pre-Industrial Levels and Related Greenhouse Gas Emission Pathways, in the Context of Strengthening the Global Response to the Threat of Climate Change, Sustainable Development, and Efforts to Eradicate Poverty; IPCC, 2018.

(5) Climate Change Threatens National Security Says Pentagon. *United Nations Climate Change*. Washington DC October 14, 2014.

(6) Price, D. This Entrepreneur Plans to Save the World, $1 Trillion at a Time. *Entrepreneur Asia Pacific*. February 17, 2015.

(7) Foehringer Merchant, E. US Surpasses 2 Million Solar Installations as Industry Looks to "Dominate" the 2020s. *Greentech Media*. May 9, 2019.

(8) Goldie-Scot, L. A Behind the Scenes Take on Lithium-Ion Battery Prices. *BloombergNEF*. March 5, 2019.

(9) Lacey, S.; Kann, S. The Deep Decarbonization Draft: Fantasy Sports for Energy Nerds.

(10) Winemiller, K. O.; McIntyre, P. B.; Castello, L.; Fluet-Chouinard, E.; Giarrizzo, T.; Nam, S.; Baird, I. G.; Darwall, W.; Lujan, N. K.; Harrison, I.; et al. Balancing Hydropower and Biodiversity in the Amazon, Congo, and Mekong. *Science* **2016**, 351, 128–129.

(11) Sharma, G. Nepal Scraps $2.5 Bln Hydropower Plant Deal with Chinese Company. *Reuters*. Kathmandu November 13, 2017.

(12) Sun, X.; Huang, D.; Wu, G. The Current State of Offshore Wind Energy Technology Development. *Energy* **2012**, 41, 298–312.

(13) Woodhouse, M.; Jones-Albertus, R.; Feldman, D.; Fu, R.; Horowitz, K.; Chung, D.; Jordan, D.; Kurtz, S. *On the Path to SunShot: The Role of Advancements in Solar Photovoltaic Efficiency, Reliablity, and Cost*; NREL/TP-6A20-65872; National Renewable Energy Laboratory, 2016.

(14) Shockley, W.; Queisser, H. J. Detailed Balance Limit of Efficiency of P-n Junction Solar Cells. *J. Appl. Phys.* **1961**, 32, 510.

(15) Rühle, S. Tabulated Values of the Shockley–Queisser Limit for Single Junction Solar Cells. *Sol. Energy* **2016**, 130, 139–147.

(16) Polman, A.; Knight, M.; Garnett, E. C.; Ehrler, B.; Sinke, W. C. Photovoltaic Materials: Present Efficiencies and Future Challenges. *Science* **2016**, 352, aad4424.

(17) Lee, S.; Hwang, D.; Jung, S. I.; Kim, D. Electron Transfer from Triplet State of TIPS-Pentacene Generated by Singlet Fission Processes to $CH_3NH_3PbI_3$ Perovskite. *J. Phys. Chem. Lett.* **2017**, 8, 884–888.

(18) Zhou, D.; Liu, D.; Jin, J.; Chen, X.; Xu, W.; Yin, Z.; Pan, G.; Li, D.; Song, H. Semiconductor Plasmon-Sensitized Broadband Upconversion and Its Enhancement Effect on the Power Conversion Efficiency of Perovskite Solar Cells. *J. Mater. Chem. A* **2017**, 5, 16559–16567.

(19) He, M.; Pang, X.; Liu, X.; Jiang, B.; He, Y.; Snaith, H.; Lin, Z. Monodisperse Dual-Functional Upconversion Nanoparticles Enabled Near-Infrared Organolead Halide Perovskite Solar Cells. *Angew. Chem. Int. Ed.* **2016**, 55, 4280–4284.

(20) Nienhaus, L.; Correa-Baena, J.-P.; Wieghold, S.; Einzinger, M.; Lin, T.-A.; Shulenberger, K. E.; Klein, N. D.; Wu, M.; Bulović, V.; Buonassisi, T.; et al. Triplet-Sensitization by Lead Halide Perovskite Thin Films for Near-Infrared-to-Visible Upconversion. *ACS Energy Lett.* **2019**, 4, 888–895.

(21) Stolle, C. J.; Schaller, R. D.; Korgel, B. A. Efficient Carrier Multiplication in Colloidal $CuInSe_2$ Nanocrystals. *J. Phys. Chem. Lett.* **2014**, 5, 3169–3174.

(22) Publicover, B. Oxford PV Raises $41m to Commercialize Perovskite Tech. *PV Magazine*. March 20, 2019.

(23) Sofia, S. E.; Mailoa, J. P.; Weiss, D. N.; Stanbery, B. J.; Buonassisi, T.; Peters, I. M. Economic Viability of Thin-Film Tandem Solar Modules in the United States. *Nat. Energy* **2018**, 3, 387–394.

(24) Amat, A.; Mosconi, E.; Ronca, E.; Quarti, C.; Umari, P.; Nazeeruddin, M. K.; Grätzel, M.; De Angelis, F. Cation-Induced Band-Gap Tuning in Organohalide Perovskites: Interplay of Spin–Orbit Coupling and Octahedra Tilting. *Nano Lett.* **2014**, 14, 3608–3616.

(25) Song, Z.; Watthage, S. C.; Phillips, A. B.; Tompkins, B. L.; Ellingson, R. J.; Heben, M. J. Impact of Processing Temperature and Composition on the Formation of Methylammonium Lead Iodide Perovskites. *Chem. Mater.* **2015**, 27, 4612–4619.

(26) Kieslich, G.; Skelton, J. M.; Armstrong, J.; Wu, Y.; Wei, F.; Svane, K. L.; Walsh, A.; Butler, K. T. Hydrogen Bonding versus Entropy: Revealing the Underlying Thermodynamics of the Hybrid Organic–Inorganic Perovskite $[CH_3NH_3]PbBr_3$. *Chem. Mater.* **2018**, 30, 8782–8788.

(27) H. L. Wells. Über die Cäsium- und Kalium-Bleihalogenide. *Z. Für Anorg. Chem.* **1893**, 3, 195–210.

(28) Christain K. Møller. Crystal Structure and Photoconductivity of Cesium Plumbohalides. *Nature* **1958**, 182, 1436.

(29) Weber, D. $CH_3NH_3PbX_3$, ein Pb(II)-System mit kubischer Perowskitstruktur/$CH_3NH_3PbX_3$, a Pb(II)-System with Cubic Perovskite Structure. *Z. Für Naturforschung B* **1978**, 33, 1443–1445.

(30) Weber, D. $CH_3NH_3SnBr_xI_{3-x}$ (x=0-3), ein Sn(II)-System mit kubischer Perowskitstruktur. *Z. Für Naturforschung B* **1978**, 33, 4.

(31) Mitzi, D. B.; Wang, S.; Feild, C. A.; Chess, C. A.; Guloy, A. M. Conducting Layered Organic-Inorganic Halides Containing -Oriented Perovskite Sheets. *Science* **1995**, 267, 1473–1476.

(32) Mitzi, D.B.; Field, C.A.; Schlesinger, Z.; Laibowitz, R.B. Transport, Optical, and Magnetic Properties of the Conducting Halide Perovskite $CH_3NH_3SnI_3$. *J. Solid State Chem.* **1995**, 114, 159–163.

(33) Chung, I.; Lee, B.; He, J.; Chang, R. P. H.; Kanatzidis, M. G. All-Solid-State Dye-Sensitized Solar Cells with High Efficiency. *Nature* **2012**, 485, 486–489.

(34) Kojima, A.; Teshima, K.; Shirai, Y.; Miyasaka, T. Organometal Halide Perovskites as Visible-Light Sensitizers for Photovoltaic Cells. *J. Am. Chem. Soc.* **2009**, 131, 6050–6051.

(35) Kim, H.-S.; Lee, C.-R.; Im, J.-H.; Lee, K.-B.; Moehl, T.; Marchioro, A.; Moon, S.-J.; Humphry-Baker, R.; Yum, J.-H.; Moser, J. E.; et al. Lead Iodide Perovskite Sensitized All-Solid-State Submicron Thin Film Mesoscopic Solar Cell with Efficiency Exceeding 9%. *Sci. Rep.* **2012**, 2, 591.

(36) Lee, M. M.; Teuscher, J.; Miyasaka, T.; Murakami, T. N.; Snaith, H. J. Efficient Hybrid Solar Cells Based on Meso-Superstructured Organometal Halide Perovskites. *Science* **2012**, 338, 643–647.

(37) Burschka, J.; Pellet, N.; Moon, S.-J.; Humphry-Baker, R.; Gao, P.; Nazeeruddin, M. K.; Grätzel, M. Sequential Deposition as a Route to High-Performance Perovskite-Sensitized Solar Cells. *Nature* **2013**, 499, 316–319.

(38) Yang, W. S.; Noh, J. H.; Jeon, N. J.; Kim, Y. C.; Ryu, S.; Seo, J.; Seok, S. I. High-Performance Photovoltaic Perovskite Layers Fabricated through Intramolecular Exchange. *Science* **2015**, 348, 1234–1237.

(39) Im, J.-H.; Chung, J.; Kim, S.-J.; Park, N.-G. Synthesis, Structure, and Photovoltaic Property of a Nanocrystalline 2H Perovskite-Type Novel Sensitizer ($CH_3CH_2NH_3$)PbI_3. *Nanoscale Res. Lett.* **2012**, 7, 353.

(40) Veldhuis, S. A.; Boix, P. P.; Yantara, N.; Li, M.; Sum, T. C.; Mathews, N.; Mhaisalkar, S. G. Perovskite Materials for Light-Emitting Diodes and Lasers. *Adv. Mater.* **2016**, *28* (32), 6804–6834. https://doi.org/10.1002/adma.201600669.

(41) Cho, H.; Kim, Y.-H.; Wolf, C.; Lee, H.-D.; Lee, T.-W. Improving the Stability of Metal Halide Perovskite Materials and Light-Emitting Diodes. *Adv. Mater.* **2018**, 30, 1704587.

(42) Yakunin, S.; Dirin, D. N.; Shynkarenko, Y.; Morad, V.; Cherniukh, I.; Nazarenko, O.; Kreil, D.; Nauser, T.; Kovalenko, M. V. Detection of Gamma Photons Using Solution-Grown Single Crystals of Hybrid Lead Halide Perovskites. *Nat. Photonics* **2016**, 10, 585–589.

(43) Ji, L.; Hsu, H.-Y.; Lee, J. C.; Bard, A. J.; Yu, E. T. High-Performance Photodetectors Based on Solution-Processed Epitaxial Grown Hybrid Halide Perovskites. *Nano Lett.* **2018**, 18, 994–1000.

(44) Jung, M.-H. White-Light Emission from the Structural Distortion Induced by Control of Halide Composition of Two-Dimensional Perovskites ($(C_6H_5CH_2NH_3)_2PbBr_{4-x}Cl_x$). *Inorg. Chem.* **2019**, 58, 6748–6757.

(45) Mao, L.; Wu, Y.; Stoumpos, C. C.; Traore, B.; Katan, C.; Even, J.; Wasielewski, M. R.; Kanatzidis, M. G. Tunable White-Light Emission in Single-Cation-Templated Three-Layered 2D Perovskites $(CH_3CH_2NH_3)_4Pb_3Br_{10-x}Cl_x$. *J. Am. Chem. Soc.* **2017**, 139, 11956–11963.

(46) Connor, B. A.; Leppert, L.; Smith, M. D.; Neaton, J. B.; Karunadasa, H. I. Layered Halide Double Perovskites: Dimensional Reduction of $Cs_2AgBiBr_6$. *J. Am. Chem. Soc.* **2018**, 140, 5235–5240.

(47) Wang, Z.; Lin, Q.; Chmiel, F. P.; Sakai, N.; Herz, L. M.; Snaith, H. J. Efficient Ambient-Air-Stable Solar Cells with 2D–3D Heterostructured Butylammonium-Caesium-Formamidinium Lead Halide Perovskites. *Nat. Energy* **2017**, 2, 17135.

(48) Slavney, A. H.; Hu, T.; Lindenberg, A. M.; Karunadasa, H. I. A Bismuth-Halide Double Perovskite with Long Carrier Recombination Lifetime for Photovoltaic Applications. *J. Am. Chem. Soc.* **2016**, 138, 2138–2141.

(49) Slavney, A. H.; Leppert, L.; Saldivar Valdes, A.; Bartesaghi, D.; Savenije, T. J.; Neaton, J. B.; Karunadasa, H. Small-Bandgap Halide Double Perovskites. *Angew. Chem. Int. Ed.* **2018**, 57, 12765-12770.

(50) Mary Loritz. Oxford PV Raises €36 Million for Its Super-Efficient Solar Cells from Chinese Renewable Giant Goldwind. *EU-Startups News*. April 1, 2019.

(51) Skansa. Skansa and Saule Technologies Commence Revolutionary Solar Panels Test. Warsaw, Poland December 13, 2018.

(52) Noh, J. H.; Im, S. H.; Heo, J. H.; Mandal, T. N.; Seok, S. I. Chemical Management for Colorful, Efficient, and Stable Inorganic–Organic Hybrid Nanostructured Solar Cells. *Nano Lett.* **2013**, 13, 1764–1769.

(53) Back, H.; Kim, G.; Kim, J.; Kong, J.; Kim, T. K.; Kang, H.; Kim, H.; Lee, J.; Lee, S.; Lee, K. Achieving Long-Term Stable Perovskite Solar Cells via Ion Neutralization. *Energy Environ. Sci.* **2016**, 9, 1258–1263.

(54) Li, Z.; Yang, M.; Park, J.-S.; Wei, S.-H.; Berry, J. J.; Zhu, K. Stabilizing Perovskite Structures by Tuning Tolerance Factor: Formation of Formamidinium and Cesium Lead Iodide Solid-State Alloys. *Chem. Mater.* **2016**, 28, 284–292.

(55) Zhou, Y.; Zhao, Y. Chemical Stability and Instability of Inorganic Halide Perovskites. *Energy Environ. Sci.* **2019**, 12, 1495–1511.

(56) Wu, Z.; Liu, Z.; Hu, Z.; Hawash, Z.; Qiu, L.; Jiang, Y.; Ono, L. K.; Qi, Y. Highly Efficient and Stable Perovskite Solar Cells via Modification of Energy Levels at the Perovskite/Carbon Electrode Interface. *Adv. Mater.* **2019**, 31, 1804284.

(57) Bailie, C. D.; Christoforo, M. G.; Mailoa, J. P.; Bowring, A. R.; Unger, E. L.; Nguyen, W. H.; Burschka, J.; Pellet, N.; Lee, J. Z.; Grätzel, M.; et al. Semi-Transparent Perovskite Solar Cells for Tandems with Silicon and CIGS. *Energy Env. Sci* **2015**, 8, 956–963.

(58) Werner, J.; Weng, C.-H.; Walter, A.; Fesquet, L.; Seif, J. P.; De Wolf, S.; Niesen, B.; Ballif, C. Efficient Monolithic Perovskite/Silicon Tandem Solar Cell with Cell Area >1 cm ^{2}. *J. Phys. Chem. Lett.* **2016**, 7, 161–166.

(59) Hoke, E. T.; Slotcavage, D. J.; Dohner, E. R.; Bowring, A. R.; Karunadasa, H. I.; McGehee, M. D. Reversible Photo-Induced Trap Formation in Mixed-Halide Hybrid Perovskites for Photovoltaics. *Chem. Sci.* **2015**, 6, 613–617.

(60) McMeekin, D. P.; Sadoughi, G.; Rehman, W.; Eperon, G. E.; Saliba, M.; Horantner, M. T.; Haghighirad, A.; Sakai, N.; Korte, L.; Rech, B.; et al. A Mixed-Cation Lead Mixed-Halide Perovskite Absorber for Tandem Solar Cells. *Science* **2016**, 351, 151–155.

(61) Bush, K. A.; Palmstrom, A. F.; Yu, Z. J.; Boccard, M.; Cheacharoen, R.; Mailoa, J. P.; McMeekin, D. P.; Hoye, R. L. Z.; Bailie, C. D.; Leijtens, T.; et al. 23.6%-Efficient Monolithic Perovskite/Silicon Tandem Solar Cells with Improved Stability. *Nat. Energy* **2017**, 2, 17009.

(62) Ramírez Quiroz, C. O.; Shen, Y.; Salvador, M.; Forberich, K.; Schrenker, N.; Spyropoulos, G. D.; Heumüller, T.; Wilkinson, B.; Kirchartz, T.; Spiecker, E.; et al. Balancing Electrical and Optical Losses for Efficient 4-Terminal Si–Perovskite Solar Cells with Solution Processed Percolation Electrodes. *J. Mater. Chem. A* **2018**, 6, 3583–3592.

(63) Jaysankar, M.; Filipič, M.; Zielinski, B.; Schmager, R.; Song, W.; Qiu, W.; Paetzold, U. W.; Aernouts, T.; Debucquoy, M.; Gehlhaar, R.; et al. Perovskite–Silicon Tandem Solar Modules with Optimised Light Harvesting. *Energy Environ. Sci.* **2018**, 11, 1489–1498.

(64) Sahli, F.; Werner, J.; Kamino, B. A.; Bräuninger, M.; Monnard, R.; Paviet-Salomon, B.; Barraud, L.; Ding, L.; Diaz Leon, J. J.; Sacchetto, D.; et al. Fully Textured Monolithic Perovskite/Silicon Tandem Solar Cells with 25.2% Power Conversion Efficiency. *Nat. Mater.* **2018**, 17, 820–826.

(65) Werner, J.; Sahli, F.; Fu, F.; Diaz Leon, J. J.; Walter, A.; Kamino, B. A.; Niesen, B.; Nicolay, S.; Jeangros, Q.; Ballif, C. Perovskite/Perovskite/Silicon Monolithic Triple-Junction Solar Cells with a Fully Textured Design. *ACS Energy Lett.* **2018**, 3, 2052–2058.

(66) Uhl, A. R.; Yang, Z.; Jen, A. K.-Y.; Hillhouse, H. W. Solution-Processed Chalcopyrite–Perovskite Tandem Solar Cells in Bandgap-Matched Two- and Four-Terminal Architectures. *J. Mater. Chem. A* **2017**, 5, 3214–3220.

(67) Jošt, M.; Bertram, T.; Koushik, D.; Marquez, J. A.; Verheijen, M. A.; Heinemann, M. D.; Köhnen, E.; Al-Ashouri, A.; Braunger, S.; Lang, F.; et al. 21.6%-Efficient Monolithic Perovskite/Cu(In,Ga)Se_2 Tandem Solar Cells with Thin Conformal Hole Transport Layers for Integration on Rough Bottom Cell Surfaces. *ACS Energy Lett.* **2019**, 4, 583–590.

(68) Heo, J. H.; Im, S. H. $CH_3NH_3PbBr_3$-$CH_3NH_3PbI_3$ Perovskite-Perovskite Tandem Solar Cells with Exceeding 2.2 V Open Circuit Voltage. *Adv. Mater.* **2016**, 28, 5121–5125.

(69) Zhang, Y.; Wu, Z.; Li, P.; Ono, L. K.; Qi, Y.; Zhou, J.; Shen, H.; Surya, C.; Zheng, Z. Fully Solution-Processed TCO-Free Semitransparent Perovskite Solar Cells for Tandem and Flexible Applications. *Adv. Energy Mater.* **2018**, 8,

(70) Eperon, G. E.; Leijtens, T.; Bush, K. A.; Prasanna, R.; Green, T.; Wang, J. T.-W.; McMeekin, D. P.; Volonakis, G.; Milot, R. L.; May, R.; et al. Perovskite-Perovskite Tandem Photovoltaics with Optimized Band Gaps. *Science* **2016**, 354, 861–865.

(71) Tong, J.; Song, Z.; Kim, D. H.; Chen, X.; Chen, C.; Palmstrom, A. F.; Ndione, P. F.; Reese, M. O.; Dunfield, S. P.; Reid, O. G.; et al. Carrier Lifetimes of >1 μs in Sn-Pb Perovskites Enable Efficient All-Perovskite Tandem Solar Cells. **2019**, 364, 475-479.

(72) Karani, A.; Yang, L.; Bai, S.; Futscher, M. H.; Snaith, H. J.; Ehrler, B.; Greenham, N. C.; Di, D. Perovskite/Colloidal Quantum Dot Tandem Solar Cells: Theoretical Modeling and Monolithic Structure. *ACS Energy Lett.* **2018**, 3, 869–874.

(73) Kim, J.; Ouellette, O.; Voznyy, O.; Wei, M.; Choi, J.; Choi, M.-J.; Jo, J. W.; Baek, S.-W.; Fan, J.; Saidaminov, M. I.; et al. Butylamine-Catalyzed Synthesis of Nanocrystal Inks Enables Efficient Infrared CQD Solar Cells. *Adv. Mater.* **2018**, 30, 1803830.

(74) Frauenhofer ISE. *Photovoltaics Report*; Frauenhofer ISE: Munich, Germany, 2019; pp 1–48.

(75) Vos, A. D. Detailed Balance Limit of the Efficiency of Tandem Solar Cells. *J. Phys. Appl. Phys.* **1980**, 13, 839–846.

HUMIDITY-INDUCED TRANSITIONS IN HOIPS AND RELATED METAL HALIDES

Chapter 2: The Stabilizing and Destabilizing Nature of Bi on $CH_3NH_3PbI_3$ (MAPI) Perovskite in Humidity[†]

2.1 INTRODUCTION

Methylammonium lead iodide ($CH_3NH_3PbI_3$, MAPI) is a hybrid organic–inorganic perovskite (HOIP) with applications in photovoltaic devices (PVs),[1,2] light-emitting diodes (LEDs),[3-5] lasers,[3,4] photocatalytic systems,[6] and radiation detectors.[7] However, MAPI is highly susceptible to degradation under humidity,[8,9] which limits its commercial application. According to previous reports, MAPI degrades via the reversible formation of monohydrate and dihydrate species before a final irreversible degradation into PbI_2 by the following reaction pathway:[8,10–14]

$$CH_3NH_3PbI_{3\,(s)}+H_2O_{(g)}\rightleftharpoons CH_3NH_3PbI_3\cdot H_2O_{(s)} \quad (2.1)$$

$$4CH_3NH_3PbI_3\cdot H_2O_{(s)}\rightleftharpoons (CH_3NH_3)_4PbI_6\cdot 2H_2O_{(s)}+3PbI_{2\,(s)}+2H_2O_{(g)} \quad (2.2)$$

$$(CH_3NH_3)_4PbI_6\cdot 2H_2O_{(s)}\longrightarrow 4CH_3NH_{2\,(g)}+4HI_{(g)}+PbI_{2\,(s)}+2H_2O_{(g)} \quad (2.3)$$

The resulting PbI_2 is the only remaining solid material. It is shown that encapsulation in hydrophobic fluoropolymers or glass can stabilize MAPI up to several months;[15,16] however, higher intrinsic stability would greatly help reach commercial viability.[17]

[†]Reprinted with permission from Siegler, T.D., Houck, D.W., Cho, S.H., Milliron, D.J., Korgel, B.A.* (**2019**) "Bismuth Enhances the Stability of $CH_3NH_3PbI_3$ (MAPI) Perovskite Under High Humidity". *J. Phys. Chem. C.* 123 (1): 963-970. http://pubsdc3.acs.org/articlesonrequest/AOR-k6nrAUfnYy25MCzExREN.Copyright 2018 American Chemical Society. TDS conceived and carried out all experiments except XPS, analyzed data, and wrote the manuscript.

The intrinsic stability of MAPI can be tuned by replacing MA^+, Pb^{2+}, or I^- with other chemical species, either by bringing the Goldschmidt tolerance factor closer to one,[18,19] improving the film morphology,[20–22] or strengthening hydrogen bonding between organic A site components and the halide moiety.[10,23–25] For enhancing stability, replacement of MA^+ with formamidinium ($CH(NH^2)_2^+$ FA^+)[26] or cesium (Cs^+),[18,27,28] and I^- with Br^-,[22] Cl^-,[20] thiocyanate,[29,30] or selenide,[31] can all improve the humidity stability of MAPI. There have also been numerous reports detailing the substitution of Pb^{2+} with other species, but most of these do not mention the resulting stability of the materials in detail. In^{3+} has been shown to stabilize $CH_3NH_3PbI_{3-x}Cl_x$ PVs stored on a benchtop,[32] and the addition of Sr^{2+} to $CsPbI_2Br$ significantly improves the stability of encapsulated PVs stored at <50% RH in the dark.[33] Improved benchtop stability of PVs has also been reported for $CH_3NH_3Pb_{0.95}Sn_{0.05}I_3$ devices with added CuBr and MAPI devices with added Co.[34,35] However, many of these humidity-induced degradation studies do not adequately control for light, humidity condition, or environment from day to day.

There has been some preliminary work detailing the impact of bismuth on HOIP stability, but it is currently limited in scope. The additions of Bi,[19,21,36] Sr,[37] and Eu[38] have been shown to stabilize the cubic perovskite α-phase of materials where the preferred phase at room temperature is the orthorhombic non-perovskite δ-phase, such as $CsPbI_3$[19,36–38] and $FAPbI_3$.[21] It has been proposed that these additives enhance the stability of the cubic perovskite phase by either modifying the tolerance factor,[19,36] increasing microstrain from reduced crystallite size,[38] or by reducing humidity degradation rates,[21] since water vapor catalyzes the α-to-δ phase transition.[39] Lehner et al.[40] suggest that $A_3Bi_2I_9$ (A = K, Rb, Cs) compounds, in general, are more durable than their lead perovskite analogues, having observed unchanging X-ray diffraction (XRD) patterns from samples stored for months in air (although the storage conditions were not specified, i.e., humidity level, lighting conditions, and no direct comparison between $A_3Bi_2I_9$ and MAPI is made). Another recent paper reported PVs with heterogeneously mixed $FA_{0.83}MA_{0.17}Pb(I_{0.83}Br_{0.17})_3$ and $MA_3Bi_2Br_9$ that demonstrated better thermal stability and comparable humidity stability to single-phase $FA_{0.83}MA_{0.17}Pb(I_{0.83}Br_{0.17})_3$.[41]

Here we explore the addition of Bi as a route for stabilizing MAPI in the presence of humidity. We find that partial substitution of Pb^{2+} with Bi^{3+} can either stabilize or destabilize MAPI depending on the relative humidity (RH). At 90%, the addition of Bi^{3+} significantly reduces the rate of degradation of MAPI. However, at 60% RH, added Bi^{3+} significantly increases the rate of degradation. We propose that the added Bi^{3+} accelerates and decelerates different reaction pathways involved in the degradation of MAPI, which results in stabilization or degradation of MAP(Bi)I depending on the amount of moisture in the environment.

2.2 Experimental Details

2.2.1 Materials

Lead iodide (PbI_2, 99.999% ultradry, Alfa Aesar), bismuth iodide (BiI_3, 99.998% ultradry, Alfa Aesar), methylammonium iodide (CH_3NH_3I, MAI, Dye-Sol), anhydrous diethyl ether ($(CH_3CH_2)_2O$, anhydrous >99.0%, BHT inhibitor, Sigma), anhydrous dimethyl sulfoxide ($(CH_3)_2SO$, anhydrous 99.9%, Sigma), anhydrous dimethylformamide ($HCON(CH3)_2$, 99.8% Sigma), ethanol (CH_3CH_2OH, 200 proof, Fisher Scientific), glycerol ($HOCH_2CH(OH)CH_2OH$, 98%, Fisher Scientific), and (3-aminopropyl)triethyoxysilane ($H_2N(CH_2)_3Si(OC_2H_5)_3$, >98%, Sigma) were all used as received.

2.2.2 Preparation of MAPI and MAP(Bi)I Films

Glass substrates (1″ × 1″, Cardinal Glass) were sonicated in ethanol for 30 min and immersed in (3-aminopropyl)triethoxysilane (APTES) in ethanol (1:9 APTES/ethanol vol ratio) for 5 min. A drop of water was added to the APTES solution to promote APTES

grafting. The substrates were rinsed with IPA and heated at 100 °C in ambient air for 10 min.

Smooth perovskite films were deposited on glass substrates using a modification of the procedure developed by Park et al.[42] A MAPI precursor solution was dissolved by adding 273 mg of PbI_2, 95 mg of MAI, and 120 mL of dimethyl sulfoxide (DMSO) to 480 mL of dimethylformamide (DMF) and stirring at room temperature for 2 h. The resultant solution had a 1:1 molar ratio of PbI_2/MAI. Likewise, 356 mg of BiI_3, 95 mg of MAI, and 120 mL of DMSO were dissolved in 480 mL of DMF in a separate vial, forming a 1:1 molar ratio BiI_3/MAI. After 2 h of stirring, to generate the MAP(Bi)I precursor solution, the lead-based solution was mixed with the bismuth-based solution in a 19:1 ratio by volume (5 mol % Bi on a metal basis), forming a solution with a 0.95:0.05:1 PbI_2/BiI_3/MAI mole ratio.

Spin-coating was performed on glass slides coated with APTES in a nitrogen glovebox with $O_2 < 5$ ppm. Respective precursor solution (50 μL) was spread evenly over the substrate, and then the substrate was spun at 5000 rpm for 30 s, with a ramp rate of 2500 rpm/s. About 12–15 s into the spin-coating process, ∼500 μL of diethyl ether was dropped onto the substrate, creating smooth, clear, uniform films. Films were immediately annealed at 60 °C for 1 min, then at 100 °C for 2 min. The resulting films were smooth and semitransparent.

2.2.3 Exposure of MAPI and MAP(Bi)I Perovskite Films to Humidity

Perovskite films were aged in a home-built humidity chamber. Humidity was controlled by mixing water and glycerol in the appropriate ratios and waiting ∼48 h for the mixture to equilibrate with the sealed atmosphere.[10,43] For 90% RH, 28 mL of DI H_2O was mixed with 12 mL of glycerol. For 60% RH, 13.4 mL of DI H_2O was added to 26.6 mL of

glycerol. MAPI and MAP(Bi)I films were exposed to humidity under controlled indoor lighting with ~2 mW/cm^2 total light intensity, as measured by a Newport Optical model 1916-C meter with an 818P-020-12 high power detector. The intensity spectrum of the light source (GE, Starcoat T5 EcoLux High Efficiency & High Output Bulbs, 46705, 3500 K operating temperature) is provided by the manufacturer in their specification sheet.[44]

2.2.4 Materials Characterization

X-ray diffraction (XRD) was carried out using a Rigaku R-Axis Spider X-Ray Diffractometer with an image plate detector and Cu Kα radiation source (λ = 0.154 nm). Samples were probed directly on prepared glass substrates using a flat substrate holder. Scans were performed for 10 min at 5°/s sample rotation under 40 kV and 40 mA radiation.

X-ray photoelectron spectroscopy (XPS) samples were prepared by depositing perovskite films onto a treated fluorinated tin oxide (FTO) glass substrate. The samples were loaded onto the sample holder with copper tape and grounded with conductive carbon tape to minimize charging of the film. Samples were exposed to ultrahigh vacuum for less than 5 h before spectra were taken to eliminate off-gassing of volatile methylamine moieties. XPS spectra were obtained with a Kratos photoelectron spectrophotometer using a monochromatic Al Kα X-ray source and a 180° hemispherical analyzer. The spectra were processed with CasaXPS software. Charging was corrected by shifting the spectra such that the C 1s peaks are at the expected binding energy of adventitious carbon (284.8 eV). Peak fitting was performed using a Shirley background subtraction and the Gaussian–Lorentzian profile. For composition estimates, each fit peak was integrated and divided by the corresponding relative sensitivity factor in the Kratos library.

Scanning electron microscopy (SEM) images were acquired with a Hitachi S550 SEM/STEM operated at 20 keV in SEM mode. Samples were imaged on FTO glass slides,

prepared as described above. Charging was minimized by grounding the sample with conductive carbon tape.

UV–vis–NIR absorptance and absorbance spectroscopy was performed on perovskite films on glass substrates in an Agilent Cary 5000 UV–vis–NIR spectrophotometer. Absorptance was measured by placing samples in an Agilent Diffuse Reflectance Accessory (DRA)-2500 series with a PbS NIR detector and a R928 photomultiplier tube for visible range detection. Spectra were collected in transflectance mode using a center mount holder. Baselines were taken by placing a piece of cleaned glass in the center mount for the 100% T baseline and by blocking the beam at the transmission port of the DRA with aluminum foil for the 0% T baseline. The absorptance, A, is related to the reflectance, R, and the transmittance T, of the film: A = 1 – R – T. The absorptance, A, is related to the absorbance A, of the sample as $A = 1 - 10^{-\mathcal{A}}$.[45]

2.3 Results and Discussion

2.3.1 Film Characterization

MAPI and MAP(Bi)I films were deposited as described. The MAPI and MAP(Bi)I films have similar appearance, as observed in the photograph in the inset of Figure 2.1a, and absorbance features consistent with literature as seen in Figure 2.1a. Specifically, MAPI exhibits an absorption edge at 800 nm (1.5 eV) and absorption plateaus at 580 and 745 nm.[10] The MAP(Bi)I film also exhibits two absorption plateaus near 580 and 745 nm, with a slightly red-shifted absorption edge. A similar red shift has been reported in previous studies on hybrid organic–inorganic perovskites doped with Bi^{3+} and has been attributed to the introduction of shallow trap states that increase the density of optically active traps states in the Urbach tail of the thin film.[46–51] The films in Figure 2.1a have similar

thickness, indicating that the absorption coefficients of the MAPI and MAP(Bi)I are similar, consistent with the expected nature of bismuth doping in hybrid organic–inorganic perovskites.[46−51]

X-ray diffraction (XRD) data in Figure 2.1b show that the MAPI and MAP(Bi)I films have tetragonal perovskite crystal structure, which is the expected room-temperature phase of MAPI.[10,29,46] There are no additional crystalline phases in either MAPI or MAP(Bi)I films, and the diffraction patterns have similar peak positions, consistent with other reports of aliovalent doping with Bi[46,49,52,53] and other B-site substitutions.[32,54,55] X-ray photoelectron spectroscopy (XPS) also confirmed the presence of Bi in the MAP(Bi)I films. Figure 2.1c shows XPS from the Bi 4f7/2 spectral region. These peaks with binding energies between 157 and 161 eV indicate that Bi has a +3 oxidation state,[56] and the Bi 4f to Pb 4f XPS peak ratios show that the Bi/Pb mole ratio in the MAP(Bi)I film is 0.04.

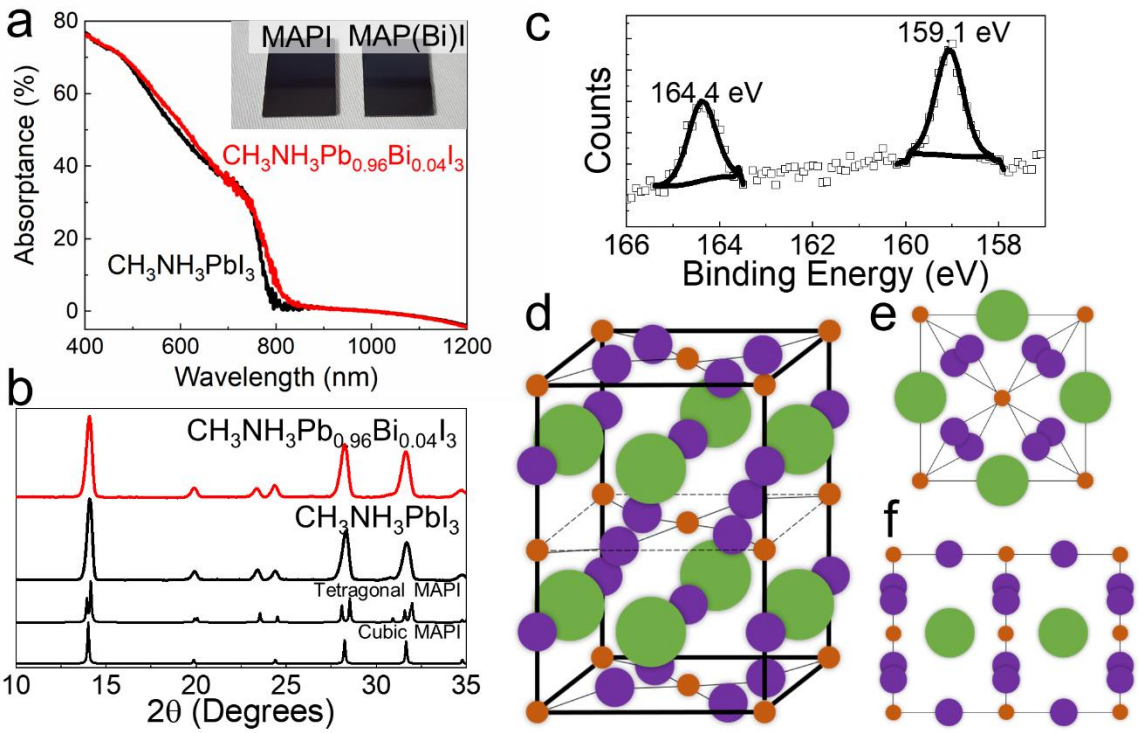

Figure 2.1: (A) UV–vis-NIR absorptance spectra of $CH_3NH_3Pb_{0.96}Bi_{0.04}I_3$ and $CH_3NH_3PbI_3$ films. Inset: photographs of MAPI (left) and MAP(Bi)I (right) films on APTES-coated glass. (B) XRD of $CH_3NH_3Pb_{0.96}Bi_{0.04}I_3$ (MAP(Bi)I) and $CH_3NH_3PbI_3$ (MAPI) films alongside reference patterns taken from the Crystallography Open Database (COD) for tetragonal and cubic phase MAPI films (COD #4124388 and #4335634, respectively), showing that both films are single-phase tetragonal MAPI films with no noticeable peak shifts or secondary phases upon bismuth incorporation. (C) XPS spectrum in the Bi 4f region for $CH_3NH_3Pb_{0.96}Bi_{0.04}I_3$, with peak positions of the fitted Gaussian–Lorentzian function labeled. Data are represented by the hollow points and fitted Gaussian–Lorentzian cures by lines. These peaks are characteristic of Bi in the 3+ oxidation state, and peak integration/comparison with the Pb 4f region gives a Bi/Pb molar ratio of 0.04:1. (D) Tetragonal crystal structure of methylammonium lead iodide and projections of MAPI viewed down the (E) ⟨001⟩ and (F) ⟨100⟩ directions. Methylammonium atoms are shown by large green circles, iodide ions are moderately sized purple circles, and lead ions are small orange circles.

2.3.2 Humidity Stability Behavior

The stability of MAPI and MAP(Bi)I films in the presence of humidity was tested in by monitoring UV-Vis-NIR absorbance spectra over time while aging in a humidity chamber. Figures 2.2 and 2.3 show photographs and optical absorptance spectra of MAPI and MAP(Bi)I films exposed to air for several days at 90 and 60% RH. Degraded MAPI films look yellow, with absorptance that decreases between 525 and 800 nm.[8,10] This is consistent with the band gaps of MAPI and its degradation byproducts. MAPI has an absorption onset at 1.55 eV (800 nm),[10] whereas PbI_2 and MAPI monohydrate, the solid degradation byproducts of MAPI, have absorption edges at 2.3 eV (540 nm) and 3.1 eV (400 nm), respectively.[8,10,12,57] Figures 2.2D,E and 2.3D,E show the absorptance spectra of MAPI and MAP(Bi)I films changing over time when exposed to air at 90 and 60% RH. The MAPI film becomes completely transparent between 525 and 800 nm after only 1 day of exposure to air at 90% RH. MAPI is significantly more stable in 60% RH, and it takes about 12 days for the film to become transparent in this optical window. At high humidity (90% RH), the MAP(Bi)I film is significantly more stable than the MAPI film, and it takes 3 days for the film to go clear. In contrast, the MAP(Bi)I film is less stable than the MAPI film at lower humidity of 60% RH, changing from the black tetragonal phase to the yellow degradation product of PbI_2 in only 8 days. Note that these degradation rates are indicative of MAPI and MAP(Bi)I films stored under room light, so degradation is slightly accelerated relative to other degradation studies.[10,58−61]

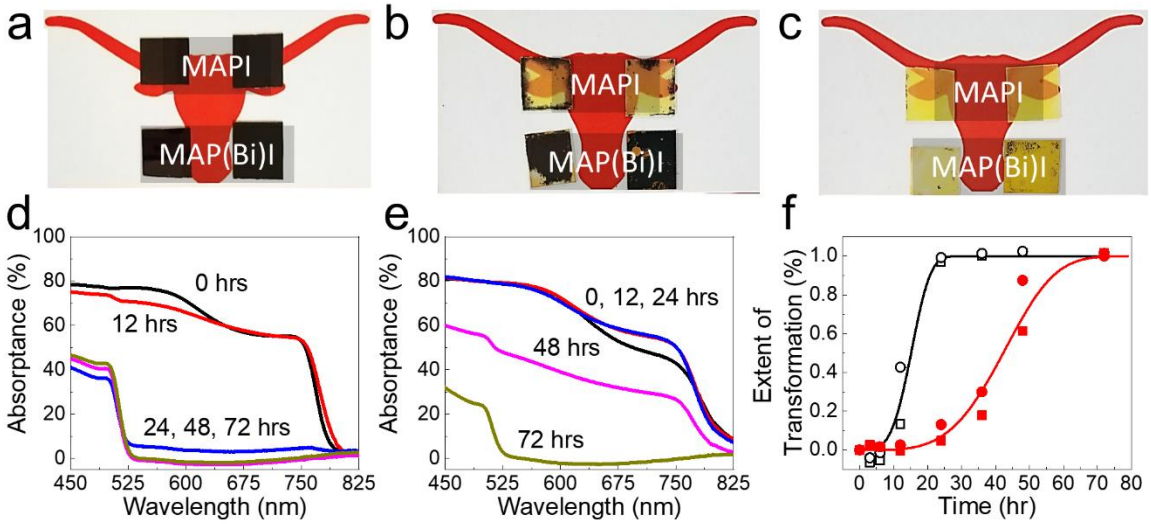

Figure 2.2: (A–C) Photographs of MAPI and MAP(Bi)I films (A) before and (B,C) after exposure to 90% RH air under indoor lighting (2 mW/cm^2) for (B) 24 h and (C) 72 h. (d, e) UV–vis-NIR absorptance spectra of (d) MAPI and (e) MAP(Bi)I thin films after exposure to air at 90% RH under controlled indoor lighting. (f) Extent of transformation of the (□, ○) MAPI and (■, ●) MAP(Bi)I films as a function of exposure time to 90% RH. The solid lines are the best fits of Eqn (2.4) to the MAPI (black line) and MAP(Bi)I (red line) data, with n = 3.9, k = 1.87 × 10^{-5} h$^{-3.9}$ (r^2 = 0.88) and n = 4.0, k = 2.17 × 10^{-7} h$^{-4.0}$ (r^2 = 0.85), respectively.

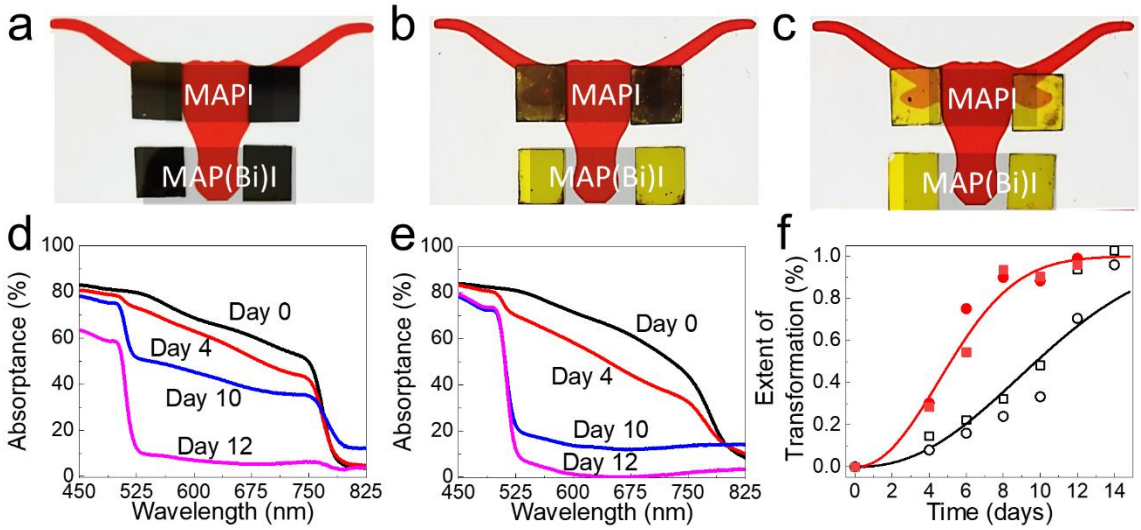

Figure 2.3: (A–C) Photographs of MAPI and MAP(Bi)I films (A) before and (B,C) after exposure to air at 60% RH under indoor lighting (2 mW/cm^2) for (B) 8 days, and (C) 14 days. The top row of films in photographs corresponds to MAPI films, whereas the bottom row corresponds to MAP(Bi)I. (D, E) UV–vis-NIR absorptance profiles of (D) MAPI and (E) MAP(Bi)I thin films after different aging times at 60% RH in indoor lighting. (F) Plot of the extent of transformation of the (□, ○) MAPI and (■, ●) MAP(Bi)I films. The solid lines are the best fits of eq 4 to the MAPI (black line) and MAP(Bi)I (red line) data, with n = 2.3, k = 3.94 × 10^{-3} day$^{-2.3}$ (r^2 = 0.81) and n = 2.1, k = 2.15 × 10^{-2} day$^{-2.1}$ (r^2 = 0.91), respectively.

The data in Figures 2.2 and 2.3 show that inclusion of bismuth stabilizes MAPI under high humidity (90% RH), while resulting in faster degradation at lower humidity (60% RH). We analyzed the data using an Avrami equation,[62,63]

$$y = 1 - \exp\left(-kt^n\right) \tag{2.4}$$

where k is a rate constant, n is the Avrami exponent, and y is extent of transformation. The extent of transformation is calculated from the logarithmic absorptance at 600 nm by y = $\log\left(1 - A_{600nm}(t)\right) / \log\left(1 - A_{600nm}(0)\right)$. Interestingly, Avrami coefficients n taken from fits of the Avrami equation (Eqn 2.4) to the data in Figures 2.2f and 2.3f are constant as a function of composition, but not as a function of humidity. At 90% RH, both MAPI

and MAP(Bi)I show Avrami coefficients close to 4, indicating that MAPI degradation occurs by concurrent nucleation and isotropic growth of domains of degradation product.[63] At lower humidity (60% RH), MAPI and MAP(Bi)I fits show values close to n = 2, indicating that the degradation products form anisotropically, perhaps nucleating and growing initially along grain boundaries.[63] The difference in the values of n is consistent with two different degradation pathways for the films at different humidity conditions. The values of k for the MAPI and MAP(Bi)I films are also significantly higher under lower humidity conditions. The characteristic times for the films to degrade, $\tau = \sqrt[n]{1/k}$, are 16.3 and 46.3 h at RH = 90% and 11.1 and 6.2 days at RH = 60% for the MAPI and MAP(Bi)I films, respectively. To our knowledge, this is the first example of a humidity-specific stability enhancement from compositional engineering in HOIP materials. Previously observed enhancements in MAPI stability under humidity with various additives have been attributed to the formation of a layered perovskite structure[29,40] or an improved film morphology.[32] These effects reduce the penetration of water vapor into the film and provide enhanced stability under a wide range of humidity. Since Bi addition only stabilizes MAPI at high humidity and actually reduces the stability at lower humidity, it probably does not reduce the rate of water vapor penetration into the film, as in these other cases, but provides enhanced stability for a different reason. Furthermore, the addition of Bi to the MAPI films did not have any obvious effect on the morphology of the film (Figure 2.4).

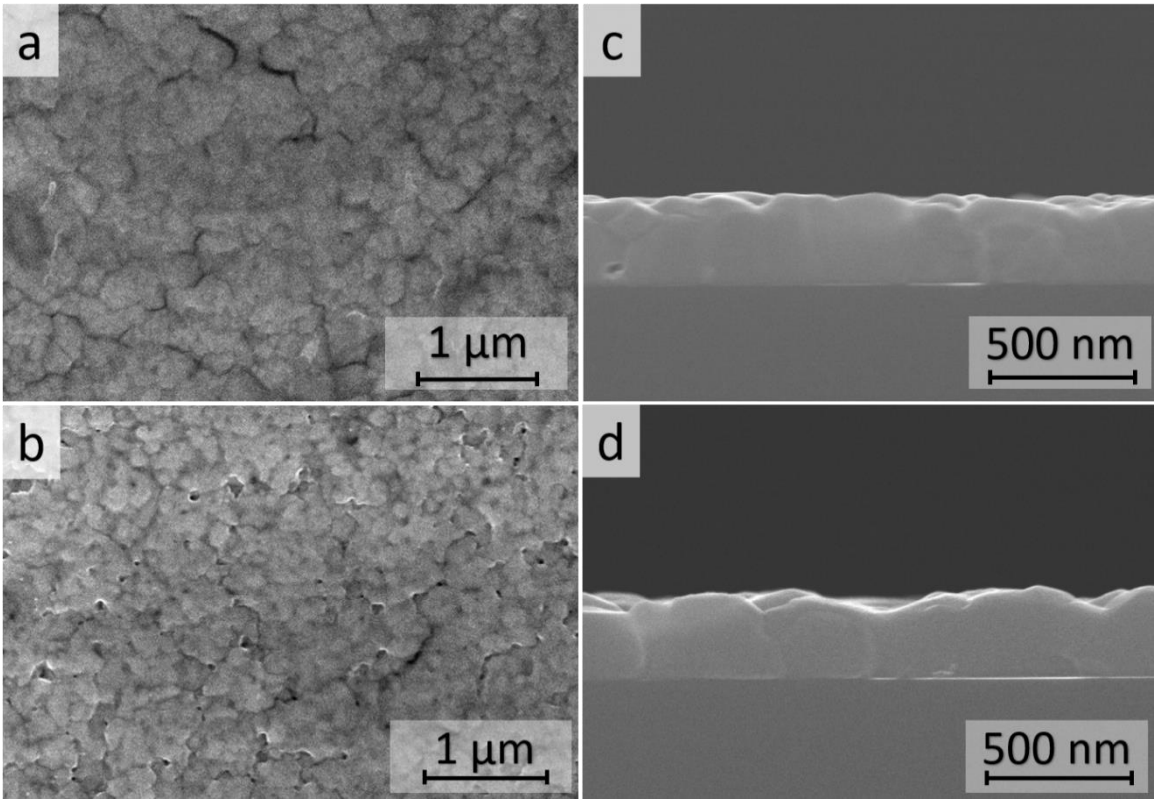

Figure 2.4 SEM images of (A,C) MAPI and (B,D) MAP(Bi)I films. The images in (A,B) are top-down views of the films on glass. The images in (C,D) are cross sections of the films on silicon. The average film thicknesses in (C) and (D) are 276 +/- 29 nm and 274 +/- 29 nm, respectively. No noticeable change in surface morphology is noted between MAPI and MAP(Bi)I

2.3.3 Probing Degradation Mechanism

The degradation of MAPI under humid conditions begins by hydration to $CH_3NH_3PbI_3 \cdot H_2O$ as seen in Eqn 2.1. Above ~80% RH, this monohydrate species is stable and can be detected spectroscopically.[10−13,64] At lower humidity, it spontaneously decomposes, either (1) reverting back to $CH_3NH_3PbI_3$ and water vapor (reversion to pristine tetragonal MAPI phase) or (2) decomposing further to a dihydrate and PbI_2, with the dihydrate decomposing rapidly soonafter.[8,10,12,13] The absorptance spectra of degraded MAPI and MAP(Bi)I films in Figure 2.5A and 2.5B all have an absorption onset at 525 nm demonstrating the presence of PbI_2; however, only films exposed to 90% RH show the additional onset of an absorption feature at 430 nm characteristic of MAPI monohydrate.[12,57] XRD (Figure 2.5C) also shows peaks that correspond to MAPI monohydrate. These observations indicate that degradation at 90% RH occurs by the reaction pathway shown in eq 1 (monohydrate formation), whereas at 60% RH, the degradation pathway follows eq 2 (dihydrate formation).

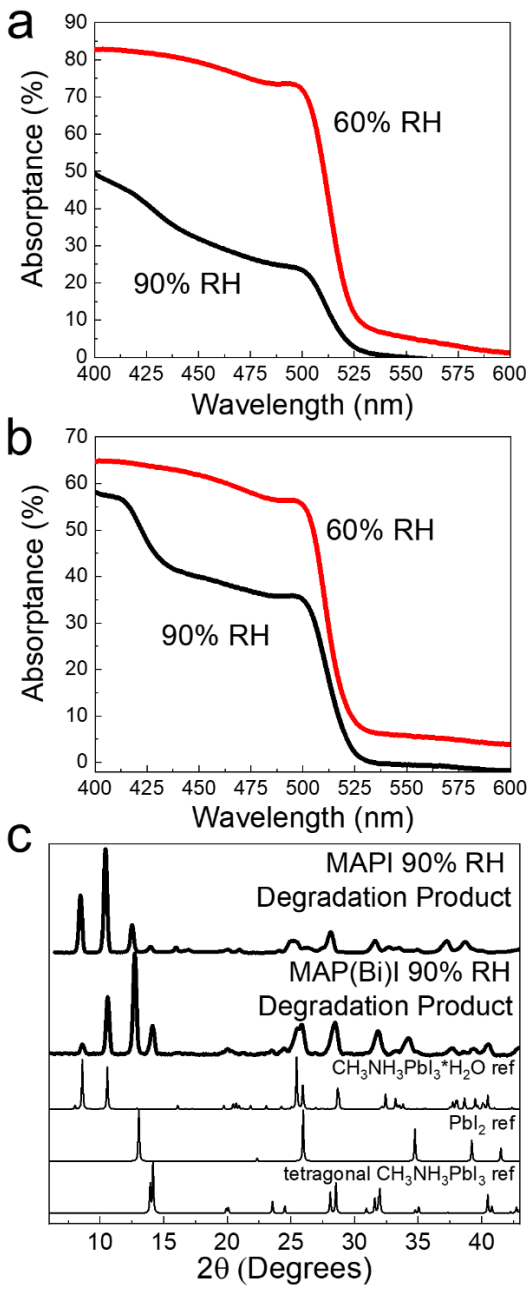

Figure 2.5. UV–vis-NIR absorptance spectroscopy of (A) MAPI and (B) MAP(Bi)I films after exposure to 60% RH for 14 and 12 days, respectively, and 90% RH for 36 h and 3 days, respectively. (C) XRD of the degradation products of MAPI and MAP(Bi)I films exposed to 90% RH. Reference patterns for tetragonal MAPI (COD #4124388), PbI_2 (COD #1010062), and MAPI monohydrate (COD #7117405) are provided for comparison.

To determine the reversibility of the MAPI and MAP(Bi)I degradation reaction and gain insight about the role of Bi in stabilizing the films at high humidity, films were degraded to their clear state by exposure to 90% RH and then heated at 100 °C in air at 50% RH for 2 min. This dehydration step forces the monohydrate to either (I) regenerate the dark state or (II) further decompose into dihydrate to MAPI and PbI_2, as in Eqn. 2.2. The amount PbI_2 generated relative to the amount of MAPI regenerated in the dehydration step provides a signature of the relative rate of the reaction in eq 2 for the MAPI and MAP(Bi)I films.[64] This is determined from the ratio of the absorptance of the film before exposure to humidity $A_0(\lambda)$, after exposure $A_{aged}(\lambda)$, and after dehydration $A_{dehyd}(\lambda)$

$$\theta(\lambda) = \frac{A_{dehyd}(\lambda) - A_{aged}(\lambda)}{A_0(\lambda) - A_{aged}(\lambda)} \tag{2.5}$$

Higher values of $\theta(\lambda)$ between 525 and 800 nm indicate a higher degree of reversion to tetragonal perovskite, and a sharper increase of $\theta(\lambda)$ at the lead iodide absorbance edge at 525 nm indicates that more PbI_2 has formed. Figures 2.6A and 2.6B show the absorptance spectra of the MAPI and MAP(Bi)I films, and Figure 2.6C shows the corresponding values of $\theta(\lambda)$. The MAP(Bi)I films demonstrate more PbI_2 generation during dehydration than the MAPI films. The XRD of the MAPI and MAP(Bi)I films after the heating step, shown in Figure 2.6D, also show that more PbI_2 has formed in the film with Bi. This indicates that the rate of reaction for Eqn 2.2 is faster when Bi is present in the film. It also explains why MAP(Bi)I is less stable than MAPI when exposed to lower humidity conditions, even though the rate of the reaction in Eqn 2.1 is reduced with addition of Bi.

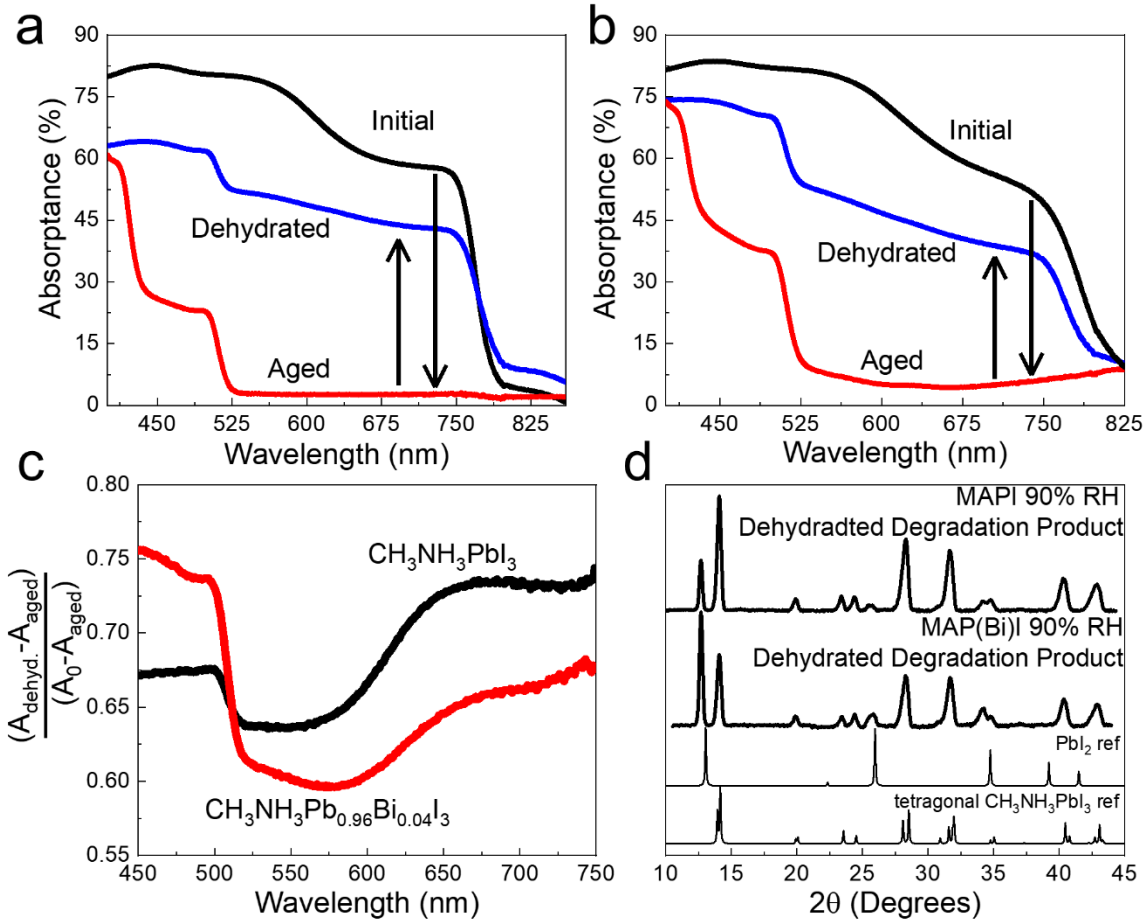

Figure 2.6. UV–vis-NIR absorptance spectra of (A) MAPI and (B) MAP(Bi)I films on glass after 1 cycle of degradation at 90% RH, followed by dehydration with heating at 100 °C in 50% RH air for 2 min. (C) Ratios of the absorptance of MAPI and MAP(Bi)I films before and after exposure to humidity and dehydration θ(λ), calculated using Eqn. 2.5. (D) XRD of MAPI and MAP(Bi)I films after degrading the MAPI and MAP(Bi)I films to the clear state with exposure to 90% RH air and then dehydration by heating at 100 °C in 50% RH air for 2 min. Peaks matching tetragonal phase of MAPI (COD #4124388) are designated with vertical gray lines, whereas dashed yellow lines designate degradation byproduct PbI_2 (COD #1010062).

2.4 Conclusion

In conclusion, the incorporation of Bi into MAPI slows the degradation of the film at high humidity (90% RH). At lower humidity (60% RH), the added Bi enhances the rate of degradation of the film. This is the result of two different degradation pathways, which are either slowed (i.e., Eqn 1) or enhanced (i.e., Eqn 2) by the addition of Bi. These results show that partial substitution of Pb in HOIPs may be an effective way to improve stability under humidity; however, more generally, they show that the compositional engineering of HOIPs may lead to differences in stabilization or destabilization that depend on the actual environmental conditions, and film stability should be tested over a range of environmental conditions to determine the overall effect of the additive on the stability of the material.

2.5 References

(1) Saliba, M.; Correa-Baena, J.-P.; Grätzel, M.; Hagfeldt, A.; Abate, A. Perovskite Solar Cells: From the Atomic Level to Film Quality and Device Performance. *Angew. Chem. Int. Ed.* **2018**, 57, 2554–2569.

(2) Unger, E. L.; Kegelmann, L.; Suchan, K.; Sörell, D.; Korte, L.; Albrecht, S. Roadmap and Roadblocks for the Band Gap Tunability of Metal Halide Perovskites. *J. Mater. Chem. A* **2017**, 5, 11401–11409.

(3) Adjokatse, S.; Fang, H.-H.; Loi, M. A. Broadly Tunable Metal Halide Perovskites for Solid-State Light-Emission Applications. *Mater. Today* **2017**, 20, 413–424.

(4) Veldhuis, S. A.; Boix, P. P.; Yantara, N.; Li, M.; Sum, T. C.; Mathews, N.; Mhaisalkar, S. G. Perovskite Materials for Light-Emitting Diodes and Lasers. *Adv. Mater.* **2016**, 28, 6804–6834.

(5) Zhang, Q.; Su, R.; Du, W.; Liu, X.; Zhao, L.; Ha, S. T.; Xiong, Q. Advances in Small Perovskite-Based Lasers. *Small Methods* **2017**, 1, 1700163.

(6) Chen, Y.-S.; Manser, J. S.; Kamat, P. V. All Solution-Processed Lead Halide Perovskite-$BiVO_4$ Tandem Assembly for Photolytic Solar Fuels Production. *J. Am. Chem. Soc.* **2015**, 137, 974–981.

(7) Yakunin, S.; Dirin, D. N.; Shynkarenko, Y.; Morad, V.; Cherniukh, I.; Nazarenko, O.; Kreil, D.; Nauser, T.; Kovalenko, M. V. Detection of Gamma Photons Using Solution-Grown Single Crystals of Hybrid Lead Halide Perovskites. *Nat. Photonics* **2016**, 10, 585–589.

(8) Manser, J. S.; Saidaminov, M. I.; Christians, J. A.; Bakr, O. M.; Kamat, P. V. Making and Breaking of Lead Halide Perovskites. *Acc. Chem. Res.* **2016**, 49, 330–338.

(9) Berhe, T. A.; Su, W.-N.; Chen, C.-H.; Pan, C.-J.; Cheng, J.-H.; Chen, H.-M.; Tsai, M.-C.; Chen, L.-Y.; Dubale, A. A.; Hwang, B.-J. Organometal Halide Perovskite Solar Cells: Degradation and Stability. *Energy Env. Sci* **2016**, 9, 323–356.

(10) Christians, J. A.; Miranda Herrera, P. A.; Kamat, P. V. Transformation of the Excited State and Photovoltaic Efficiency of $CH_3NH_3PbI_3$ Perovskite upon Controlled Exposure to Humidified Air. *J. Am. Chem. Soc.* **2015**, 137, 1530–1538.

(11) Müller, C.; Glaser, T.; Plogmeyer, M.; Sendner, M.; Döring, S.; Bakulin, A. A.; Brzuska, C.; Scheer, R.; Pshenichnikov, M. S.; Kowalsky, W.; et al. Water Infiltration in Methylammonium Lead Iodide Perovskite: Fast and Inconspicuous. *Chem. Mater.* **2015**, 27, 7835–7841.

(12) Leguy, A. M. A.; Hu, Y.; Campoy-Quiles, M.; Alonso, M. I.; Weber, O. J.; Azarhoosh, P.; van Schilfgaarde, M.; Weller, M. T.; Bein, T.; Nelson, J.; et al. Reversible Hydration of $CH_3NH_3PbI_3$ in Films, Single Crystals, and Solar Cells. *Chem. Mater.* **2015**, 27, 3397–3407.

(13) Schlipf, J.; Bießmann, L.; Oesinghaus, L.; Berger, E.; Metwalli, E.; Lercher, J. A.; Porcar, L.; Müller-Buschbaum, P. In Situ Monitoring the Uptake of Moisture into Hybrid Perovskite Thin Films. *J. Phys. Chem. Lett.* **2018**, 9, 2015–2021.

(14) Ciccioli, A.; Latini, A. Thermodynamics and the Intrinsic Stability of Lead Halide Perovskites $CH_3NH_3PbX_3$. *J. Phys. Chem. Lett.* **2018**, 9, 3756–3765.

(15) Bella, F.; Griffini, G.; Correa-Baena, J.-P.; Saracco, G.; Grätzel, M.; Hagfeldt, A.; Turri, S.; Gerbaldi, C. Improving Efficiency and Stability of Perovskite Solar Cells with Photocurable Fluoropolymers. *Science* **2016**, 354, 203-206.

(16) Zhou, Y.; Zhu, K. Perovskite Solar Cells Shine in the "Valley of the Sun." *ACS Energy Lett.* **2016**, 1, 64–67.

(17) Woodhouse, M.; Jones-Albertus, R.; Feldman, D.; Fu, R.; Horowitz, K.; Chung, D.; Jordan, D.; Kurtz, S. On the Path to SunShot: The Role of Advancements in Solar Photovoltaic Efficiency, Reliablity, and Cost; NREL/TP-6A20-65872; National Renewable Energy Laboratory, 2016.

(18) Li, Z.; Yang, M.; Park, J.-S.; Wei, S.-H.; Berry, J. J.; Zhu, K. Stabilizing Perovskite Structures by Tuning Tolerance Factor: Formation of Formamidinium and Cesium Lead Iodide Solid-State Alloys. *Chem. Mater.* **2016**, 28, 284–292.

(19) Hu, Y.; Bai, F.; Liu, X.; Ji, Q.; Miao, X.; Qiu, T.; Zhang, S. Bismuth Incorporation Stabilized α-$CsPbI_3$ for Fully Inorganic Perovskite Solar Cells. *ACS Energy Lett.* **2017**, 2, 2219–2227.

(20) Chae, J.; Dong, Q.; Huang, J.; Centrone, A. Chloride Incorporation Process in $CH_3NH_3PbI_{3-x}Cl_x$ Perovskites via Nanoscale Bandgap Maps. *Nano Lett.* **2015**, 15 (12), 8114–8121.

(21) Hu, Y.; Qiu, T.; Bai, F.; Miao, X.; Zhang, S. Enhancing Moisture-Tolerance and Photovoltaic Performances of $FAPbI_3$ by Bismuth Incorporation. *J. Mater. Chem. A* **2017**, 5, 25258–25265.

(22) Noh, J. H.; Im, S. H.; Heo, J. H.; Mandal, T. N.; Seok, S. I. Chemical Management for Colorful, Efficient, and Stable Inorganic–Organic Hybrid Nanostructured Solar Cells. *Nano Lett.* **2013**, 13, 1764–1769.

(23) Quarti, C.; Grancini, G.; Mosconi, E.; Bruno, P.; Ball, J. M.; Lee, M. M.; Snaith, H. J.; Petrozza, A.; Angelis, F. D. The Raman Spectrum of the $CH_3NH_3PbI_3$ Hybrid Perovskite: Interplay of Theory and Experiment. *J. Phys. Chem. Lett.* **2014**, 5, 279–284.

(24) Yamamoto, K.; Iikubo, S.; Yamasaki, J.; Ogomi, Y.; Hayase, S. Structural Stability of Iodide Perovskite: A Combined Cluster Expansion Method and First-Principles Study. *J. Phys. Chem. C* **2017**, 121, 27797–27804.

(25) Chun-Ren Ke, J.; Walton, A. S.; Lewis, D. J.; Tedstone, A.; O'Brien, P.; Thomas, A. G.; Flavell, W. R. In Situ Investigation of Degradation at Organometal Halide Perovskite Surfaces by X-Ray Photoelectron Spectroscopy at Realistic Water Vapour Pressure. *Chem. Commun.* **2017**, 53, 5231–5234.

(26) Li, W.-G.; Rao, H.-S.; Chen, B.-X.; Wang, X.-D.; Kuang, D.-B. A Formamidinium–Methylammonium Lead Iodide Perovskite Single Crystal Exhibiting Exceptional Optoelectronic Properties and Long-Term Stability. *J. Mater. Chem. A* **2017**, 5, 19431–19438.

(27) Kulbak, M.; Gupta, S.; Kedem, N.; Levine, I.; Bendikov, T.; Hodes, G.; Cahen, D. Cesium Enhances Long-Term Stability of Lead Bromide Perovskite-Based Solar Cells. *J. Phys. Chem. Lett.* **2016**, 7, 167–172.

(28) Saliba, M.; Matsui, T.; Seo, J.-Y.; Domanski, K.; Correa-Baena, J.-P.; Nazeeruddin, M. K.; Zakeeruddin, S. M.; Tress, W.; Abate, A.; Hagfeldt, A.; et al. Cesium-Containing Triple Cation Perovskite Solar Cells: Improved Stability, Reproducibility and High Efficiency. *Energy Env. Sci* **2016**, 9, 1989–1997.

(29) Jiang, Q.; Rebollar, D.; Gong, J.; Piacentino, E. L.; Zheng, C.; Xu, T. Pseudohalide-Induced Moisture Tolerance in Perovskite $CH_3NH_3Pb(SCN)_2$ I Thin Films. *Angew. Chem. Int. Ed.* **2015**, 54, 7617–7620.

(30) Tai, Q.; You, P.; Sang, H.; Liu, Z.; Hu, C.; Chan, H. L. W.; Yan, F. Efficient and Stable Perovskite Solar Cells Prepared in Ambient Air Irrespective of the Humidity. *Nature Commun.* **2016**, 7, 11105.

(31) Gong, J.; Yang, M.; Rebollar, D.; Rucinski, J.; Liveris, Z.; Zhu, K.; Xu, T. Divalent Anionic Doping in Perovskite Solar Cells for Enhanced Chemical Stability. *Adv. Mater.* **2018**, *30*, 1800973.

(32) Wang, Z.-K.; Li, M.; Yang, Y.-G.; Hu, Y.; Ma, H.; Gao, X.-Y.; Liao, L.-S. High Efficiency Pb-In Binary Metal Perovskite Solar Cells. *Adv. Mater.* **2016**, *28*, 6695-6703.

(33) Lau, C. F. J.; Zhang, M.; Deng, X.; Zheng, J.; Bing, J.; Ma, Q.; Kim, J.; Hu, L.; Green, M. A.; Huang, S.; et al. Strontium-Doped Low-Temperature-Processed $CsPbI_2Br$ Perovskite Solar Cells. *ACS Energy Lett.* **2017**, *2*, 2319–2325.

(34) Li, M.; Wang, Z.-K.; Zhuo, M.-P.; Hu, Y.; Hu, K.-H.; Ye, Q.-Q.; Jain, S. M.; Yang, Y.-G.; Gao, X.-Y.; Liao, L.-S. Pb-Sn-Cu Ternary Organometallic Halide Perovskite Solar Cells. *Adv. Mater.* **2018**, 30, 1800258.

(35) Xu, W.; Zheng, L.; Zhang, X.; Cao, Y.; Meng, T.; Wu, D.; Liu, L.; Hu, W.; Gong, X. Efficient Perovskite Solar Cells Fabricated by Co Partially Substituted Hybrid Perovskite. *Adv. Energy Mater.* **2018**, 8, 1703178.

(36) Swarnkar, A.; Mir, W. J.; Nag, A. Can B-Site Doping or Alloying Improve Thermal- and Phase-Stability of All-Inorganic $CsPbX_3$ (X = Cl, Br, I) Perovskites? *ACS Energy Lett.* **2018**, 3, 286–289.

(37) Lu, M.; Zhang, X.; Zhang, Y.; Guo, J.; Shen, X.; Yu, W. W.; Rogach, A. L. Simultaneous Strontium Doping and Chlorine Surface Passivation Improve Luminescence Intensity and Stability of $CsPbI_3$ Nanocrystals Enabling Efficient Light-Emitting Devices. *Adv. Mater.* **2018**, 30, 1804691.

(38) Jena, A. K.; Kulkarni, A.; Sanehira, Y.; Ikegami, M.; Miyasaka, T. Stabilization of α-$CsPbI_3$ in Ambient Room Temperature Conditions by Incorporating Eu into $CsPbI_3$. *Chem. Mater.* **2018**, 30, 6668-6674.

(39) Zhou, Y.; Kwun, J.; Garces, H. F.; Pang, S.; Padture, N. P. Observation of Phase-Retention Behavior of the $HC(NH_2)_2PbI_3$ Black Perovskite Polymorph upon Mesoporous TiO_2 Scaffolds. *Chem. Commun.* **2016**, 52, 7273–7275.

(40) Lehner, A. J.; Fabini, D. H.; Evans, H. A.; Hébert, C.-A.; Smock, S. R.; Hu, J.; Wang, H.; Zwanziger, J. W.; Chabinyc, M. L.; Seshadri, R. Crystal and Electronic Structures of Complex Bismuth Iodides $A_3Bi_2I_9$ (A = K, Rb, Cs) Related to Perovskite: Aiding the Rational Design of Photovoltaics. *Chem. Mater.* **2015**, 27, 7137–7148.

(41) Chen, C.; Liu, D.; Zhang, B.; Bi, W.; Li, H.; Jin, J.; Chen, X.; Xu, L.; Song, H.; Dai, Q. Carrier Interfacial Engineering by Bismuth Modification for Efficient and Thermoresistant Perovskite Solar Cells. *Adv. Energy Mater.* **2018**, 8, 1703659.

(42) Ahn, N.; Son, D.-Y.; Jang, I.-H.; Kang, S. M.; Choi, M.; Park, N.-G. Highly Reproducible Perovskite Solar Cells with Average Efficiency of 18.3% and Best Efficiency of 19.7% Fabricated via Lewis Base Adduct of Lead(II) Iodide. *J. Am. Chem. Soc.* **2015**, 137, 8696–8699.

(43) Forney, C. F.; Brandl, D. G. Control of Humidity in Small Controlled-Environment Chambers Using Glycerol-Water Solutions. *HortTechnology* **1992**, 2, 52–54.

(44) Starcoat® T5 High Efficiency and High Output. 2013.

(45) Thomas A Germer; Joanne C Zwinkels; Benjamin K Tsai. *Spectrophotometry: Accurate Measurement of Optical Properties of Materials*; Experimental Methods in the Physical Sciences; Elsevier Science: Waltham, MA, USA, 2014; Vol. 46.

(46) Abdelhady, A. L.; Saidaminov, M. I.; Murali, B.; Adinolfi, V.; Voznyy, O.; Katsiev, K.; Alarousu, E.; Comin, R.; Dursun, I.; Sinatra, L.; et al. Heterovalent Dopant Incorporation for Bandgap and Type Engineering of Perovskite Crystals. *J. Phys. Chem. Lett.* **2016**, 7, 295–301.

(47) Zhou, Y.; Yong, Z.-J.; Zhang, W.; Ma, J.-P.; Sadhanala, A.; Chen, Y.-M.; Liu, B.-M.; Zhou, Y.; Song, B.; Sun, H.-T. Ultra-Broadband Optical Amplification at Telecommunication Wavelengths Achieved by Bismuth-Activated Lead Iodide Perovskites. *J Mater. Chem. C* **2017**, 5, 2591–2596.

(48) Yamada, Y.; Hoyano, M.; Akashi, R.; Oto, K.; Kanemitsu, Y. Impact of Chemical Doping on Optical Responses in Bismuth-Doped $CH_3NH_3PbBr_3$ Single Crystals: Carrier Lifetime and Photon Recycling. *J. Phys. Chem. Lett.* **2017**, 8, 5798–5803.

(49) Nayak, P. K.; Sendner, M.; Wenger, B.; Wang, Z.; Sharma, K.; Ramadan, A. J.; Lovrinčić, R.; Pucci, A.; Madhu, P. K.; Snaith, H. J. Impact of Bi^{3+} Heterovalent Doping in Organic–Inorganic Metal Halide Perovskite Crystals. *J. Am. Chem. Soc.* **2018**, 140, 574–577.

(50) Mosconi, E.; Merabet, B.; Meggiolaro, D.; Zaoui, A.; De Angelis, F. First-Principles Modeling of Bismuth Doping in the $MAPbI_3$ Perovskite. *J. Phys. Chem. C* **2018,** 122, 14107-14112.

(51) Lozhkina, O. A.; Murashkina, A. A.; Shilovskikh, V. V.; Kapitonov, Y. V.; Ryabchuk, V. K.; Emeline, A. V.; Miyasaka, T. Invalidity of Band-Gap Engineering Concept for Bi^{3+} Heterovalent Doping in $CsPbBr_3$ Halide Perovskite. *J. Phys. Chem. Lett.* **2018**, 9, 5408–5411.

(52) Zhang, Z.; Ren, L.; Yan, H.; Guo, S.; Wang, S.; Wang, M.; Jin, K. Bandgap Narrowing in Bi-Doped $CH_3NH_3PbCl_3$ Perovskite Single Crystals and Thin Films. *J. Phys. Chem. C* **2017**, 121, 17436–17441.

(53) Zhou, Y.; Yong, Z.-J.; Zhang, K.-C.; Liu, B.-M.; Wang, Z.-W.; Hou, J.-S.; Fang, Y.-Z.; Zhou, Y.; Sun, H.-T.; Song, B. Ultrabroad Photoluminescence and Electroluminescence at New Wavelengths from Doped Organometal Halide Perovskites. *J. Phys. Chem. Lett.* **2016**, 7, 2735–2741.

(54) Zhang, J.; Shang, M.; Wang, P.; Huang, X.; Xu, J.; Hu, Z.; Zhu, Y.; Han, L. N-Type Doping and Energy States Tuning in $CH_3NH_3Pb_{1-x}Sb_{2x/3}I_3$ Perovskite Solar Cells. *ACS Energy Lett.* **2016**, 1, 535–541.

(55) Wang, J. T.-W.; Wang, Z.; Pathak, S.; Zhang, W.; deQuilettes, D. W.; Wisnivesky-Rocca-Rivarola, F.; Huang, J.; Nayak, P. K.; Patel, J. B.; Mohd Yusof, H. A.; et al. Efficient Perovskite Solar Cells by Metal Ion Doping. *Energy Env. Sci* **2016**, 9, 2892–2901.

(56) Naumkin, A. V.; Kraut-Vass, A.; Gaarenstroom, S. W.; Powell, C. J. NIST X-Ray Photoelectron Spectroscopy Database, NIST Standard Reference Database Number 20. National Institute of Standards and Technology, Gaithersburg, MD, 20899 2000.

(57) Ferreira da Silva, A.; Veissid, N.; An, C. Y.; Pepe, I.; Barros de Oliveira, N.; Batista da Silva, A. V. Optical Determination of the Direct Bandgap Energy of Lead Iodide Crystals. *Appl. Phys. Lett.* **1996**, 69, 1930–1932.

(58) Li, Y.; Xu, X.; Wang, C.; Ecker, B.; Yang, J.; Huang, J.; Gao, Y. Light-Induced Degradation of $CH_3NH_3PbI_3$ Hybrid Perovskite Thin Film. *J. Phys. Chem. C* **2017**, 121, 3904–3910.

(59) Manshor, N. A.; Wali, Q.; Wong, K. K.; Muzakir, S. K.; Fakharuddin, A.; Schmidt-Mende, L.; Jose, R. Humidity versus Photo-Stability of Metal Halide Perovskite Films in a Polymer Matrix. *PhysChemChemPhys* **2016**, 18, 21629–21639.

(60) Xu, W.; Liu, L.; Yang, L.; Shen, P.; Sun, B.; McLeod, J. A. Dissociation of Methylammonium Cations in Hybrid Organic–Inorganic Perovskite Solar Cells. *Nano Lett.* **2016**, 16, 4720–4725.

(61) Merdasa, A.; Bag, M.; Tian, Y.; Källman, E.; Dobrovolsky, A.; Scheblykin, I. G. Super-Resolution Luminescence Microspectroscopy Reveals the Mechanism of Photoinduced Degradation in $CH_3NH_3PbI_3$ Perovskite Nanocrystals. *J. Phys. Chem. C* **2016**, 120, 10711–10719.

(62) Avrami, M. Kinetics of Phase Change. I General Theory. *J. Chem. Phys.* **1939**, 7, 1103–1112.

(63) Christian, J. W. *The Theory of Transformations in Metals and Alloys*; Elsevier Science: Kidlington, Oxford, UK, 2002.

(64) Halder, A.; Choudhury, D.; Ghosh, S.; Subbiah, A. S.; Sarkar, S. K. Exploring Thermochromic Behavior of Hydrated Hybrid Perovskites in Solar Cells. *J. Phys. Chem. Lett.* **2015**, 6, 3180–3184.

HUMIDITY-INDUCED TRANSITIONS IN HOIPS AND RELATED METAL HALIDES

Chapter 3: Deliquescent Chromism in Nickel (II) Iodide Thin Films[†]

3.1 INTRODUCTION

Color-changing materials are used in a variety of applications, ranging from sensors[1] to dynamic window coatings[2,3] to photovoltaic windows.[4–6] These materials can change color in response to shifts in temperature, applied voltage, or chemical environment. Nickel compounds, especially organometallic Ni(II) halides, have been widely studied in this context because of their propensity to change color when halide ligands are exchanged or undergo structural rearragnement.[7–16] Several patents have mentioned ligand exchange of nickel complexes as a useful strategy to create glass that exhibits color neutral switching between transparent and dark states with uniform light absorption across the visible spectrum, commonly known as color neutrality.[9,17,18] Color neutral transitions are especially desirable to minimize distortions in the appearance of objects viewed through tinted window glass.[9,18–20] Color neutrality has traditionally been achieved by layering different thermochromic materials,[9,18] or by using materials that undergo insulator–metal transitions to switch between transparent and mirror states.[20,21] Here, we report a new color neutral deliquescent chromism in thin films of nickel(II) iodide (NiI_2) that does not occur for bulk NiI_2 powders. When exposed to humidity, the thin films rapidly take up water and transition to an amorphous, optically transparent state that can be reversibly switched back to the dark crystalline state with mild heating. A transitory, intermediate solid NiI_2-hydrate phase is also observed, which is most likely the pentahydrate or hexadydrate phases known to occur in the bulk.

[†]Reprinted with permission from Siegler, T.D., Reimnitz, L.C., Suri, M., Cho, S.H., Bergerud, A.J., Abney, M. K., Milliron, D.J., Korgel, B.A.* (**2019**) "Deliquescent Chromism of Nickel (II) Iodide Thin Films". *Langmuir*. 35 (6): https://pubs.acs.org/articlesonrequest/AOR-FzfJiAVZAVKaYhB8v9ft. Copyright 2019 American Chemical Society. TDS conceived all experiments and carried out static UV Vis and characterization in full; and SEM, FTIR and TFA in part. TDS also analyzed data and wrote the manuscript.

3.2 Experimental Details

3.2.1 Materials

Nickel(II) iodide (NiI_2, 99.5%, VWR), anhydrous dimethylformamide ($HCON(CH_3)_2$, DMF, 99.8%, Sigma), anhydrous dimethyl sulfoxide ($(CH_3)_2SO$, 99.9%, Sigma), and (3-aminopropyl)triethyoxysilane ($H_2N(CH_2)_3Si(OC_2H_5)_3$, >98%, Sigma) were purchased and used as received.

3.2.2 Preparation of Silane Coated Glass Substrates

Glass slides were sonicated in ethanol for 30 min. The slides were then immersed into a solution of (3-aminopropyl)triethoxysilane (APTES) in ethanol with a volumetric ratio of ethanol:APTES of 9. A drop of water was added to the ethanol/APTES solution to catalyze APTES grafting to the glass substrate. After 5 min, glass substrates were rinsed with isopropanol (IPA) and then heated at 100 °C in ambient air for 10 min.[22]

3.2.3 Preparation of Nickel (II) Iodide Thin Films

Nickel(II) iodide thin films were deposited on APTES-treated glass substrates by spin coating a solution of 1 mmol (313 mg) NiI_2 in 200 μL of DMSO and 800 μL of DMF. This solution is prepared by heating for 2 h at 125 °C. If this solution cools to room temperature, it changes color from brown to green and forms a viscous gel; therefore, the solution temperature is maintained at 125 °C by stirring on a hot plate throughout the deposition. 50 μL of solution was pipetted directly from the heated solution on the hot plate and deposited onto the substrate by dynamically spin coating at 5000 rpm for 30 s in a nitrogen-filled glovebox. After deposition, the film was heated at 150 °C for 48 h to remove DMSO from the film and eliminate any possibility of ligand–metal chromism. The thickness of films spin-coated at 5000 rpm was around 600 nm. Films that were 900 nm or

15 μm thick were deposited by spin coating at lower speeds of 1000 and 100 rpm, respectively. Films with 140 μm thickness were deposited by drop casting 150 μL of solution onto glass substrates heated to 150 °C.

3.2.4 Optical Switching

UV-vis-NIR transmittance spectra were obtained using an ASD LabSpec 4 Standard-Res UV-vis-NIR spectrophotometer with a Linkam LTS420 heating stage equipped with the LNP95 cooling system and Linksys 32 software (Linkam Scientific) to control the film temperature. Stepped temperature profiles were generated using a heating rate of 10 °C/min between steps, and holding the temperature at each step for 10 min before acquiring spectra. Experiments with continuous ramping of the temperature were performed with rates of 0.25, 1, or 10 °C/min.

The experiments examining the optical switching of the NiI_2 films by thermal cycling all began with a film in the dark state and exposure to air at 50% RH (relative humidity). Before cycling, initially dark NiI_2 films were taken out of the glovebox, transferred to the heating stage and heated at 100 °C for 1 h to drive off any water vapor the film may have taken up during the transfer. The reversibility of the color change was tested by exposing the initially dark NiI_2 film to 50% RH air at 20 °C for 15 min to obtain the clear state. This film was then heated to 80 °C for 15 min, causing the film to become dark again. This cycle was repeated 10 times

3.2.5 Materials Characterization

Powder X-ray diffraction (XRD) was performed with a Rigaku R-Axis Spider X-ray diffractometer using an image plate detector and Cu Kα radiation ($\lambda = 1.54$ nm). XRD samples were transferred to a Hampton Research Mounted CryoLoop mount by scraping

material from a film. XRD data were acquired for 10 min with 5 deg/s sample rotation under 40 kV and 40 mA radiation.

Fourier transform infrared (FTIR) spectra were measured using a Bruker Vertex 70 FTIR spectrophotometer. Nickel iodide films were spin coated onto silicon substrates and placed in an airtight Buck Scientific Circular Aperture Cell Mount 6500 S liquid FTIR cell with a CaF_2 window. Dark and clear films were sealed into the cell mount in a nitrogen glovebox or in 50% RH air, respectively.

Scanning electron microscopy (SEM) was performed using a Quanta 650 SEM operated at 30 kV. To minimize exposure to air, the cross-sectioned films were loaded into the SEM using a Quorum Technologies Cryo-SEM Preparation System (model PP2000TR/FEI). All reported film thicknesses were determined from SEM images of cross-sectioned films.

Optical microscopy images were obtained with the optical microscope attachment on a Horiba LabRAM HR Evolution Raman microscope using a 10× zoom lens. Film temperatures were controlled with a Linkam LTS420 stage equipped with the LNP95 cooling system.

Thermogravimetric analysis (TGA) was performed with a Mettler Toledo TGA 2. For TGA, the nickel iodide films were spin-coated at 5000 rpm onto the flat surfaces of a 40 μL Mettler Toledo aluminum crucible standard lid.

The amount of water absorbed by the film when switching between dark and clear states was determined secondarily using a Mettler Toledo XSE205 DualRange balance. Films in the dark state were weighed immediately after preparation in a nitrogen-filled glovebox with less than 15 s of air exposure. The weight of the clear state films was then measured after the weight stabilized under exposure to ambient air at room temperature and 50% RH.

3.3 Results and Discussion

3.3.1 Optical Modulation of Nickel Iodide Films

Figure 3.1 shows a thin film of NiI_2 on glass reversibly switched between a color neutral dark state and an optically transparent state. The initially dark film shown in Figure 3.1A was stable in dry air until exposed to air with >30% RH (50% RH in all experiments in this report) for 5 min, at which point it turned to the clear film shown in the photograph in Figure 3.1B. The film was then heated at 100 °C for 5 s, and it reverted back to the dark state shown in Figure 3.1C. As shown in the UV-vis-NIR transmittance spectra in Figure 3.2A, the clear state of the NiI_2 film exhibits 90% optical transmittance between 350 and 2250 nm; whereas the dark state has less than 10% optical transmittance through the visible spectrum, with a gradually increasing transmittance through the near IR spectrum up to 2250 nm. Figure 3.2C shows an SEM image of a typical NiI_2 film without any exposure to air, with a thickness of about 625 nm.

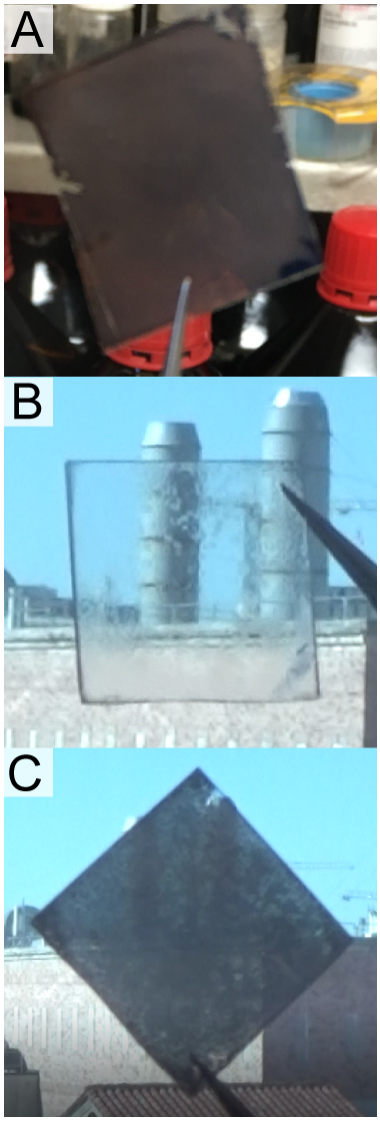

Figure 3.1: Thin film of NiI_2 (thickness 625 ± 125 nm) on glass cycled between its (A,C) dark and (B) clear states. The film is shown (A) immediately after spin coating and annealing, (B) after 5 min of exposure to air (~50% RH, 20 °C), and (C) after it had been heated at 100 °C for 10 s. (See the Supplementary Files for accompanying videos.)

Figure 3.2B shows XRD patterns from a film in its dark and clear states. Powder XRD shows the dark state is composed of crystalline, rhombohedral NiI_2 with a trace amount of hexagonal $NiI_2 \cdot 6H_2O$, while the XRD pattern of the clear film is featureless. We

attribute the trace amount of hexagonal $NiI_2 \cdot 6H_2O$ observed in the dark state XRD pattern in Figure 3.2B to brief air exposure during the sample preparation. NiI_2 is known to be hygroscopic, and in its bulk form, exposure to humidity changes the material from the black rhombohedral phase to crystalline penta- or hexahydrate, which has a green color.[23–25] XRD of the clear film does not show any evidence of hexagonal $NiI_2 \cdot 6H_2O$ or any other crystalline hydrate phase.

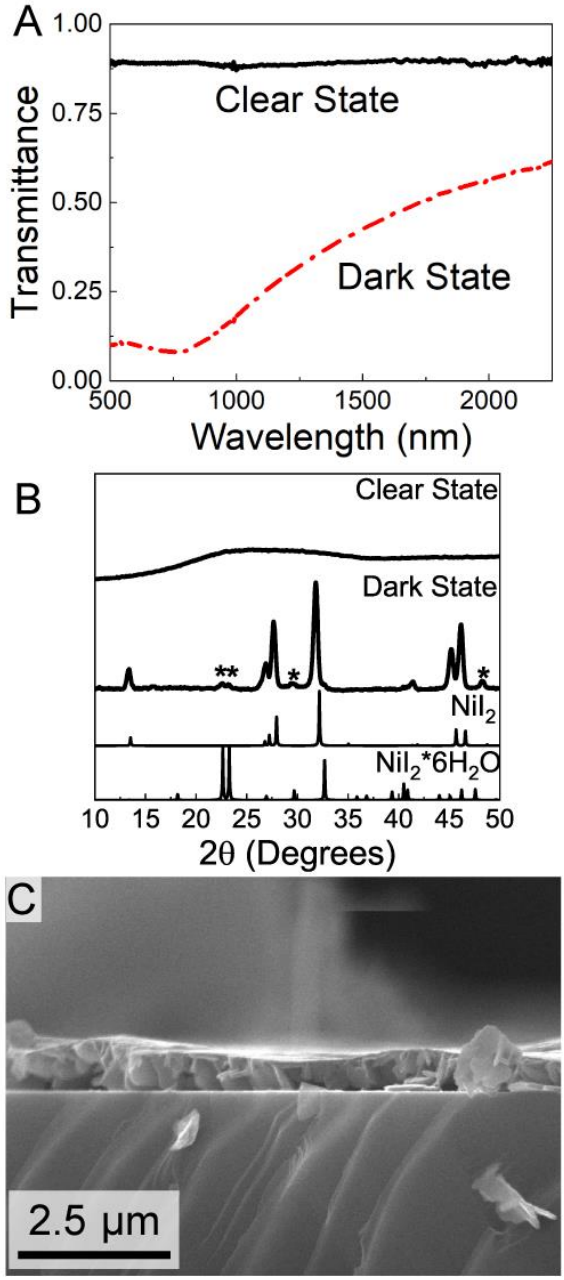

Figure 3.2: (A) UV-vis-NIR transmittance spectra and (B) XRD of an NiI_2 film on glass in its optically clear and dark states. The diffraction peaks in the dark film correspond to rhombohedral NiI_2 (PDF #00-020-0785) and trace hexagonal $NiI_2 \cdot 6H_2O$ (marked by *, PDF #00-016-0565). (C) SEM image of a cross sectioned NiI_2 film on glass in the dark state without exposure to air. The film is 625 ± 125 nm thick.

3.3.2 Characterization of Clear and Dark States

FTIR spectra were measured to determine if the clear film presented any evidence that the color change was due to ligand exchange or rearrangement. The FTIR spectrum of the dark film in Figure 3.3A is featureless. There is no residual DMF or DMSO in the film that could possibly give rise to a nickel-ligand rearrangement or a change in d-splitting of nickel due to change in coordination geometry.[10,26–28] The FTIR spectrum of the clear film in Figure 3.3B exhibits two strong absorption bands at 3460 and 1610 cm^{-1}. Although these could come from nickel iodide hexahydrate;[24] these bands also correspond to the stretching and bending region of condensed water.[29–32] Since there is no evidence of $NiI_2 \cdot 6H_2O$ by XRD (Figure 3.2B), we conclude these bands arise from condensed water. TGA (Figure 3.3D) also indicates a significant amount of water in the clear film, with a H_2O:NiI_2 molar ratio of at least 10, corresponding to a dissolved nickel iodide concentration of ~5.5 M.

The FTIR spectra also reveal that there is an "intermediate" state occurring as the film switches between dark and clear states. As shown in Figure 3.3C, this intermediate state of the film exhibits the water bending mode at 1610 cm^{-1}, similar to the spectra in Figure 3.3B for the clear film, but with an additional splitting of the stretching mode ν_1 into two peaks at 3460 and 3330 cm^{-1}. The additional ν_1 peak at 3330 cm^{-1} corresponds to water with a lower degree of vibrational freedom and stronger hydrogen bonding.[33] These data indicate that this intermediate solid is a hydrate phase of nickel iodide with a lower hydration state than the clear liquid. Possibly, this intermediate is the penta- or hexahydrate phase of nickel(II) iodide. The intermediate phase is also observed during switching in optical microscopy images and in the transmittance spectra, as discussed below.

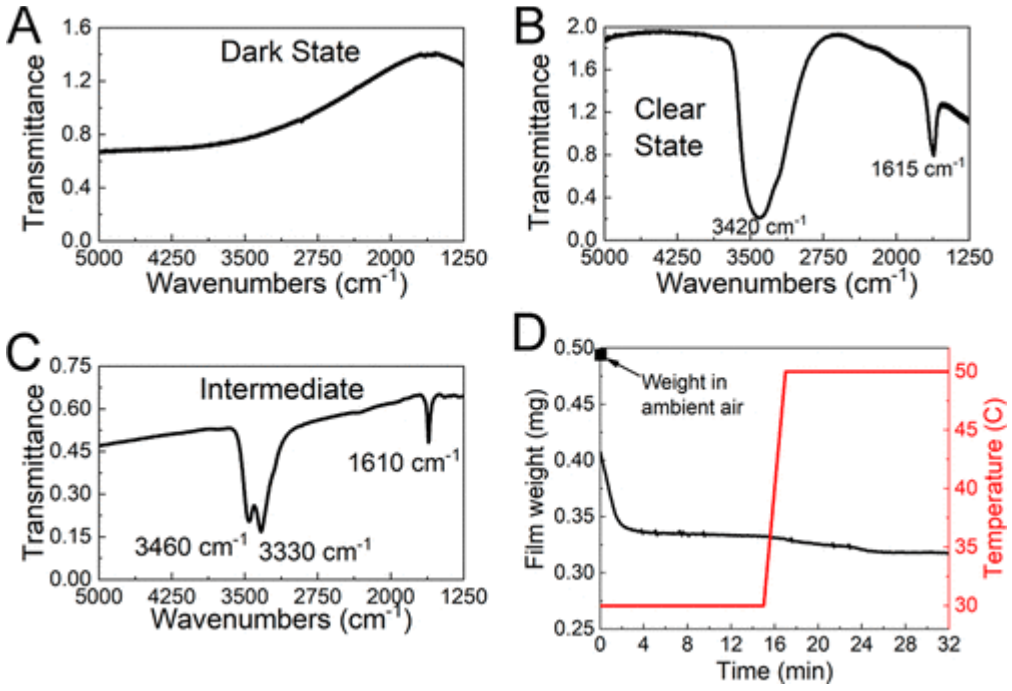

Figure 3.3: FTIR spectra for a thin film of NiI_2 in (A) the dark state, (B) the clear state, and (C) 30 s after removal from an inert atmosphere (i.e., an intermediate state). The FTIR on the clear state shows water is present in the clear film, with a characteristic stretching mode ν_1 peak at 3420 cm^{-1} and a characteristic bending mode peak ν_2 at 1615 cm^{-1}. FTIR on the intermediate state shows two condensed O–H ν_1 stretching modes. Transmissions greater than one in FTIR spectra are due to reduced reflection of the silicon substrate once the thin film is deposited. (D) TGA of a clear hydrated NiI_2 thin film. Note that some weight loss has occurred during sample loading into the TGA and purging with dry nitrogen prior to beginning the measurement. The initial mass measured in ambient conditions with a benchtop balance is shown here as a solid black square at time 0. From this, we calculate a H_2O/NiI_2 molar ratio of 9.7 ± 0.6.

Figure 3.4A and 3.4B shows optical microscopy images of a NiI_2 film as it is switched between dark and clear states. When the dark film (Figure 3.4A) is cooled, a transparent solid forms (Figure 3.4C,D) before the film finally turns clear (Figure 3.4D,E). This transparent solid material is the intermediate phase formed during switching. When

the clear film is heated (Figure 3.4G), the clear solid material again appears (Figure 3.4G,H) before the entire film transitions to the solid dark state material (Figure 3.4I,J).

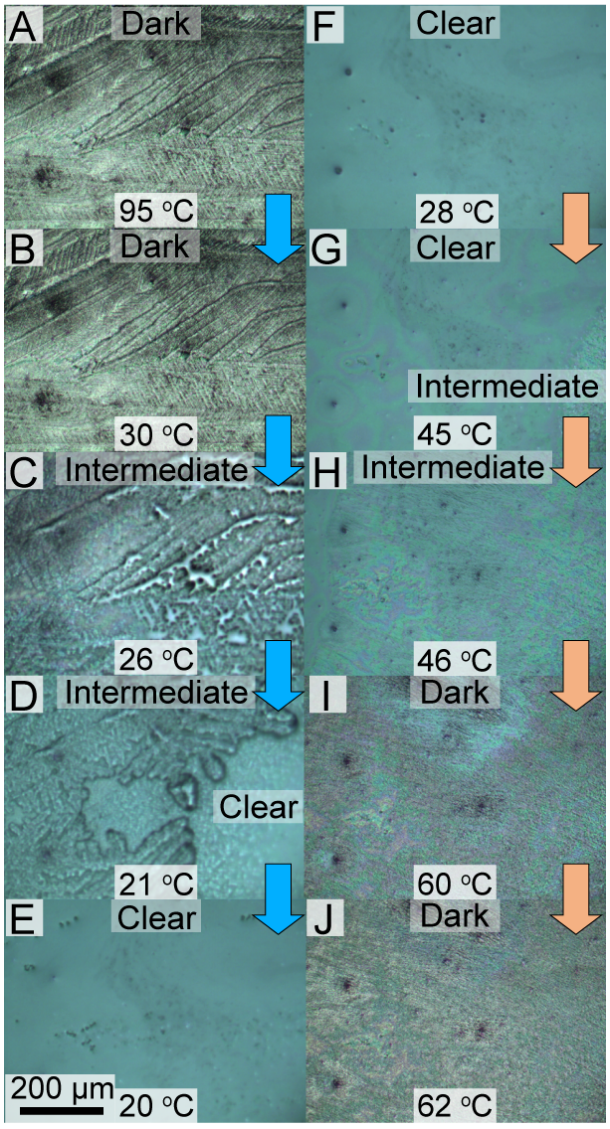

Figure 3.4: Optical microscope images of a nickel iodide film on glass as it is (A–E) cooled, as indicated by blue arrows and subsequently (F–J) heated, indicated by red arrows. Optical microscopy shows the coexistence of (D–G) a clear liquid and (C,D,G,H) clear solid phase during the clear-to-dark transition to (A,B,I,J) the dark solid phase, and that these transitions happen in a nucleation-and-growth mechanism.

The intermediate is also observed as a step in the optical transmittance when the NiI_2 film is heated and cooled, as shown in Figure 3.5. Optical switching of the film occurs at 35 to 50 °C when heated and then at 30 to 35 °C when cooled. The observed hysteresis indicates that the transition temperatures are influenced by the kinetics of the transition. For example, the transition temperatures observed from the *in-situ* transmittance spectra in Figure 3.5 are lower than those observed in the optical microscopy experiments in Figure 3.4 due to the difference in temperature ramp rate.

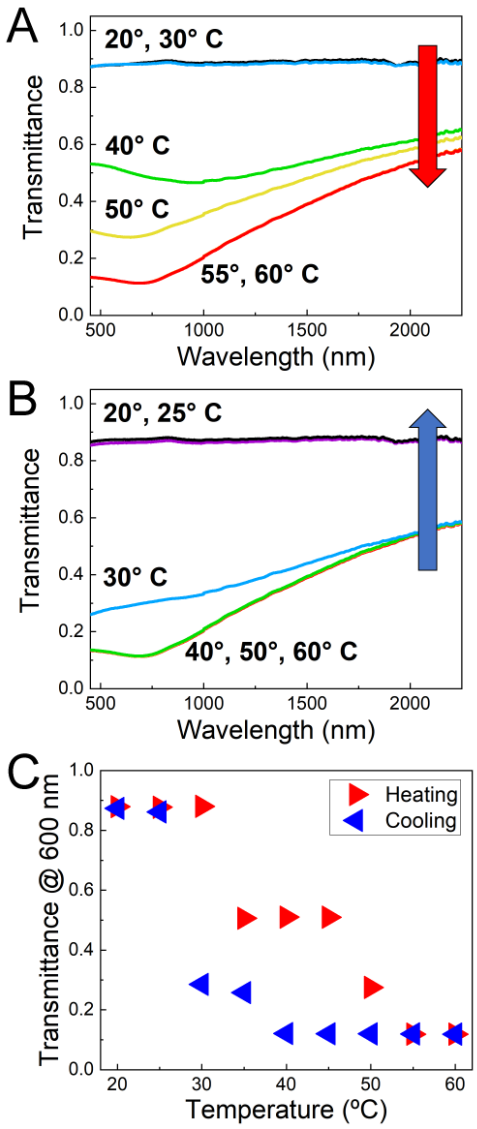

Figure 3.5: In situ UV-vis-NIR transmittance spectra of clear state films heated to different temperatures via a 10 °C/min ramp and 10 min hold in ambient air (50% RH). Spectra show a broad clear-to-dark transition centered around ~40 °C. (B) Temperature-dependent spectra of the dark-to-clear transition cooled using the same procedure as (A), showing a sharper transition centered around ~30 °C. In plots (A) and (B), different colored lines correspond to different temperatures: 20 °C is represented by a black line, 25 °C by purple, 30 °C by blue, 40 °C by green, 50 °C by yellow, 55 °C by orange, and 60 °C by red. (C) Transmittance of the film at 600 nm plotted versus temperature. This transition exhibits a temperature hysteresis of ~10 °C at 50% RH.

3.3.3 Effect of Heating Rate and Film Thickness

The rate dependence of the optical switching was further tested by measuring the transmittance of the film with various heating rates. Figure 3.6A–C shows the transmittance of NiI_2 films heated and cooled at three different rates: 10, 1, and 0.25 °C/min. The transmittance of the intermediate state and the amount of hysteresis is seen to depend on the heating rate, with faster rates increasing the transition temperature during heating and lowering the transition temperature during cooling. When heated at 1 °C/min or slower, the films exhibit identical temperature-dependent changes in transmittance, similar to those shown in Figure 3.5.

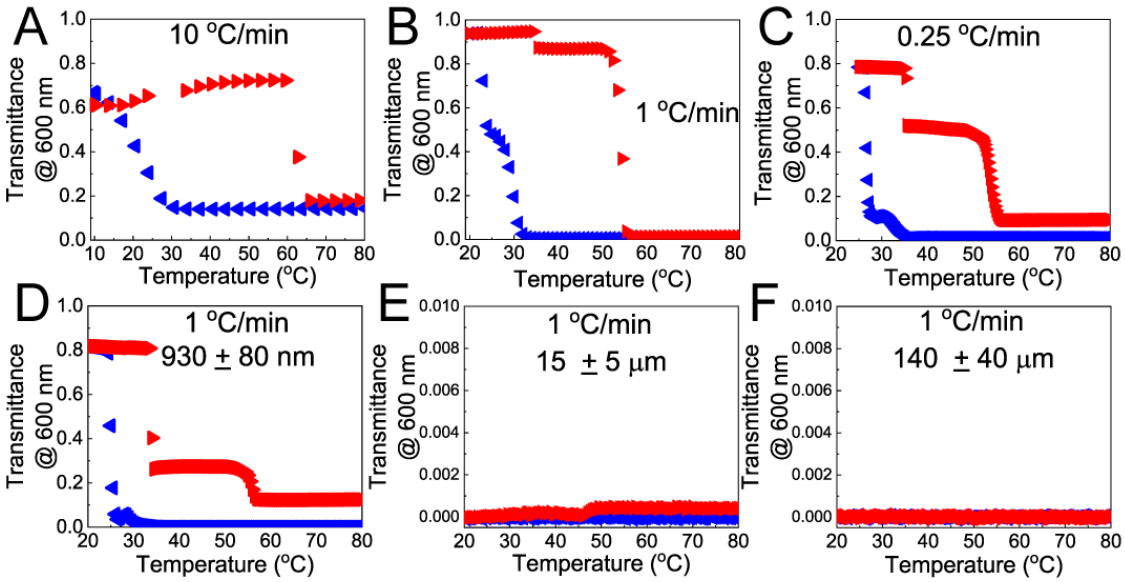

Figure 3.6. (A–C) Optical transmittance at 600 nm for NiI_2 films (625 ± 125 nm thick) heated (red) and then cooled (blue) in 50% RH air at various heating and cooling rates: (A) 10 °C/min, (B) 1 °C/min, and (C) 0.25 °C/min. At high ramp rates as in (A), the transition hysteresis widens. (D–F) Optical transmittance at 600 nm as a function of temperature for (D) 930 ± 80 nm, (E) 15 ± 5 µm, and (F) 140 ± 40 µm thick films. Cross-sectional images of films are shown in Figure 3.7. Above 1 µm in film thickness, the optical transition disappears.

Figure 3.6D–F shows transmittance of NiI_2 films with varying thickness heated at 1 °C/min. The 930 nm thick film exhibits a similar optical behavior as the thinner 625 nm films, but the transmittance of the intermediate state is significantly lower. Much thicker films, with thickness of 15 μm or more, did not exhibit the dark-to-clear optical transition. (See the Figure 3.7 for SEM images of the cross-sectioned films.) While these films did not exhibit a change in optical transmittance, they still showed deliquescence, turning into a black sludge upon exposure to 50% RH air.

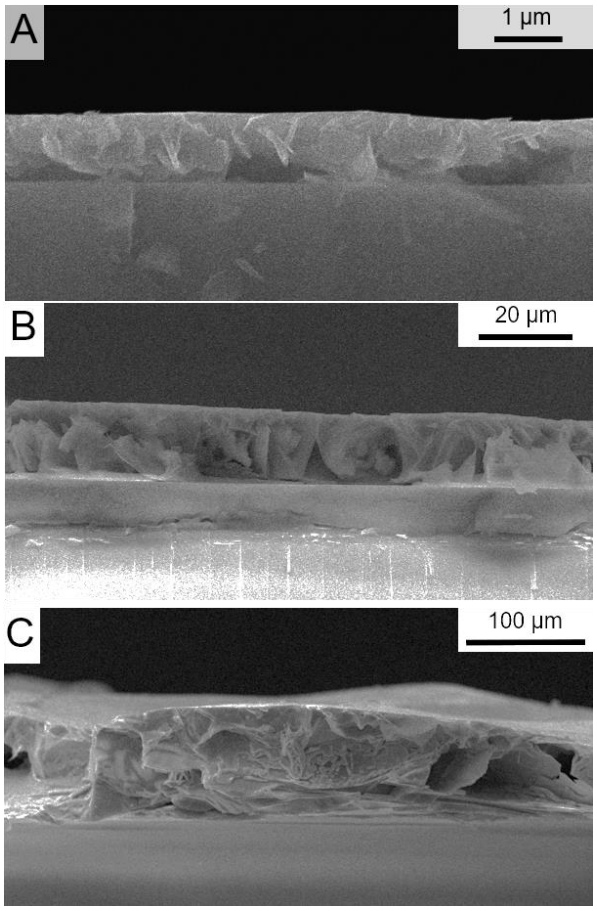

Figure 3.7. SEM images of cross-sectioned NiI_2 films with thicknesses of (a) 930 $\pm$ 80 nm, (b) 15 $\pm$ 5 μm, and (c) 140 $\pm$ 40 μm. The reported thicknesses were determined by averaging 100 discrete points along the film for each sample.

3.3.4 Cycling Stability

We also tested the reversibility of the optical transition of the NiI_2 films. Figure 3.8 shows UV-vis-NIR transmittance spectra for an initially dark NiI_2 film exposed to air at 20 °C for 15 min, heated to 80 °C at 10 °C/min, and then held at 80 °C for 15 min. The transparency of the dark state of the film increases over the course of the first three to four cycles, with a slight decrease in transparency in subsequent cycles. This initial loss of dark state optical density most likely results from poor adhesion of the wet film to the substrate. To improve adhesion of the films to glass substrates, they were treated with APTES to improve the wettability of the polar solvents used in the spin coating procedure (DMF and DMSO); however, even with the polar APTES coating, the contact angle of water with the substrate remains as high as 58°, which is problematic for aqueous clear state films.[34] The hydrated, clear NiI_2 films often dewetted and moved off the substrate during the thermal cycling experiments. This also explains the observed increase in transmittance of the clear state with each cycle. As shown in Figure 3.8D, the optical transitions of the film stabilize after five cycles, and the change in transmission between clear and dark states never drops below 90% of its initial value.

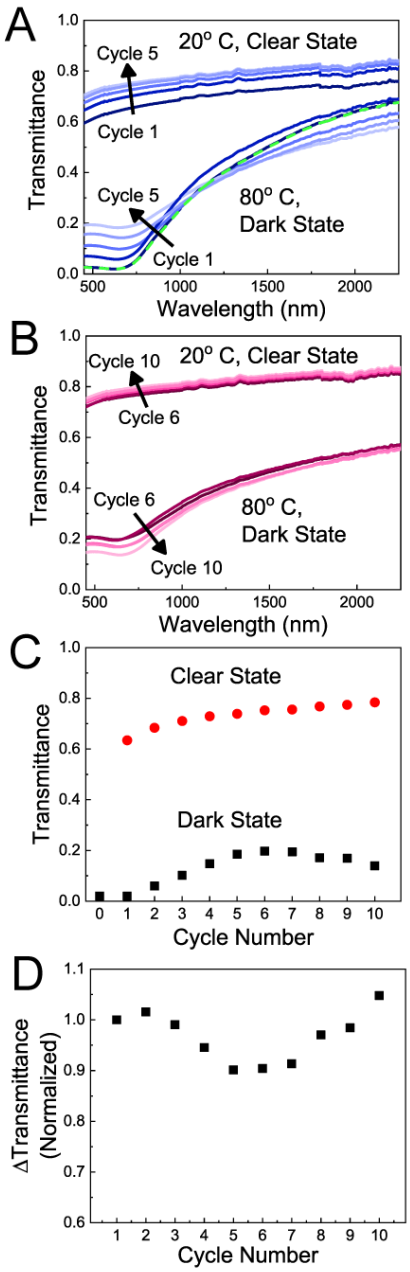

Figure 3.8. UV-vis-NIR transmittance spectra of a 550 nm thick film of NiI_2 undergoing thermal cycling from 20 to 80 °C in air at RH 50% over (A) cycles 1–5 and (B) cycles 6–10. Absorbance spectra are shown for both the clear state at 20 °C and the dark state at 80 °C. The green dashed line is the initial absorbance of the film. (C) Transmittance at 600 nm of the film in the dark and clear states. (D) Change in transmittance between light and dark states at 600 nm normalized to the first cycle.

3.4 CONCLUSION

Thin films of NiI_2 exhibit reversible, deliquescent chromism that does not occur in the bulk material. When exposed to humidity, the dark brown crystalline NiI_2 film absorbs water and becomes transparent. This deliquescence is reversible: the film turns back to the dark crystalline NiI_2 state when heated to drive off the moisture. The transition involves a solid intermediate species, most likely one of the known solid pentahydrate or hexahydrate phases of NiI_2. The transition is different than the known nickel halide chromism due to d–d transitions in nickel metal centers of organometallic complexes.[10,26,35,36] The optically clear hydrated state of nickel(II) iodide has a H_2O:NiI_2 molar ratio of at least 10, which has not previously been reported. The kinetics of this optical transition depend on the humidity of the environment and the film thickness. With further research, this deliquescent chromism of NiI_2 thin films may find use in color-changing devices, such as smart windows, thermal sensors, or thermochromic inks.[20,21]

3.5 REFERENCES

(1) Kim, H. N.; Ren, W. X.; Kim, J. S.; Yoon, J. Fluorescent and Colorimetric Sensors for Detection of Lead, Cadmium, and Mercury Ions. *Chem. Soc. Rev.* **2012**, 41, 3210–3244.

(2) Kamalisarvestani, M.; Saidur, R.; Mekhilef, S.; Javadi, F. S. Performance, Materials and Coating Technologies of Thermochromic Thin Films on Smart Windows. *Renew. Sustain. Energy Rev.* **2013**, 26, 353–364.

(3) Granqvist, C. G.; Lansåker, P. C.; Mlyuka, N. R.; Niklasson, G. A.; Avendaño, E. Progress in Chromogenics: New Results for Electrochromic and Thermochromic Materials and Devices. *Sol. Energy Mater. Sol. Cells* **2009**, 93, 2032–2039.

(4) Lin, J.; Lai, M.; Dou, L.; Kley, C. S.; Chen, H.; Peng, F.; Sun, J.; Lu, D.; Hawks, S. A.; Xie, C.; Cui, F.; Alivisatos, A. P.; Limmer, D. T.; Yang, P. Thermochromic Halide Perovskite Solar Cells. *Nat. Mater.* **2018**, 17, 261–267.

(5) De Bastiani, M.; Saidaminov, M. I.; Dursun, I.; Sinatra, L.; Peng, W.; Buttner, U.; Mohammed, O. F.; Bakr, O. M. Thermochromic Perovskite Inks for Reversible Smart Window Applications. *Chem. Mater.* **2017**, 29, 3367–3370.

(6) Wheeler, L.M., Moore, D.T., Ihly, R., Stanton, N.J., Miller, E.M., Tenent, R.C., Blackburn, J.L., Neale, N.R. Switchable Photovoltaic Windows Enabled by Reversible Photothermal Complex Dissociation from Methylammonium Lead Iodide. *Nature Commun.* **2017**, 8, 1722.

(7) Pariya, C.; Ghosh, A.; Chaudhuri, N. R. Thermal Studies of N^1-Isopropyl-2-Methyl-1,2-Propanediamine Complexes of Nickel(II)X_2 [X = I^-, CF_3CO^{-2}, $0.5SO_2^{-4}$, and $0.5SeO_2^{-4}$] in the Solid State. *Thermochim. Acta* **1995**, 268, 153–160. https://doi.org/10.1016/0040-6031(95)02436-0.

(8) Zhu, J.; Huang, A.; Ma, H.; Ma, Y.; Tong, K.; Ji, S.; Bao, S.; Cao, X.; Jin, P. Composite Film of Vanadium Dioxide Nanoparticles and Ionic Liquid–Nickel–Chlorine Complexes with Excellent Visible Thermochromic Performance. *ACS Appl. Mater. Interfaces* **2016**, 8, 29742–29748.

(9) Harlan J. Byker; Paul H. Ogburn Jr; Vander Griend, D. A.; Brad S. Veldkamp; Derick D. Winkle. Ligand Exchange Thermochromic Systems and High Epsilon Ligands for Same. US 8,182,718 B2, May 22, 2012.

(10) Gu, C.-D.; Tu, J.-P. Thermochromic Behavior of Chloro-Nickel(II) in Deep Eutectic Solvents and Their Application in Thermochromic Composite Films. *RSC Adv.* **2011**, 1, 1220–1227.

(11) Day, J. H. Thermochromism of Inorganic Compounds. *Chem. Rev.* **1968**, 68, 649–657.

(12) Schumann, H. Synthese Und Spektroskopische Untersuchungen von Nickelkomplexen mit Substituierten Dibenzotetraaza[14] Annulenliganden. *Z. Naturforschung B* **1996**, 51, 989–998.

(13) Bhattacharya, R.; Ghosh, A. Thermal Analysis of Pyridinium Tetrachloronickelate(II); Tetrahedral Octahedral Structural Transformation. *J. Chem. Res.* **2001**, 332–333.

(14) Ihara, Y.; Fukuda, Y.; Sone, K. Solid-Phase Thermal Square-Planar-to-Octahedral Isomeric Transformation of Nickel(II) Complexes Containing 1,2-Cyclohexanediamines. *Inorg. Chem.* **1987**, 26, 3745–3750.

(15) De Santis, G.; Fabbrizzi, L.; Poggi, A.; Taglietti, A. Nickel(III)-Promoted Deprotonation of an Amide Group of Cyclam. Characterization of the Violet Transient through Stopped-Flow Spectrophotometric Techniques and Determination of the pKA Value. *Inorg. Chem.* **1994**, 33, 134–139.

(16) Collins, T. J.; Nichols, T. R.; Uffelman, E. S. A Square-Planar Nickel(III) Complex of an Innocent Ligand System. *J. Am. Chem. Soc.* **1991**, 113, 4708–4709.

(17) Anderson, C. D.; Harlan J. Byker; De Jong, S. J.; Lameris, J. L.; Winkle, D. D. Anti-Yellowing for Thermochromic Systems. US 8,623,243 B2, January 7, 2014.

(18) Byker, H. J.; Ogburn Jr., P. H.; Vander Griend, D. A.; Winkle, D. D. Ligand Exchange Thermochromic Systems Containing Exchange Metals. US 7,538,931 B2, May 26, 2009.

(19) Anderson, C. D.; Broekhuis, M. D.; Byker, H. J.; DeJong, S. J. Color Neutral Thermochromic Layers and Laminates. US 9,465,239, October 11, 2016.

(20) Yoshimura, K.; Bao, S. Color-Neutral Reflective Control Switchable Thin Film Material. US 7,414,772 B2, August 19, 2008.

(21) Miller, S. Temperature Controlled Variable Reflectivity Coatings. US 9,422,712 B2, August 23, 2016.

(22) Majoul, N.; Aouida, S.; Bessaïs, B. Progress of Porous Silicon APTES-Functionalization by FTIR Investigations. *Appl. Surf. Sci.* **2015**, 331, 388–391.

(23) McPherson, G. L.; Wall Jr, J. E.; Hermann, A. M. Electrical, Magnetic, and Spectroscopic Properties of $CsNiI_3$. *Inorg. Chem.* **1974**, 13, 2230–2233.

(24) Cariati, F.; Bruni, S.; Martini, M.; Spinolo, G. Raman and Infrared Spectra of NiI_2•$6H_2O$. *J. Raman Spectrosc.* **1991**, 22, 397–401.

(25) Stirrat, C. R.; Newman, P. R.; Cowen, J. A. $NiI_2 \cdot 6H_2O$: A Disordered Linear Chain Magnet. *AIP Conference Proceedings.* **1976**, 34, 199–201.

(26) McCleverty, J.A.; Meyer, T.J. Comprehensive Coordination Chemistry II From Biology to Nanotechnology. Elsivier, Amsterdam, 2003.

(27) Meek, D. W.; Straub, D. K.; Drago, R. S. Transition Metal Ion Complexes of Dimethyl Sulfoxide. *J. Am. Chem. Soc.* **1960**, 82, 6013–6016.

(28) Kang, S.-G.; Ryu, K.; Jung, S.-K.; Kim, J. Template Synthesis, Crystal Structure, and Solution Behavior of a Hexaaza Macrocyclic Nickel(II) Complex Containing Two N-Aminoethyl Pendant Arms. *Inorganica Chim. Acta* **1999**, 293, 140–146.

(29) Middlebrook, A. M.; Iraci, L. T.; McNeill, L. S.; Koehler, B. G.; Wilson, M. A.; Saastad, O. W.; Tolbert, M. A.; Hanson, D. R. Fourier Transform-Infrared Studies of Thin H_2SO_4/H_2O Films: Formation, Water Uptake, and Solid-Liquid Phase Changes. *J. Geophys. Res. Atmospheres* **1993**, 98, 20473–20481.

(30) Al-Abadleh, H. A.; Grassian, V. H. FT-IR Study of Water Adsorption on Aluminum Oxide Surfaces. *Langmuir* **2002**, 19, 341–347.

(31) Peters, S. J.; Ewing, G. E. Water on Salt: An Infrared Study of Adsorbed H_2O on NaCl (100) under Ambient Conditions. *J. Phys. Chem. B* **1997**, 101, 10880–10886.

(32) Maeda, Y.; Nakamura, T.; Ikeda, I. Changes in the Hydration States of Poly(N - Alkylacrylamide)s during Their Phase Transitions in Water Observed by FTIR Spectroscopy. *Macromolecules* **2001**, 34, 1391–1399.

(33) Scatena, L. F.; Brown, M.G.; Richmond, G.L. Water at Hydrophobic Surfaces: Weak Hydrogen Bonding and Strong Orientation Effects. *Science* **2001**, 292, 908–912.

(34) Janssen, D.; De Palma, R.; Verlaak, S.; Heremans, P.; Dehaen, W. Static Solvent Contact Angle Measurements, Surface Free Energy and Wettability Determination of Various Self-Assembled Monolayers on Silicon Dioxide. *Thin Solid Films* **2006**, 515, 1433–1438.

(35) Kahani, S. A.; Abdevali, F. Mechanochemical Synthesis and Characterization of a Nickel(II) Complex as a Reversible Thermochromic Nanostructure. *RSC Adv.* **2016**, 6, 5116–5122.

(36) Bussière, G.; Beaulac, R.; Cardinal-David, B.; Reber, C. Coupled Electronic States in trans-$MCl_2(H_2O)_4^{n+}$ Complexes (M: Ni^{2+}, Co^{2+}, V^{3+}, Cr^{3+}) Probed by Absorption and Luminescence Spectroscopy. *Coord. Chem. Rev.* **2001**, 219–221, 509–543.

PEROVSKITE-CDTE TANDEM PHOTOVOLTAICS

Chapter 4: Development of Wide Band Gap $APbBr_3$ Perovskites for Next-Generation Tandem Solar Cells[†]

4.1 INTRODUCTION

A photovoltaic (PV) solar cell is a solid-state semiconductor device that converts sunlight directly to electricity without generating emissions.[1] PV devices represent an important renewable energy resource that is helping to address the global challenge of energy sustainability. One of the biggest successes in the PV industry in recent years is that utility-scale PV has achieved cost-competitiveness with fossil fuels without subsidy in certain situations (<US$ 0.04–0.05/kWh).[2] This has driven significant demand for solar; for example, the US installed a record 14.7 GW in 2016, nearly double the installed capacity of 2015.[3] In 2016, the PV market broke several volume records with continued global expansion, bringing the market to 75 GW.[4] However, in the longer term, more significant technology improvements must be made to maintain the ongoing trend in solar cell cost reductions and increased adoption. As we approach the Shockley-Queisser limit- the thermodynamic limit for a traditional PV- these continued efficiency improvements will begin to be more challenging and require creative strategies to implement. The simplest way to overcome this limit is through the development of tandem or multijunction solar cells that combine multiple light absorbers with different bandgap energy.[5-7]

[†]Reprinted under author rights in the Elsevier publishing agreement from Siegler, T.D.; Shimpi, T.M.; Sampath, W.S.; Korgel, B.A.* (**2019**) "Development of Wide Bandgap Perovskites for Next-Generation Low-Cost CdTe Tandem Solar Cells" *Chem. Eng. Sci.* 199: 388-397. www.doi.org/10.1016/j.ces.2019.01.003. Copyright 2019 Elsevier Ltd. TDS conceived and carried out the experiments, performed data analysis, contributed to the design component of this work, carried out simulations with assistance, and wrote the manuscript.

Current commercial tandem PV products are plagued by high cost or low efficiency, which limit their commercial application. Therefore, there has been an active search to develop a next-generation, low-cost thin film tandem solar cell technology that can yield the high efficiencies needed to continue long-term price reductions of solar power. This has accelerated interest in tandem cells made up of subcells employing thin film PV technologies.

At the moment, the most commercially successful thin film solar cell technology is CdTe. Although Si dominates the solar cell market, CdTe PVs are less expensive to fabricate, having consistently demonstrated the lowest cost for utility-scale power production[8,9] and lower energy manufacturing and payback time compared to silicon and CIGS technology.[10,11] For this reason, tandem solar cells based on CdTe have been widely discussed in the literature, predominantly in conjunction with either silicon or copper indium gallium selenide (CIGS).[5,12] However, the band gap of high efficiency CIGS devices and CdTe are too similar for tandem cells to dramatically improve PCE. To overcome this, other semiconductor materials have been proposed for tandem devices with CdTe, such as wide bandgap CdMgTe and CdZnTe,[13] or lower bandgap HgCdTe.[14] However, the high processing temperatures of these materials can damage underlying CdTe layers or be damaged by the CdTe deposition process when paired in a tandem configuration.[14]

Hybrid organic-inorganic perovskites, because of their lower processing temperature and high efficiencies, offer an interesting possibility for a thin film tandem cell configuration with CdTe. Solar cells based on hybrid organic-inorganic perovskites (HOIPs) have achieved power conversion efficiencies in excess of 24% (www.nrel.gov/pv/cell-efficiency). Additionally, HOIPs have readily tunable band gaps, which have made HOIPs attractive candidates for tandem PVs with a variety of different

materials.[15-17] Tandem PVs have been made with HOIPs coupled to silicon,[6,18-53] CIGS,[22,54-66] CZTS,[67] organic,[68] polymer,[69,70] DSSC,[71] quantum dot,[72,73] and other HOIP PVs.[74-84] Perhaps surprisingly, there has been little discussion about coupling HOIPs in tandem with CdTe PV technology, in spite of verified 22% PCE CdTe devices[7] and commercial success of CdTe module manufacturers. Furthermore, with an effective top absorber layer, CdTe is theoretically predicted to make efficient triple junction solar cells when coupled with silicon or germanium.[85] Finally, CdTe-HOIP tandems offer the potential for low cost manufacturing. For example, a recent technoeconomic study[12] showed that CdTe-CIGS tandems could achieve levelized cost of electricity (LCOE) as low as US$ 0.095/kWhr for residential solar and US$ 0.04/kWh for utility scale solar.

Here, we address the challenges that may be hindering the development of perovskite-CdTe tandem PVs and outline the prospects for this architecture going forward. We fabricate PVs from wide bandgap $CH_3NH_3PbBr_3$ (MAPBr) and demonstrate that these materials can provide reasonable efficiency as a top absorber layer, but that they also have high optical haze, which limits the light absorption by the CdTe layer and the performance of the perovskite-CdTe tandem cell. We use the Solar Cell Capacitance Simulator (SCAPS) software package to simulate a four-terminal (4T) tandem MAPBr-CdTe architecture to determine how much haze could be tolerated in the perovskite layer in such a device to still achieve an enhancement in device efficiency over the single-junction CdTe cell. Finally, we extend this simulation to other bottom cell materials, calculating the degree of optical opacity that can be tolerated in MAPBr for a variety of different MAPBr tandem architectures.

4.2 Experimental Details

4.2.1 Materials

Dimethylformamide (99.8% anhydrous), dimethylsulfoxide (≥99.9% anhydrous), zinc purum powder (99%), titanium diisopropoxide bis-acetylacetonate (75% in isopropanol), 1-butanol (99.8% anhydrous), titanium tetrachloride (99.9%), chlorobenzene (99.8% anhydrous), lithium bistrifluoromethanesulfonimidate (99.95%), acetonitrile (99.8% anhydrous), and 4-tert-butylpyridine (96%) were purchased from Sigma-Aldrich. Ethanol (200 proof, ≥99.5%) and reagent-grade hydrochloric acid (37%) were purchased from Fisher Chemical. Lead bromide ($PbBr_2$) was purchased from Alfa Aesar (Ultradry, 99.999%). Methylammonium bromide (CH_3NH_3Br, MABr) and 30 NR-D Nanoparticulate Titanium Dioxide paste were purchased from Greatcell Solar. Spiro-OMeTAD (N2,N2,N2′,N2′,N7,N7,N7′,N7′-octakis(4-methoxyphenyl)-9,9′-spirobi[9H-fluorene]-2,2′,7,7′-tetramine) was purchased from Merck. Tin-doped indium oxide (ITO) sputter targets were purchased from Kurt J. Lesker (99.99% In_2O_3:SnO_2 9:1), and glass coated with fluorene-doped tin oxide (FTO) was purchased from Hartford Glass Co.

4.2.2 Fabrication and Processing

4.2.2.1 TiO_2 Substrate Preparation

FTO substrates (2.5 cm × 2.5 cm) were cleaned with commercial dish soap (Dawn), doubly-distilled deionized water (DI-H_2O), and ethanol and a 0.8 cm × 2.5 cm area of FTO was etched away from the side of the substrate using concentrated HCl and zinc powder. The etched FTO glass was thoroughly washed in DI-H_2O and ethanol, immediately followed by 30 min of bath sonication in ethanol. Following sonication and one hour of UV-ozone exposure (Jelight Company Incorporated Model 42 UVO Cleaner), the n-type TiO_2 contact layers were cast onto the glass substrates. Then, 75 wt% titanium

diisopropoxide bis-acetylacetonate in isopropanol (TAA) was diluted to 72.5 µL/mL in anhydrous 1-butanol, while 210 g of 30 NR-D nanoparticle TiO_2 paste was mixed 3 mL of ethanol, forming a 70 mg/mL paste solution. The TAA solution was spin-coated at 700 rpm for 10 s, followed by 1000 rpm for 10 s and 2000 rpm for 30 s, and then heated for 10 min at 125 °C. Then the TiO_2 paste suspension was spin-coated onto the substrate using the same procedure as used for the TAA solution and heated for 5 min at 70 °C. Finally, the TiO_2 films were annealed for 1 h in air at 550 °C, which yields a film of 30 nm of compact TiO_2 under 150 nm of mesoporous TiO_2. The substrates were immersed for 10 min in 20 mM aqueous $TiCl_4$ at 90 °C and then heated in air at 500 °C for 30 min.

4.2.2.2 $CH_3NH_3PbBr_3$ (MAPBr) Deposition

Methylammonium lead bromide ($CH_3NH_3PbBr_3$; MAPBr) films were deposited in a nitrogen glove box (<5 ppm O_2, H_2O) following published procedures.[86] In a vial, 459 mg of $PbBr_2$ and 124 mg of CH_3NH_3Br were dissolved in 0.8 mL of DMF and 0.2 mL of DMSO for 2 h at room temperature, yielding a solution of 1.25 M $PbBr_2$ and 1.11 M CH_3NH_3Br in 4:1 v/v DMF:DMSO. Then, 50 µL of the solution was dropped onto the 6.5 cm^2 TiO_2-coated substrate as a thin layer and then spun at 1000 rpm for 10 s followed by 4000 rpm at 30 s. After 15 s of the second spin coating step, 100 µL of anhydrous chlorobenzene was dropped onto the center of the substrate. The substrates were heated in the glove box for 1 h at 100 °C.

4.2.2.3 Solar Cell Fabrication

Photovoltaic devices (PVs) were fabricated by spin coating spiro-OMeTAD onto the MAPBr films. Spiro-OMeTAD was dissolved in 72 mg/mL anhydrous chlorobenzene, along with 7.5 µL/mL 4-tert-butylpyridine and 24 µL/mL lithium

bistrifluoromethanesulfonimidate (LiTFSI) solution (170 mg LiTFSI salt in 1 mL acetonitrile). The spiro-OMeTAD solution was spin-coated onto the MAPBr film at 5000 rpm for 30 s. The substrate was placed in a desiccator for >12 h and then 100 nm of indium-doped tin oxide (ITO) was deposited by rf sputtering.[87]

4.2.3 Materials Characterization

UV–Vis-NIR absorbance and absorptance spectroscopy was performed using an Aligent Cary 5000 UV–Vis-NIR spectrophotometer with a PbS near infrared (NIR) detector and a photomultiplier tube. Absorptance measurements were collected in an Aligent Diffuse Reflectance Accessory DRA-2500 (DRA) using a center mount holder attachment with the direct beam aimed at ~8° relative to the angle of incident light. For reflectance and diffuse reflectance measurements, samples were mounted on the black cover of a Labsphere URS-99-020 reflectance standard in the reflectance port of the DRA with a PbS NIR detector and photomultiplier tube. Diffuse reflectance was collected with the light trap that came standard with the DRA-2500 positioned at ~10° relative to the incident beam with the direct reflectance beam aimed at the trap.[88]

Differential Image Contrast (DIC) images were acquired using a Leica DM2500 Compound Light Microscope with polarized plates positioned between the source and sample, and between the sample and camera.

Scanning electron microscopy (SEM) images were acquired with a Hitachi S-5500 SEM/STEM using an accelerating voltage of 30 kV and an emission current of ~15 μA in SEM mode. For SEM imaging, MAPBr films were prepared following the procedures used to fabricate PVs, except that the substrates were cut pieces of a p-type Si wafer with a resistivity of 10 Ω cm. The Si wafer was exposed to UV-ozone for 1 h before MAPBr

deposition. The substrate was electrically grounded to the SEM mount with carbon tape prior to imaging.

PV device performance was measured using a xenon lamp and a Keithley 2400 general purpose source meter. Current-voltage (J-V) curves were measured using a constant voltage sweep rate of 150 mV/s. There was no voltage or light biasing before taking the measurements, or between forward and reverse sweeps. Incident light was passed through an AM 1.5 filter and set at one sun intensity (100 mW/cm^2) via calibration with a Hamamatsu single crystal silicon diode.

4.2.4 SCAPS Simulations

The device response of CdTe PVs was simulated using the SCAPS software package.[89,90] Tables 4.1-4.4 list the parameters used for the calculations. In modeling CdTe devices with 15.5% power conversion efficiency (PCE), two types of defect states were included: a CdS/CdTe interfacial defect with 10^{10} cm^{-2} density ($S_n = 10^5$) and a bulk CdTe defect with 10^{14} cm^{-2} density.[90] The work function of the back contact was taken to be 5.4 eV. CdTe devices with 22.05% PCE were simulated by removing these defects and increasing the work function of the back contact to 5.6 eV.

In modeling CIGS devices, two types of defects similar to those used for the 15.5% PCE CdTe devices were included. The parameters for the CIGS device simulations were taken from the "Numos CIGS baseline.def" file that accompanies the SCAPS software.[91a] Table 4.2 lists the material properties and defect densities used in the simulations.

For all-perovskite tandem devices, the MAPI device layer was simulated using the MAPI model found in SCAPS 3.307 titled "Realistic perfect MAPI cell.def." These parameters are provided in Table 4.3. The modeling of amorphous silicon (a-Si) cells was

done following the procedures of Lee et al.[92] with the defect concentrations shown in Table 4.4. Table 4.4 also shows the other bulk material parameters used in the model calculations.

The device response of the bottom cell in four-terminal (4T) solar cells were simulated by filtering the light incident on the bottom cell. The total device response of the 4T device was then calculated based on the combined device responses of the top and bottom cells in the 4T tandem configuration.

Table 4.1 Parameters input into the SCAPS simulations for the CdTe PV device layer.

Parameter	**CdTe**	**CdS**	**$ZnSnO_x$**
Thickness (nm)	2500	50	150
E_g (eV)	1.5	2.4	3.6
χ (eV)	4.4	4.5	4.4
$\varepsilon/\varepsilon_0$	9.4	10	9
N_C (cm^{-3})	8e17	2.2e18	2.2e18
N_v (cm^{-3})	1.8e19	1.8e19	1.8e19
μ_e (cm^2/Vs)	320	100	100
μ_h (cm^2/Vs)	40	25	25
N_D (cm^{-3})	0	1e15	1e18
N_A (cm^{-3})	2e14	0	0

Table 4.2 Material parameters used for the SCAPS simulation of the CIGS JV curve. The work functions of the back and front contacts were 5.4 eV and 4.45 eV, respectively.

Parameter	**CIGS**	**CdS**	**ZnO_2**
Thickness (nm)	3000	50	150
E_g (eV)	1.1	2.4	3.3
χ (eV)	4.5	4.2	4.45
$\varepsilon/\varepsilon_0$	13.6	10	9
N_C (cm^{-3})	2.2e18	2.2e18	2.2e18
N_v (cm^{-3})	1.8e19	1.8e19	1.8e19
μ_e (cm^2/Vs)	100	100	100
μ_h (cm^2/Vs)	25	25	25
N_D (cm^{-3})	0	1e17	1e18
N_A(cm^{-3})	2e16	0	0
N_T(cm^{-3})	1.77e13	1.77e17	1.77e16

Table 4.3 Material parameters used for the SCAPS simulation of the $CH_3NH_3PbI_3$ J-V curve. The work functions of both contacts were set using the flat band approximation in the SCAPS software. The traps in MAPI were modeled by using two individual traps, one acceptor at $1*10^{15}$ cm^{-2} density and another donor at $1*10^{15}$ cm^{-2} density.

Parameter	**TiO_2**	**MAPI**	**Spiro**
Thickness (nm)	50	450	450
E_g (eV)	3.5	1.55	3.0
χ (eV)	4.0	3.9	2.2
$\varepsilon/\varepsilon_0$	9	6.5	3
N_C (cm^{-3})	2.2e18	2.2e18	2.2e18
N_v (cm^{-3})	1.8e19	1.8e19	1.8e19
μ_e (cm^2/Vs)	20	20	2e-4
μ_h (cm^2/Vs)	10	20	2e-4
N_D (cm^{-3})	1e19	1e13	0
N_A(cm^{-3})	0	0	2e18
N_T(cm^{-3})	1e15	2e15	1e15

Table 4.4 Material parameters used for the SCAPS simulation of the amorphous silicon J-V curve. The work functions of both contacts were set using the flat band approximation in the SCAPS software. The device was illuminated from the p-type front contact.

Parameter	**p-a-Si**	**i-a-Si**	**n-a-Si**
Thickness (nm)	25	400	20
E_g (eV)	1.92	1.82	1.82
χ (eV)	4.5	4.5	4.5
$\varepsilon/\varepsilon_0$	12	12	12
N_C (cm^{-3})	2.5e20	2.5e20	2.5e20
N_v (cm^{-3})	2.5e20	2.5e20	2.5e20
μ_e (cm^2/Vs)	10	20	20
μ_h (cm^2/Vs)	1	2	2
N_D (cm^{-3})	0	1e15	1e18
N_A(cm^{-3})	3e18	0	0
N_T(cm^{-3})	1e18	1e16	1e17

4.3 RESULTS AND DISCUSSION

4.3.1 Materials Property Considerations for a HOIP-CdTe Tandem Cell

By combining a CdTe PV with another absorber layer in a tandem configuration, the resulting tandem solar cell can achieve higher device efficiency by exploiting a wider range of the solar spectrum and reducing thermalization losses.[5-7] The first consideration of designing a perovskite-CdTe tandem cell is to determine the optimal band gap of the perovskite. Once this is known, a suitable material needs to be identified. And finally, an architecture that will accommodate the materials and the processing constraints must be realized.[1]

Zincblende CdTe has a band gap of 1.5 eV.[9,90] Recent high efficiency CdTe devices have employed a selenium grading that lowers the band gap to 1.42 eV,[9] and therefore, the optimal CdTe tandem cell with 1.42 eV CdSeTe requires either a bottom cell absorber layer

with a band gap of 0.85 eV[85,93] or a top cell with a wider band gap of 2.0–2.3 eV,[95] with the narrower band gap pairing having a higher theoretical efficiency. In terms of low bandgap perovskites as a bottom layer, $MAPb_{0.5}Sn_{0.5}PbI_3$ offers the lowest band gap yet observed from an HOIP (at 1 atm pressure), which is 1.17 eV.[95] While this is slightly higher than desired, it is not too far from the optimal band gap value.[85,93] However, tin-containing HOIPs—including $MAPb_{0.5}Sn_{0.5}PbI_3$—undergo rapid oxidative degradation in air[95,96] and have not performed well in solar cells.[97] Another alternative could be the HOIP-inspired double perovskite, $Cs_2AgTlBr_6$, which has recently been reported with a band gap of 0.95 eV. However, solar cells of this material have not yet been fabricated.[98] Therefore, pairing a wide bandgap HOIP with CdTe seems to be the most effective path towards perovskite-CdTe tandem PVs.

Fig. 4.1a provides a summary of the band gap energy of HOIP materials that might be used in a perovskite-CdTe tandem cell architecture. The HOIPs that have exhibited very high PV device efficiency like MAPI, FAPI and $CsPbI_3$ have band gaps that are too similar to CdTe and CdSeTe for tandem cells.[85,93,94] By incorporating bromide into these materials, the band gap can be increased above 2 eV as needed for tandem cells with CdTe;[100,102] however, most HOIP alloys with band gap energies in the range between 1.8 and 2.2 eV have been found to be unstable, exhibiting spontaneous photoinduced phase segregation.[104,107] This leaves the bromide HOIPs such as $FAPbBr_3$ ($E_g = 2.26$ eV), $MAPbBr_3$ ($E_g = 2.3$ eV), and $CsPbBr_3$ ($E_g = 2.35$ eV) as the most promising candidate materials for HOIP-CdTe tandems.

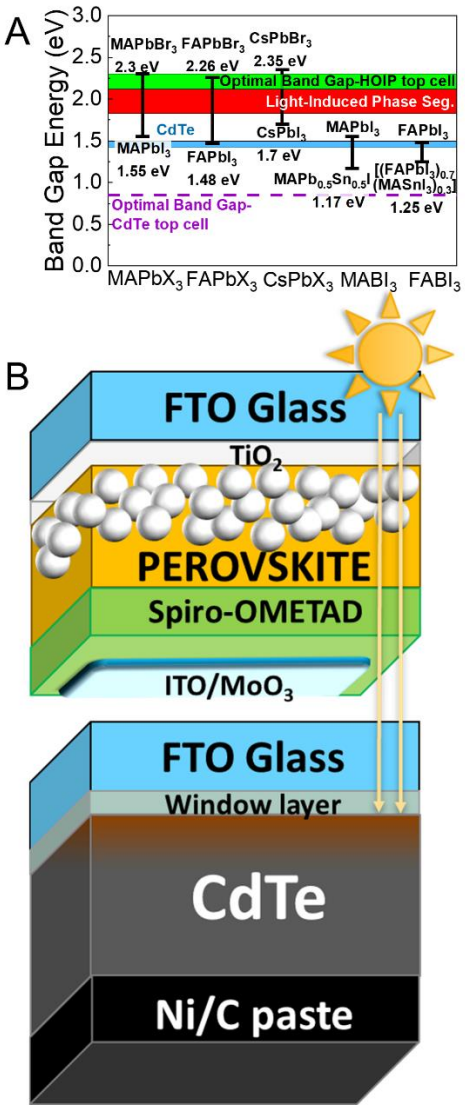

Figure 4.1: (A) Summary of the band gap energies of known perovskite materials compared to the band gap range of CdSeTe used in CdTe PV devices (1.42–1.5 eV). The band gap energies are taken from[45,67,95,99-106]. Most HOIPs with bandgap energies between 1.8 and 2.2 eV undergo light-induced phase segregation that limits device performance.[104,107,108] (B) Proposed 4T architecture of a HOIP-CdTe tandem PV. The high thermal processing temperature of the CdTe layer, the poor device performance of superstrate CdTe devices with reverse illumination, and the low efficiency of CdTe PVs with a substrate configuration limits the potential for monolithic two-terminal (2T) HOIP-CdTe tandem designs.

4.3.2 Architecture Design Considerations of a HOIP-CdTe Tandem Cell

The tandem cell can be configured into either a mechanically stacked four-terminal (4T) design or a monolithically integrated two-terminal design (2T). There is a preference in industry towards monolithic 2T devices, due to their lower operational complexity and balance of system (BoS) costs.[12] Monolithic 2T perovskite tandem cells have been made on Si,[25] CIGS,[56] and other perovskites[74] to achieve enhanced efficiency. For perovskite-CdTe tandems, 2T device integration will be a challenge because of the way high efficiency CdTe PVs are fabricated.

CdTe PVs are superstrate devices that have an n-type window layer of CdS (or more recently, a buffer layer of MgZnO)[90] that is first deposited on FTO-coated glass, followed by the CdTe absorber layer. The CdTe thin films are vacuum deposited at a substrate temperature of 550 °C and then treated with $CdCl_2$ at 450 °C to achieve commercially suitable device efficiency.[9,90] In a 2T HOIP-CdTe tandem, one would optimally design the structure to have the HOIP layer positioned between the glass and the CdTe absorber. In this case, however, such a design is infeasible, as the CdTe deposition temperature is considerably higher than the typical decomposition temperature of most HOIP PVs of about 200 °C.[109-111] A monolithic HOIP-CdTe tandem solar cell would therefore require deposition of the HOIP layer onto the CdTe device layer. This would require significant changes in the design of the CdTe device. If the perovskite were simply deposited on the CdTe layer, the device would require illumination on the side opposite to the window layer of the CdTe device. CdTe PVs are well-known to require illumination from the window layer for proper operation.[112,113] In fact, this requirement has long inhibited the short wavelength spectral response of CdTe devices.[90,113] Therefore, this configuration also seems untenable. The final monolithic option would be to employ an inverse CdTe device in a substrate configuration (i.e., CdTe deposited on the FTO-coated

glass followed by the window layer of CdS or MZO) and then deposit the perovskite device layer in a p-i-n architecture. This strategy introduces efficiency issues, as inverse substrate CdTe devices have yet to achieve a PCE above a relatively modest 14%.[60] Therefore, in order to create an efficient 2T monolithic HOIP-CdTe tandem, improvements are either needed in the performance of CdTe PVs with a substrate configuration (as opposed to superstrate), or superstrate CdTe PVs that exhibit high efficiency under reverse illumination. Neither one of these options are guaranteed to ever reach the high performance that is presently achieved in state-of-the-art commercial CdTe PVs.

It is also worth mentioning that although the 2T cells are preferred from an installation perspective (wiring, inverter integration, operation, etc), 4T designs do provide some preferred performance characteristics. For example, 4T designs are much more forgiving in their design constraints, allowing for a greater variation in top cell bandgap energy without efficiency dropoff.[6] The 4T configuration allows for greater process and materials flexibility since the materials in the two absorber layers can be processed independently. They also have a higher theoretical PCE due to relaxed current matching restrictions.[94] Therefore, we focus on the design and performance of a 4T HOIP-CdTe tandem cell, which seems most realistically realizable in the short-to-medium term.

4.3.3 A Wide Bandgap HOIP PV: Device Characteristics and Optical Properties

As a first step towards realizing a perovskite/CdTe tandem solar cell, we fabricated a single junction MAPBr PV using the device architecture shown in Fig. 4.1b. Fig. 4.2a shows the response of the device under simulated sunlight. Devices with an ITO top contact were made with 3.5% PCE reverse scans, and an open circuit voltage of 1.35 V. Note that the transparent top and bottom contacts of these devices—particularly the ITO layer—have not been optimized and work on higher efficiency semi-transparent wide band gap HOIP

PVs is ongoing. This involves for example the optimization of the ITO sputter deposition and use of a MoO_x interlayer. The optical properties of the functioning, semi-transparent MAPBr PV were then measured so that the HOIP-CdTe tandem cell performance could be modeled using SCAPS.

In the 4T device, light is being absorbed by the top MAPBr device layer and contributing to the power output of the device. Ideally, all of the photons that are not absorbed and converted into electricity make it through the top cell and reach the bottom CdTe cell. In reality, there is some degree of optical loss in the MAPBr top cell layer. The optical loss from top cell illumination was measured, as shown in Fig. 4.2a and 4.2b. There is a sharp drop in transmitted light at wavelengths less than 540 nm, which corresponds to the expected bandgap of MAPBr of 2.3 eV. At wavelengths above 540 nm, there is also a reduction in transmitted light of about 25%, with MAPBr being the single largest contributor of light loss in the device stack. After accounting for all of the light incident on an FTO/TiO_2/MAPBr thin film using an integrating sphere, the specular reflectance, specular transmittance, and diffuse reflectance of the thin film were determined and the contributions of reflection, parasitic absorption, and scattering processes to optical losses were estimated. Fig. 4.2c shows that parasitic absorption and reflection accounts for about 20% of the optical loss in the sub-gap region, which agrees with previous reports.[56,58,79] However, diffuse light scattering, otherwise referred to as optical haze, also has a very large contribution to optical losses in the sub-gap region. Haze is defined formally as all transmitted light that is scattered more than 2.5° relative to the incident beam, or as all reflected light that is scattered more than 2.5° relative to the spot of specular reflection.[114]

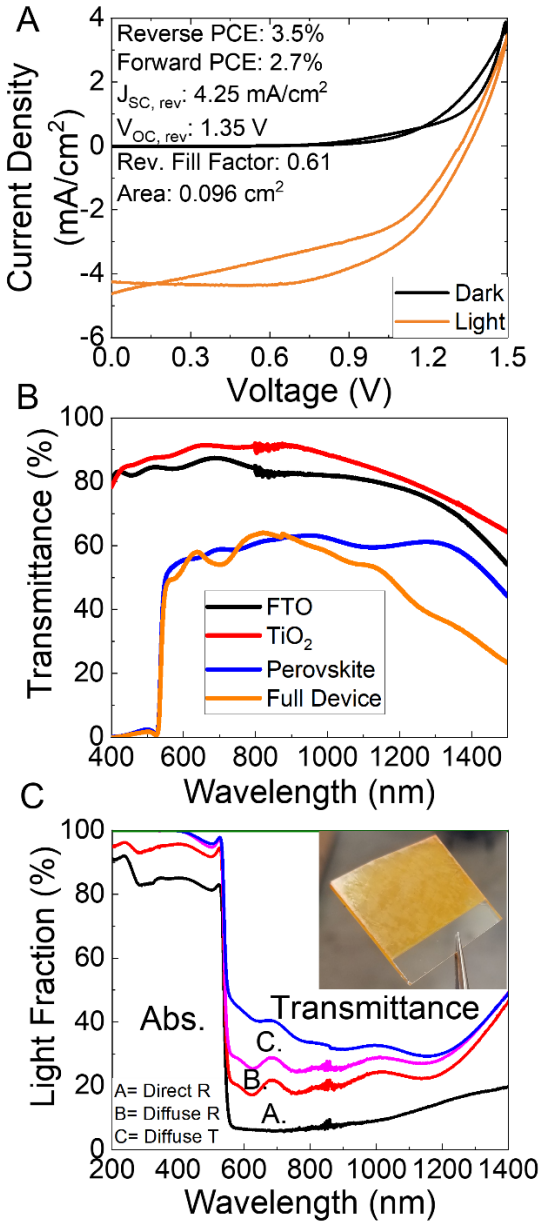

Figure 4.2: (A) Current-voltage (J-V) curves for a semi-transparent $MAPbBr_3$ device. (B) Direct transmittance curves taken after each layer in the MAPBr device was deposited. Each label in the legend corresponds to the last layer of the device that was deposited, using an architecture similar to Fig. 4.1b, but with ITO instead of gold as a top contact (C) Full light accounting of all incident light on a MAPBr-coated TiO_2 substrate. We observe a large portion of optical loss in MAPBr films is due to diffuse reflectance and transmission (i.e. optical haze). The inset in (C) shows a photograph of the MAPBr-coated TiO_2 substrate.

Differential image contrast (DIC) light microscopy of MAPBr deposited on TiO_2-coated FTO glass substrates revealed that the haze results from thickness non-uniformities in the perovskite layer. Fig. 4.3 shows DIC images and an SEM image of an MAPBr layer. DIC light microscopy is commonly used to characterize birefringent materials,[115] but it also reveals spatial variations of light scattering.[116] Regions of the film with significant light scattering appear darker when imaged in parallel polarized orientation and brighter under crossed polarized orientation. The variations in light scattering in the film appear to correlate with surface roughness in the film, similar to the features referred to in the literature as "wrinkles" in $Cs_xFA_{1-x}Pb(Br_yI_{1-y})_3$.[117,118] In one of these studies it was mentioned that device layers made with wider band gap materials exhibit more wrinkling.[117] The DIC and SEM images indicate that it is the wrinkling of the MAPBr film that creates the observed haze. Perhaps alternative methods for depositing wide band gap HOIPs could alleviate this problem, such as two-step deposition processes,[119] antisolvent engineering of the Hagfeldt process,[120] and the use of nanocrystals as opposed to bulk thin films.[121] Ultimately, the optical quality of the films made using these processes must be considered alongside their performance in functioning solar cells in order to determine their viability in HOIP-CdTe tandems.

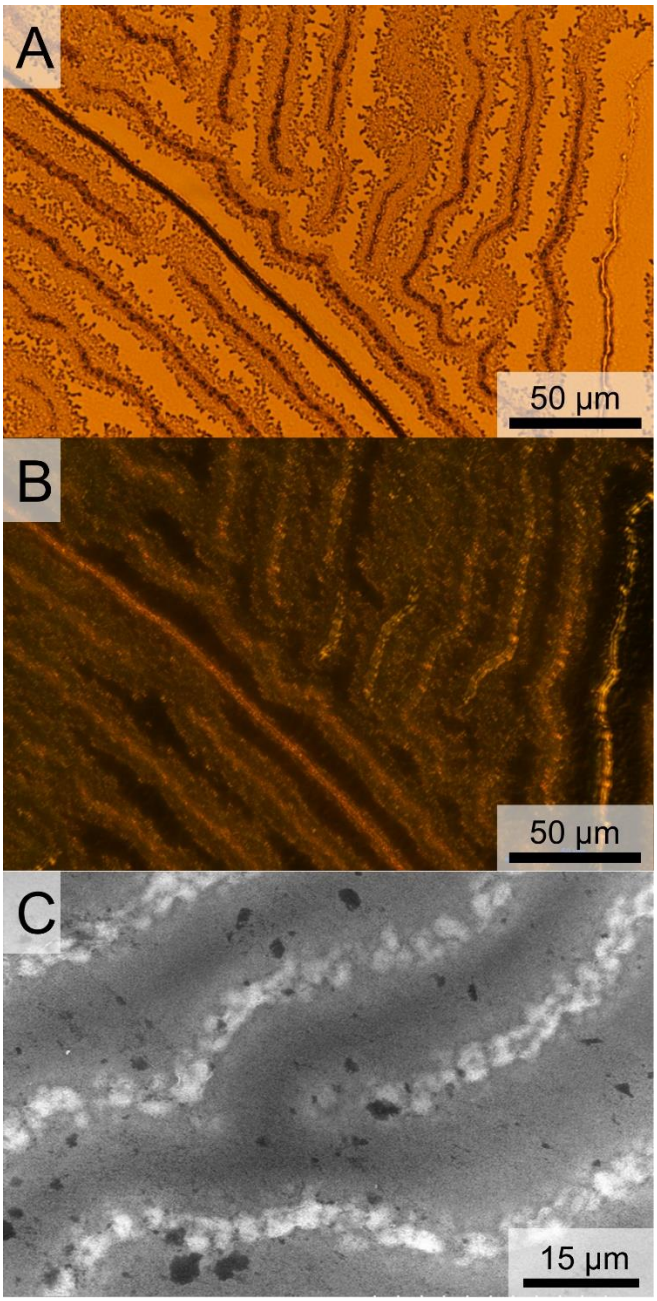

Figure 4.3: DIC microscopy images of a MAPBr thin film with source and analyzer polarizers in a (A) parallel and (B) crossed/perpendicular orientation. (C) A top down SEM image of a MAPBr thin film. Film "wrinkling" is observed consistent with reports on lower band gap HOIPs.[116,117]

4.3.4 SCAPS Modeling of 4T MAPBr-CdTe Tandem Devices

The device performance of 4T MAPBr/CdTe tandems was modeled using the measured optical and device characteristics of the MAPBr top cell and the Solar Cell Capacitance Simulator (SCAPS) software package using known parameters for CdTe devices.[89,90] Fig. 4 shows the J-V response of the CdTe bottom cell with a top cell having no haze or other sub-band gap optical loss. Device simulations of the CdTe cell were then performed considering the haze of the top cell by placing an appropriate optical filter over the CdTe bottom cell to mimic the 4T device. Less haze in the MAPBr layer is obviously desirable, but MAPBr device layers with higher PCE can tolerate more haze and still contribute to increasing the overall performance of a single junction CdTe PV. By subtracting the PCE of the filtered device from the PCE of the initial device, we determine the PCE of the top cell needed to "break even" or begin to improve the efficiency of the system relative to the baseline single junction CdTe PV. The PCEs of the top perovskite cell needed to break even are shown in Fig. 4.4 for two different CdTe devices—the 15.5% PCE device of Kephart et. al.[90] and an optimized CdTe device with no simulated defects and 22.05% PCE. For a MAPBr top cell (Eg = 2.3 eV) with 100% sub-band gap transmission and a 15.54% PCE CdTe bottom cell, an efficiency of at least 4.2% is needed to create a more efficient tandem. Note that the record PCE for MAPBr is 10.4%[122] and the Shockley-Queisser limit is 16.4%.[123] Using the commonly studied perovskite $FA_{0.83}Cs_{0.17}Pb(I_{0.6}Br_{0.4})_3$ (Eg = 1.75 eV) at least 11.1% PCE is needed to break even. For reference, the literature record for $FA_{0.83}Cs_{0.17}Pb(I_{0.6}Br_{0.4})_3$ is 17.8%,[124] and the Shockley Queisser limit is 27.5%.[123] The MAPBr top cell efficiency needed to improve the efficiency of a 22.05% PCE CdTe device is higher, with break-even PCEs for MAPBr and $FA_{0.83}Cs_{0.17}Pb(I_{0.6}Br_{0.4})_3$ of 6.9% and 16.2%, respectively.

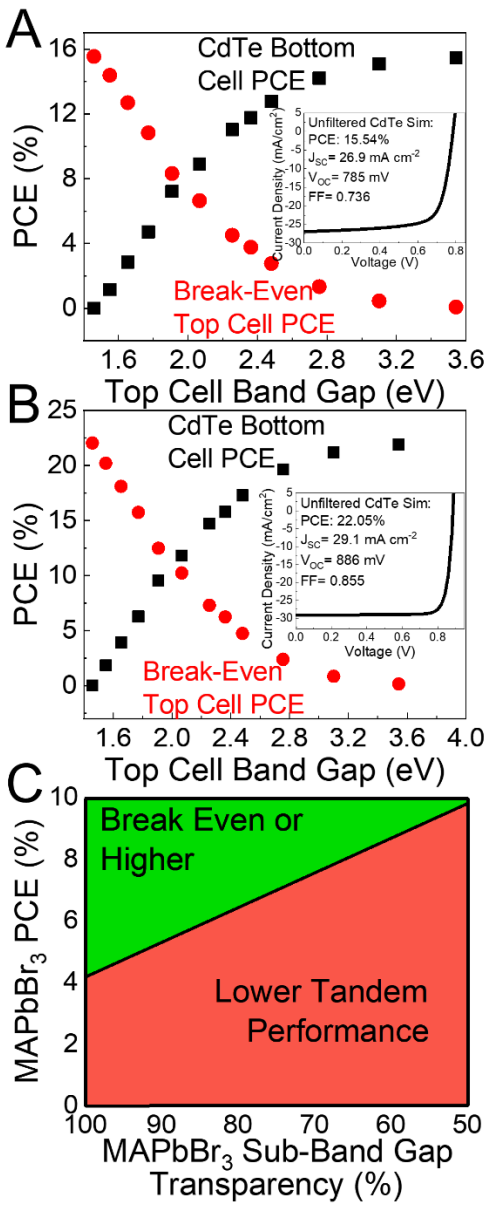

Figure 4.4 Simulation of wide band gap semiconductor-CdTe tandem PVs, given a CdTe PCE of (A) 15.5% and (B) 22.05%. In both cases, we plot the "break even" top cell PCE, defined here as the PCE of the top cell that is needed for the tandem device to eclipse the PCE of the CdTe cell without the top cell acting as an optical filter. The insets show the simulated JV curves of the unfiltered CdTe device. (C) Break even PCE of a CdTe tandem cell as a function of the sub-band gap transmission of the top cell, given a 2.3 eV band gap top cell and 15.5% PCE CdTe device. With higher top cell optical losses, a higher top cell PCE is needed.

Tandems utilizing MAPBr ($E_g = 2.3$ eV) top cells with haze were also simulated using SCAPS. For the simulations, top cell optical transmission curves were simplified to have uniform optical loss across the sub-band gap region (constant transmission $E(h\nu) < E_{g,HOIP}$, 0% transmission $E(h\nu) > E_{g,HOIP}$). Fig. 4.4c shows the break-even curves simulated using SCAPS, for 15.5% CdTe devices. With MAPBr top cells exhibiting 75% optical transmittance sub-band gap, 6.9% efficiency is needed in the top cell for the HOIP-CdTe tandem to outperform the CdTe bottom cell.

To compare perovskite-CdTe tandems with other perovskite-based tandems, SCAPS device modeling was carried out using CIGS, methylammonium lead iodide (MAPI) and amorphous Si as a bottom cell. Fig. 4.5 summarizes the results in terms of the acceptable amount of optical loss for MAPBr pairings with a CIGS ($E_g = 1.1$ eV; 17.4% PCE), methylammonium lead iodide/MAPI ($E_g = 1.5$ eV; 21.5% PCE), and amorphous silicon ($E_g = 1.82$ eV; 12.3% PCE). Parameters used for simulation are provided in Tables 4.2–4.4. For a MAPBr with 75% sub-band gap transmittance, the break-even PCE is 7.4%, 10.7%, and 8.4% respectively for CIGS, MAPI, and a-Si cells modeled here. The slightly higher break-even PCEs for the MAPI and CIGS tandems results in part from the higher PCE of the bottom cells.

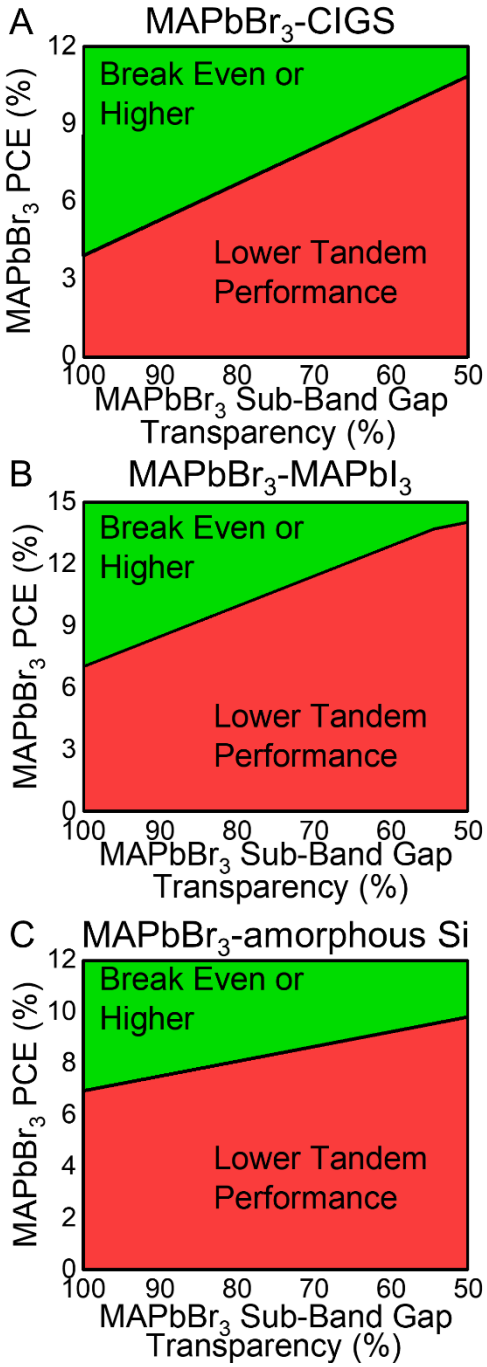

Figure 4.5 Break even PCE of perovskite top cell tandems as a function of sub-band gap optical transmission with a 2.3 eV $CH_3NH_3PbBr_3$ top cell: (A) a 1.1 eV band gap CIGS cell with 17.4% PCE, (B) a 1.55 eV band gap $CH_3NH_3PbI_3$ PV with 21.5% PCE, and (C) a 1.82 eV band gap amorphous silicon PV with 12.3% PCE.

4.4 CONCLUSION

The approach of increasing CdTe PV efficiency by the addition of a wide bandgap perovskite layer in a 4T tandem device configuration appears to be a plausible way to increase efficiency without significantly increasing manufacturing cost. The 4T configuration leads to higher BOS costs than a 2T tandem, but the increased efficiency might make it worthwhile to pursue such a device configuration.[12] In addition to the need to fabricate 4T devices, another challenge to perovskite-CdTe tandem cells appears to be the occurrence of haze in perovskite layers with the wide band gap needed for efficient operation with CdTe. Haze deteriorates the performance of the tandem by preventing light from reaching the bottom cell. SCAPS device modeling shows that it should still be possible to improve upon the bottom CdTe cell efficiency with a top perovskite cell with some amount of haze, but the necessary efficiency for this becomes much higher when the CdTe cell efficiency further increases towards its ideal high efficiency. It will require further layer optimization to eliminate the "wrinkles" that cause haze. Another challenge will be in the fabrication of highly transparent, conductive top and bottom contacts for the MAPBr top cell to eliminate parasitic light absorption. Again, a 2T device configuration can help alleviate this problem; however, only if high efficiency can somehow be achieved from CdTe PVs with alternative device fabrication (i.e., substrate) or illumination conditions (i.e., reverse illumination). Since the point is to take advantage of the tremendous progress in developing low-cost high-throughput manufacturing of CdTe thin film PVs to make low-cost, higher efficiency tandems, it may be the best strategy to figure out device designs that do not require significant changes to the CdTe cell design and operation. This will probably be the main challenge facing the development of perovskite-CdTe tandem PV technology.

4.5 REFERENCES

(1) Nelson, J. *The Physics of Solar Cells*. Imperial College Press: London, UK, 2003.

(2) Lazard Inc. 2018. Lazard's Levelized Cost of Electricity, Version 11.0. Lazard, New York, NY, USA

(3) SEIA and Greentech Media, 2017. Solar Market Insight Report 2016 Year in Review. SEIA, Washington, D.C. USA

(4) IEA, 2017. Tracking Clean Energy Progress: 2017. IEA, Paris, France.

(5) Todorov, T.K.; Gunawan, O.; Guha, S. In *Halide Perovskites: Photovoltaics, Light Emitting Diodes, and Beyond*; T.C. Sum, N. Mathews, Eds.; Wiley: Weinheim, Germany, 2018; Chapter 2.5 pp 83-99

(6) Werner, J.; Niesen, B.; Ballif, C. Perovskite/Silicon Tandem Solar Cells: Marriage of Convenience or True Love Story? - An Overview. *Adv. Mater. Interfaces*. **2018,** 5, 1700731.

(7) Green, M.A.; Hishikawa, Y.; Dunlop, E.D.; Levi, D.H.; Hohl-Ebinger, J.; Ho-Baillie, A.W.Y. Solar cell efficiency tables (version 52). *Prog. Photovolt. Res. Appl.*, **2018,** 26, 427–436.

(8) Munsi, A.; Sampath, W.S. CdTe Photovoltaics for Sustainable Electricity Generation. *J. Elect. Mat.* **2016**, 45, 4612-4619.

(9) Munshi, A.H.; Kephart, J.; Abbas, A.; Raguse, J.; Beaudry, J.-N.; Barth, K.; Sites, J.; Walls, J.; Sampath, W. Polycrystalline CdSeTe/CdTe Absorber Cells With 28 mA/cm^2 Short-Circuit Current. *IEEE J. Photovolt.* **2018**, 8, 310–314.

(10) Alsema, E.A.; de Wild-Scholten, M.J. Environmental Impacts of PV Electricity Generation- a Critical Comparison of Energy Supply Options. *21st European Photovoltaics Conference*. **2006**, 21

(11) Raugei, M.; Bargigli, S.; Ulgiati, S. Life cycle assessment and energy pay-back time of advanced photovoltaic modules: CdTe and CIS compared to poly-Si. *Energy.* **2007,** 32, 1310–1318.

(12) Sofia, S.E.; Mailoa, J.P.; Weiss, D.N.; Stanbery, B.J.; Buonassisi, T.; Peters, I.M. Economic viability of thin-film tandem solar modules in the United States. *Nat. Energy*, **2018**, 3, 387–394.

(13) Swanson, D.E.; Reich, C.; Abbas, A.; Shimpi, T.; Liu, H.; Ponce, F.A.; Walls, J.M.; Zhang, Y.-H.; Metzger, W.K.; Sampath, W.S.; Holman, Z.C. $CdCl_2$ passivation of polycrystalline CdMgTe and CdZnTe absorbers for tandem photovoltaic cells. *J. Appl. Phys.*, **2018**, 123, 203101.

(14) Compaan, A.D.; Gupta, A.; Lee, S.; Wang, S.; Drayton, J. High efficiency, magnetron sputtered CdS/CdTe solar cells. *Sol. Energy*, **2004**, 77, 815–822.

(15) Green, M.A.; Ho-Baillie, A.; Snaith, H.J. The emergence of perovskite solar cells. *Nat. Photonics*, **2014**, 8, 506–514.

(16) Lal, N.N.; Dkhissi, Y.; Li, W.; Hou, Q.; Cheng, Y.-B.; Bach, U. Perovskite Tandem Solar Cells. *Adv. Energy Mater.*, **2017** 7, 1602761.

(17) Liu, M.; Johnston, M.B.; Snaith, H.J. Efficient planar heterojunction perovskite solar cells by vapour deposition. *Nature*, **2013**, 501, 395–398.

(18) Adhyaksa, G.W.P.; Johlin, E.; Garnett, E.C. Nanoscale Back Contact Perovskite Solar Cell Design for Improved Tandem Efficiency. *Nano Lett.*, **2017**, 17, 5206–5212.

(19) Albrecht, S.; Saliba, M.; Correa Baena, J.P.; Lang, F.; Kegelmann, L.; Mews, M.; Steier, L.; Abate, A.; Rappich, J.; Korte, L.; Schlatmann, R.; Nazeeruddin, M.K.; Hagfeldt, A.; Grätzel, M.; Rech, B. Monolithic perovskite/silicon-heterojunction tandem solar cells processed at low temperature. *Energy Env. Sci.*, **2016** 9, 81–88.

(20) Albrecht, S.; Saliba, M.; Correa-Baena, J.P.; Jäger, K.; Korte, L.; Hagfeldt, A.; Grätzel, M.; Rech, B. Towards optical optimization of planar monolithic perovskite/silicon-heterojunction tandem solar cells. *J. Opt.*, **2016** 18, 064012.

(21) Ba, L.; Liu, H.; Shen, W. Perovskite/c-Si tandem solar cells with realistic inverted architecture: Achieving high efficiency by optical optimization. *Prog. Photovolt. Res. Appl.*, **2018**, 26, 924-933.

(22) Bailie, C.D.; Christoforo, M.G.; Mailoa, J.P.; Bowring, A.R.; Unger, E.L.; Nguyen, W.H.; Burschka, J.; Pellet, N.; Lee, J.Z.; Grätzel, M.; Noufi, R.; Buonassisi, T.; Salleo, A.; McGehee, M.D. Semi-transparent perovskite solar cells for tandems with silicon and CIGS. *Energy Env. Sci.*, **2015**, 8, 956–963.

(23) Bett, A.J.; Schulze, P.S.C.; Winkler, K.; Gasparetto, J.; Ndione, P.F.; Bivour, M.; Hinsch, A.; Kohlstädt, M.; Lee, S.; Mastroianni, S.; Mundt, L.E.; Mundus, M.; Reichel, C.; Richter, A.; Veit, C.; Wienands, K.; Würfel, U.; Veurman, W.; Glunz, S.W.; Hermle, M.; Goldschmidt, J.C. Low temperature perovskite solar cells with an evaporated TiO_2 compact layer for perovskite silicon tandem solar cells. *Energy Procedia*, **2017**, 124, 567–576.

(24) Bush, K.A.; Bailie, C.D.; Chen, Y.; Bowring, A.R.; Wang, W.; Ma, W.; Leijtens, T.; Moghadam, F.; McGehee, M.D. Thermal and Environmental Stability of Semi-Transparent Perovskite Solar Cells for Tandems Enabled by a Solution-Processed Nanoparticle Buffer Layer and Sputtered ITO Electrode. *Adv. Mater.*, **2016**, 28, 3937–3943.

(25) Bush, K.A.; Palmstrom, A.F.; Yu, Z.J.; Boccard, M.; Cheacharoen, R.; Mailoa, J.P.; McMeekin, D.P.; Hoye, R.L.Z.; Bailie, C.D.; Leijtens, T.; Peters, I.M.; Minichetti, M.C.; Rolston, N.; Prasanna, R.; Sofia, S.; Harwood, D.; Ma, W.; Moghadam, F.; Snaith, H.J.; Buonassisi, T.; Holman, Z.C.; Bent, S.F.; McGehee, M.D. 23.6%-efficient monolithic perovskite/silicon tandem solar cells with improved stability. *Nat. Energy*, **2017**, 2, 17009.

(26) Chen, B.; Bai, Y.; Yu, Z.; Li, T.; Zheng, X.; Dong, Q.; Shen, L.; Boccard, M.; Gruverman, A.; Holman, Z.; Huang, J. Efficient Semitransparent Perovskite Solar Cells for 23.0%-Efficiency Perovskite/Silicon Four-Terminal Tandem Cells. *Adv. Energy Mater.*, **2016**, 6, 1601128.

(27) Duong, T.; Lal, N.; Grant, D.; Jacobs, D.; Zheng, P.; Rahman, S.; Shen, H.; Stocks, M.; Blakers, A.; Weber, K.; White, T.P.; Catchpole, K.R. Semitransparent Perovskite Solar Cell With Sputtered Front and Rear Electrodes for a Four-Terminal Tandem. *IEEE J. Photovolt.*, **2016**, 6, 679–687.

(28) Duong, T.; Wu, Y.; Shen, H.; Peng, J.; Fu, X.; Jacobs, D.; Wang, E.-C.; Kho, T.C.; Fong, K.C.; Stocks, M.; Franklin, E.; Blakers, A.; Zin, N.; McIntosh, K.; Li, W.; Cheng, Y.-B.; White, T.P.; Weber, K.; Catchpole, K. Rubidium Multication Perovskite with Optimized Bandgap for Perovskite-Silicon Tandem with over 26% Efficiency. *Adv. Energy Mater.*, **2017**, 7, 1700228.

(29) Fan, R.; Zhou, N.; Zhang, L.; Yang, R.; Meng, Y.; Li, L.; Guo, T.; Chen, Y.; Xu, Z.; Zheng, G.; Huang, Y.; Li, Liang, Qin, L.; Qiu, X.; Chen, Q.; Zhou, H. Toward Full Solution Processed Perovskite/Si Monolithic Tandem Solar Device with PCE Exceeding 20%. *Sol. RRL*, **2017**, 1, 1700149.

(30) Degans, H. Imec Reports Record Conversion Efficiency of 23.9 Percent on a 4 cm^2 Perovskite/Silicon Solar Module. *IMEC*, **2017**, https://www.imec-int.com/en/articles/imec-reports-record-conversion-efficiency-of-23-9-percent-on-a-4cm2-perovskite-silicon-solar-module

(31) Jaysankar, M.; Filipič, M.; Zielinski, B.; Schmager, R.; Song, W.; Qiu, W.; Paetzold, U.W.; Aernouts, T.; Debucquoy, M.; Gehlhaar, R.; Poortmans, J. Perovskite–silicon tandem solar modules with optimised light harvesting. *Energy Environ. Sci.*, **2018**, 11, 1489–1498.

(32) Jaysankar, M.; Qiu, W.; van Eerden, M.; Aernouts, T.; Gehlhaar, R.; Debucquoy, M.; Paetzold, U.W.; Poortmans, J. Four-Terminal Perovskite/Silicon Multijunction Solar Modules. *Adv. Energy Mater.*, **2017**, 7, 1602807.

(33) Jošt, M.; Albrecht, S.; Lipovšek, B.; Krč, J.; Korte, L.; Rech, B.; Topič, M. Back- and Front-side Texturing for Light-management in Perovskite / Silicon-heterojunction Tandem Solar Cells. *Energy Procedia*, **2016**, 102, 43–48.

(34) Li, Y.; Hu, H.; Chen, B.; Salim, T.; Zhang, J.; Ding, J.; Yuan, N.; Lam, Y.M. Reflective perovskite solar cells for efficient tandem applications. *J. Mater. Chem. C*, **2017**, 5, 134–139.

(35) Löper, P.; Moon, S.-J.; de Nicolas, S.M.; Niesen, B.; Ledinsky, M.; Nicolay, S.; Bailat, J.; Yum, J.-H.; De Wolf, S.; Ballif, C. Organic–inorganic halide perovskite/crystalline silicon four-terminal tandem solar cells. *Phys. Chem. Chem. Phys.*, **2015**, 17, 1619–1629.

(36) Mailoa, J.P.; Bailie, C.D.; Johlin, E.C.; Hoke, E.T.; Akey, A.J.; Nguyen, W.H.; McGehee, M.D.; Buonassisi, T. A 2-terminal perovskite/silicon multijunction solar cell enabled by a silicon tunnel junction. *Appl. Phys. Lett.*, **2015**, 106, 121105.

(37) McMeekin, D.P.; Sadoughi, G.; Rehman, W.; Eperon, G.E.; Saliba, M.; Hörantner, M.T.; Haghighirad, A.; Sakai, N.; Korte, L.; Rech, B.; Johnston, M.B.; Herz, L.M.; Snaith, H.J. A mixed-cation lead mixed-halide perovskite absorber for tandem solar cells. *Science*, **2016**, 351, 151–155.

(38) Peng, J.; Duong, T.; Zhou, X.; Shen, H.; Wu, Y.; Mulmudi, H.K.; Wan, Y.; Zhong, D.; Li, J.; Tsuzuki, T.; Weber, K.J.; Catchpole, K.R.; White, T.P. Efficient Indium-Doped TiOx Electron Transport Layers for High-Performance Perovskite Solar Cells and Perovskite-Silicon Tandems. *Adv. Energy Mater.*, **2017**, 7, 1601768.

(39) Ramírez Quiroz, C.O.; Shen, Y.; Salvador, M.; Forberich, K.; Schrenker, N.; Spyropoulos, G.D.; Heumüller, T.; Wilkinson, B.; Kirchartz, T.; Spiecker, E.; Verlinden, P.J.; Zhang, X.; Green, M.A.; Ho-Baillie, A.; Brabec, C.J. Balancing electrical and optical losses for efficient 4-terminal Si–perovskite solar cells with solution processed percolation electrodes. *J. Mater. Chem. A*, **2018**, 6, 3583–3592.

(40) Sahli, F.; Kamino, B.A.; Werner, J.; Bräuninger, M.; Paviet-Salomon, B.; Barraud, L.; Monnard, R.; Seif, J.P.; Tomasi, A.; Jeangros, Q.; Hessler-Wyser, A.; De Wolf, S.; Despeisse, M.; Nicolay, S.; Niesen, B.; Ballif, C. Improved Optics in Monolithic Perovskite/Silicon Tandem Solar Cells with a Nanocrystalline Silicon Recombination Junction. *Adv. Energy Mater.*, **2018**, 8, 1701609.

(41) Sahli, F.; Werner, J.; Kamino, B.A.; Bräuninger, M.; Monnard, R.; Paviet-Salomon, B.; Barraud, L.; Ding, L.; Diaz Leon, J.J.; Sacchetto, D.; Cattaneo, G.; Despeisse, M.; Boccard, M.; Nicolay, S.; Jeangros, Q.; Niesen, B.; Ballif, C. Fully textured monolithic perovskite/silicon tandem solar cells with 25.2% power conversion efficiency. *Nat. Mater.*, **2018**, 17, 820-826.

(42) Schneider, B.W.; Lal, N.N.; Baker-Finch, S.; White, T.P. Pyramidal surface textures for light trapping and antireflection in perovskite-on-silicon tandem solar cells. *Opt. Express*, **2014**, 22, A1422-A1430.

(43) Shi, D.; Zeng, Y.; Shen, W. Perovskite/c-Si tandem solar cell with inverted nanopyramids: realizing high efficiency by controllable light trapping. *Sci. Rep.*, **2015**, 5, 16504.

(44) Song, Z.; Werner, J.; Shrestha, N.; Sahli, F.; De Wolf, S.; Niesen, B.; Watthage, S.C.; Phillips, A.B.; Ballif, C.; Ellingson, R.J.; Heben, M.J. Probing Photocurrent Nonuniformities in the Subcells of Monolithic Perovskite/Silicon Tandem Solar Cells. *J. Phys. Chem. Lett.*, **2016**, 7, 5114–5120.

(45) Uzu, H.; Ichikawa, M.; Hino, M.; Nakano, K.; Meguro, T.; Hernández, J.L.; Kim, H.-S.; Park, N.-G.; Yamamoto, K. High efficiency solar cells combining a perovskite and a silicon heterojunction solar cells via an optical splitting system. *Appl. Phys. Lett.*, **2015**, 106, 013506.

(46) Werner, J.; Barraud, L.; Walter, A.; Bräuninger, M.; Sahli, F.; Sacchetto, D.; Tétreault, N.; Paviet-Salomon, B.; Moon, S.-J.; Allebé, C.; Despeisse, M.; Nicolay, S.; De Wolf, S.; Niesen, B.; Ballif, C. Efficient Near-Infrared-Transparent Perovskite Solar Cells Enabling Direct Comparison of 4-Terminal and Monolithic Perovskite/Silicon Tandem Cells. *ACS Energy Lett.*, **2016**, 1, 474–480.

(47) Werner, J.; Dubuis, G.; Walter, A.; Löper, P.; Moon, S.-J.; Nicolay, S.; Morales-Masis, M.; De Wolf, S.; Niesen, B.; Ballif, C. Sputtered rear electrode with broadband transparency for perovskite solar cells. *Sol. Energy Mater. Sol. Cells*, **2015**, 141, 407–413.

(48) Werner, J.; Sahli, F.; Fu, F.; Diaz Leon, J.J.; Walter, A.; Kamino, B.A.; Niesen, B.; Nicolay, S.; Jeangros, Q.; Ballif, C. Perovskite/Perovskite/Silicon Monolithic Triple-Junction Solar Cells with a Fully Textured Design. *ACS Energy Lett.*, **2018**, 3, 2052–2058.

(49) Werner, J.; Walter, A.; Rucavado, E.; Moon, S.-J.; Sacchetto, D.; Rienaecker, M.; Peibst, R.; Brendel, R.; Niquille, X.; De Wolf, S.; Löper, P.; Morales-Masis, M.; Nicolay, S.; Niesen, B.; Ballif, C. Zinc tin oxide as high-temperature stable recombination layer for mesoscopic perovskite/silicon monolithic tandem solar cells. *Appl. Phys. Lett.*, **2016**, 109, 233902.

(50) Werner, J.; Weng, C.-H.; Walter, A.; Fesquet, L.; Seif, J.P.; De Wolf, S.; Niesen, B.; Ballif, C. Efficient Monolithic Perovskite/Silicon Tandem Solar Cell with Cell Area >1 cm^2. *J. Phys. Chem. Lett.*, **2016**, 7, 161–166.

(51) Wu, Y.; Yan, D.; Peng, J.; Duong, T.; Wan, Y.; Phang, S.P.; Shen, H.; Wu, N.; Barugkin, C.; Fu, X.; Surve, S.; Grant, D.; Walter, D.; White, T.P.; Catchpole, K.R.; Weber, K.J. Monolithic perovskite/silicon-homojunction tandem solar cell with over 22% efficiency. *Energy Environ. Sci.*, **2017**, 10, 2472–2479.

(52) Zhang, Yaokang, Wu, Z.; Li, P.; Ono, L.K.; Qi, Y.; Zhou, J.; Shen, H.; Surya, C.; Zheng, Z. Fully Solution-Processed TCO-Free Semitransparent Perovskite Solar Cells for Tandem and Flexible Applications. *Adv. Energy Mater.*, **2018**, 8, 1701569.

(53) Zheng, J.; Lau, C.F.J.; Mehrvarz, H.; Ma, F.-J.; Jiang, Y.; Deng, X.; Soeriyadi, A.; Kim, J.; Zhang, M.; Hu, L.; Cui, X.; Lee, D.S.; Bing, J.; Cho, Y.; Chen, C.; Green, M.A.; Huang, S.; Ho-Baillie, A.W.Y. Large area efficient interface layer free monolithic perovskite/homo-junction-silicon tandem solar cell with over 20% efficiency. *Energy Environ. Sci.*, **2018**, 11, 2432–2443.

(54) Fu, F.; Feurer, T.; Jäger, T.; Avancini, E.; Bissig, B.; Yoon, S.; Buecheler, S.; Tiwari, A.N. Low-temperature-processed efficient semi-transparent planar perovskite solar cells for bifacial and tandem applications. *Nat. Commun.*, **2015**, 6, 8932.

(55) Fu, F.; Feurer, T.; Weiss, T.P.; Pisoni, S.; Avancini, E.; Andres, C.; Buecheler, S.; Tiwari, A.N. High-efficiency inverted semi-transparent planar perovskite solar cells in substrate configuration. *Nat. Energy*, **2016**, 2, 16190.

(56) Guchhait, A.; Dewi, H.A.; Leow, S.W.; Wang, H.; Han, G.; Suhaimi, F.B.; Mhaisalkar, S.; Wong, L.H.; Mathews, N. Over 20% Efficient CIGS–Perovskite Tandem Solar Cells. *ACS Energy Lett.*, **2017**, 2, 807–812.

(57) Han, Q.; Hsieh, Y.-T.; Meng, L.; Wu, J.-L.; Sun, P.; Yao, E.-P.; Chang, S.-Y.; Bae, S.-H.; Kato, T.; Bermudez, V.; Yang, Y. High-performance perovskite/Cu(In,Ga)Se_2 monolithic tandem solar cells. *Science*, **2018**, 361, 904-908.

(58) Jang, Y.H.; Lee, J.M.; Seo, J.W.; Kim, I.; Lee, D.-K. Monolithic tandem solar cells comprising electrodeposited $CuInSe_2$ and perovskite solar cells with a nanoparticulate ZnO buffer layer. *J. Mater. Chem. A*, **2017**, 5, 19439–19446.

(59) Kranz, L.; Abate, A.; Feurer, T.; Fu, F.; Avancini, E.; Löckinger, J.; Reinhard, P.; Zakeeruddin, S.M.; Grätzel, M.; Buecheler, S.; Tiwari, A.N. High-Efficiency Polycrystalline Thin Film Tandem Solar Cells. *J. Phys. Chem. Lett.*, **2015**, 6, 2676–2681.

(60) Kranz, L.; Schmitt, R.; Gretener, C.; Perrenoud, J.; Pianezzi, F.; Uhl, A.R.; Keller, D.; Buecheler, S.; Tiwari, A.N. Progress towards 14% efficient CdTe solar cells in substrate configuration. *IEEE Photovoltaics Specialists Conference (PVSC)*, **2013**, pp. 1644–1648.

(61) Paetzold, U.W.; Jaysankar, M.; Gehlhaar, R.; Ahlswede, E.; Paetel, S.; Qiu, W.; Bastos, J.; Rakocevic, L.; Richards, B.S.; Aernouts, T.; Powalla, M.; Poortmans, J. Scalable perovskite/CIGS thin-film solar module with power conversion efficiency of 17.8%. *J. Mater. Chem. A*, **2017**, 5, 9897–9906.

(62) Pisoni, S.; Fu, F.; Feurer, T.; Makha, M.; Bissig, B.; Nishiwaki, S.; Tiwari, A.N.; Buecheler, S. Flexible NIR-transparent perovskite solar cells for all-thin-film tandem photovoltaic devices. *J. Mater. Chem. A*, **2017**, 5, 13639–13647.

(63) Shen, H.; Duong, T.; Peng, J.; Jacobs, D.; Wu, N.; Gong, J.; Wu, Y.; Karuturi, S.K.; Fu, X.; Weber, K.; Xiao, X.; White, T.P.; Catchpole, K. Mechanically-stacked perovskite/CIGS tandem solar cells with efficiency of 23.9% and reduced oxygen sensitivity. *Energy Environ. Sci.*, **2018**, 11, 394–406.

(64) Todorov, T.; Gershon, T.; Gunawan, O.; Lee, Y.S.; Sturdevant, C.; Chang, L.-Y.; Guha, S. Monolithic Perovskite-CIGS Tandem Solar Cells via In Situ Band Gap Engineering. *Adv. Energy Mater.*, **2015**, 5, 1500799.

(65) Uhl, A.R.; Yang, Z.; Jen, A.K.-Y.; Hillhouse, H.W.. Solution-processed chalcopyrite–perovskite tandem solar cells in bandgap-matched two- and four-terminal architectures. *J. Mater. Chem. A*, **2017**, 5, 3214–3220.

(66) Yang, Y. (Michael), Chen, Q.; Hsieh, Y.-T.; Song, T.-B.; Marco, N.D.; Zhou, H.; Yang, Y. Multilayer Transparent Top Electrode for Solution Processed Perovskite/Cu(In,Ga)$(Se,S)_2$ Four Terminal Tandem Solar Cells. *ACS Nano*, **2015**, 9, 7714–7721.

(67) Todorov, T.; Gershon, T.; Gunawan, O.; Sturdevant, C.; Guha, S. Perovskite-kesterite monolithic tandem solar cells with high open-circuit voltage. *Appl. Phys. Lett.*, **2014**, 105, 173902.

(68) Chen, C.-C.; Bae, S.-H.; Chang, W.-H.; Hong, Z.; Li, G.; Chen, Q.; Zhou, H.; Yang, Y. Perovskite/polymer monolithic hybrid tandem solar cells utilizing a low-temperature, full solution process. *Mater. Horiz.*, **2015**, 2, 203–211.

(69) Chen, W.; Zhang, J.; Xu, G.; Xue, R.; Li, Y.; Zhou, Y.; Hou, J.; Li, Y. A Semitransparent Inorganic Perovskite Film for Overcoming Ultraviolet Light Instability of Organic Solar Cells and Achieving 14.03% Efficiency. *Adv. Mater.*, **2018**, 30, 1800855.

(70) Liu, Y.; Renna, L.A.; Bag, M.; Page, Z.A.; Kim, P.; Choi, J.; Emrick, T.; Venkataraman, D.; Russell, T.P. High Efficiency Tandem Thin-Perovskite/Polymer Solar Cells with a Graded Recombination Layer. *ACS Appl. Mater. Interfaces*, **2016**, 8, 7070–7076.

(71) Kinoshita, T.; Nonomura, K.; Joong Jeon, N.; Giordano, F.; Abate, A.; Uchida, S.; Kubo, T.; Seok, S.I.; Nazeeruddin, M.K.; Hagfeldt, A.; Grätzel, M.; Segawa, H. Spectral splitting photovoltaics using perovskite and wideband dye-sensitized solar cells. *Nat. Commun.*, **2015**, 6, 8834.

(72) Karani, A.; Yang, L.; Bai, S.; Futscher, M.H.; Snaith, H.J.; Ehrler, B.; Greenham, N.C.; Di, D. Perovskite/Colloidal Quantum Dot Tandem Solar Cells: Theoretical Modeling and Monolithic Structure. *ACS Energy Lett.*, **2018**, 3, 869–874.

(73) Kim, J.; Ouellette, O.; Voznyy, O.; Wei, M.; Choi, J.; Choi, M.-J.; Jo, J.W.; Baek, S.-W.; Fan, J.; Saidaminov, M.I.; Sun, B.; Li, P.; Nam, D.-H.; Hoogland, S.; Lu, Z.-H.; García de Arquer, F.P.; Sargent, E.H. Butylamine-Catalyzed Synthesis of Nanocrystal Inks Enables Efficient Infrared CQD Solar Cells. *Adv. Mater.*, **2018**, 30, 1803830.

(74) Eperon, G.E.; Leijtens, T.; Bush, K.A.; Prasanna, R.; Green, T.; Wang, J.T.-W.; McMeekin, D.P.; Volonakis, G.; Milot, R.L.; May, R.; Palmstrom, A.; Slotcavage, D.J.; Belisle, R.A.; Patel, J.B.; Parrott, E.S.; Sutton, R.J.; Ma, W.; Moghadam, F.; Conings, B.; Babayigit, A.; Boyen, H.-G.; Bent, S.; Giustino, F.; Herz, L.M.; Johnston, M.B.; McGehee, M.D.; Snaith, H.J. Perovskite-perovskite tandem photovoltaics with optimized band gaps. *Science*, **2016**, 354, 861–865.

(75) Forgács, D.; Gil-Escrig, L.; Pérez-Del-Rey, D.; Momblona, C.; Werner, J.; Niesen, B.; Ballif, C.; Sessolo, M.; Bolink, H.J. Efficient Monolithic Perovskite/Perovskite Tandem Solar Cells. *Adv. Energy Mater.*, **2017**, 7, 1602121.

(76) Heo, J.H.; Im, S.H. $CH_3NH_3PbBr_3$-$CH_3NH_3PbI_3$ Perovskite-Perovskite Tandem Solar Cells with Exceeding 2.2 V Open Circuit Voltage. *Adv. Mater.*, **2016**, 28, 5121–5125.

(77) Jiang, F.; Liu, T.; Luo, B.; Tong, J.; Qin, F.; Xiong, S.; Li, Z.; Zhou, Y. A two-terminal perovskite/perovskite tandem solar cell. *J. Mater. Chem. A*, **2016**, 4, 1208–1213.

(78) Leijtens, T.; Prasanna, R.; Bush, K.A.; Eperon, G.; Raiford, J.A.; Gold-Parker, A.; Wolf, E.J.; Swifter, S.A.; Boyd, C.C.; Wang, H.-P.; Toney, M.F.; Bent, S.; McGehee, M.D. Tin-lead halide perovskites with improved thermal and air stability for efficient all-perovskite tandem solar cells. *Sustain. Energy Fuels.*, **2018**, 2, 2450-2459

(79) Rajagopal, A.; Yang, Z.; Jo, S.B.; Braly, I.L.; Liang, P.-W.; Hillhouse, H.W.; Jen, A.K.-Y. Highly Efficient Perovskite-Perovskite Tandem Solar Cells Reaching 80% of the Theoretical Limit in Photovoltage. *Adv. Mater.*, **2017**, 29, 1702140.

(80) Sheng, R.; Ho-Baillie, A.W.Y.; Huang, S.; Keevers, M.; Hao, X.; Jiang, L.; Cheng, Y.-B.; Green, M.A. Four-Terminal Tandem Solar Cells Using $CH_3NH_3PbBr_3$ by Spectrum Splitting. *J. Phys. Chem. Lett.*, **2015**, 6, 3931–3934.

(81) Sheng, R.; Hörantner, M.T.; Wang, Z.; Jiang, Y.; Zhang, W.; Agosti, A.; Huang, S.; Hao, X.; Ho-Baillie, A.; Green, M.; Snaith, H.J. Monolithic Wide Band Gap Perovskite/Perovskite Tandem Solar Cells with Organic Recombination Layers. *J. Phys. Chem. C*, **2017**, 121, 27256–27262.

(82) Yang, Z.; Rajagopal, A.; Chueh, C.-C.; Jo, S.B.; Liu, B.; Zhao, T.; Jen, A.K.-Y. Stable Low-Bandgap Pb-Sn Binary Perovskites for Tandem Solar Cells. *Adv. Mater.*, **2016**, 28, 8990–8997.

(83) Zhao, D.; Wang, C.; Song, Z.; Yu, Y.; Chen, C.; Zhao, X.; Zhu, K.; Yan, Y. Four-Terminal All-Perovskite Tandem Solar Cells Achieving Power Conversion Efficiencies Exceeding 23%. *ACS Energy Lett.*, **2018**, 3, 305–306.

(84) Zhao, D.; Yu, Y.; Wang, C.; Liao, W.; Shrestha, N.; Grice, C.R.; Cimaroli, A.J.; Guan, L.; Ellingson, R.J.; Zhu, K.; Zhao, X.; Xiong, R.-G.; Yan, Y. Low-bandgap mixed tin–lead iodide perovskite absorbers with long carrier lifetimes for all-perovskite tandem solar cells. *Nat. Energy*, **2017**, 2, 17018.

(85) Vos, A.D. Detailed balance limit of the efficiency of tandem solar cells. *J. Phys. D: Appl. Phys.*, **1980**, 13, 839–846.

(86) Jesper Jacobsson, T.; Correa-Baena, J.-P.; Pazoki, M.; Saliba, M.; Schenk, K.; Grätzel, M.; Hagfeldt, A. Exploration of the compositional space for mixed lead halogen perovskites for high efficiency solar cells. *Energy Environ. Sci.*, **2016**, 9, 1706–1724.

(87) Voggu, V.R.; Sham, J.; Pfeffer, S.; Pate, J.; Fillip, L.; Harvey, T.B.; Brown Jr.; R.M.; Korgel, B.A. Flexible $CuInSe_2$ Nanocrystal Solar Cells on Paper. *ACS Energy Lett.*, **2017**, 2, 574–581.

(88) Holmberg, V.C.; Bogart, T.D.; Chockla, A.M.; Hessel, C.M.; Korgel, B.A. 2012. Optical Properties of Silicon and Germanium Nanowire Fabric. *J. Phys. Chem. C*, **2012**, 116, 22486–22491.

(89) Burgelman, M.; Nollet, P.; Degrave, S. Modelling polycrystalline semiconductor solar cells. *Thin Solid Films*, **2000**, 361–362, 527–532.

(90) Kephart, J.M.; Geisthardt, R.M.; Sampath, W.S. Optimization of CdTe thin-film solar cell efficiency using a sputtered, oxygenated CdS window layer. *Prog. Photovolt. Res. Appl.*, **2015**, 23, 1484–1492.

(91) Chelvanathan, P.; Hossain, M.I.; Amin, N. Performance analysis of copper–indium–gallium–diselenide (CIGS) solar cells with various buffer layers by SCAPS. *Curr. Appl. Phys.*, **2010**, 10, S387–S391.

(92) Lee, C.; Efstathiadis, H.; Raynolds, J.E.; Haldar, P. Two-dimensional computer modeling of single junction a-Si:H solar cells. *IEEE Photovoltaic Specialists Conference (PVSC)*, **2009**, 34, 1118–1122.

(93) Mailoa, J.P.; Lee, M.; Peters, I.M.; Buonassisi, T.; Panchula, A.; Weiss, D.N. Energy-yield prediction for II–VI-based thin-film tandem solar cells. *Energy Environ. Sci.*, **2016**, 9, 2644–2653.

(94) Rühle, S. The detailed balance limit of perovskite/silicon and perovskite/CdTe tandem solar cells. *Phys. Status Solidi A*, **2017**, 214, 1600955.

(95) Hao, F.; Stoumpos, C.C.; Chang, R.P.H.; Kanatzidis, M.G. Anomalous Band Gap Behavior in Mixed Sn and Pb Perovskites Enables Broadening of Absorption Spectrum in Solar Cells. *J. Am. Chem. Soc.*, **2014**, 136, 8094–8099.

(96) Hao, F.; Stoumpos, C.C.; Cao, D.H.; Chang, R.P.H.; Kanatzidis, M.G. Lead-free solid-state organic–inorganic halide perovskite solar cells. *Nat. Photonics*, **2014**, 8, 489–494.

(97) Kapil, G.; Ripolles, T.S.; Hamada, K.; Ogomi, Y.; Bessho, T.; Kinoshita, T.; Chantana, J.; Yoshino, K.; Shen, Q.; Toyoda, T.; Minemoto, T.; Murakami, T.N.; Segawa, H.; Hayase, S. Highly Efficient 17.6% Tin–Lead Mixed Perovskite Solar Cells Realized through Spike Structure. *Nano Lett.*, **2018**, 18, 3600–3607.

(98) Slavney, A.H.; Leppert, L.; Saldivar Valdes, A.; Bartesaghi, D.; Savenije, T.J.; Neaton, J.B.; Karunadasa, H. Small-Bandgap Halide Double Perovskites. *Angew. Chem. Int. Ed.*, **2018**, 57, 12765-12770.

(99) Eperon, G.E.; Paternò, G.M.; Sutton, R.J.; Zampetti, A.; Haghighirad, A.A.; Cacialli, F.; Snaith, H.J. Inorganic caesium lead iodide perovskite solar cells. *J. Mater. Chem. A*, **2015**, 3, 19688–19695.

(100) Kulbak, M.; Gupta, S.; Kedem, N.; Levine, I.; Bendikov, T.; Hodes, G.; Cahen, D. Cesium Enhances Long-Term Stability of Lead Bromide Perovskite-Based Solar Cells. *J. Phys. Chem. Lett.*, **2016**, 7, 167–172.

(101) Lee, J.-W.; Seol, D.-J.; Cho, A.-N.; Park, N.-G. High-Efficiency Perovskite Solar Cells Based on the Black Polymorph of $HC(NH_2)_2PbI_3$. *Adv. Mater.*, **2014**, 26, 4991–4998.

(102) Noh, J.H.; Im, S.H.; Heo, J.H.; Mandal, T.N.; Seok, S.I. Chemical Management for Colorful, Efficient, and Stable Inorganic–Organic Hybrid Nanostructured Solar Cells. *Nano Lett.*, **2013**, 13, 1764–1769.

(103) Parrott, E.S.; Green, T.; Milot, R.L.; Johnston, M.B.; Snaith, H.J.; Herz, L.M. Interplay of Structural and Optoelectronic Properties in Formamidinium Mixed Tin-Lead Triiodide Perovskites. *Adv. Funct. Mater*, **2018**, 28, 1802803.

(104) Rehman, W.; Milot, R.L.; Eperon, G.E.; Wehrenfennig, C.; Boland, J.L.; Snaith, H.J.; Johnston, M.B.; Herz, L.M. Charge-Carrier Dynamics and Mobilities in Formamidinium Lead Mixed-Halide Perovskites. *Adv. Mater.*, **2015**, 27, 7938–7944.

(105) Sutton, R.J.; Eperon, G.E.; Miranda, L.; Parrott, E.S.; Kamino, B.A.; Patel, J.B.; Hörantner, M.T.; Johnston, M.B.; Haghighirad, A.A.; Moore, D.T.; Snaith, H.J. Bandgap-Tunable Cesium Lead Halide Perovskites with High Thermal Stability for Efficient Solar Cells. *Adv. Energy Mater.*, **2016**, 6, 1502458.

(106) Wang, Y.; Fu, W.; Yan, J.; Chen, J.; Yang, W.; Chen, H. Low-bandgap mixed tin–lead iodide perovskite with large grains for high performance solar cells. *J. Mater. Chem. A*, **2018**, 6, 13090–13095.

(107) Hoke, E.T.; Slotcavage, D.J.; Dohner, E.R.; Bowring, A.R.; Karunadasa, H.I.; McGehee, M.D. Reversible photo-induced trap formation in mixed-halide hybrid perovskites for photovoltaics. *Chem. Sci.*, **2015**, 6, 613–617.

(108) Rehman, W.; McMeekin, D.P.; Patel, J.B.; Milot, R.L.; Johnston, M.B.; Snaith, H.J.; Herz, L.M. Photovoltaic mixed-cation lead mixed-halide perovskites: links between crystallinity, photo-stability and electronic properties. *Energy Environ. Sci.*, **2017**, 10, 361–369.

(109) Alberti, A.; Deretzis, I.; Mannino, G.; Smecca, E.; Sanzaro, S.; Numata, Y.; Miyasaka, T.; La Magna, A. Revealing a Discontinuity in the Degradation Behavior of $CH_3NH_3PbI_3$ during Thermal Operation. *J. Phys. Chem. C*, **2017**, 121, 13577–13585.

(110) Domanski, K.; Correa-Baena, J.P.; Mine, N.; Nazeeruddin, M.K.; Abate, A.; Saliba, M.; Tress, W.; Hagfeldt, A.; Grätzel, M. Not All That Glitters Is Gold: Metal-Migration-Induced Degradation in Perovskite Solar Cells. *ACS Nano,* **2016**, 10, 6306–6314.

(111) Long, M.; Zhang, T.; Liu, M.; Chen, Z.; Wang, C.; Xie, W.; Xie, F.; Chen, J.; Li, G.; Xu, J. Abnormal Synergetic Effect of Organic and Halide Ions on the Stability and Optoelectronic Properties of a Mixed Perovskite via In Situ Characterizations. *Adv. Mater.*, **2018**, 30, 1801562.

(112) Brown, G.F.; Wu, J. Third generation photovoltaics. *Laser Photonics Rev.*, **2009**, 3, 394–405.

(113) Durose, K.; Edwards, P.R.; Halliday, D.P. Materials aspects of CdTe/CdS solar cells. *J. Cryst. Growth*, **1999**, 197, 733–742.

(114) ASTM International, 2015. Standard Test Method for Reflection Haze of High-Gloss Surfaces. ASTM International.

(115) MacKintosh, F.C.; Zhu, J.X.; Pine, D.J.; Weitz, D.A. Polarization memory of multiply scattered light. *Phys. Rev. B*, **1989**, 40, 9342–9345.

(116) Sigman, M.B.; Korgel, B.A. Strongly Birefringent $Pb_3O_2Cl_2$ Nanobelts. *J. Am. Chem. Soc.*, **2005**, 127, 10089–10095.

(117) Braunger, S.; Mundt, L.E.; Wolff, C.M.; Mews, M.; Rehermann, C.; Jošt, M.; Tejada, A.; Eisenhauer, D.; Becker, C.; Guerra, J.A.; Unger, E.; Korte, L.; Neher, D.; Schubert, M.C.; Rech, B.; Albrecht, S. $Cs_xFA_{1-x}Pb(I_{1-y}Br_y)_3$ Perovskite Compositions: the Appearance of Wrinkled Morphology and its Impact on Solar Cell Performance. *J. Phys. Chem. C*, **2018**, 122, 17123–17135.

(118) Bush, K.A.; Rolston, N.; Gold-Parker, A.; Manzoor, S.; Hausele, J.; Yu, Z.J.; Raiford, J.A.; Cheacharoen, R.; Holman, Z.C.; Toney, M.F.; Dauskardt, R.H.; McGehee, M.D. Controlling Thin-Film Stress and Wrinkling during Perovskite Film Formation. *ACS Energy Lett.*, **2018**, 3, 1225–1232.

(119) Zhang, Y.; Liang, Y.; Wang, Y.; Guo, F.; Sun, L.; Xu, D. Planar $FAPbBr_3$ Solar Cells with Power Conversion Efficiency above 10%. ACS Energy Lett., **2018**, 3, 1808–1814.

(120) Zheng, X.; Chen, B.; Wu, C.; Priya, S. Room temperature fabrication of $CH_3NH_3PbBr_3$ by anti-solvent assisted crystallization approach for perovskite solar cells with fast response and small J–V hysteresis. *Nano Energy*, **2015**, 17, 269–278.

(121) Hoffman, J.B.; Zaiats, G.; Wappes, I.; Kamat, P.V. $CsPbBr_3$ Solar Cells: Controlled Film Growth through Layer-by-Layer Quantum Dot Deposition. *Chem. Mater.*, **2017**, 29, 9767–9774.

(122) Heo, J.H.; Song, D.H.; Im, S.H. Planar $CH_3NH_3PbBr_3$ Hybrid Solar Cells with 10.4% Power Conversion Efficiency, Fabricated by Controlled Crystallization in the Spin-Coating Process. *Adv. Mater.*, **2014**, 26, 8179–8183.

(123) Rühle, S. Tabulated values of the Shockley–Queisser limit for single junction solar cells. *Sol. Energy*, **2016**, 130, 139–147.

(124) Kim, J.; Saidaminov, M.I.; Tan, H.; Zhao, Y.; Kim, Y.; Choi, J.; Jo, J.W.; Fan, J.; Quintero-Bermudez, R.; Yang, Z.; Quan, L.N.; Wei, M.; Voznyy, O.; Sargent, E.H. Amide-Catalyzed Phase-Selective Crystallization Reduces Defect Density in Wide-Bandgap Perovskites. Adv. Mater., **2018**, 30, 1706275.

PEROVSKITE-CDTE TANDEM PHOTOVOLTAICS

Chapter 5: Addition of Silver Cations to $CH_3NH_3PbBr_3$ Produces Crystallographically Ordered Perovskite Thin Films[†]

5.1 INTRODUCTION

Methylammonium lead bromide ($CH_3NH_3PbBr_3$, MAPBr) is a lead halide perovskite with a wide band gap (2.3 eV).[1] It can be deposited from solution to fabricate a variety of optoelectronic devices, including light-emitting diodes (LEDs), photodetectors and photovoltaics (PVs).[2-4] The crystallographic orientation, or texture, of the films is often important and device performance has been improved using crystallographically-oriented perovskite films.[5-11] The charge carrier mobility, photoconductivity, trap state density and degradation rates also show a dependance on the crystal orientation of the film.[8,12-14] Recently, the addition of Ag^+ to tetragonal methylammonium lead iodide ($CH_3NH_3PbI_3$, MAPI) has generated weakly (011) oriented films.[5] In that case, there was also a "dedoping" effect that enhanced PV performance.[5] In this *Letter*, we show that the inclusion of Ag^+ in wider bandgap MAPBr leads to (001)-oriented films on a wide variety of substrates, but does not improve PV performance.

[†]Reprinted with permission from Siegler, T.D.; Zhang, Y.; Dolocan, A.; Reimnitz, L.C.; Torabi, A.; Abney, M; Choi, J.; Cossio, G.; Houck, D.W.; Yu, E.T.; Li, X.; Harvey, T.B.; Milliron, D.J.; Korgel, B.A.* (**2019**) "Addition of Monovalent Silver Cations to $CH_3NH_3PbBr_3$ Produces Crystallographically Ordered Perovskite Thin Films" *Submitted to ACS Applied Energy Materials*. TDS conceived the whole experiment, and carried out either in part or in full experiments on X-Ray scattering, elemental analysis, SEM imaging, EDS mapping, and PV fabrication. TDS also analyzed data and wrote the manuscript.

5.2 EXPERIMENTAL DETAILS

5.2.1 Materials

Lead bromide (>99.999% (metals basis) Puratonic®, Alfa Aesar), silver bromide (99.998% (metals basis) Premion®, Alfa Aesar), methylammonium bromide (CH_3NH_3Br, Greatcell Solar), dimethylformamide ($HCON(CH_3)_2$, 99.8%, anhydrous, Sigma), dimethylsulfoxide ($(CH_3)_2SO$, $\geq$99.9%, anhydrous, Sigma), chlorobenzene (C_6H_5Cl, 99.8%, anhydrous, Sigma), zinc purum powder (99%, Sigma), hydrochloric acid (Reagent grade, 37%, Fisher Chemical), titanium diisopropoxide bis-acetylacetanoate (TAA, $C_{16}H_{32}O_6Ti$, 75 wt% in isopropanol, Sigma), 1-butanol (C_4H_9OH, 99.8%, anhydrous, Sigma), 30 NR-D Nanoparticulate Titanium Dioxide paste (TiO_2, Greatcell Solar), ethanol (200 proof, Fisher Chemical), spiro-OMeTAD ($(N^2,N^2,N^{2'},N^{2'},N^7,N^7,N^{7'},N^{7'}$-octakis(4-methoxyphenyl)-9,9′-spirobi[9H-fluorene]-2,2′,7,7′-tetramine, Merck), lithium bistriflurormethanesulfonimide (LiTFSI, $LiC_2F_6NO_4S_2$, 99.95%, Sigma), acetonitrile (C_2H_3N, 99.8%, anhydrous, Sigma), 4-tert-butylpyridine ($C_9H_{13}N$, 96%, Sigma), and titanium tetrachloride ($TiCl_4$, 99.9%, Sigma) were used as received without further purification. Gold for evaporation (99.99%, 0.5 mm diameter wire) was purchased from Kurt J. Lesker.

Silicon substrates (University Wafer, 8-10 Ωcm, polished (100) surface), tin-doped indium oxide (ITO) coated glass (Thin Film Devices, 100 Ω/sq, >90% transparency), and fluorine-doped tin oxide (FTO) coated glass (Hartford Glass) were used as received. Immediately prior to deposition of the perovskite films, substrates were rinsed with ethanol, placed in a Jelight Co. Inc. Model 42 UV Ozone cleaner for 1 h, and immediately transferred into a nitrogen-filled glove box for perovskite deposition.

5.2.2 Deposition of $CH_3NH_3PbBr_3$ (MAPBr) Thin Films

First, 514 mg of $PbBr_2$ and 157 of mg CH_3NH_3Br (MABr) are dissolved in 0.8 mL DMF and 0.2 mL DMSO by stirring for 2 h at room temperature to obtain reactant concentrations of 1.4 M of each $PbBr_2$ and MABr. In a separate vial, 263 mg of AgBr and 157 mg of MABr are dissolved in 0.8 mL DMF and 0.2 mL DMSO in a similar manner, resulting in solution concentrations of 1.4 M AgBr and MABr. (Note: we observe that AgBr does not dissolve in DMF/DMSO without the parallel dissolution of equimolar MABr) The precursor solution is then prepared by mixing these AgBr and $PbBr_2$ solutions to achieve the desired Ag:Pb mole ratio (*e.g.* 1:9 AgBr:$PbBr_2$ for "10% Ag" samples) and deposited on the desired substrate using a Laurel spin coater in a nitrogen glove box (<10 ppm O_2, <10 ppm H_2O). Films are spun using a two-step program (1000 rpm for 10 s and 4000 rpm for 30 s) with 50 μL of precursor solution spread evenly across the substrate. After 15 s into the second step, 100 μL of chlorobenzene is pipetted onto the center of the substrate to induce crystallization of the film. The films are then annealed at 100 ^oC for 1 h on a hot plate in a nitrogen glove box while continuous purging the box with nitrogen to avoid solvent vapor accumulation.

5.2.3 PV Device Fabrication and Testing

Photovoltaic devices (PVs) were fabricated using established procedures in the literature.[15] FTO-coated glass is rinsed with dilute dish soap, DI-water, and ethanol, and then patterned by chemically etching the FTO from unwanted areas with zinc powder and concentrated hydrochloric acid. After neutralizing the acid with water, the patterned substrates are rinsed with DI-water, sonicated in ethanol for 30 min, and treated with UV-ozone plasma for 1 h. A compact TiO_2 layer is deposited by dissolving 72.5 μL titanium diisopropoxide bis-acetylacetanoate in 1 mL 1-butanol and then spin coating this solution

at 700 rpm for 10 s, 1000 rpm for 10 s, and 2000 rpm for 30 s. The film is dried by heating at 125 ^{o}C for 10 min and then 30 NR-D TiO_2 nanoparticulate paste dissolved at a concentration of 100 mg/mL in ethanol is deposited using the same 3-step spin coat process used for TAA. The substrates are then heated at 550 ^{o}C for 1 h in air, which forms a mesoporous TiO_2 substrate. Immediately before solar cell fabrication, the TiO_2 films are immersed in aqueous 20 μM $TiCl_4$ for 10 min at 90 ^{o}C. The substrates are then rinsed with water and ethanol, cooled, and then annealed at 500 ^{o}C for 30 min in air. After exposing the substrates to UV-ozone for 1 h, MAPBr is deposited using the previously described spin-coating procedure. Spiro-OMeTAD is then deposited by spin-coating a solution of 72 mg/mL spiro-OMeTAD dissolved in 1 mL chlorobenzene with 7.5 μL/mL tert-butylpyridine and 24 μL/mL lithium tetrafluorosulfonimide stock solution (170 mg LiTFSI salt in 1 mL acetonitrile) at 5000 rpm for 30 s. Spiro-coated MAPBr films are then left to sit overnight in dry air desiccator before gold (~60 nm) is thermally evaporated at a rate of 2 Å/s and at a base pressure of 5×10^{-5} Torr on the substrates.

PV device testing was carried out using light from a Xe lamp passed through an AM 1.5 filter with 100 mW cm^{-2} intensity, with intensity calibration carried out on a Hamamatsu silicon diode. Current-voltage (*J-V*) profiles were obtained without light or voltage pre-biasing using a Keithley 2400 general purpose source meter swept at a rate of ~100 mV/s. External quantum efficiency (EQE) measurements were taken with a commercial solar cell spectral response measurement system (model QEX10, PV Measurements, Inc) using a Xe arc lap source and a dual-grating monochromator with respective color filters. The EQE measurements were calibrated with a NIST certified silicon photodiode (SN: 98599).

5.2.4 Materials Characterization

Grazing incidence wide-angle X-ray scattering (GIWAXS) was performed on samples in vacuum using a SAXSLAB Ganesha SAXS-WAXS system with monochromatic Cu Kα X-rays (λ=1.54 Å) with a 5° incident beam angle. Scattered X-rays were captured for 10 min with a 487×619 pixel Pilatus3 R 300k (pixel size of 172×172 μm^2) detector and a sample-to-detector distance of 131 mm. Ewald sphere correction and linear integration (azimuth angle and 2θ) were processed with Fit2D software (version: 12_077_i686_WXP). Azimuth integration of the (001) peak was performed between q=10.2 nm^{-1} and q=11.6 nm^{-1} (14.3° to 16.4° 2θ) with 180 azimuth bins.

A Kratos Axis Ultra DLD X-ray photoelectron spectrometer (XPS) equipped with a monochromatic aluminum X-ray source was used to carry out X-ray photoelectron spectroscopy (XPS) measurements. Exposure of the samples to air was avoided using a patented transfer system developed at the Texas Materials Institute (TMI) at the University of Texas at Austin.[16] Samples are loaded and sealed into a pressure-to-vacuum (P2V) transfer chamber in a nitrogen glove box. The P2V chamber is then taken to the XPS instrument and evacuated before samples are transferred to the analysis chamber as described by Celio.[16] XPS data were analyzed using CasaXPS software, correcting for sample charging by normalizing the C1s signal from adventitious carbon to a binding energy of 284.8 eV. Peak fitting was performed using Shirley, Tougaard, or Linear backgrounds, depending on the shape of the background in the specific region of fitting,[17] and a Gaussian-Lorentzian peak shape. Compositional data were obtained by integrating the peaks with corrected intensities based on the relative sensitivity factor provided by the Kratos library.

Time of flight secondary ion mass spectrometry (TOF-SIMS) data were acquired using an ION-TOF GmbH 2010 TOF.SIMS 5 instrument with a pulsed Bi^+ analysis beam

(20 ns pulse width, 30 keV ion energy, and ~3.5 pA measured sample current) and a O_2^+ sputtering beam (1 keV and 41.3 nA measured sample current current) at ~10^{-9} Torr base pressure. During depth profiling the analysis beam was raster-scanned over a 0.1×0.1 mm^2 area centered within the 0.3×0.3 mm^2 sputtered area of the sputtering beam. Analysis was performed in interlaced mode as described by Wang et. al.,[18] and in positive mode, i.e. all secondary ions detected were positively charged fragments. To alleviate electrical charging of the sample, a constant energy (21 eV) electron beam was directed at the sample during analysis. All depth profiles were acquired in high current bunched mode. For TOF-SIMS mapping with high lateral resolution, the analysis beam was set in the burst alignment mode using 7 bursts. Before data acquisition, a very thin layer of sample was removed from the surface using 30 s of O_2^+ sputter. The O_2^+ sputtering rate was calculated to be ~0.2 nm s^{-1} based on the depth profile of the $InSnO^+$ secondary ion fragment and sample thickness from cross section SEM. To avoid peak overlap of Ag^+ and $SiBr^+$ ion fragments, ITO-coated borosilicate glass was used as a substrate for TOF-SIMS measurements.

Scanning electron microscopy (SEM) and energy dispersive X-ray spectroscopy (EDS) data were obtained with a Hitachi S550 SEM/STEM operated at 30 kV and 10 μA with a Bruker AXS XFlash Detector 4010. The MAPBr films were spin coated on silicon substrates (University Wafer, 8-10 Ωcm, polished (100) surface). SEM images and compositional profiles of the cross-sectioned films were obtained using a JEOL-7610F SEM equipped with a 1040 Oxford Instruments EDX detector.

Solid state photoluminescence emission (PL) was measured on a Fluorolog-3 spectrophotometer (Horiba Jobin Yvon) using an excitation wavelength of 400 nm and a slit size of 5 for both excitation and emission. Photoluminescence (PL) was measured on a Fluorolog-3 spectrophotometer (Horiba Jobin Yvon) using an excitation wavelength of 400 nm and a slit size of 5 for both excitation and emission. TRPL measurements were

performed in a home-made time-correlated single photon counting (TCSPC) setup equipped with a picosecond pulse laser diode (FWHM=100 ps, λ= 446 nm, repetition rate=1 MHz). A 10x (0.28 Numerical Aperture) objective focused the light to the sample, and the same objective collected PL signal. The collected PL was directed through a band-pass filter, a spectrograph, and an avalanche photodiode (APD, SPCM-AQRH-14) The measured instrument response function is 600 ps, much lower than measured lifetimes.

5.3 Results and Discussion

5.3.1 Preferred Orientation of MAPBr Upon Ag^+ Addition

Figure 5.1 shows grazing incidence wide-angle X-ray scattering (GIWAXS) from MAPBr films deposited on silicon substrates by room temperature spin-coating with increasing amounts of AgBr in the precursor solution. Molar ratios of $[Ag^+]/([Ag^+]+[Pb^{2+}])$ ranged from 0.5% to 10% and the films were annealed at 100°C after deposition.[19] All patterns index to cubic MAPBr with a lattice constant of 5.92 Å. Substitutional replacement of Pb^{2+} with Ag^+ does not change the lattice constant because of the similar ionic radii of Pb^{2+} (119 pm) and Ag^+ (115 pm).[20] When $[Ag^+]:[Pb^{2+}]$ ratios exceeded 2%, the GIWAXS data exhibited significant texture. In Figure 5.1D-F and 5.1J-L, the enhanced diffraction of the (001) and (011) rings at $\phi=90^o$ and $\phi=45^o$ respectively indicate that the films are predominantly oriented with (001) lattice planes parallel to the substrate. A faint texture is also present in the pure MAPBr films in Figures 5.1A and 5.1G, which corresponds to a different, weakly preferred (011) crystal orientation.

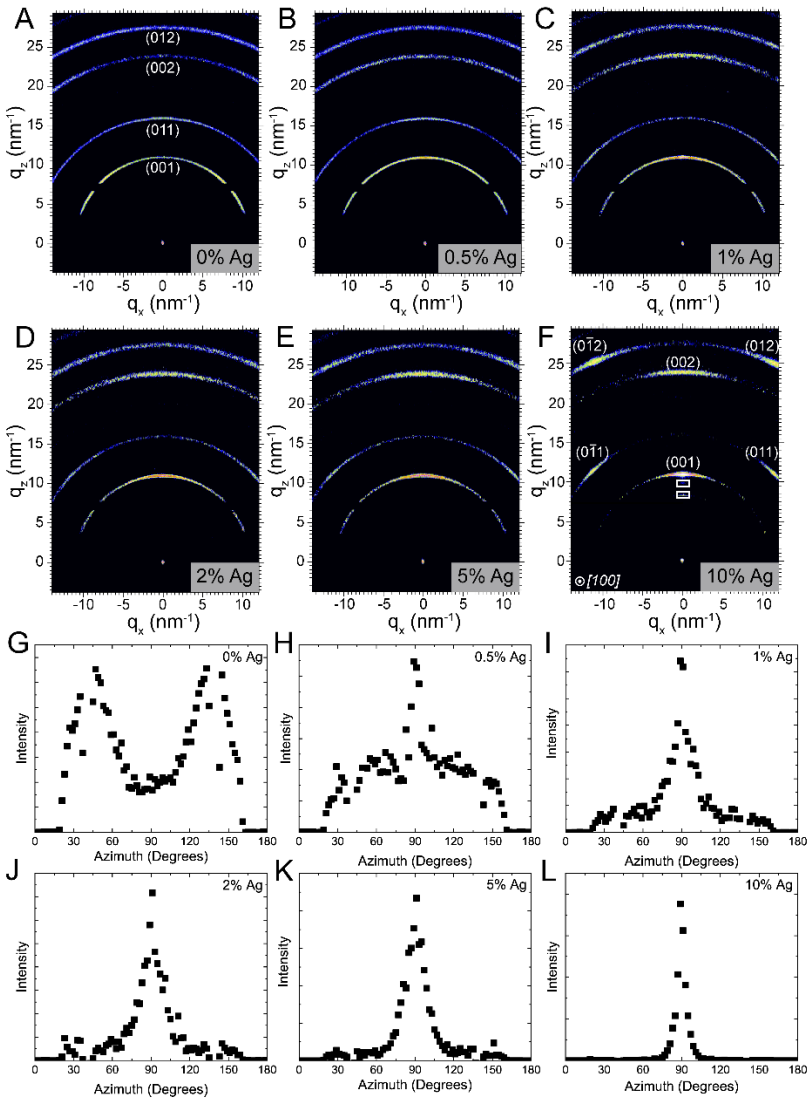

Figure 5.1: (A-F) GIWAXS of MAPBr films on silicon substrates with varying amounts of Ag^+. The Ag concentration corresponds to the molar percentage of Ag^+ added to the precursor solution with respect to Pb^{2+}. The indexing in (F) corresponds to cubic MAPBr (PDF #01-084-9476) with a [100] beam direction. Additional diffraction spots are observed in (F), which are enclosed in rectangles. (G-L) The diffraction intensity of the (001) ring ($10.3\ nm^{-1} < q < 11.6\ nm^{-1}$ or $14.3^o < 2\theta < 16.4^o$) from the GIWAXS patterns in (A-F) plotted as a function of azimuthal angle. The (001) peaks at 45^o and 135^o in (G) indicate that MAPBr without added Ag^+ exhibits some preferential (011) orientation. Silver addition leads to significant sharpening of the (001) signal at 90^o, indicating that the film is oriented with (001) planes parallel to the substrate

MAPBr films were also deposited on glass, ITO-coated glass and FTO glass coated with mesoporous TiO_2. Figure 5.2 shows GIWAXS data for films on each substrate with 10% Ag^+. There is a significant amount of texture and all of the patterns show a (001) crystallographic orientation. The same impurity features as in Figure 5.1F are also observed in these films with high Ag^+ concentration.

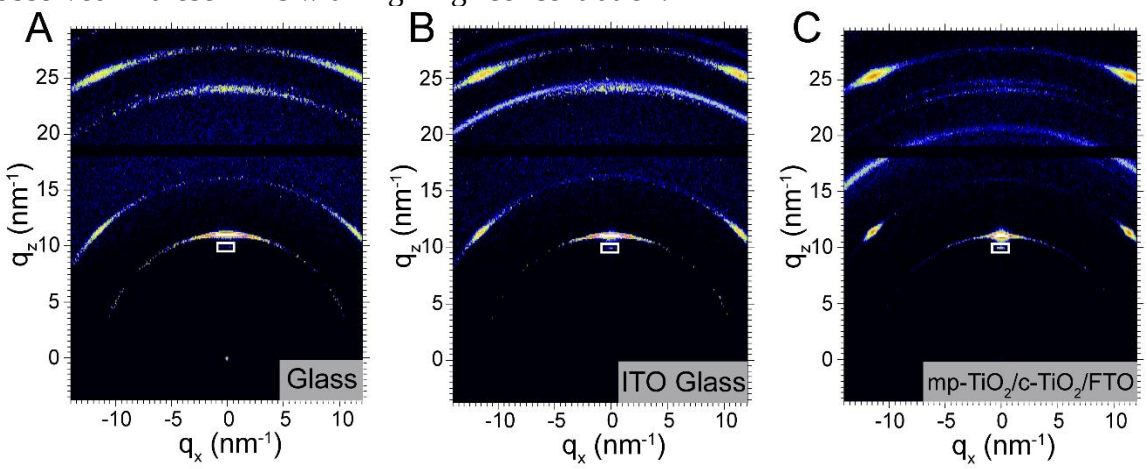

Figure 5.2. GIWAXS of MAPBr films deposited with 10 mol% Ag^+ in the precursor solution on (A) glass, (B) ITO-coated glass, and (C) FTO glass coated with a compact and mesoporous TiO_2 layer. The films exhibit a (001) crystal orientation. The diffraction spots outlined with rectangles correspond to an impurity phase.

5.3.2 Elemental Analysis and Origins of Induced (001) Ordering

Compositional profiles were obtained using X-ray photoelectron spectroscopy (XPS), energy-dispersive X-ray spectroscopy (EDS), and time-of-flight secondary ion mass spectroscopy (TOF-SIMS). XPS and EDS data are shown in Table 5.1. MAPBr films deposited without Ag^+ are stoichiometric. The addition of Ag^+ led to higher Br:Pb and N:Pb ratios, indicating that some unreacted CH_3NH_3Br is present. The silver concentrations measured by XPS are higher than those measured by EDS. XPS is surface-sensitive,[21,22] while EDS provides a depth averaged composition. Therefore, higher silver

content measured by XPS indicates that Ag^+ accumulates at the surface. TOF-SIMS was used to map this depth composition in greater detail.

Table 5.1. Elemental composition of MAPBr films determined by EDS† and XPS.

	Ag/(Ag+Pb)		Br:Pb		N:Pb
Ag mol% in soln.	XPS	EDS	XPS	EDS	XPS
0%	0	Below LOD†	2.6 ± 0.2	3.1 ± 0.6	0.94 ± 0.14
0.5%	3.2% ± 0.5%	Below LOD†	2.6 ± 0.2	3.0 ± 0.5	0.99 ± 0.13
1%	8.2% ± 0.5%	Below LOD†	2.6 ± 0.3	3.2 ± 0.6	0.96 ± 0.12
2%	8.8% ± 0.5%	4% ± 7%	2.7 ± 0.2	3.7 ± 1.4	1.1 ± 0.12
5%	10.3% ± 0.6%	12% ± 8%	2.9 ± 0.2	3.3 ± 0.1	1.3 ± 0.14
10%	8.7% ± 0.5%	18 ± 9%	2.9 ± 0.2	3.5 ± 0.3	1.5 ± 0.20

†The limit of detection (LOD) for EDS is ~3 at%.

In TOF-SIMS, the concentrations of species in a film are determined as a function of depth by sputtering the layers and measuring the composition of the fragments, as illustrated in Figure 5.3A.[23] Figure 5.3B shows the Ag secondary ion yield, and Figures 5.3C-K show TOF-SIMS profiles of three secondary ion fragments from MAPBr films on ITO-coated glass substrates. In its absolute amount, the secondary ion yield of a given fragment is proportional to the concentration of the corresponding element/molecule in the film. These ion fragments were chosen due to their secondary ion yield and to what they correspond with in the film: Ag corresponds to silver; CH_3NH_3PbBr corresponds to MAPBr; and InSnO corresponds to the ITO substrate. The signal of CH_3NH_3PbBr secondary ion yield is similar for all of the samples whereas the Ag secondary ion yield increased with the amount of Ag^+ added to the film. The depth localization of the elements/molecules is inferred by normalizing the secondary ion yields to the maximum

yield value of each species. The Ag concentration is highest at the top and bottom interfaces of the MAPBr film. There is also evidence of Ag penetration into the ITO layer.

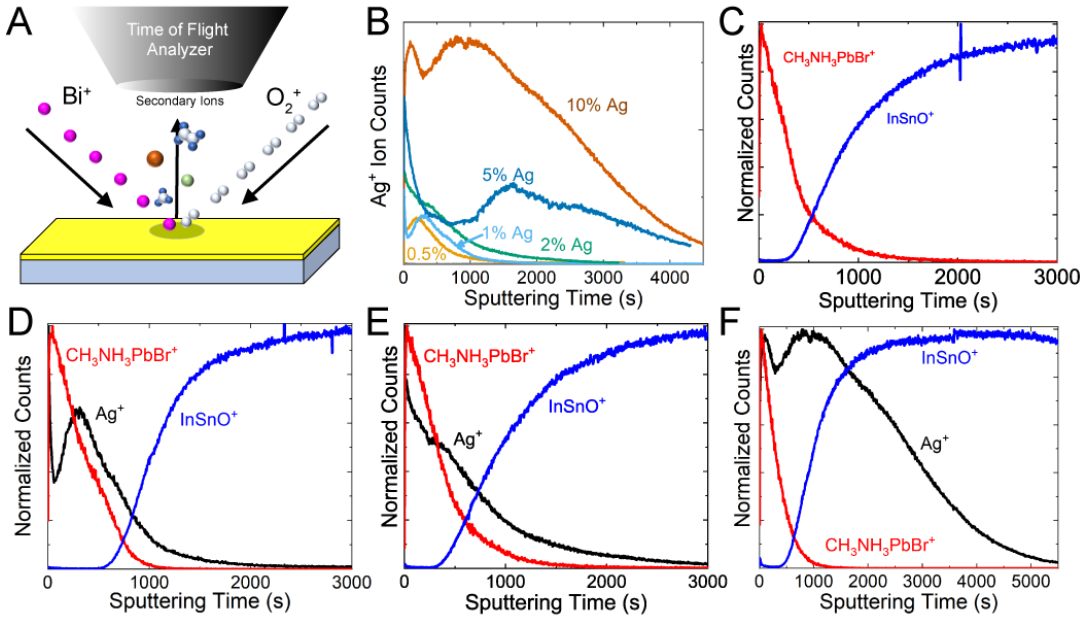

Figure 5.3. (A) Schematic of the TOF-SIMS measurement. (B) TOF-SIMS profiles of Ag secondary ion yield. (C-F) TOF-SIMS depth profiles of Ag, CH_3NH_3PbBr, and InSnO secondary ion fragments in MAPBr films deposited with (C) 0%, (D) 1%, (E) 2%, and (F) 10% Ag^+ in the precursor solution.

The composition on the surface of the films was also mapped. Figures 5.4G-I show EDS maps of Pb, Br and Ag in the region of the MAPBr film imaged by SEM in Figure 5.4J. There are features concentrated in Ag. Figures 5.4K-N show higher resolution compositional profiles obtained by TOF-SIMS. These maps confirm the presence of these phase-segregated regions rich in Ag. The spatial distributions of Pb, CH_5N, and Ag secondary ions are relatively uniform, except for bright spots of Ag from phase segregated areas of the film and wave-like features. The dark waves are shadows in the TOF-SIMS signal resulting from wrinkles, or thickness undulations.[9,24,25] The maps of Pb and CH_5N

secondary ion yields in Figures 5.4K and 5.4L indicate that the Ag^+-rich regions contain Pb^{2+}, but not $CH_3NH_3^+$. The absence of $CH_3NH_3^+$ in the Ag^+-rich regions is more apparent in the overlay of Ag and CH_5N secondary ion yield maps in Figure 5.4N. We propose that these domains of composed of Ag, Pb and Br are giving rise to the additional diffraction spots at low q in the GIWAXS patterns in Figures 5.1F and 5.2, although the diffraction spots did not match any known silver-containing compounds in the COD or ICDD diffraction databases.

5.3.3 Impacts on Optoelectronic Performance

Photovoltaic devices (PVs) were fabricated with Ag^+-doped MAPBr films using the materials stack in Figure 5.5A. As shown in Figures 5.5B-F, the addition of Ag^+ degraded device performance, decreasing the power conversion efficiency (PCE), stabilized power output (SPO), short circuit current (J_{SC}), and open circuit voltage (V_{OC}). This is not due to differences in film morphology, as the MAPBr films look similar in top-down SEM images (Figures 5.4A-F). In fact, films with more Ag^+ have larger crystal grain size and even smoother morphology—most likely due to the increased crystallographic orientation of the films. Films deposited with more than 10% Ag^+ in the deposition solution did form pinholes near grain boundaries, but the devices still functioned. The reduction in device performance became significant once the Ag^+ concentration exceeded 2%, corresponding to the point where the Ag-Pb-Br impurity emerged.

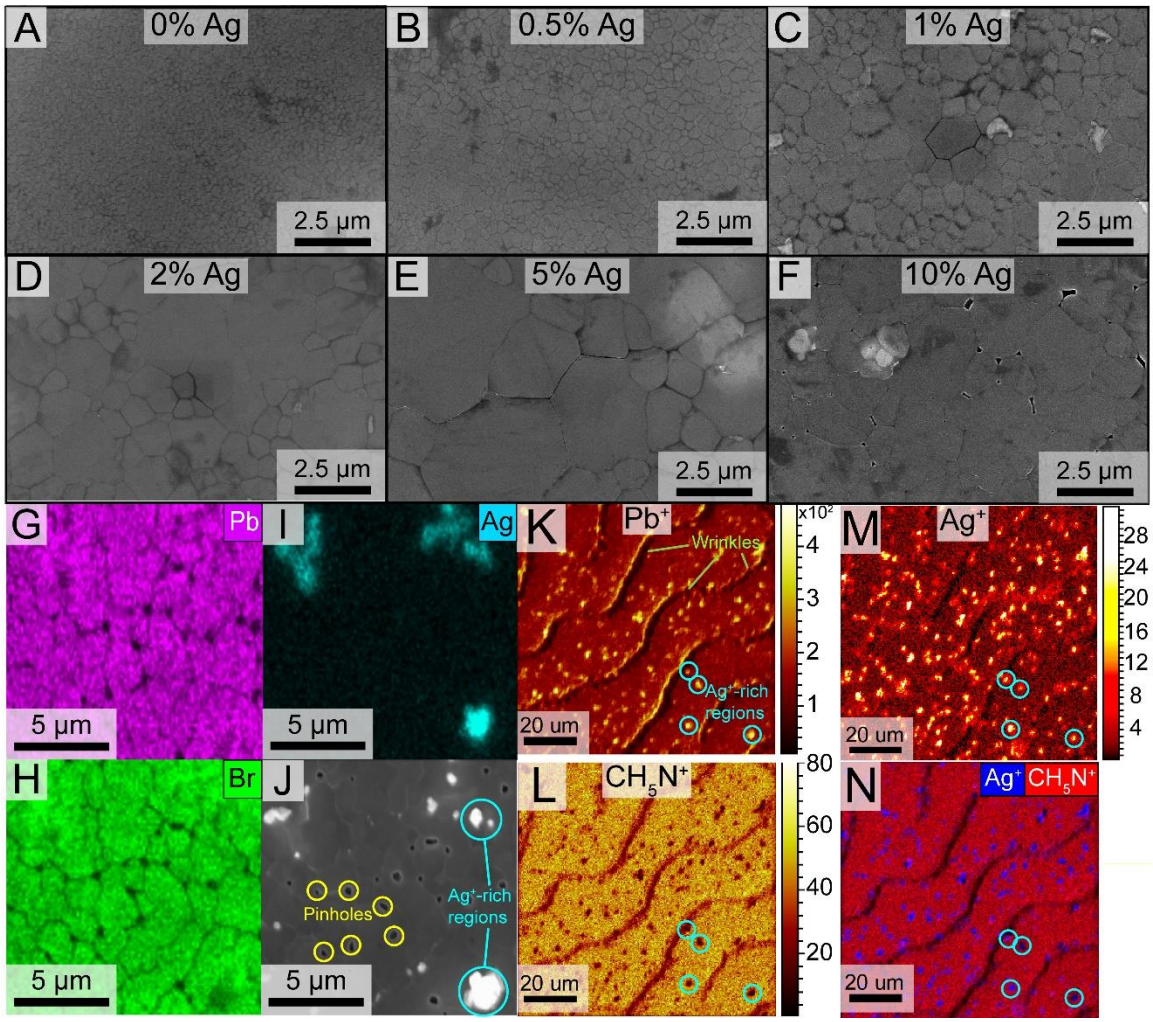

Figure 5.4. (A-F) Top-down SEM images of MAPBr films on silicon deposited with (A) 0%, (B) 0.5%, (C) 1%, (D) 2%, (E) 5%, and (F) 10% Ag^+ added to the precursor solution. The crystal grain size increases with increasing Ag^+ and pinholes are observed when the Ag^+ concentration reaches 10% Ag^+. (G-I) EDS maps of (G) Pb, (H) Br, and (I) Ag corresponding to the region imaged by SEM in (J) for a MAPBr film with 10% Ag^+. (K-N) TOF-SIMS mapping of a 2% Ag MAPBr thin film on ITO showing the (K) lead, (L) methylamine, (M) silver, and (N) an overlay of the Ag and CH_5N^+ signals. The wave-like features in are due to thickness variations in the film.

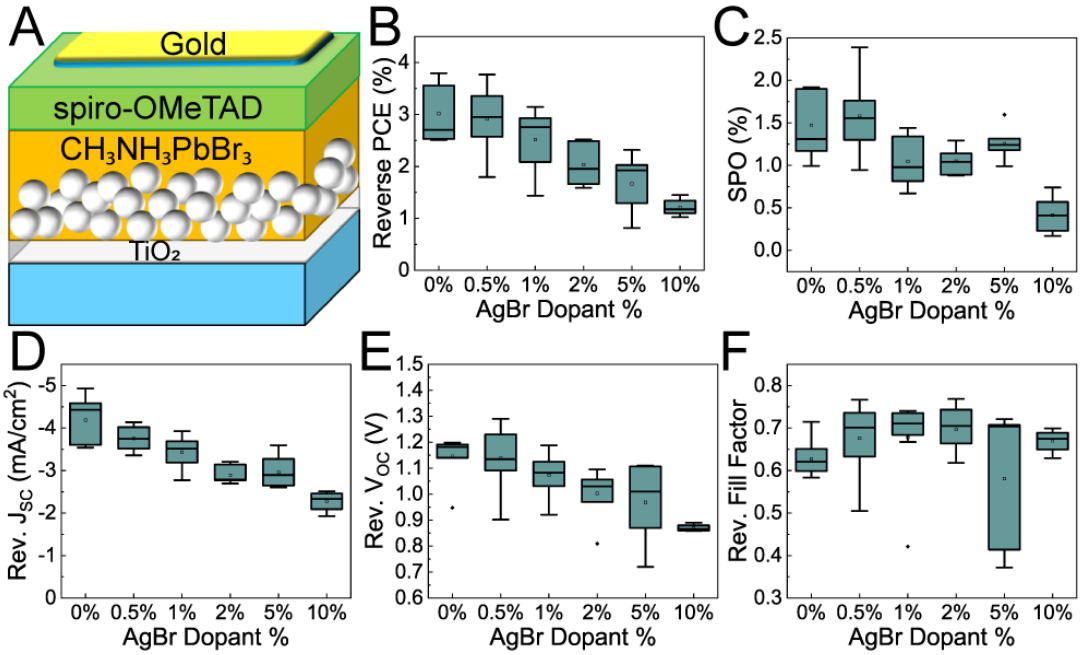

Figure 5.5. (A) PV device architecture and materials stack. (B-F) Histograms of (B) reverse scan PCE, (C) stabilized power output (SPO), (D) short circuit current (JSC) of the reverse scan, (E) open circuit voltage (VOC) of the reverse scan, and (F) fill factor of the reverse scan of MAPBr PVs with different amounts of AgBr added to the precursor solution.

Ag^+-doped MAPBr films on UV-Ozone treated glass underwent PL measurement to determine the impact of silver doping on the luminescence behavior of thin films. Results are shown in Figure 5.6. The PL spectra and time-resolved photoluminescence (TRPL) decay do not change dramatically as a function of silver content, seen in Figure 5.6A and 5.6B respectively. The only noticeable change is in the static PL spectra in Figure 5.6A, where the PL peak slightly blueshifts and the red shoulder noticeably decreases above 5% Ag^+ incorporation. This red shoulder is observed in thick films and single crystals, and has been recently attributed to radiative recombination via indirect Rashba transitions.[26]

Interestingly, in contrast to literature observations of Ag-free MAPBr, this red shoulder disappears as the film thickness increases (see Supporting Information for cross sectional SEM images).[26] Time-resolved PL data taken at 540 nm, however, do not exhibit any change or trend with increasing Ag^+ content, seen in Figure 5.6B. 5% Ag samples appear to have much lower lifetimes, which may be due to the introduction of trap states in the material. Curves are fit to a biexponential function, with fitting parameters shown in Table 5.2 and fitting curves shown in the Figure 5.7.

Others have also reported on the effects of silver in perovskite optoelectronics. Silver doping has improved some devices,[27-29] and increased the mobility of hybrid organic-inorganic perovskite (HOIP) nanoparticle films;[30] yet, it has also degraded device performance when present in the form of silver halide as a product of corrosion.[31-35] Surface segregation of Ag^+ can negatively impact the depletion region, increase surface recombination, and lead to unwanted band offsets in the MAPBr film.[36-38] Unreacted CH_3NH_3Br can also harm PV performance.[31-33,39-41]

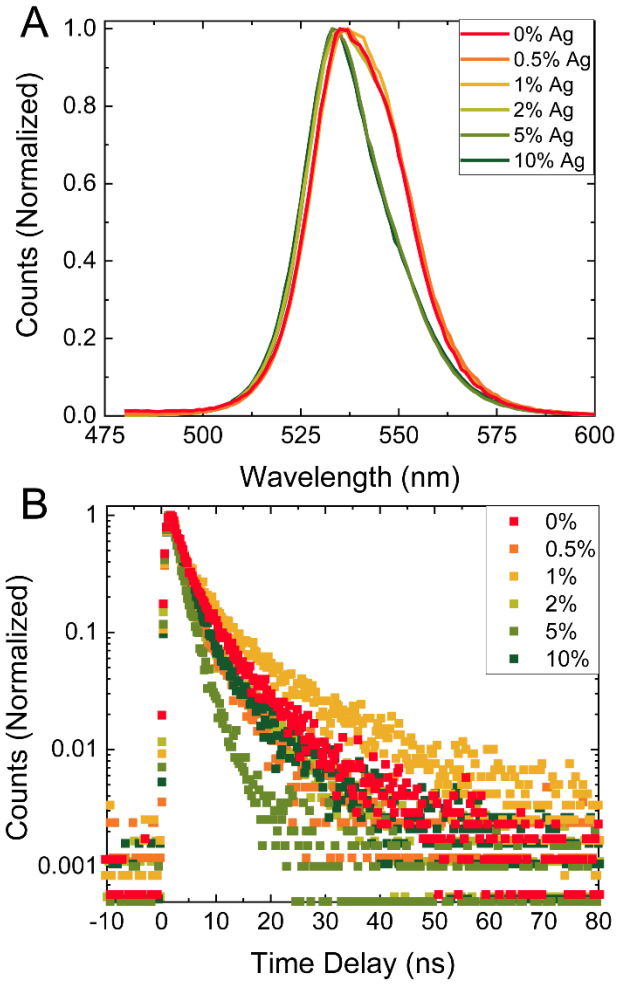

Figure 5.6. (A) Steady-state photoluminescence spectra and (B) Time resolved photoluminescence decay at 540 nm for Ag^+ doped MAPBr thin films. Above 5% Ag^+ incorporation, a subtle blueshift is observed, and the red shoulder of the MAPBr PL spectra reduces in intensity. No significant trend in PL lifetime is observed in (B), with the exception of the 5% Ag^+ film, which has a shorter lifetime, likely due to trap states introduced with the introduction of Ag^+.

Table 5.2. Fitting parameters for biexponential fits of the PL decay at 540 nm.

Ag mol% in soln.	A_1	τ_1 (ns)	A_2	τ_2 (ns)
0%	0.87	2.87	0.13	10.9
0.5%	0.84	1.92	0.16	7.23
1%	0.77	2.60	0.23	12.2
2%	0.88	1.89	0.12	9.60
5%	0.99	2.06	0.0090	15.5
10%	0.94	2.65	0.059	13.8

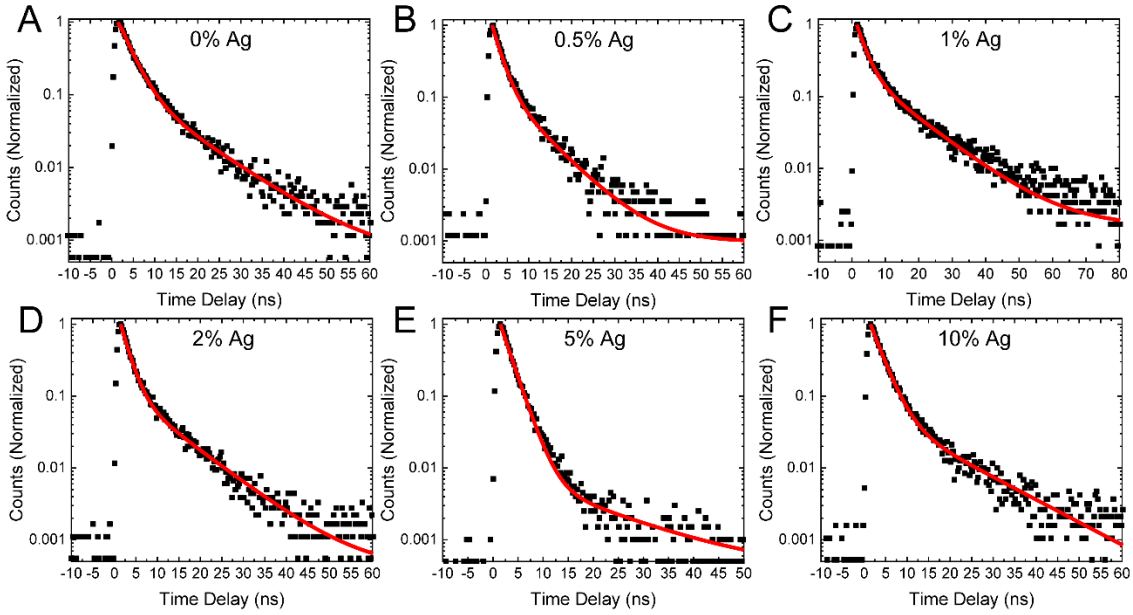

Figure 5.7. TRPL decay curves at 540 nm of MAPBr films on glass deposited with the addition of (A) 0%, (B) 0.5%, (C) 1%, (D) 2%, (E) 5%, and (F) 10% Ag^+. Data is in black squares and the fit curve is denoted by a red line. Data was fit to a biexponential decay function with parameters seen in Table 5.2.

5.3.4 Discussion

Based on the TOF-SIMS results and the compositional maps, we propose that segregation of Ag^+ to the interfaces of the MAPBr film—or "surface doping"—templates the (001) crystallographic orientation. This surface doping mechanism is illustrated in

Figure 5.8. This is different than what occurs in MAPI films. In oriented MAPI films, the addition of Ag^+ significantly slows the crystallization rate, affecting nucleation and growth and ultimately the orientation of the film. In the case of MAPBr, there is no observed slowing of crystallization when Ag^+ is added. This is because the solvent-antisolvent spin coating process that is used here induces crystallization within a few seconds of antisolvent exposure and does not depend on precursor composition.[19] Anisotropy in the interfacial energy of crystal surfaces tends to orient crystallizing grains to minimize surface energy in a film,[42-45] and the interfacial energies of crystal planes can be significantly modified by impurities or the adsorption of small molecules.[46-50] Silver(I) has been shown to be particularly active in this role in a wide variety of different instances, ranging from superconductor materials like $(Bi,Pb)_2Sr_2Ca_2Cu_3O_x$,[51,52] and Y_2BaCuO_5,[53] to plasmonic gold nanocrystals and nanorods.[54,55] High concentrations of Ag at the back interface of the MAPBr films observed in the TOF-SIMS profiles might lower the (001) surface energy. Alternatively, MAPBr crystallization could be initiating at the liquid-air interface and proceeding towards the substrate, as in the "oriented crust" crystallization mechanism,[56-58] with Ag^+ templating (001)-oriented growth at the liquid-air interface. Either of these mechanisms would explain why the crystallographic orientation was not affected by the substrate.

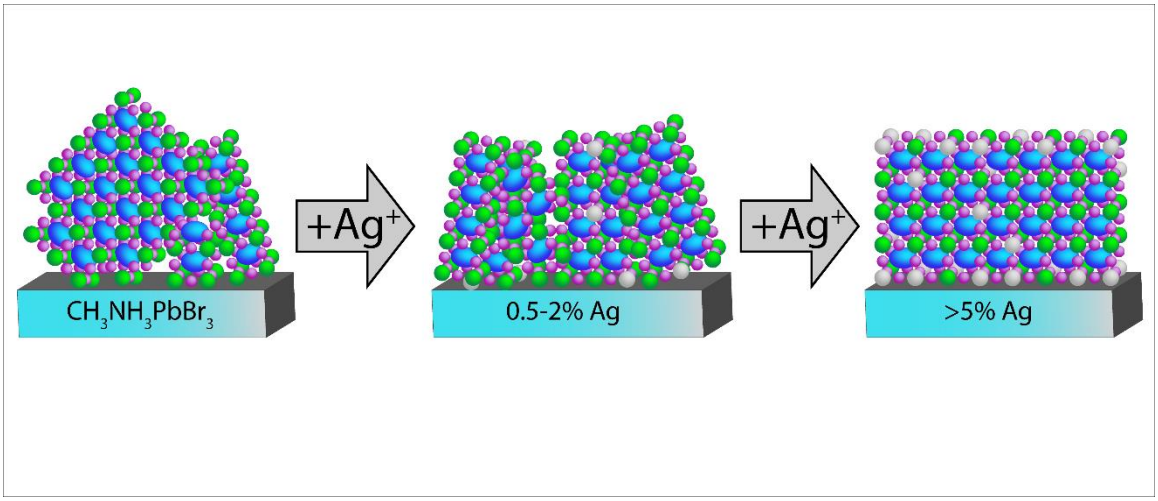

Figure 5.8. Illustration of an Ag^+ cation surface doping mechanism that induces crystallographic orientation of MAPBr films. Blue ellipsoids depict methylammonium, green are lead, purple are bromide, and grey are silver atoms. MAPBr exhibits a weakly favored (011) orientation on the substrate. The addition of Ag^+ at low concentrations (0.5-2% Ag^+) leads to a weakly preferred (001) orientation, and higher Ag^+ concentrations (>5% Ag^+) leads to strongly preferred (001) crystal orientation.

The crystallographic orientation of other perovskites has also been manipulated. In Ruddleston-Popper phases, where optoelectronic performance is strongly correlated with the orientation of the 2D inorganic layers with respect to the substrate, crystal orientation has been manipulated by either increasing the number of 3D layers between organic spacer ions,[59] controlling the annealing process,[56] or changing precursor stoichiometry.[10,60] Crystal texture has been controlled by arresting crystal nucleation with chlorine or acetate salts,[6,8,61,62] recrystallization in methylamine vapor,[6,7,63] alloying or ion exchange,[46,47,64] adjusting precursor stoichiometry,[13,65-67] seeding with nanoparticles,[68] or vapor phase epitaxy (VPE) on single crystal substrates of $SrTiO_3$ or NaCl.[69,70] Our method of inducing (001) crystal orientation involves the simple addition of Ag^+ to the precursor solution, and does not appreciably impact thermal processing time or temperature, nor does it

significantly impact PL. Additionally, it does not require the use of the expensive, atomically smooth single crystals needed for VPE.

5.4 Conclusion

We have identified a mechanism of Ag^+ surface doping that produces crystallographically-oriented MAPBr films. Silver preferentially segregates to grain boundaries and interfaces and induces a preferred orientation of (001) MAPBr crystal planes parallel to the substrate. Although the PV performance did not improve with Ag^+ addition—most likely due to the formation of a separate phase of silver lead and bromide—this report demonstrates more broadly that surface segregation of dopants can change the crystallographic orientation of a perovskite film.

5.5 References

(1) Park, J.-S.; Choi, S.; Yan, Y.; Yang, Y.; Luther, J. M.; Wei, S.-H.; Parilla, P.; Zhu, K. Electronic Structure and Optical Properties of α-$CH_3NH_3PbBr_3$ Perovskite Single Crystal, *J. Phys. Chem. Lett.* **2015**, *6*, 4304-4308.

(2) Kojima, A.; Teshima, K.; Shirai, Y.; Miyasaka, T. Organometal Halide Perovskites as Visible-Light Sensitizers for Photovoltaic Cells. *J. Am. Chem. Soc.* **2009**, *131*, 6050-6051

(3) Heo, J.H.; Song, D. E.; Im, S.H. Planar $CH_3NH_3PbBr_3$ Hybrid Solar Cells with 10.4% Power Conversion Efficiency, Fabricated by Controlled Crystallization in the Spin-Coating Process. *Adv. Mat.* **2104**, *26*, 8179-8183.

(4) Lee, S.; Park, J. H.; Nam, Y. S.; Lee, B. R.; Zhao, B.; Di Nuzzo, D.; Jung, E. D.; Jeon,

H.; Kim, J.-Y.; Jeong, H. Y.; Friend, R. H.; Song, M. H. Growth of Nano-Sized Single Crystals for Efficient Perovskite Light-Emitting Diodes. *ACS Nano* **2018**, *12*, 3417-3423.

(5) Abdi-Jalebi, M.; Pazoki, M.; Philippe, B.; Dar, M. I.; Alsari, M.; Sadhanala, A.; Divitini, G.; Imani, R.; Lilliu, S.; Kullgren, J.; Rensmo, H.; Grätzel, M.; Friend, R. H. Dedoping of Lead Halide Perovskites Incorporating Monovalent Cations. *ACS Nano* **2018**, *12*, 7301–7311.

(6) Dou, B.; Whitaker, J. B.; Bruening, K.; Moore, D. T.; Wheeler, L. M.; Ryter, J.; Breslin, N. J.; Berry, J. J.; Garner, S. M.; Barnes, F. S.; Shaheen, S. E.; Tassone, C. J.; van Hest, M. F. A. M. Roll-to-Roll Printing of Perovskite Solar Cells. *ACS Energy Lett.* **2018**, *3*, 2558–2565.

(7) Foley, B. J.; Cuthriell, S.; Yazdi, S.; Chen, A. Z.; Guthrie, S. M.; Deng, X.; Giri, G.; Lee, S.-H.; Xiao, K.; Doughty, B.; Ma, Y.-Z.; Choi, J. J. Impact of Crystallographic Orientation Disorders on Electronic Heterogeneities in Metal Halide Perovskite Thin Films. *Nano Lett.* **2018**, *18*, 6271–6278.

(8) Kim, D. H.; Park, J.; Li, Z.; Yang, M.; Park, J.-S.; Park, I. J.; Kim, J. Y.; Berry, J. J.; Rumbles, G.; Zhu, K. 300% Enhancement of Carrier Mobility in Uniaxial-Oriented Perovskite Films Formed by Topotactic-Oriented Attachment. *Adv. Mater.* **2017**, *29*, 1606831.

(9) Li, M.; Wang, Z.-K.; Zhuo, M.-P.; Hu, Y.; Hu, K.-H.; Ye, Q.-Q.; Jain, S. M.; Yang, Y.-G.; Gao, X.-Y.; Liao, L.-S. Pb-Sn-Cu Ternary Organometallic Halide Perovskite Solar Cells. *Adv. Mater.* **2018**, *30*, 1800258.

(10) Li, M.-H.; Yeh, H.-H.; Chiang, Y.-H.; Jeng, U.-S.; Su, C.-J.; Shiu, H.-W.; Hsu, Y.-J.; Kosugi, N.; Ohigashi, T.; Chen, Y.-A.; Shen, P.-S.; Chen, P.; Guo, T.-F. Highly Efficient 2D/3D Hybrid Perovskite Solar Cells via Low-Pressure Vapor-Assisted Solution Process. *Adv. Mater.* **2018**, *30*, 1801401.

(11) Ji, L.; Hsu, H.-Y.; Lee, J. C.; Bard, A. J.; Yu, E. T. Solution-Processed Epitaxial Growth of Hybrid Halide Perovskites and High-Performance Photodetectors. *Nano Lett.* **2018**, *18*, 994-1000.

(12) Jing, L.; Cheng, X.; Yuan, Y.; Du, S.; Ding, J.; Sun, H.; Zhan, X.; Zhou, T-L. Design Growth of Triangular Pyramid $MAPBr_3$ Single Crystal and its Photoelectric Anisotropy between (100) and (111) Facets. *J. Phys. Chem. C* **2019**, *123*, 10826-10830.

(13) Zheng, G.; Zhu, C.; Ma, J.; Zhang, X.; Tang, G.; Li, R.; Chen, Y.; Li, L.; Hu, J.; Hong, J.; Chi, Q.; Gao, X.; Zhou, H. Manipulation of Facet Orientation in Hybrid Perovskite Polycrystalline Films by Cation Cascade. *Nat. Commun.* **2018**, *9*, 2793.

(14) Lv, Q.; He, W.; Lian, Z.; Ding, J.; Li, Q.; Yan, Q. Anisotropic Moisture Erosion of $CH_3NH_3PbI_3$ Single Crystals. *CrystEngComm* **2017**, *19*, 901–904.

(15) Christians, J. A.; Miranda Herrera, P. A.; Kamat, P. V. Transformation of the Excited State and Photovoltaic Efficiency of $CH_3NH_3PbI_3$ Perovskite upon Controlled Exposure to Humidified Air. *J. Am. Chem. Soc.* **2015**, *137*, 1530–1538.

(16) Celio, H. Interface Designed with Differential Pumping and Built-in Figure of Merit to Monitor Chambers Where Environmentally Sensitive Samples Are Prepared or Transferred for Analysis. 9,945,761 B2, April 17, 2018.

(17) Castle, J. E.; Chapman-Kpodo, H.; Proctor, A.; Salvi, A. M. Curve-Fitting in XPS Using Extrinsic and Intrinsic Background Structure. *J. Electron Spectrosc. Relat. Phenom.* **2000**, *106*, 65–80.

(18) Wang, Z.; Jin, K.; Zhang, Y.; Wang, F.; Zhu, Z. ToF-SIMS Depth Profiling of Insulating Samples, Interlaced Mode or Non-Interlaced Mode? *Surf. Interface Anal.* **2014**, *46*, 257–260.

(19) Jesper Jacobsson, T.; Correa-Baena, J.-P.; Pazoki, M.; Saliba, M.; Schenk, K.; Grätzel, M.; Hagfeldt, A. Exploration of the Compositional Space for Mixed Lead Halogen Perovskites for High Efficiency Solar Cells. *Energy Environ. Sci.* **2016**, *9*, 1706–1724.

(20) Shannon, R. D. Revised Effective Ionic Radii and Systematic Studies of Interatomic Distances in Halides and Chalcogenides. *Acta Crystallogr. A* **1976**, *32*, 751–767.

(21) Katari, J. E. B.; Colvin, V. L.; Alivisatos, A. P. X-Ray Photoelectron Spectroscopy of CdSe Nanocrystals with Applications to Studies of the Nanocrystal Surface. *J. Phys. Chem.* **1994**, *98*, 4109–4117.

(22) Murali, B.; Dey, S.; Abdelhady, A. L.; Peng, W.; Alarousu, E.; Kirmani, A. R.; Cho, N.; Sarmah, S. P.; Parida, M. R.; Saidaminov, M. I.; Zhumekenov, A. A.; Sun, J.; Alias, M. S.; Yengel, E.; Ooi, B. S.; Amassian, A.; Bakr, O. M.; Mohammed, O. F. Surface Restructuring of Hybrid Perovskite Crystals. *ACS Energy Lett.* **2016**, *1*, 1119–1126.

(23) Matteocci, F.; Busby, Y.; Pireaux, J.-J.; Divitini, G.; Cacovich, S.; Ducati, C.; Di Carlo, A. Interface and Composition Analysis on Perovskite Solar Cells. *ACS Appl. Mater. Interfaces* **2015**, *7*, 26176-26183.

(24) Griffin, M. P.; Gearba, R.; Stevenson, K.J.; Vanden Bout, D. A.; Colocan, A.

Revealing the Chemistry and Morphology of Buried Donor/Acceptor Interfaces in Organic Photovoltaics. *J. Phys. Chem. Lett.* **2017**. *8*, 2764.

(25) Siegler, T.D.; Shimpi, T.M.; Sampath, W.S.; Korgel, B.A. Development of Wide Bandgap Perovskites for Next-Generation Tandem Solar Cells. *Chem. Eng. Sci.* **2019**. *199*, 388-397.

(26) Wu, B.; Yuan, H.; Xu, Q.; Steele, J. A.; Giovanni, D.; Puech, P.; Fu, J.; Ng, Y. F.; Jamaludin, N. F.; Solanki, A.; Mhaisalkar, S.; Mathews, N.; Roeffaers, M. B. J.; Grätzel, M.; Hofkens, J.; Sum, T. C. Indirect Tail States Formation by Thermal-Induced Polar Fluctuations in Halide Perovskites. *Nat. Commun.* **2019**, *10*, 484.

(27) Lu, M.; Zhang, X.; Bai, X.; Wu, H.; Shen, X.; Zhang, Y.; Zhang, W.; Zheng, W.; Song, H.; Yu, W. W.; Rogach, A. L. Spontaneous Silver Doping and Surface Passivation of $CsPbI_3$ Perovskite Active Layer Enable Light-Emitting Devices with an External Quantum Efficiency of 11.2%. *ACS Energy Lett.* **2018**, *3*, 1571–1577.

(28) Chen, Q.; Chen, L.; Ye, F.; Zhao, T.; Tang, F.; Rajagopal, A.; Jiang, Z.; Jiang, S.; Jen, A. K.-Y.; Xie, Y.; Cai, J.; Chen, L. Ag-Incorporated Organic–Inorganic Perovskite Films and Planar Heterojunction Solar Cells. *Nano Lett.* **2017**, *17*, 3231–3237.

(29) Mahmoudi, T.; Wang, Y.; Hahn, Y.-B. Stability Enhancement in Perovskite Solar Cells with Perovskite/Silver–Graphene Composites in the Active Layer. *ACS Energy Lett.* **2018**, *4*, 235–241.

(30) Zhou, S.; Ma, Y.; Zhou, G.; Xu, X.; Qin, M.; Li, Y.; Hsu, Y.-J.; Hu, H.; Li, G.; Zhao, N.; Xu, J.; Lu, X. Ag-Doped Halide Perovskite Nanocrystals for Tunable Band Structure and Efficient Charge Transport. *ACS Energy Lett.* **2019**, *4*534–541.

(31) Kato, Y.; Ono, L. K.; Lee, M. V.; Wang, S.; Raga, S. R.; Qi, Y. Silver Iodide Formation in Methyl Ammonium Lead Iodide Perovskite Solar Cells with Silver Top Electrodes. *Adv. Mater. Interfaces* **2015**, *2*, 1500195.

(32) Guerrero, A.; You, J.; Aranda, C.; Kang, Y. S.; Garcia-Belmonte, G.; Zhou, H.; Bisquert, J.; Yang, Y. Interfacial Degradation of Planar Lead Halide Perovskite Solar Cells. *ACS Nano* **2016**, *10*, 218–224.

(33) Back, H.; Kim, G.; Kim, J.; Kong, J.; Kim, T. K.; Kang, H.; Kim, H.; Lee, J.; Lee, S.; Lee, K. Achieving Long-Term Stable Perovskite Solar Cells via Ion Neutralization. *Energy Environ. Sci.* **2016**, *9*, 1258–1263.

(34) Sanehira, E. M.; Tremolet de Villers, B. J.; Schulz, P.; Reese, M. O.; Ferrere, S.; Zhu, K.; Lin, L. Y.; Berry, J. J.; Luther, J. M. Influence of Electrode Interfaces on the Stability of Perovskite Solar Cells: Reduced Degradation Using MoO_x/Al for Hole Collection. *ACS Energy Lett.* **2016**, *1*, 38–45.

(35) Fransishyn, K. M.; Kundu, S.; Kelly, T. L. Elucidating the Failure Mechanisms of Perovskite Solar Cells in Humid Environments Using In Situ Grazing-Incidence Wide-Angle X-Ray Scattering. *ACS Energy Lett.* **2018**, *3*, 2127–2133.

(36) Liu, Z.; Krückemeier, L.; Krogmeier, B.; Klingebiel, B.; Márquez, J. A.; Levcenko, S.; Öz, S.; Mathur, S.; Rau, U.; Unold, T.; Kirchartz, T. Open-Circuit Voltages Exceeding 1.26 V in Planar Methylammonium Lead Iodide Perovskite Solar Cells. *ACS Energy Lett.* **2019**, *4*, 110–117.

(37) Wang, J.; Fu, W.; Jariwala, S.; Sinha, I.; Jen, A. K.-Y.; Ginger, D. S. Reducing Surface Recombination Velocities at the Electrical Contacts Will Improve Perovskite

Photovoltaics. *ACS Energy Lett.* **2019**, *4*, 222–227.

(38) Qiao, H. W.; Yang, S.; Wang, Y.; Chen, X.; Wen, T. Y.; Tang, L. J.; Cheng, Q.; Hou, Y.; Zhao, H.; Yang, H. G. A Gradient Heterostructure Based on Tolerance Factor in High-Performance Perovskite Solar Cells with 0.84 Fill Factor. *Adv. Mater.* **2019**, *31*, 1804217.

(39) Srimath Kandada, A. R.; Neutzner, S.; D'Innocenzo, V.; Tassone, F.; Gandini, M.; Akkerman, Q. A.; Prato, M.; Manna, L.; Petrozza, A.; Lanzani, G. Nonlinear Carrier Interactions in Lead Halide Perovskites and the Role of Defects. *J. Am. Chem. Soc.* **2016**, *138*, 13604–13611.

(40) Zhang, M.; Zheng, Z.; Fu, Q.; Guo, P.; Zhang, S.; Chen, C.; Chen, H.; Wang, M.; Luo, W.; Tian, Y. Determination of Defect Levels in Melt-Grown All-Inorganic Perovskite $CsPbBr_3$ Crystals by Thermally Stimulated Current Spectra. *J. Phys. Chem. C* **2018**, *122*, 10309–10315.

(41) Stewart, R. J.; Grieco, C.; Larsen, A. V.; Doucette, G. S.; Asbury, J. B. Molecular Origins of Defects in Organohalide Perovskites and Their Influence on Charge Carrier Dynamics. *J. Phys. Chem. C* **2016**, *120*, 12392–12402.

(42) Winterbottom, W. L. Equilibrium Shape of a Small Particle in Contact with a Foreign Substrate. *Acta Metall.* **1967**, *15*, 303–310.

(43) Seifert, A.; Vojta, A.; Speck, J. S.; Lange, F. F. Microstructural Instability in Single-Crystal Thin Films. *J. Mater. Res.* **1996**, *11*, 1470–1482.

(44) Thompson, C. V. Structure Evolution During Processing of Polycrystalline Films. *Annu. Rev. Mater. Sci.* **2000**, *30*, 159–190.

(45) Ohring, M. *Material Science of Thin Films*, 2nd ed.; Academic Press: San Diego, 2002.

(46) Lee, D. S.; Yun, J. S.; Kim, J.; Soufiani, A. M.; Chen, S.; Cho, Y.; Deng, X.; Seidel, J.; Lim, S.; Huang, S.; Ho-Baillie, A. W. Y. Passivation of Grain Boundaries by Phenethylammonium in Formamidinium-Methylammonium Lead Halide Perovskite Solar Cells. *ACS Energy Lett.* **2018**, *3*, 647–654.

(47) Wang, Z.; Lin, Q.; Chmiel, F. P.; Sakai, N.; Herz, L. M.; Snaith, H. J. Efficient Ambient-Air-Stable Solar Cells with 2D–3D Heterostructured Butylammonium-Caesium-Formamidinium Lead Halide Perovskites. *Nat. Energy* **2017**, *2*, 17135.

(48) Weissbuch, I.; Guo, S.; Edgar, R.; Cohen, S.; Howes, P.; Kjaer, K.; Als-Nielsen, J.; Lahav, M.; Leiserowitz, L. Oriented Crystalline Thin Films of Tetracosanedioic Acid and Its Metal Salts at the Air-Aqueous Solution Interface. *Adv. Mater.* **1998**, *10*, 117–121.

(49) Tao, A. R.; Habas, S.; Yang, P. Shape Control of Colloidal Metal Nanocrystals. *Small* **2008**, *4*, 310–325.

(50) Cho, S. H.; Ghosh, S.; Berkson, Z. J.; Hachtel, J. A.; Shi, J.; Zhao, X.; Reimnitz, L. C.; Dahlman, C. J.; Ho, Y.; Yang, A.; Liu, Y; Idrobo, J.-C.; Chmelka, B. F; Milliron, D. J. Syntheses of Colloidal F:In_2O_3 Cubes: Fluorine-Induced Faceting and Infrared Plasmonic Response. *Chem. Mater.* **2019**, *31*, 2661-2676.

(51) Mao, C.; Zhou, L.; Wu, X.; Sun, X. New Understanding of Silver-Induced Texture in Powder-in-Tube Processed Ag/Bi(2223) Tape. *Physica C Supercond.* **1997**, *281*, 159–175.

(52) Luo, J. S.; Merchant, N.; Maroni, V. A.; Riley, G. N.; Carter, W. L. Influence of Silver Cladding on the Formation and Alignment of the $(Bi_{2-x}Pb_x)Sr_2Ca_2Cu_3O_{10+\delta}$ Phase. *Appl. Phys. Lett.* **1993**, *63*, 690–692.

(53) Aswal, D. K.; Gupta, S. K.; Debnath, A. K.; Kothiyal, G. P.; Sabharwal, S. C.; Gupta, M. K. Preparation of Adherent Y-Ba-Cu-O Thick Films and the Effect of Silver Doping. *Supercond. Sci. Technol.* **1991**, *4*, 188–191.

(54) Kim, F.; Connor, S.; Song, H.; Kuykendall, T.; Yang, P. Platonic Gold Nanocrystals. *Angew. Chem.* **2004**, *116*, 3759–3763.

(55) Liu, M.; Guyot-Sionnest, P. Mechanism of Silver(I)-Assisted Growth of Gold Nanorods and Bipyramids. *J. Phys. Chem. B* **2005**, *109*, 22192-22200.

(56) Chen, A. Z.; Shiu, M.; Ma, J. H.; Alpert, M. R.; Zhang, D.; Foley, B. J.; Smilgies, D.-M.; Lee, S.-H.; Choi, J. J. Origin of Vertical Orientation in Two-Dimensional Metal Halide Perovskites and Its Effect on Photovoltaic Performance. *Nat. Commun.* **2018**, *9*, 1336.

(57) Chen, A. Z.; Shiu, M.; Deng, X.; Mahmoud, M.; Zhang, D.; Foley, B. J.; Lee, S.-H.; Giri, G.; Choi, J. J. Understanding the Formation of Vertical Orientation in Two-Dimensional Metal Halide Perovskite Thin Films. *Chem. Mater.* **2019**, *31*, 1336-1343.

(58) Lin, Y.; Fang, Y.; Zhao, J.; Shao, Y.; Stuard, S. J.; Nahid, M. M.; Ade, H.; Wang, Q.; Shield, J. E.; Zhou, N.; Moran, A. M.; Huang, J. Unveiling the Operation Mechanism of Layered Perovskite Solar Cells. *Nat. Commun.* **2019**, *10*, 1008.

(59) Venkatesan, N. R.; Labram, J. G.; Chabinyc, M. L. Charge-Carrier Dynamics and Crystalline Texture of Layered Ruddlesden–Popper Hybrid Lead Iodide Perovskite

Thin Films. *ACS Energy Lett.* **2018**, *3*, 380–386.

(60) Fu, W.; Wang, J.; Zuo, L.; Gao, K.; Liu, F.; Ginger, D. S.; Jen, A. K.-Y. Two-Dimensional Perovskite Solar Cells with 14.1% Power Conversion Efficiency and 0.68% External Radiative Efficiency. *ACS Energy Lett.* **2018**, *3*, 2086–2093.

(61) Giesbrecht, N.; Schlipf, J.; Grill, I.; Rieder, P.; Dyakonov, V.; Bein, T.; Hartschuh, A.; Müller-Buschbaum, P.; Docampo, P. Single-Crystal-like Optoelectronic-Properties of $MAPbI_3$ Perovskite Polycrystalline Thin Films. *J. Mater. Chem. A* **2018**, *6*, 4822–4828.

(62) Saliba, M.; Tan, K. W.; Sai, H.; Moore, D. T.; Scott, T.; Zhang, W.; Estroff, L. A.; Wiesner, U.; Snaith, H. J. Influence of Thermal Processing Protocol upon the Crystallization and Photovoltaic Performance of Organic–Inorganic Lead Trihalide Perovskites. *J. Phys. Chem. C* **2014**, *118*, 17171–17177.

(63) Ji, F.; Pang, S.; Zhang, L.; Zong, Y.; Cui, G.; Padture, N. P.; Zhou, Y. Simultaneous Evolution of Uniaxially Oriented Grains and Ultralow-Density Grain-Boundary Network in $CH_3NH_3PbI_3$ Perovskite Thin Films Mediated by Precursor Phase Metastability. *ACS Energy Lett.* **2017**, *2*, 2727–2733.

(64) Zhao, T.; Liu, H.; Ziffer, M. E.; Rajagopal, A.; Zuo, L.; Ginger, D. S.; Li, X.; Jen, A. K. Y. Realization of a Highly Oriented $MAPbBr_3$ Perovskite Thin Film via Ion Exchange for Ultrahigh Color Purity Green Light Emission. *ACS Energy Lett.* **2018**, *3*, 1662–1669.

(65) Park, B.; Kedem, N.; Kulbak, M.; Lee, D. Y.; Yang, W. S.; Jeon, N. J.; Seo, J.; Kim, G.; Kim, K. J.; Shin, T. J.; Hodes, G.; Cahen, D.; Seok, S.I. Understanding How Excess

Lead Iodide Precursor Improves Halide Perovskite Solar Cell Performance. *Nat. Commun.* **2018**, *9*, 3301.

(66) Chiang, C.-H.; Wu, C.-G. A Method for the Preparation of Highly Oriented $MAPbI_3$ Crystallites for High-Efficiency Perovskite Solar Cells to Achieve an 86% Fill Factor. *ACS Nano* **2018**, *12*, 10355–10364.

(67) Meng, L.; Sun, C.; Wang, R.; Huang, W.; Zhao, Z.; Sun, P.; Huang, T.; Xue, J.; Lee, J.-W.; Zhu, C.; Huang, Y.; Li, Y.; Yang, Y. Tailored Phase Conversion under Conjugated Polymer Enables Thermally Stable Perovskite Solar Cells with Efficiency Exceeding 21%. *J. Am. Chem. Soc.* **2018**. *140*, 17255-17262.

(68) Zhao, Y.; Tan, H.; Yuan, H.; Yang, Z.; Fan, J. Z.; Kim, J.; Voznyy, O.; Gong, X.; Quan, L. N.; Tan, C. S.; Hofkens, J.; Yu, D.; Zhao, Q.; Sargent, E. H. Perovskite Seeding Growth of Formamidinium-Lead-Iodide-Based Perovskites for Efficient and Stable Solar Cells. *Nat. Commun.* **2018**, *9*, 1607.

(69) Wang, Y.; Sun, X.; Chen, Z.; Sun, Y.-Y.; Zhang, S.; Lu, T.-M.; Wertz, E.; Shi, J. High-Temperature Ionic Epitaxy of Halide Perovskite Thin Film and the Hidden Carrier Dynamics. *Adv. Mater.* **2017**, *29*, 1702643.

(70) Chen, J.; Morrow, D. J.; Fu, Y.; Zheng, W.; Zhao, Y.; Dang, L.; Stolt, M. J.; Kohler, D. D.; Wang, X.; Czech, K. J.; Hautzinger, M. P.; Shen, S.; Guo, L.; Pan, A.; Wright, J. C.; Jin, S. Single-Crystal Thin Films of Cesium Lead Bromide Perovskite Epitaxially Grown on Metal Oxide Perovskite ($SrTiO_3$). *J. Am. Chem. Soc.* **2017**, *139*, 13525–13532.

PEROVSKITE-CDTE TANDEM PHOTOVOLTAICS

Chapter 6: TlBr and Tl_2AgBr_3 Nanocrystals

6.1 INTRODUCTION

Thallium has attracted recent interest as a substitutional dopant for halide perovskites (HaPs). Recent reports have detailed thallium substitution in the A-site[1] for new wide bandgap perovskites and thallium inclusion in the B-sites of double perovskite structures.[2–5] Inclusion of Tl^{3+} in double perovskites is particularly interesting, as the low energy levels of unoccupied Tl^{3+} 6s bands have led to double perovskites with direct band gaps as low as 0.95 eV, the lowest band gap energy observed in a known HaP material.[2] Additionally, thallium bromide materials have applications in radiation detectors due to their high carrier mobility and large average atomic weight.[6–8] Unfortunately, due to the high acute toxicity of thallium, thin film processing of these materials is limited. Traditional bulk thin-film processing of HaPs involves the use of polar complexing agents such as dimethylsulfoxide (DMSO)[9] which may permeate skin, carrying heavy metal atoms to the bloodstream.[10] Therefore, the risk associated with using conventional HaP thin film processing techniques for thallium-based HaPs is too great for utilization in optoelectronic devices, even at a lab or testing scale.

A relatively safe alternative to bulk HaP thin film processing is nanocrystal synthesis and post-reaction film processing. Complex chemistry with polar solvents is not needed for efficient nanocrystal HaP PV, and there is greater flexibility in the method of film deposition,[11] which allows for better design of safe deposition processes. Recent reports have shown that solar cells made with HaP nanocrystals can achieve high performance comparable to bulk HaP devices.[12,13] However, such methods would require deeper knowledge of thallium halide nanoparticle synthesis, which is currently lacking.

TlBr nanostructures were first synthesized by Akhbari and Morsali, who developed a method to make nonuniform particles by exposing cetyltrimethylammonium bromide (CTAB) to a thallium polymer.[14] Mir et. al. recently developed the first chemical route to TlI nanocrystals with high carrier mobility and large carrier diffusion lengths by injecting a solution of tetra-butyl ammonium iodide into a thallium nitrate solution.[15] They were also able to synthesize larger (~28 nm) TlBr nanocrystals using tetra-butyl ammonium bromide in the same synthetic method.[15] Finally, Vanishita et. al. recently developed a method to synthesize uniform Tl_3PbX_5 (X=I,Br,Cl) nanocrystals via injection of thallium oleate into a solution of lead halide.[1]

Here, we report the synthesis of uniform TlBr and Tl_2AgBr_3 nanocrystals. Injecting trimethylsilyl bromide (TMSBr) into a solution of thallium (III) acetate in oleylamine and oleic acid at 70 ^oC yields uniform nanocrystals of CsCl-type cubic TlBr with a size distribution of ~10.4 $\pm$ 1 nm. Adding silver (I) acetate to this solution in a 2:1 Tl:Ag molar ratio yields dolomite-type trigonal Tl_2AgBr_3 nanocrystals with a size distribution of 15 $\pm$ 3 nm. Limited size tunability is shown in the synthesis, with TlBr particles exhibiting a smaller average particle size at higher temperature, while Tl_2AgBr_3 nanocrystals exhibit a broader size distribution at longer reaction times. Optical properties are characterized for both nanocrystals, and dolomite-type Tl_2AgBr_3 is shown for the first time to have an indirect band gap of 3.0 eV. Finally, assembly is characterized in these particles. While scanning electron microscopy (SEM) shows both nanocrystals form face centered cubic (FCC) superlattices, the extent of superlattice formation is hindered by particle aggregation during the drying of concentrated solutions of nanocrystals. To our knowledge, this is the first report of Tl_2AgBr_3 nanocrystal synthesis.

6.2 Experimental Details

6.2.1 Materials

Thallium (III) acetate ($(CH_3COO)_3Tl$, >90%, Sigma-Aldrich), silver (I) acetate (CH_3COOAg, 99.99% metals basis, Sigma-Aldrich), bromotrimethylsilane ($(CH_3)_3SiBr$, purum >97%, Sigma-Aldrich), oleylamine ($CH_3(CH_2)_7CH=CH(CH_2)_7CH_2NH_2$, technical grade 70%, Sigma-Aldrich), oleic acid ($CH_3(CH_2)_7CH=CH(CH_2)_7COOH$, Sigma, 90%), 1-octadecene ($CH_3(CH_2)_{15}CH=CH_2$, Sigma, 90%), toluene (C_7H_8, Fisher, >99.5%), methyl acetate (CH_3COOCH_3, anhydrous 99.5%, Sigma-Aldrich), and potassium bromide (KBr, Sigma-Aldrich) were used as received without further purification. Silicon wafers (University Wafer, 8-10 Ωcm, (100) surface) and glass slides (Cardinal) were cut into substrates of various sizes without modification.

6.2.2 Fabrication and Processing

SAFETY WARNING: Thallium salts are very toxic, and extreme care should be taken at all times when dealing with them. Thallium toxicity is associated with gastrointestinal distress, swelling, and nerve damage, which usually begins to manifest in the form of numbness in appendages.[16] These symptoms are pernicious on account of their delayed effects which often occur 24-48 h after exposure and mild preliminary symptoms which are often misattributed to other illnesses or conditions. Additionally, chronic thallium overexposure can result in hair loss on the time frame of weeks to months.[16] Seek medical attention if you experience any of these symptoms.

We have designed special safety procedures to deal with these acute health concerns. All work involving thallium powders is done in a glove box when possible. If it is impossible to work with thallium powders in the glove box, a particulate mask is worn in addition to standard PPE. In either case, foil is laid out underneath the work space to

catch all stray or spilled powder. All vessels containing thallium solutions are either disposed or thoroughly washed immediately after use. Care is used when washing with coordinating solvents that have moderate skin permeability, and gloves are exchanged after every washing step. **Never expose thallium salts to DMF or DMSO, as such molecules are highly coordinating with transition metals such as thallium and are highly skin-permeable**.[10] Aqua regia is used on reaction vessels frequently to prevent buildup of insoluble thallium.

6.2.2.1 TlBr Nanocrystal Synthesis

In a typical TlBr nanocrystal synthesis, 0.5 mmol thallium (III) acetate (190 mg) was loaded in a 50 mL three-neck flask in a glove box. The three-neck flask was then sealed and transferred to a Schlenk line without exposing the thallium (III) acetate to air. Then, the thallium (III) acetate was mixed with 9 mmol of oleylamine (3 mL), 9 mmol of oleic acid (2.8 mL), and 10 mL of octadecene. This mixture was stirred and degassed at 110 ^{o}C for 1 h, resulting in a pale-yellow translucent solution of dissolved thallium (III) acetate. The mixture was then cooled to the desired reaction temperature, and 2.7 mmol (350 μL) of bromotrimethylsilane was transferred from the glove box and swiftly injected into the solution. The reaction was kept at the desired reaction temperature for 5 min, after which, it was rapidly cooled using an ice bath. As the reaction mixture cooled to ~60 ^{o}C, 10 mL of toluene was rapidly injected to prevent particle aggregation.

This mixture was transferred to a centrifuge tube and centrifuged at 20,500 rcf for 5 min. The precipitate, which consists of a mixture of nanoparticles that are too poorly capped to disperse well in nonpolar solvents and large aggregates, was discarded, and methyl acetate was added to the supernatant in a 1:1 volume ratio. The solution was again centrifuged at 20,500 rcf for 5 min, and the supernatant from this second centrifuge step

was discarded. The precipitate was suspended in 10 mL of toluene, and then 10 mL of methyl acetate was added to the slightly hazy suspension to form an opaque white solution. This solution was again centrifuged at 20,500 rcf for 5 min and the supernatant was discarded. The toluene-methyl acetate washing step was repeated two more times. After the final washing step, the nanocrystals were suspended in toluene, yielding a slightly hazy colorless solution which was stored in a dark refrigerator in air. Particles were colloidally stable for ~4 days in the refrigerator and ~36 h at room temperature, after which, suspensions would become opaque with a milky consistency. Reactions yielded 40 mg of TlBr nanocrystals in 10 mL of toluene (25% yield).

6.2.2.2 Tl_2AgBr_3 Nanocrystal Synthesis

Tl_2AgBr_3 nanocrystals were synthesized in a process similar to that of TlBr nanocrystals. In a typical synthesis, 1 mmol thallium (III) acetate (380 mg) and 0.5 mmol silver (I) acetate (85 mg) were loaded into a 50 mL three-arm flask in the glove box, after which the flask was sealed and transferred to the Schlenk line. The flask was then loaded with 9 mmol oleic acid (2.8 mL), 9 mmol oleylamine (3 mL), and 15 mL of octadecene and degassed at 110 ^{o}C for 1 hr, yielding a burnt orange translucent solution. The reaction was then cooled to the desired reaction temperature and 2.7 mmol of TMSBr (350 μL) was rapidly injected into the mixture. Within ~5 s of injection, the reaction was quickly cooled by submerging the three-neck flask in an ice bath. As the solution was cooled to ~60 ^{o}C, 15 mL of toluene was injected to prevent aggregation.

Particles were washed in a process identical to that used for TlBr synthesis with the exception of the last two washes, where only ~6-8 mL of methyl acetate was added to the 10 mL toluene suspension to minimize particle aggregation. Resulting suspensions were

hazy pale yellow and had ~2 days of colloidal stability in a refrigerator. Reactions yielded 100 mg of nanocrystals in 10 mL of toluene (20% yield).

6.2.3 Materials Characterization

Low-resolution Transmission Electron Microscopy (TEM) was performed on a FEI Tecnai Spirit Bio Twin TEM at an accelerating voltage of 80 kV. High-resolution imaging, electron diffraction patterns, and Energy-Dispersive X-Ray Spectroscopy (EDS) maps were acquired on a JEOL 2010F TEM at an accelerating voltage of 200 kV. Images and diffraction patterns were analyzed using the Gatan Digital Micrograph software (v. 3.30.2016.0). Lattice spacing was determined from fast Fourier transforms (FFT) of high-resolution images.

X-Ray Diffraction (XRD) was performed on a Rigaku R-Axis Spider X-Ray Diffractometer with an image plate detector and Cu Kα radiation (λ=1.54 Å, 40 mA, 40 mV). Samples were probed by drying nanocrystal suspensions on glass slides at room temperature and then mounting scraped powder on a Hampton Research Mounted CryoLoop. Special care was taken to mount nanocrystalline powder without creating toxic thallium dust. Data was taken for 10 min with cryoloops rotating at 5^{o}/min.

Solution UV–Vis-NIR absorbance and absorptance spectroscopy was performed using a Varian Cary 50 Bio UV-Vis spectrophotometer. Kubelka-Munk data were collected using an Aligent Cary 5000 UV–Vis-NIR spectrophotometer with a PbS near infrared (NIR) detector and a photomultiplier tube mounted in an attached Aligent Diffuse Reflectance Accessory DRA-2500 (DRA). Powder samples were directly taped onto a black cover of a Labsphere URS-99-020 reflectance standard in the reflectance port using black double-sided carbon tape. The direct reflection beam was directed at ~8° relative to the angle of incident light into a light trap that came standard with the DRA-2500.[17] KBr

powder was used as a non-absorbing reference material. Absorbance coefficient k/s was calculated from diffuse reflectance using the Kubelka-Munk equation $\frac{k}{s}=(1-R_\infty)^2/2R_\infty$, where R_∞ is the diffuse reflectance, and k/s is the ratio of absorbance to scattering coefficient.[18]

Scanning electron microscopy (SEM) images were acquired with a Hitachi S-5500 SEM/STEM using an accelerating voltage of 15 kV and an emission current of ~10 μA in SEM mode. Samples were drop cast onto cut pieces of a p-type Si wafer with a resistivity of 10 Ω cm for imaging. The substrate was electrically grounded to the SEM mount with carbon tape prior to imaging. EDS spectra were taken in vacuum using a Bruker XFlash 5010 attachment to a FEI Quanta 650 ESEM operating at 30 kV at 10,000x magnification

Grazing-incidence small- and wide-angle X-Ray scattering (GISAXS and GIWAXS) and solution small-angle X-Ray scattering (solution SAXS) was carried out in vacuum on a SAXSLAB Ganesha SAXS-WAXS system with Cu Kα radiation (λ=1.54 Å). GIXS measurements were taken with a 0.2° incident beam angle. Scattered X-Rays were collected on a Pilatus3 R 300k image plate detector 487x619 pixels in size, with each pixel having an area of 0.172x0.172 mm^2. GIXS patterns were taken for 30 minutes, and solution SAXS patterns were taken for 1 hr. GISAXS and SAXS experiments employed a sample-to-detector distance of 1084 mm and GIWAXS was taken with a sample-to-detector distance of 134 mm. Ewald sphere correction and linear 2θ integration were processed with Fit2D software (version: 12_077_i686_WXP). Solution SAXS data were fit using previously reported fit equations.[19]

X-ray Photoelectron Spectroscopy was performed with a Kratos Axis Ultra DLD photoelectron spectrophotometer. Samples were prepared by drop casting nanocrystal dispersions in toluene onto conductive silicon substrates. Spectra where acquired with a monochromatic AlKα X-ray source (hν = 1486.5 eV) and an automated charge neutralizer.

The spectra were processed using CasaXPS analysis software. The XPS peaks were fit to a Gaussian-Lorentzian distribution and a Shirley background. Composition estimates were calculated by dividing the peak area by the corresponding Kratos sensitivity factor from the Kratos library.

6.3 Results and Discussion

6.3.1 Synthesis of TlBr Nanocrystals

Nanocrystals of TlBr were synthesized by mixing thallium (III) acetate with oleic acid and oleylamine in an octadecene solvent. This mixture is degassed at 110 ^{o}C for ~1 h to allow for full dissolution of the precursors, and cooled to 70 ^{o}C for the reaction. Rapid injection of trimethylsilylbromide (TMSBr), a common bromine source for HaP nanocrystals,[20] induces a rapid reaction via the proposed mechanism of Cruetz et. al.[20] in Eqn 6.1

$$M^{+}RCOOH^{-}+(CH_3)_3SiBr \rightarrow MBr+RCOO\text{-}Si(CH_3)_3 \qquad (6.1)$$

where M stands for any transition metal (in this case, Tl^{3+}). The exposure of trimethylsilyl halide to a solution of metal acetates will result in a rapid exchange of the halide and acetate moieties, resulting in the precipitation of metal halide or HaP nanocrystals. This is demonstrated again in this reaction, with thallium (III) acetate yielding uniform TlBr nanocrystals upon exposure to TMSBr. Unique to this reaction, the transition metal Tl undergoes a reduction from 3+ to 1+ either during the reaction or prior to injection, likely undergoing redox coupling with the oleylamine ligand. TEM images of the nanocrystal product, seen in Figure 6.1A-B, show that particles are relatively uniform with a size distribution of 13 $\pm$ 3 nm. HRTEM of a single particle shown in Figure 6.1C and XRD of a nanoparticle ensemble in Figure 6.1D confirm these particles are crystalline CsCl-type TlBr (PDF #01-071-4695). The HRTEM in Figure 6.1C shows (110) lattice fringes with a

d-spacing of 2.9 Å. Fitting solution SAXS data in Figure 6.1E confirms single particle counting results, showing particles have a size distribution of 10.4 $\pm$ 1 nm.[19] Additionally, XPS and EDS data presented in Table 6.1 demonstrate samples are stochiometric, having a Tl:Br ratio close to the expected value of 1.

In the case of TlBr nanocrystals, mean particle diameter is not strongly impacted by reaction time, in contrast with other HaP hot injection syntheses.[20,21] However, from TEM images of particles in Figure 6.2, it is apparent that nanocrystal size uniformity is optimized at a reaction time of 5 min. Using the conventional HaP NC synthesis process, which involves quenching in ice water immediately following hot injection (i.e. a 0 min reaction), nanocrystals with relatively random sizes between 3-28 nm are observed. At reaction times longer than 5 min, large particles begin to form, leading to a broader size distribution of particles. Yield is consistent as a function of reaction time.

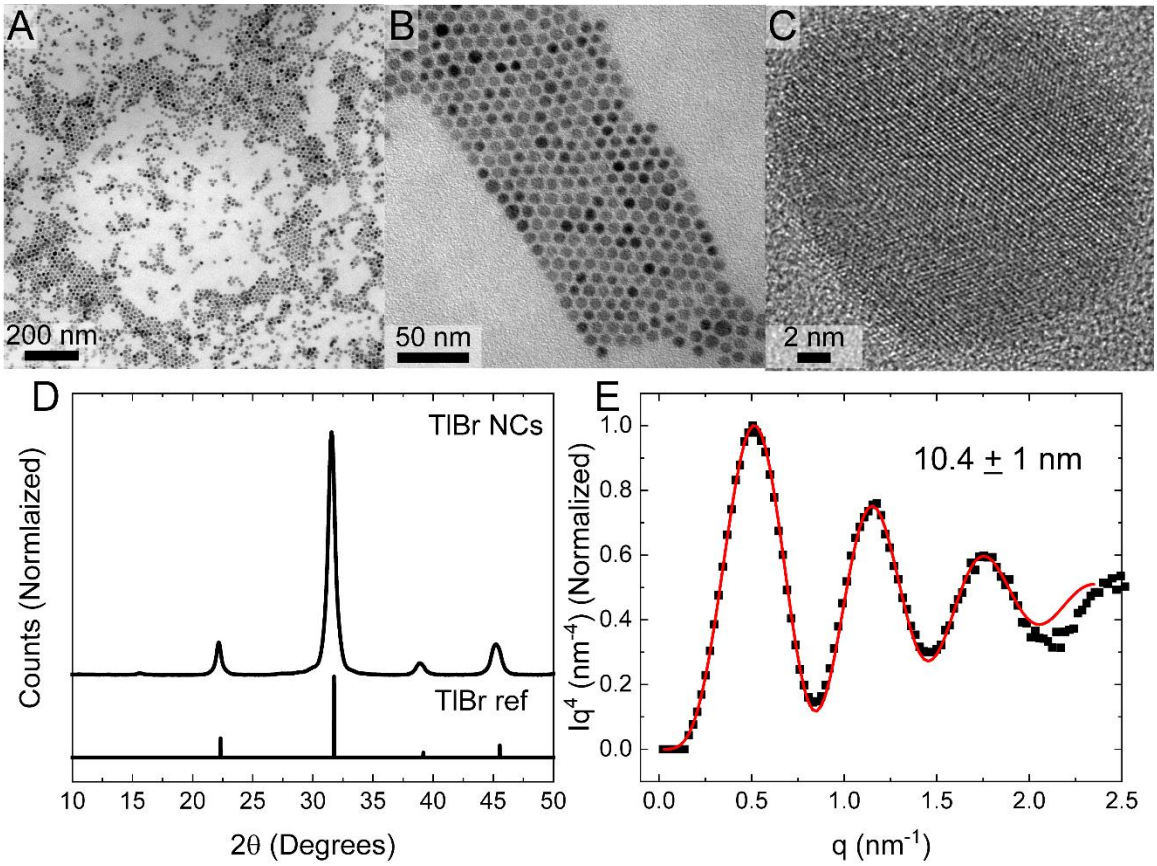

Figure 6.1 (A-B) TEM images of TlBr nanocrystals, showing particles have a uniform spheroid shape and size distribution of 13 ± 3 nm. (C) HRTEM image of a TlBr particle, showing (110) lattice fringes with a d-spacing of 0.29 nm. (D) XRD pattern of the nanocrystal product, showing the particles are crystalline CsCl-type cubic TlBr (PDF #01-071-4695) with no large phase impurities. A small peak at ~16° 2θ may be due to organic contamination. (E) Porod plot calculated from solution small-angle X-Ray scattering (SAXS) of TlBr nanocrystals in toluene. A fit of the data[19] shows dispersed particles exhibit a uniform size distribution of 10.4 ± 1 nm. The fit diverges at high q-values, indicating the distribution of particle sizes may not be perfectly Gaussian in the limit of small particle size.

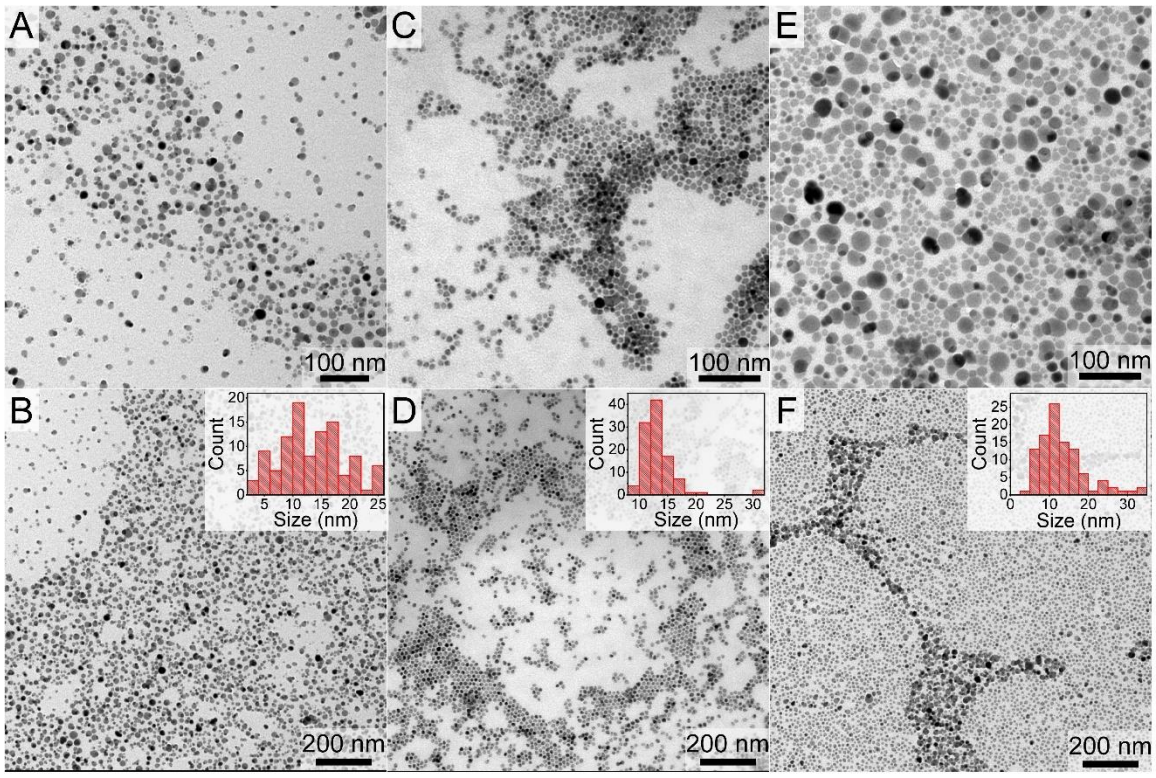

Figure 6.2. TEM images and size distributions from particle counting for a TlBr nanocrystal reaction at 70 ^{o}C held for (A,B) 0 min, (C,D) 5 min, and (E,F) 30 min. Histograms of counted particles are in the inset of (B), (D), and (F).

Changing reaction temperature exhibited limited size control on TlBr nanocrystals, seen in Figure 6.3. Reactions held for 5 min at 30 ^{o}C before quenching in ice water exhibit a similar size distribution to reactions held at 70 ^{o}C, with a slightly larger standard deviation. However, nanocrystals synthesized at 110 ^{o}C exhibited nonspherical shapes and a much smaller average size, with a size distribution of 5 $\pm$ 2 nm. This reaction at higher temperature also produced several large aggregated particles that were not easily separated from the smaller particles.

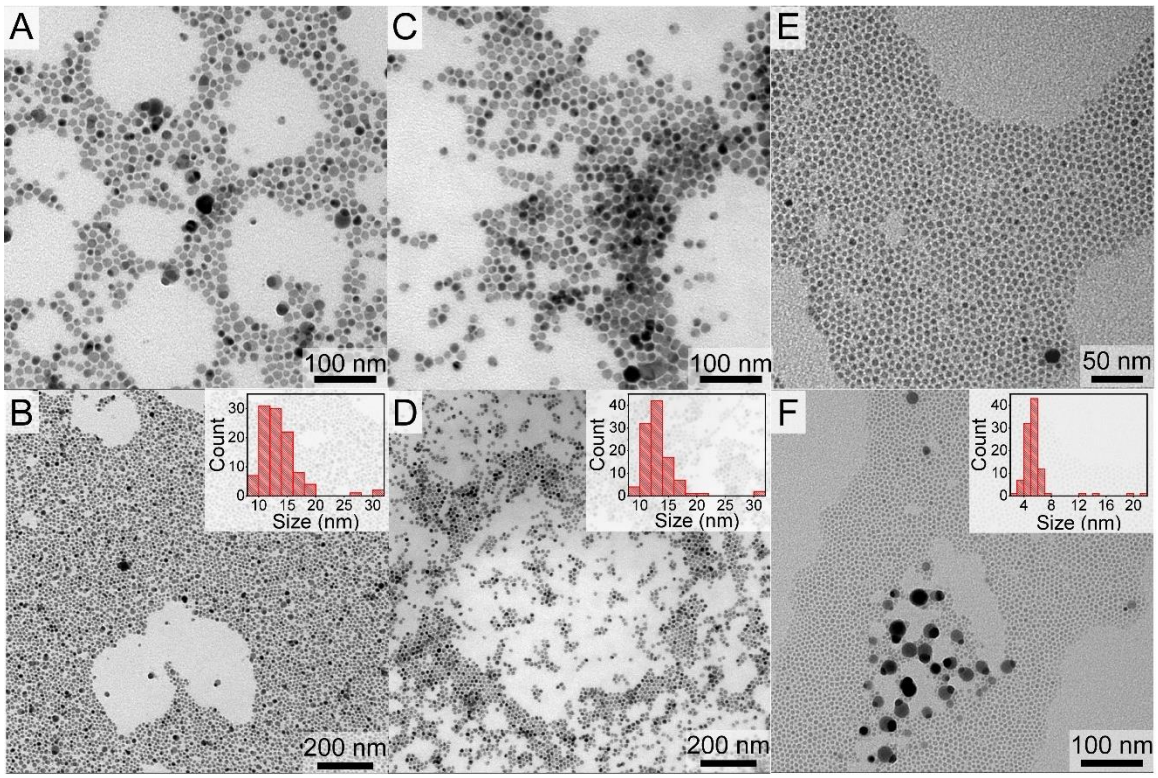

Figure 6.3 TEM images and size distributions from particle counting for a TlBr reaction held for 5 min at (A,B) 30 °C, (C,D) 70 °C, and (E,F) 110 °C. Histograms of counted particles are in the inset of (B), (D), and (F).

Table 6.1 Elemental analyses of TlBr and Tl_2AgBr_3 nanocrystals from XPS and EDS

	Tl:Br		Ag:Br	
	XPS	EDS	XPS	EDS
TlBr	0.91	1.3	0	0
Tl_2AgBr_3	0.55	0.7	0.44	0.6

6.3.2 Synthesis of Tl_2AgBr_3 Nanocrystals

Tl_2AgBr_3 nanocrystals were synthesized in a similar method to the described TlBr synthesis using a 2:1 molar ratio of thallium (III) acetate to silver (I) acetate. Upon TMSBr

injection, silver (I) and thallium (III) acetate precipitate to form uniform dolomite Tl_2AgBr_3 nanocrystals via the mechanism in Eqn 6.1.

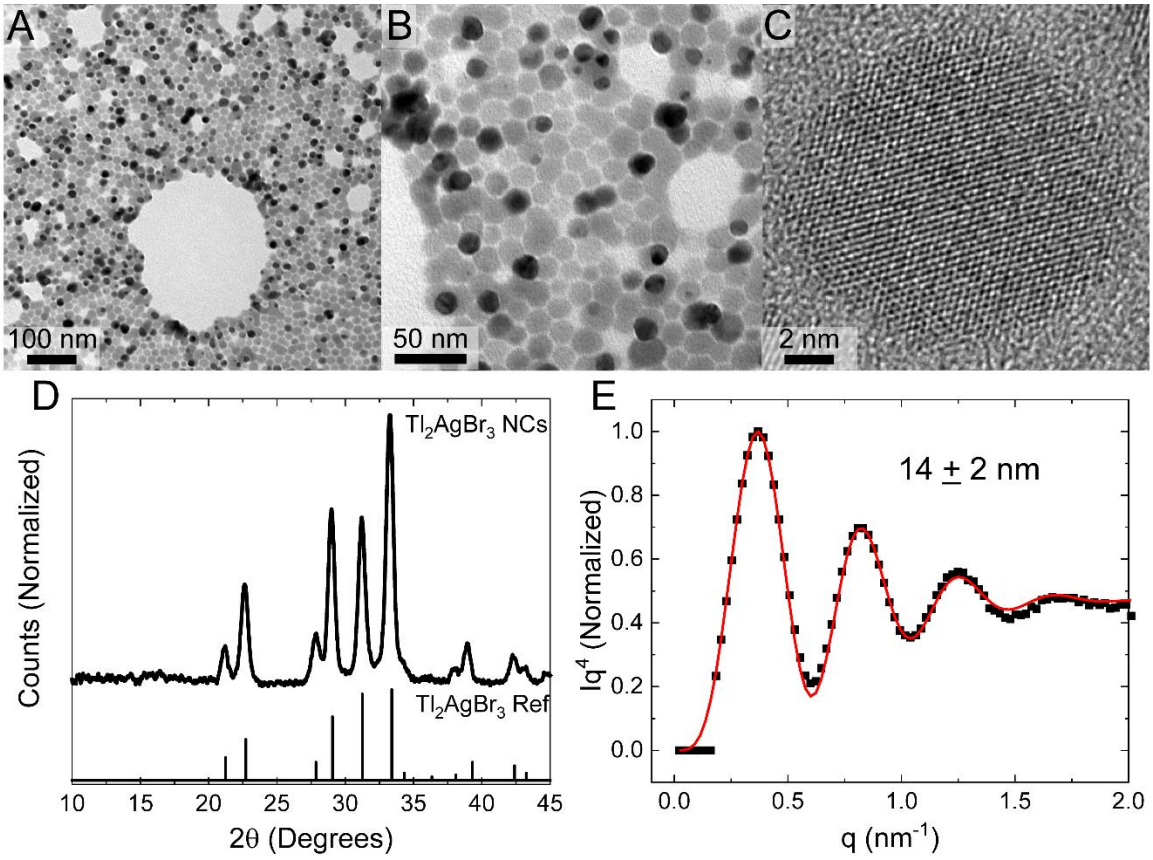

Figure 6.4 (A-B) TEM images of Tl_2AgBr_3 nanocrystals, showing particles have a uniform spheroid shape and size distribution of 15 $\pm$ 3 nm. (C) HRTEM image of a Tl_2AgBr_3 particle, showing (300) lattice fringes and a d-spacing of 0.28 nm. (D) XRD pattern of the nanocrystals, showing the particles are crystalline dolomite-type trigonal structure (PDF #00-017-0631) with no large phase impurities. (E) Porod plot calculated from solution small-angle X-Ray scattering (SAXS) of a solution of Tl_2AgBr_3 nanocrystals in toluene. A fit of the data[19] shows dispersed particles exhibit a uniform size distribution of 14 $\pm$ 2 nm.

Nanocrystal characterization is seen in Figure 6.4. Tl_2AgBr_3 nanoparticles formed via this method are relatively uniform, as seen by TEM in Figures 6.4A-B, with a size

distribution of 15 ± 3 nm as measured by particle counting. Solution SAXS seen in Figure 6.4E shows a similar distribution of 14 ± 2 nm. XRD patterns of nanocrystal samples in Figure 6D correspond to the trigonal phase of the material previously observed in literature (PDF #00-017-0631),[22,23] and this assignment is confirmed via HRTEM, where (300) planes with a d-spacing of 2.8 Å are observed. Elemental analysis in Table 6.1 shows that samples are slightly rich in silver compared to expected stoichiometry; this may explain the presence of small secondary particles decorating the surface of the uniform particles in TEM images, which may consist of amorphous silver. Further work is underway to confirm the identity of these smaller particles.

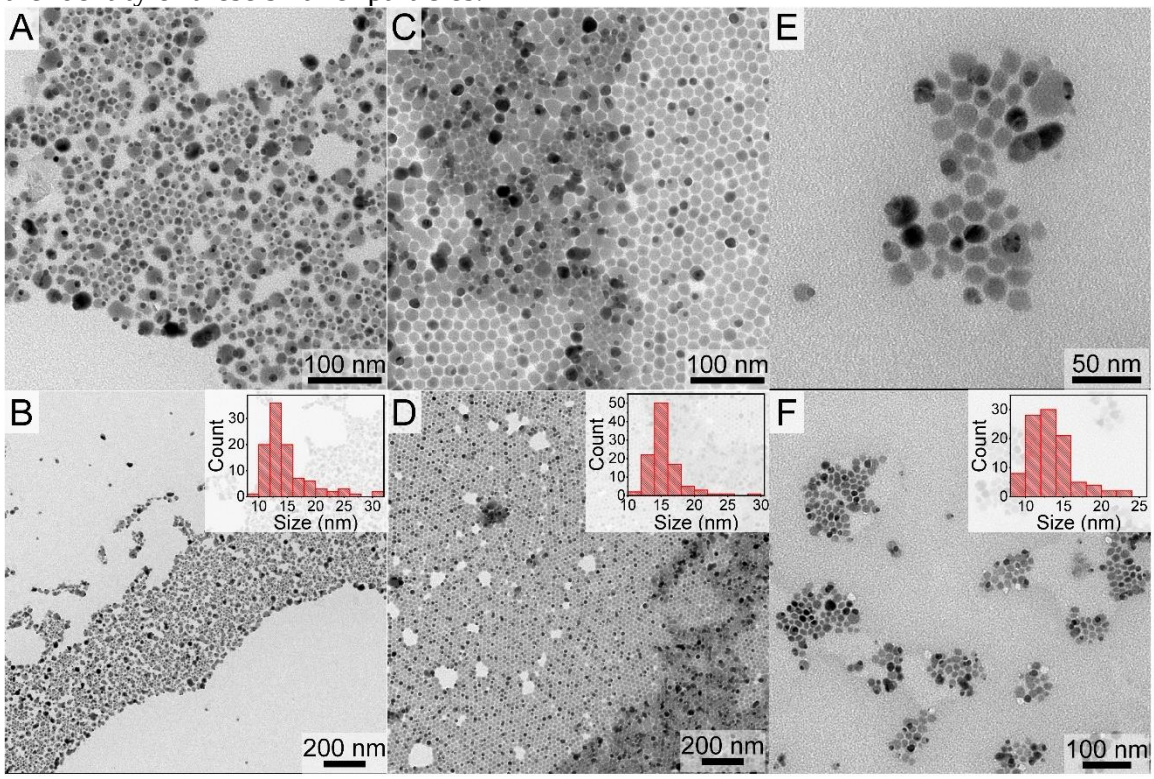

Figure 6.5 TEM images and size distributions from particle counting for a Tl_2AgBr_3 reaction held for 0 min at (A,B) 30 °C, (C,D) 70 °C, and (E,F) 110 °C. Reactions above 110 °C introduced a TlBr phase impurity to the nanocrystal product. Histograms of counted particles are in the inset of (B), (D), and (F).

Unlike in TlBr synthesis, Tl_2AgBr_3 nanocrystal size distribution does not vary much with reaction temperature. Figure 6.5 shows that nanocrystal size and shape is consistent in reactions carried out between 30-110 ^oC. At reaction temperatures greater than 140 ^oC, TlBr crystal impurities begin to appear in the XRD pattern of the reaction product. However, reaction time plays a crucial role in the uniformity of the nanocrystal product, seen in Figure 6.6. Nanocrystals characterized in Figure 6.4 were produced by quenching the reaction vessel in ice water immediately after TMSBr injection at 70 ^oC. Reactions carried at 110 ^oC that were quenched immediately after injection also show size uniformity, seen in Figures 6.5 E-F and 6.6 A-B. However, reactions carried out for 5 min at 110 ^oC, seen in Figure 6.6C-D, yield large aggregates in addition to more uniform nanocrystals. These particles tend to phase segregate when dried on a substrate or TEM grid, yet are difficult to separate from the rest of the product in solution. Yield at 5 min reaction time was 50%, higher than the 20% yield of a reaction that was immediately quenched in ice. Interestingly, reactions held for 30 min produced no nanocrystals, likely due to further aggregation.

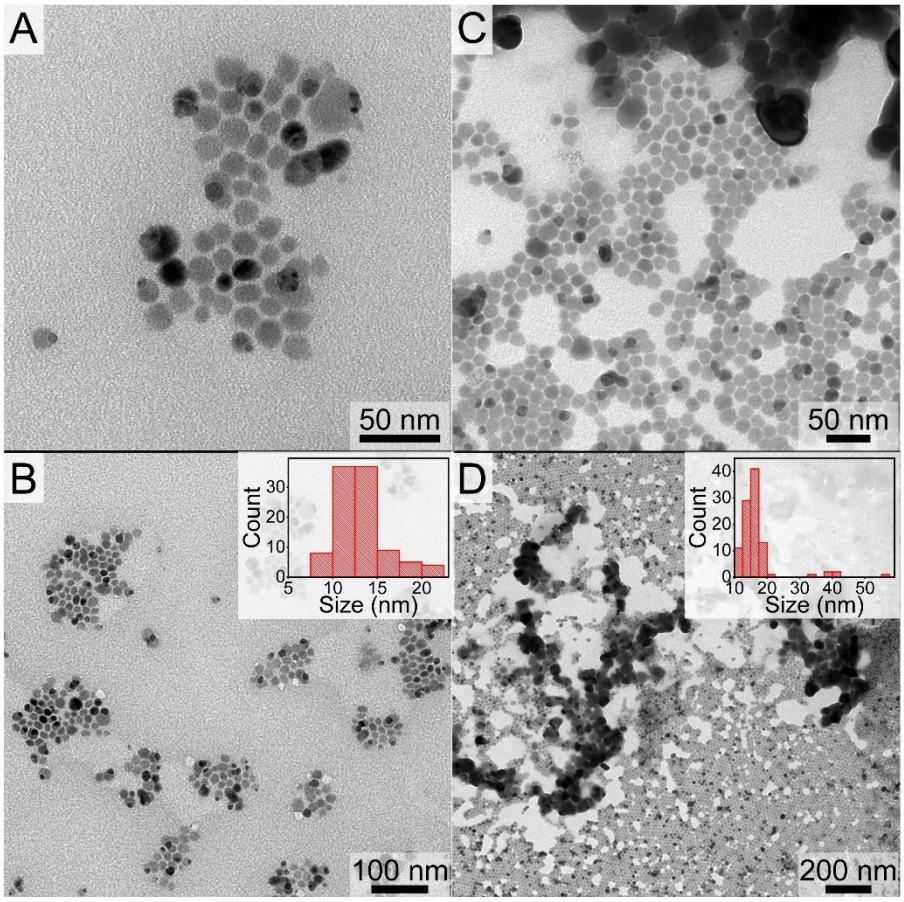

Figure 6.6 TEM images and size distributions from particle counting for a Tl_2AgBr_3 nanocrystal reaction at 110 ^oC held for (A,B) 0 min and (C,D) 5 min. Reactions held for 30 min did not yield dispersible nanocrystals. Histograms of counted particles are in the inset of (B) and (D).

In each of these reactions, the oxidation state of thallium is reduced from the 3+ state to the 1+ state. This makes sense in the case of TlBr, as anhydrous crystalline $TlBr_3$ has not been reported in literature due to its spontaneous decomposition via Eqn 6.2.[24-26]

$$TlBr_{3(s)} \rightarrow TlBr_{(s)} + Br_{2(l)} \quad (6.2)$$

However, tertiary and quaternary thallium (III) bromide crystals have been shown to be stable and not undergo this redox pathway,[2,26,27] and thallium (III) bromide can be complexed in solution without spontaneous thallium reduction.[28,29] Therefore, there is

likely something within the reaction itself that is causing the reduction of thallium. This challenge needs to be addressed for synthetic development of thallium (III) halide nanomaterials.

6.3.3 Optical characterization

Optical properties of TlBr and Tl_2AgBr_3 nanocrystals are characterized in Figure 6.7. Figure 6.7A shows that TlBr nanocrystals synthesized at 70 ^oC exhibit a first exciton peak at 3.1 eV, consistent with the bulk band gap of TlBr.[30,31] Figures 6.7B-C show Tauc plots of the Kubelka-Munk function of dried Tl_2AgBr_3 nanocrystal powder.[18] Kubelka-Munk analysis was used instead of solution absorbance due to the moderate degree of optical haze present in dispersions of Tl_2AgBr_3 nanocrystals in nonpolar solvents, which complicates band edge determination. From fitting of the Kubelka-Munk data to a Tauc function, Tl_2AgBr_3 is seen to have an indirect band gap of 3.0 eV. While this material is unsuitable for PV applications, its high indirect band gap may find use in radiation detectors with long carrier lifetimes or for RF transmitters. We could not conclude definitively if TlBr or Tl_2AgBr_3 nanocrystal samples emit light, as oleylamine and oleic acid emit strongly in the same spectral range as the expected luminescence of these nanocrystals.[15,32]

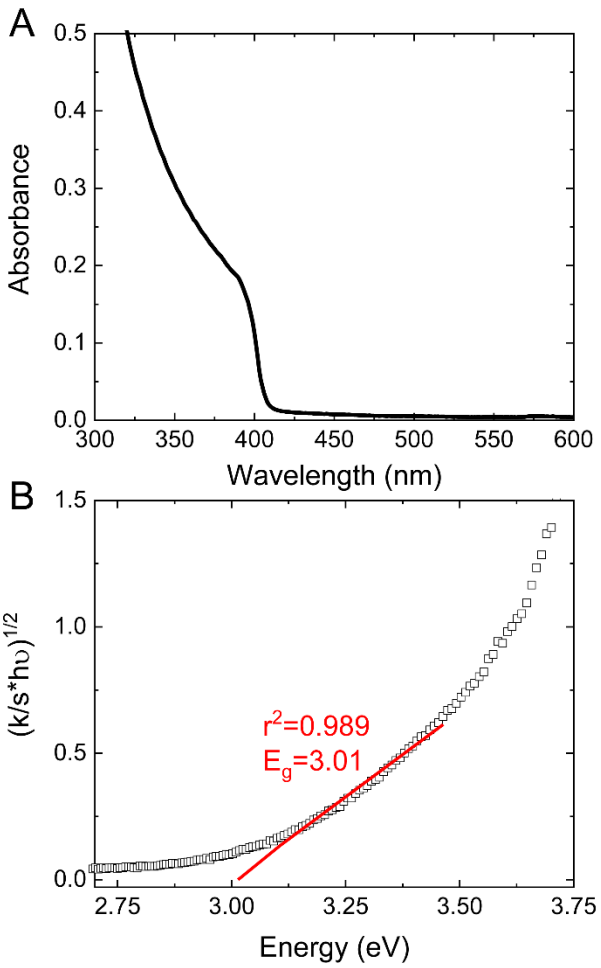

Figure 6.7 (A) Solution absorbance of TlBr nanocrystals synthesized at 70 °C for 5 min, exhibiting a weak exciton signal around 3.1 eV, consistent with reports of the band gap of bulk TlBr.[29,30] (B) Tauc analysis taken from the Kubelka-Munk curve of dried Tl_2AgBr_3 nanocrystals, showing nanocrystals exhibit an indirect band gap of 3.0 eV.

6.3.4 Self-assembly

Finally, preliminary characterization of the assembly of these uniform nanocrystals into nanocrystal superlattices is observed in Figure 6.8. SEM images of TlBr and Tl_2AgBr_3 nanocrystals in Figures 6.8A and 6.8B respectively show both nanocrystals form FCC assemblies when drop cast from toluene onto silicon substrates. However, the uniform size distribution observed in TEM images and by solution SAXS is lost, as large aggregates are seen in SEM images. Furthermore, these aggregates seem to increase in number when depositing more concentrated solutions of both TlBr and Tl_2AgBr_3 nanocrystals. This may be a result of particle aggregation when nanocrystals are dried from concentrated dispersions, limiting the extent of superlattice formation in both TlBr and Tl_2AgBr_3 nanocrystal films. The observation that TlBr and Tl_2AgBr_3 suspensions turn milky white within ~4 days of storage at 5 ^oC and within ~36 h at 20 ^oC demonstrates these nanocrystals are very susceptible to aggregation.

Nonetheless, TlBr nanocrystals still form extended superlattice networks which can be characterized in GISAXS/GIWAXS, seen in Figure 6.8C-D. GISAXS patterns show TlBr nanocrystals order into FCC superlattices with (111) orientation. GIWAXS patterns show rings corresponding to diffraction from TlBr, confirming XRD patterns in Figure 6.1D. An unidentified contaminant peak, which is also seen very subtly in Figure 6.1D, appears in the GIWAXS pattern in Figure 6.8D as well. This peak is difficult to identify, as it is low in intensity and the only peak in the XRD spectra that does not correspond to TlBr, but may be either the only noticeable peak of a contaminant TlI-type orthorhombic phase[15] or some other contaminant we cannot identify presently. Interestingly, TlBr crystal lattices do not seem to be as well-aligned in the superlattices as in other superlattice systems.[18,33] This may be in part due to aggregated particles outside of the superlattice structure having randomly oriented crystal domains or to the spherical nature of the

nanocrystals allowing for a variety of different crystal orientations while maintaining the superlattice structure. Tl_2AgBr_3 nanocrystals do not form extended superlattices which can be consistently detected in GISAXS.

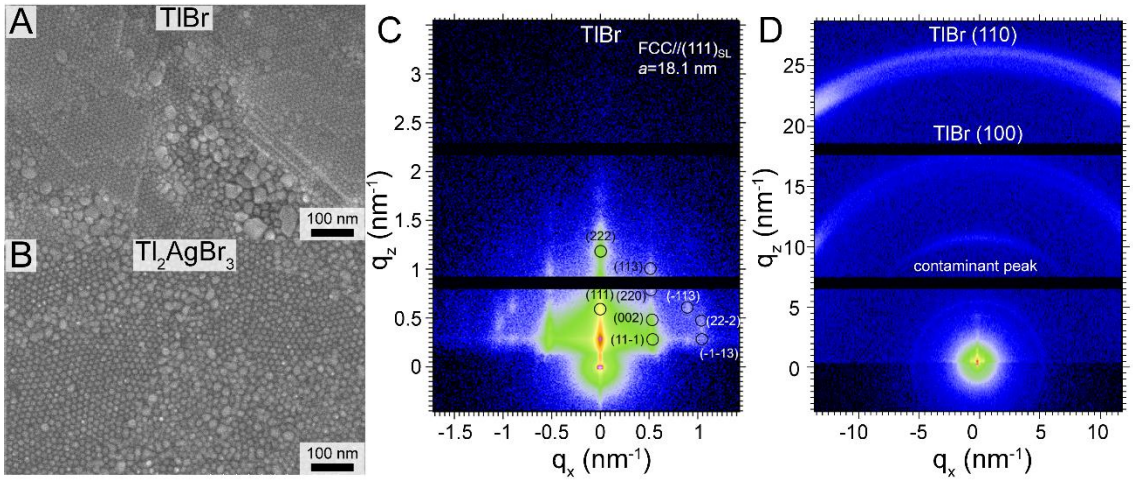

Figure 6.8 SEM images of (A) TlBr and (B) Tl_2AgBr_3 nanocrystal superlattices. Both nanocrystal systems exhibit some degree of ordering on substrates, but the extent of superlattice formation is inhibited by aggregates that form during drying. (C) GISAXS and (D) GIWAXS images of TlBr nanocrystal superlattices, showing that TlBr nanocrystals form an FCC superlattice with (111) orientation on the substrate. Tl_2AgBr_3 nanocrystals did not order with long enough range to consistently produce GISAXS patterns.

6.4 CONCLUSION

In conclusion, uniform TlBr and Tl_2AgBr_3 nanocrystals are synthesized via injection of TMSBr into a solution of thallium (III) acetate or thallium (III) acetate with silver (I) acetate, respectively. Limited size control of these particles is observed via manipulation of reaction temperature for TlBr and reaction time for Tl_2AgBr_3. Optical properties of the nanocrystals are characterized, and Tl_2AgBr_3 is reported to have an indirect band gap of 3.0 eV. Finally, we demonstrate assembly of TlBr nanocrystals into simple FCC superlattices on silicon substrates.

6.5 REFERENCES

(1) Vashishtha, P.; Metin, D. Z.; Cryer, M. E.; Chen, K.; Hodgkiss, J. M.; Gaston, N.; Halpert, J. E. Shape-, Size-, and Composition-Controlled Thallium Lead Halide Perovskite Nanowires and Nanocrystals with Tunable Band Gaps. *Chem. Mater.* **2018**, 30, 2973–2982.

(2) Slavney, A. H.; Leppert, L.; Saldivar Valdes, A.; Bartesaghi, D.; Savenije, T. J.; Neaton, J. B.; Karunadasa, H. Small-Bandgap Halide Double Perovskites. *Angew. Chem. Int. Ed.* **2018**, 57, 12765–12770.

(3) Deng, Z.; Wei, F.; Sun, S.; Kieslich, G.; Cheetham, A. K.; Bristowe, P. D. Exploring the Properties of Lead-Free Hybrid Double Perovskites Using a Combined Computational-Experimental Approach. *J. Mater. Chem. A* **2016**, 4, 12025–12029.

(4) Slavney, A. H.; Leppert, L.; Bartesaghi, D.; Gold-Parker, A.; Toney, M. F.; Savenije, T. J.; Neaton, J. B.; Karunadasa, H. I. Defect-Induced Band-Edge Reconstruction of a Bismuth-Halide Double Perovskite for Visible-Light Absorption. *J. Am. Chem. Soc.* **2017**, 139, 5015–5018.

(5) Xiao, Z.; Yan, Y.; Hosono, H.; Kamiya, T. Roles of Pseudo-Closed s^2 Orbitals for Different Intrinsic Hole Generation between Tl–Bi and In–Bi Bromide Double Perovskites. *J. Phys. Chem. Lett.* **2018**, 9, 258–262.

(6) Yakunin, S.; Dirin, D. N.; Shynkarenko, Y.; Morad, V.; Cherniukh, I.; Nazarenko, O.; Kreil, D.; Nauser, T.; Kovalenko, M. V. Detection of Gamma Photons Using Solution-Grown Single Crystals of Hybrid Lead Halide Perovskites. *Nat. Photonics* **2016**, 10, 585–589.

(7) Shah, K.S.; Lund, J.C.; Olschner, F.; Moy, L.; Squillante, M.R. Thallium Bromide Radiation Detectors. *IEEE Trans. Nucl. Sci.* **1989**, 36, 199–202.

(8) Hitomi, K.; Shoji, T.; Ishii, K. Advances in TlBr Detector Development. *J. Cryst. Growth* **2013**, 379, 93–98.

(9) Jesper Jacobsson, T.; Correa-Baena, J.-P.; Pazoki, M.; Saliba, M.; Schenk, K.; Grätzel, M.; Hagfeldt, A. Exploration of the Compositional Space for Mixed Lead Halogen Perovskites for High Efficiency Solar Cells. *Energy Environ. Sci.* **2016**, 9, 1706–1724.

(10) Notman, R.; den Otter, W. K.; Noro, M. G.; Briels, W. J.; Anwar, J. The Permeability Enhancing Mechanism of DMSO in Ceramide Bilayers Simulated by Molecular Dynamics. *Biophys. J.* **2007**, 93, 2056–2068.

(11) Voggu, V. R.; Sham, J.; Pfeffer, S.; Pate, J.; Fillip, L.; Harvey, T. B.; Brown, R. M.; Korgel, B. A. Flexible $CuInSe_2$ Nanocrystal Solar Cells on Paper. *ACS Energy Lett.* **2017**, 2, 574–581.

(12) Sanehira, E. M.; Marshall, A. R.; Christians, J. A.; Harvey, S. P.; Ciesielski, P. N.; Wheeler, L. M.; Schulz, P.; Lin, L. Y.; Beard, M. C.; Luther, J. M. Enhanced Mobility $CsPbI_3$ Quantum Dot Arrays for Record-Efficiency, High-Voltage Photovoltaic Cells. *Sci. Adv.* **2017**, 3, eaao4204.

(13) Wheeler, L. M.; Sanehira, E. M.; Marshall, A. R.; Schulz, P.; Suri, M.; Anderson, N. C.; Christians, J. A.; Nordlund, D.; Sokaras, D.; Kroll, T.; Harvey, S.P; Berry, J.J; Lin, L.Y; Luther, J.M. Targeted Ligand-Exchange Chemistry on Cesium Lead Halide Perovskite Quantum Dots for High-Efficiency Photovoltaics. *J. Am. Chem. Soc.* **2018**, 140, 10504–10513.

(14) Akhbari, K.; Morsali, A. A Thallium(I) Tetranuclear Cubic Cage Unit in an Interpenetrated Supramolecular Polymer: A New Precursor for the Preparation of Tl_2O_3 Nanostructures. *Polyhedron* **2011**, 30, 2459–2465.

(15) Mir, W. J.; Warankar, A.; Acharya, A.; Das, S.; Mandal, P.; Nag, A. Colloidal Thallium Halide Nanocrystals with Reasonable Luminescence, Carrier Mobility and Diffusion Length. *Chem. Sci.* **2017**, 8, 4602–4611.

(16) Sun, T.-W.; Xu, Q.-Y.; Zhang, X.-J.; Wu, Q.; Liu, Z.-S.; Kan, Q.-C.; Sun, C.-Y.; Wang, L. Management of Thallium Poisoning in Patients with Delayed Hospital Admission. *Clin. Toxicol.* **2012**, 50, 65–69.

(17) Holmberg, V. C.; Bogart, T. D.; Chockla, A. M.; Hessel, C. M.; Korgel, B. A. Optical Properties of Silicon and Germanium Nanowire Fabric. *J. Phys. Chem. C* **2012**, 116, 22486–22491.

(18) Paul Kubelka; Franz Munk. Ein Beitrag zur Optik der Farbenstriche. *Z. Tech. Phys.* **1931**, 12, 593–601.

(19) Korgel, B. A.; Fullam, S.; Connolly, S.; Fitzmaurice, D. Assembly and Self-Organization of Silver Nanocrystal Superlattices: Ordered "Soft Spheres." *J. Phys. Chem. B* **1998**, 102, 8379–8388.

(20) Creutz, S. E.; Crites, E. N.; De Siena, M. C.; Gamelin, D. R. Colloidal Nanocrystals of Lead-Free Double-Perovskite (Elpasolite) Semiconductors: Synthesis and Anion Exchange to Access New Materials. *Nano Lett.* **2018**, 18, 1118–1123.

(21) Protesescu, L.; Yakunin, S.; Bodnarchuk, M. I.; Krieg, F.; Caputo, R.; Hendon, C. H.; Yang, R. X.; Walsh, A.; Kovalenko, M. V. Nanocrystals of Cesium Lead Halide Perovskites ($CsPbX_3$, X=Cl, Br, and I): Novel Optoelectronic Materials Showing Bright Emission with Wide Color Gamut. *Nano Lett.* **2015**, 15, 3692–3696.

(22) H. Hirsch. The Co-Precipitation of Thallous Thallium in Photographic Emulsions. *J. Photogr. Sci.* **1963**, 11, 321–325.

(23) Hillebrecht, H.; Ade, M. Trimeric Units $[Ag_3X_8]^{5-}$ with Face-Sharing Polyhedra in the Series Tl_2AgX_3 (*X*=Cl, Br, I): Synthesis, Crystal Structure, and Vibrational Spectra: Trimeric Units $[Ag_3X_8]^{5-}$ with Face-Sharing Polyhedra in the Series Tl_2AgX_3 (*X*=Cl, Br, I): Synthesis, Crystal Structure, and Vibrational Spectra. *Z. Für Anorg. Allg. Chem.* **2018**, 644, 288–292.

(24) Allen J. Bard; Larry R. Faulkner. *Electrochemical Methods: Fundamentals and Applications*, 2nd ed.; John Wiley & Sons, Inc: New York, 2001.

(25) L. Schellhorn. *Dissertation*; University of Freiburg: Freiburg, 1987.

(26) Ackermann, R.; Hirschle, C.; Rotter, H. W.; Thiele, G. Mixed-Valence Thallium(I,III) Bromides The Crystal Structure of α-Tl_2Br_3. *Z Anorg Allg Chem* **2002**, 628, 2675-2682.

(27) Zimmermann, K.; Thiele, G. Polymorphie von $Cs_3Tl_2Br_9$. *Z. Naturforsch. B* **1987**, 42, 818–824.

(28) Blixt, J.; Glaser, J.; Mink, J.; Persson, I.; Persson, P.; Sandstroem, M. Structure of Thallium(III) Chloride, Bromide, and Cyanide Complexes in Aqueous Solution. *J. Am. Chem. Soc.* **1995**, 117, 5089–5104.

(29) Banyai, I.; Glaser, J. Equilibrium Dynamics in the Thallium(III)-Bromide System in Acidic Aqueous Solution. A Thallium-205 NMR Study. *J. Am. Chem. Soc.* **1990**, 112, 4703–4710.

(30) Heidrich, K.; Staude, W.; Treusch, J.; Overhof, H. Optical Properties and Electronic Structure of Polymorphous TlCl and TlBr. *Phys. Rev. Lett.* **1974**, 33, 1220–1223.

(31) Bachrach, R. Z.; Brown, F. C. Exciton-Optical Properties of TlBr and TlCl. *Phys. Rev. B* **1970**, 1, 818–831.

(32) Kennaway, E. L.; Hieger, I. Carcinogenic Substances and their Fluorescence Spectra. *BMJ* **1930**, 1, 1044–1046.

(33) Guillaussier, A.; Yu, Y.; Voggu, V. R.; Aigner, W.; Cabezas, C. S.; Houck, D. W.; Shah, T.; Smilgies, D.-M.; Pereira, R. N.; Stutzmann, M.; Korgel, B.A. Silicon Nanocrystal Superlattice Nucleation and Growth. *Langmuir* **2017**, 33, 13068–13076.

Chapter 7: Conclusions and Future Direction

7.1 Conclusions

Hybird organic-inorganic perovskites (HOIPs) have tremendous potential to make a significant impact in the greentech industry. Perovskites for PV have been studied for only a decade, and already their reach is tremendous. While issues with HOIPs still exist, the field is rapidly working towards effective solutions. I am confident that with another decade, perovskites will be a ubiquitous technology in the optoelectronic and semiconductor industries.

7.1.1 Humidity Interactions with Water Vapor-Book 1

In chapter 2, bismuth was studied as a new HOIP additive to improve humidity stability at high humidity levels. However, bismuth incorporation decreased humidity stability at more moderate humidity levels in the first example of an additive having both a stabilizing and destabilizing effect on the humidity stability of a HOIP. By measuring degradation rates using UV-Vis-NIR absorbance spectroscopy and the Avrami model,[1] it was determined that degradation at low and high humidity was proceeding by different reaction paths, confirming the mechanism reported previously in literature.[2] These results demonstrated that additives do not impact humidity stability uniformly across all humidity conditions and provided a framework for designing accelerated aging tests moving forward.

In chapter 3, the humidity instability of HOIPs and related metal halides was applied for smart window applications, using thin films of nickel iodide as a model system. A deliquescent chromic transition that could be reversibly cycled between dark and clear states with uniform transmission modulation over the entire visible spectrum was observed. This transition demonstrated reversibility around a mild transition temperature (~30 ^{o}C)

and was shown to be stable over many cycles. Characterization showed this was a humidity-induced transition, with water being taken up in nickel iodide films in a ~10:1 water:nickel iodide molar ratio during the dark-to-clear transition. Finally, this transition was shown to be somewhat arrested when employing a temperature ramp rate greater than 1 ^{o}C/min, and thickness-limited, with films >1 μm thick exhibiting no optical modulation.

7.1.2 CdTe-HOIP Tandem Cells-Book 2

Chapter 4 explored the feasibility of CdTe-HOIP tandem cells. Potential tandem architectures were vetted, and a four-terminal CdTe-HOIP tandem design utilizing wide band gap HOIP methylammonium lead bromide (MAPBr) was determined to be the most optimal tandem architecture given the current state of the technology. Additionally, a need for low band gap HOIP materials for ideal tandem pairing with CdTe was identified. Initial semitransparent MAPBr PVs were constructed, and a large degree of optical loss in the HOIP layer was identified and characterized as optical haze localized on surface morphology features (i.e. "wrinkles") via DIC microscopy. Finally, SCAPS simulations determined the degree of optical loss or haze in the top layer that would be tolerable in practical tandem devices with CdTe, MAPI, a-Si, and CIGS bottom cells.[3]

In chapter 5, the addition of Ag^{+} to thin films of MAPBr was shown to induce uniform crystal ordering in the (100) direction of MAPBr thin films. Depth profiling of the elemental composition of the thin film revealed that Ag^{+} likely induces this ordering via preferential surface attachment at interfaces, which lowers the surface energy of (100) surfaces relative to other surface facets. However, increased silver content is shown to significantly reduce PCE in PV devices due to phase segregation of Ag-rich domains and had little to no effect on photoluminescence properties.

Chapter 6 detailed a new synthetic method to fabricate TlBr nanocrystals and demonstrated a synthetic path to Tl_2AgBr_3 nanoparticles, the first Tl_2AgBr_3 nanocrystal synthesis reported thus far in literature. Monodisperse TlBr and Tl_2AgBr_3 nanocrystals were synthesized via injection of a bromide precursor into a solution of thallium (III) acetate (and silver (I) acetate for Tl_2AgBr_3). Size control was demonstrated for the TlBr nanocrystal synthesis, with smaller nanoparticles forming at higher reaction temperatures. TlBr nanoparticles with high monodispersity also were shown to self-assemble into extended FCC superlattices. Interestingly, this superlattice formation did not occur in Tl_2AgBr_3 nanocrystals, as concentrated suspensions of nanoparticles aggregated during drying. Finally, the optical properties of Tl_2AgBr_3 were characterized for the first time, and it was determined that Tl_2AgBr_3 had an indirect band gap of ~3.0 eV.

7.2 Future Directions

The field of hybrid organic-inorganic perovskites moves with such pace and vigor that this section will likely be laughably outdated by the time the hold on this thesis expires. Nonetheless, there are follow-ups to the work here presented that would be of interest to the general community and could help make the progress presented here relevant to a broader audience.

7.2.1 Development of accelerated aging protocols

Chapter 2 detailed how changes in composition of HOIP thin films can have a different impact on stability behavior depending on the exact humidity level. Accelerating aging tests, on which the stability of PV modules is assessed, assume the opposite to be true, with many tests using elevated humidity levels as an environmental accelerant. For example, standard aging test IEC 61215[4] involves humidity ramping tests to 85% RH and

a damp heat test at 85% RH and 85 ºC for 1000 h as a way of simulating how a solar module will behave for longer durations of time at more moderate humidity. However, from our most recent work, aging above ~70-80% RH may not be reflective of true PV stability, as the decomposition pathway above this threshold changes. Therefore, as the perovskite industry continues to grow and commercialize, there is a great need to develop accelerating aging tests that are appropriate for perovskite PVs and which reflect the real-world stability of HOIP solar cells.

7.2.2 Low band gap HOIPs

Chapter 6 acts as a first step towards the development of low band gap halide perovskite $Cs_2AgTlBr_6$, which with a band gap of 0.95 eV is the lowest band gap HaP synthesized to date.[5] Nanocrystal synthesis is important for the future implementation of this material system for two reasons: (1) to allow for facile thin film processing, and (2) to avoid complexes of thallium with skin-porous carrier molecules. This second step is very important for safety concerns, not just in industry, but in a lab scale as well. Traditional HOIPs, as seen in the experimental sections of Chapters 2-5, routinely rely on metal halide complexes with dimethylsulfoxide (DMSO) to solubilize the metal halides in dimethylformamide (DMF). However, DMSO is readily taken up through the skin, and can permeate (to some extent) most disposable gloves. DMSO can, in this way, carry heavy metals in small quantities through the skin via transport of DMSO complexes.[6] When using thallium, one of the most toxic elements known to man, this is untenable. Perhaps in the future, vacuum processing technology could be used to deposit thin films of $Cs_2AgTlBr_6$, but for solution processed systems, the only safe, responsible way to process thin films of $Cs_2AgTlBr_6$ appears to be through nanoparticle formation and deposition.

Within this motif, results presented in Chapter 6 reveal an interesting problem: thallium (III) is reduced when it is exposed to the reaction mixture commonly used to make perovskite nanocrystals.[7] Finding a way to fabricate nanoparticles without reduction of the Tl (III) to Tl (I) seems to be an important scientific challenge moving forward. Once this challenge is completed and $Cs_2AgTlBr_6$ nanoparticles are synthesized, other questions arise. Can we expand to new materials synthesis via halide exchange?[8] Can we synthesize nanoparticles with different A-sites?[9] What is the band gap tunability of these nanocrystals? Do they exhibit interesting photophysical properties the wider band gap perovskites do not have access to? Such interesting questions provide a wealth of further research direction.

Furthermore, new materials discovery can be utilized to synthesize new materials with lower band gaps. Already, Cu-doped $Cs_2AgSbCl_6$ has been synthesized and shown to have an optical band gap of ~1.0 eV.[10] Whether this reduced optical gap is truly due to electronic band-to-band transitions or merely the result of a shallow dopant state as in Bi-doped MAPI[11] is yet to be determined. However, additional doping to achieve low band gaps is worth consideration, given its success thus far.

7.2.3 CdTe Tandem Cell Realization

While initial work in Chapter 4 focused on the theoretical development of CdTe-HOIP tandems, efficient CdTe-HOIP tandems have not yet been developed. Chapter 4 provides a roadmap for development of 4-terminal tandems with a smooth, transparent MAPBr top cell. However, the more promising-and scientifically interesting- path forward is development of lower band gap HOIPs. As seen in Figure 4.1, the ideal HOIP for matching with CdTe in a tandem cell would have a band gap of ~0.85 eV. Development of lower band gap HOIPs as described in section 7.2.2 would allow for this ideal band gap

pairing, and may have greater potential for tandem cell applications. First, materials suitable for tandems must be realized. Then, safe and uniform thin film processing methods must be developed, and optimal electron- and hole-selective contact materials must be found and implemented for effective single junction PV architectures employing these low band gap HOIPs. Finally, replacing the opaque metallic top contact with a TCO would allow for HOIP-CdTe tandems with optimized band gaps.

7.2.4 Multiexciton Generation in HOIP PVs

These low band gap HOIP PVs, processed in nanocrystal form, may also lead to solar cells with efficient multiple exciton generation, which would allow standalone cells to break the Shockley-Queisser limit. As described in the introductory chapter, multiple exciton generation is the phenomenon by which one photon of incident light with energy equal to at least twice the band gap of the material is absorbed, creating an electron-hole pair. When this pair relaxes, it excites a second electron from the valence band across the band gap, generating two electrons from one incident photon.[12] MEG is extremely inefficient in bulk semiconductors, but has been observed in a variety of quantum-confined nanocrystal systems.[12] Current HOIP NCs may exhibit MEG; however, due to their wide band gaps, potential increases in solar cell current are insignificantly low. However, if lower band gap HOIPs were produced, MEG may significantly increase current generation in a device, allowing nanocrystal HOIP PVs to break the Shockley-Queisser limit in a substantial way. Work needs to be carried forward to first synthesize these particles, then characterize if MEG occurs in the standalone nanocrystals, and finally to see if the MEG is efficient enough to be realized in devices operating at real-world conditions.

7.3 REFERENCES

(1) Avrami, M. Kinetics of Phase Change. I General Theory. *J. Chem. Phys.* **1939**, *7*, 1103–1112.

(2) Christians, J. A.; Miranda Herrera, P. A.; Kamat, P. V. Transformation of the Excited State and Photovoltaic Efficiency of $CH_3NH_3PbI_3$ Perovskite upon Controlled Exposure to Humidified Air. *J. Am. Chem. Soc.* **2015**, *137*, 1530–

(3) Burgelman, M.; Nollet, P.; Degrave, S. Modelling Polycrystalline Semiconductor Solar Cells. *Thin Solid Films* **2000**, *361–362*, 527–532.

(4) Matsui, T.; Yamamoto, T.; Nishihara, T.; Morisawa, R.; Yokoyama, T.; Sekiguchi, T.; Negami, T. Compositional Engineering for Thermally Stable, Highly Efficient Perovskite Solar Cells Exceeding 20% Power Conversion Efficiency with 85 °C/85% 1000 h Stability. *Adv. Mater.* **2019**, *31*, 1806823.

(5) Slavney, A. H.; Leppert, L.; Saldivar Valdes, A.; Bartesaghi, D.; Savenije, T. J.; Neaton, J. B.; Karunadasa, H. Small-Bandgap Halide Double Perovskites. *Angew. Chem. Int. Ed.* **2018**, *57*, 12765–12770.

(6) Notman, R.; den Otter, W. K.; Noro, M. G.; Briels, W. J.; Anwar, J. The Permeability Enhancing Mechanism of DMSO in Ceramide Bilayers Simulated by Molecular Dynamics. *Biophys. J.* **2007**, *93*, 2056–2068.

(7) Protesescu, L.; Yakunin, S.; Bodnarchuk, M. I.; Krieg, F.; Caputo, R.; Hendon, C. H.; Yang, R. X.; Walsh, A.; Kovalenko, M. V. Nanocrystals of Cesium Lead Halide Perovskites ($CsPbX_3$, X = Cl, Br, and I): Novel Optoelectronic Materials Showing Bright Emission with Wide Color Gamut. *Nano Lett.* **2015**, *15*, 3692–3696.

(8) Creutz, S. E.; Crites, E. N.; De Siena, M. C.; Gamelin, D. R. Colloidal Nanocrystals of Lead-Free Double-Perovskite (Elpasolite) Semiconductors: Synthesis and Anion Exchange To Access New Materials. *Nano Lett.* **2018**, *18*, 1118–1123.

(9) Protesescu, L.; Yakunin, S.; Kumar, S.; Bär, J.; Bertolotti, F.; Masciocchi, N.; Guagliardi, A.; Grotevent, M.; Shorubalko, I.; Bodnarchuk, M. I.; et al. Dismantling the "Red Wall" of Colloidal Perovskites: Highly Luminescent Formamidinium and Formamidinium–Cesium Lead Iodide Nanocrystals. *ACS Nano* **2017**, *11*, 3119–3134.

(10) Karmakar, A.; Dodd, M. S.; Agnihotri, S.; Ravera, E.; Michaelis, V. K. Cu(II)-Doped $Cs_2SbAgCl_6$ Double Perovskite: A Lead-Free, Low-Bandgap Material. *Chem. Mater.* **2018**, *30*, 8280–8290.

(11) Mosconi, E.; Merabet, B.; Meggiolaro, D.; Zaoui, A.; De Angelis, F. First-Principles Modeling of Bismuth Doping in the $MAPbI_3$ Perovskite. *J. Phys. Chem. C* **2018**, *122*, 14107-14112.

(12) Stolle, C. J.; Schaller, R. D.; Korgel, B. A. Efficient Carrier Multiplication in Colloidal $CuInSe_2$ Nanocrystals. *J. Phys. Chem. Lett.* **2014**, *5*, 3169–3174.

References

Abdelhady, A. L.; Saidaminov, M. I.; Murali, B.; Adinolfi, V.; Voznyy, O.; Katsiev, K.; Alarousu, E.; Comin, R.; Dursun, I.; Sinatra, L.; et al. Heterovalent Dopant Incorporation for Bandgap and Type Engineering of Perovskite Crystals. *J. Phys. Chem. Lett.* **2016**, 7, 295–301.

Abdi-Jalebi, M.; Pazoki, M.; Philippe, B.; Dar, M. I.; Alsari, M.; Sadhanala, A.; Divitini, G.; Imani, R.; Lilliu, S.; Kullgren, J.; Rensmo, H.; Grätzel, M.; Friend, R. H. Dedoping of Lead Halide Perovskites Incorporating Monovalent Cations. *ACS Nano* **2018**, *12*, 7301–7311.

Ackermann, R.; Hirschle, C.; Rotter, H. W.; Thiele, G. Mixed-Valence Thallium(I,III) Bromides The Crystal Structure of α-Tl_2Br_3. *Z Anorg Allg Chem* **2002**, 628, 2675-2682.

Adhyaksa, G.W.P.; Johlin, E.; Garnett, E.C. Nanoscale Back Contact Perovskite Solar Cell Design for Improved Tandem Efficiency. *Nano Lett.*, **2017**, 17, 5206–5212.

Adjokatse, S.; Fang, H.-H.; Loi, M. A. Broadly Tunable Metal Halide Perovskites for Solid-State Light-Emission Applications. *Mater. Today* **2017**, 20, 413–424.

Ahn, N.; Son, D.-Y.; Jang, I.-H.; Kang, S. M.; Choi, M.; Park, N.-G. Highly Reproducible Perovskite Solar Cells with Average Efficiency of 18.3% and Best Efficiency of 19.7% Fabricated via Lewis Base Adduct of Lead(II) Iodide. *J. Am. Chem. Soc.* **2015**, 137, 8696–8699.

Akhbari, K.; Morsali, A. A Thallium(I) Tetranuclear Cubic Cage Unit in an Interpenetrated Supramolecular Polymer: A New Precursor for the Preparation of Tl_2O_3 Nanostructures. *Polyhedron* **2011**, 30, 2459–2465.

Al-Abadleh, H. A.; Grassian, V. H. FT-IR Study of Water Adsorption on Aluminum Oxide Surfaces. *Langmuir* **2002**, 19, 341–347.

Alberti, A.; Deretzis, I.; Mannino, G.; Smecca, E.; Sanzaro, S.; Numata, Y.; Miyasaka, T.; La Magna, A. Revealing a Discontinuity in the Degradation Behavior of $CH_3NH_3PbI_3$ during Thermal Operation. *J. Phys. Chem. C*, **2017**, 121, 13577–13585.

Albrecht, S.; Saliba, M.; Correa Baena, J.P.; Lang, F.; Kegelmann, L.; Mews, M.; Steier, L.; Abate, A.; Rappich, J.; Korte, L.; Schlatmann, R.; Nazeeruddin, M.K.; Hagfeldt, A.; Grätzel, M.; Rech, B. Monolithic perovskite/silicon-heterojunction tandem solar cells processed at low temperature. *Energy Env. Sci.*, **2016** 9, 81–88.

Albrecht, S.; Saliba, M.; Correa-Baena, J.P.; Jäger, K.; Korte, L.; Hagfeldt, A.; Grätzel, M.; Rech, B. Towards optical optimization of planar monolithic perovskite/silicon-heterojunction tandem solar cells. *J. Opt.*, **2016** 18, 064012.

Allen J. Bard; Larry R. Faulkner. *Electrochemical Methods: Fundamentals and Applications*, 2nd ed.; John Wiley & Sons, Inc: New York, 2001.

Alsema, E.A.; de Wild-Scholten, M.J. Environmental Impacts of PV Electricity Generation- a Critical Comparison of Energy Supply Options. *21st European Photovoltaics Conference*. **2006**, 21

Amat, A.; Mosconi, E.; Ronca, E.; Quarti, C.; Umari, P.; Nazeeruddin, M. K.; Grätzel, M.; De Angelis, F. Cation-Induced Band-Gap Tuning in Organohalide Perovskites: Interplay of Spin–Orbit Coupling and Octahedra Tilting. *Nano Lett.* **2014**, 14, 3608–3616.

Anderson, C. D.; Broekhuis, M. D.; Byker, H. J.; DeJong, S. J. Color Neutral Thermochromic Layers and Laminates. US 9,465,239, October 11, 2016.

Anderson, C. D.; Harlan J. Byker; De Jong, S. J.; Lameris, J. L.; Winkle, D. D. Anti-Yellowing for Thermochromic Systems. US 8,623,243 B2, January 7, 2014.

ASTM International, 2015. Standard Test Method for Reflection Haze of High-Gloss Surfaces. ASTM International.

Aswal, D. K.; Gupta, S. K.; Debnath, A. K.; Kothiyal, G. P.; Sabharwal, S. C.; Gupta, M. K. Preparation of Adherent Y-Ba-Cu-O Thick Films and the Effect of Silver Doping. *Supercond. Sci. Technol.* **1991**, *4*, 188–191.

Avrami, M. Kinetics of Phase Change. I General Theory. *J. Chem. Phys.* **1939**, *7*, 1103–1112.

Ba, L.; Liu, H.; Shen, W. Perovskite/c-Si tandem solar cells with realistic inverted architecture: Achieving high efficiency by optical optimization. *Prog. Photovolt. Res. Appl.*, **2018**, 26, 924-933.

Bachrach, R. Z.; Brown, F. C. Exciton-Optical Properties of TlBr and TlCl. *Phys. Rev. B* **1970**, 1, 818–831.

Back, H.; Kim, G.; Kim, J.; Kong, J.; Kim, T. K.; Kang, H.; Kim, H.; Lee, J.; Lee, S.; Lee, K. Achieving Long-Term Stable Perovskite Solar Cells via Ion Neutralization. *Energy Environ. Sci.* **2016**, *9*, 1258–1263.

Bailie, C.D.; Christoforo, M.G.; Mailoa, J.P.; Bowring, A.R.; Unger, E.L.; Nguyen, W.H.; Burschka, J.; Pellet, N.; Lee, J.Z.; Grätzel, M.; Noufi, R.; Buonassisi, T.; Salleo, A.; McGehee, M.D. Semi-transparent perovskite solar cells for tandems with silicon and CIGS. *Energy Env. Sci.*, **2015**, 8, 956–963.

Banyai, I.; Glaser, J. Equilibrium Dynamics in the Thallium(III)-Bromide System in Acidic Aqueous Solution. A Thallium-205 NMR Study. *J. Am. Chem. Soc.* **1990**, 112, 4703–4710.

Bella, F.; Griffini, G.; Correa-Baena, J.-P.; Saracco, G.; Grätzel, M.; Hagfeldt, A.; Turri, S.; Gerbaldi, C. Improving Efficiency and Stability of Perovskite Solar Cells with Photocurable Fluoropolymers. *Science* **2016**, 354, 203-206.

Berhe, T. A.; Su, W.-N.; Chen, C.-H.; Pan, C.-J.; Cheng, J.-H.; Chen, H.-M.; Tsai, M.-C.; Chen, L.-Y.; Dubale, A. A.; Hwang, B.-J. Organometal Halide Perovskite Solar Cells: Degradation and Stability. *Energy Env. Sci* **2016**, 9, 323–356.

Bett, A.J.; Schulze, P.S.C.; Winkler, K.; Gasparetto, J.; Ndione, P.F.; Bivour, M.; Hinsch, A.; Kohlstädt, M.; Lee, S.; Mastroianni, S.; Mundt, L.E.; Mundus, M.; Reichel, C.; Richter, A.; Veit, C.; Wienands, K.; Würfel, U.; Veurman, W.; Glunz, S.W.; Hermle, M.; Goldschmidt, J.C. Low temperature perovskite solar cells with an evaporated TiO_2 compact layer for perovskite silicon tandem solar cells. *Energy Procedia*, **2017**, 124, 567–576.

Bhattacharya, R.; Ghosh, A. Thermal Analysis of Pyridinium Tetrachloronickelate(II); Tetrahedral Octahedral Structural Transformation. *J. Chem. Res.* **2001**, 332–333.

Blixt, J.; Glaser, J.; Mink, J.; Persson, I.; Persson, P.; Sandstroem, M. Structure of Thallium(III) Chloride, Bromide, and Cyanide Complexes in Aqueous Solution. *J. Am. Chem. Soc.* **1995**, 117, 5089–5104.

Braunger, S.; Mundt, L.E.; Wolff, C.M.; Mews, M.; Rehermann, C.; Jošt, M.; Tejada, A.; Eisenhauer, D.; Becker, C.; Guerra, J.A.; Unger, E.; Korte, L.; Neher, D.; Schubert, M.C.; Rech, B.; Albrecht, S. $Cs_xFA_{1-x}Pb(I_{1-y}Br_y)_3$ Perovskite Compositions: the Appearance of Wrinkled Morphology and its Impact on Solar Cell Performance. *J. Phys. Chem. C*, **2018**, 122, 17123–17135.

Brown, G.F.; Wu, J. Third generation photovoltaics. *Laser Photonics Rev.*, **2009**, 3, 394–405.

Burgelman, M.; Nollet, P.; Degrave, S. Modelling Polycrystalline Semiconductor Solar Cells. *Thin Solid Films* **2000**, *361–362*, 527–532.

Burschka, J.; Pellet, N.; Moon, S.-J.; Humphry-Baker, R.; Gao, P.; Nazeeruddin, M. K.; Grätzel, M. Sequential Deposition as a Route to High-Performance Perovskite-Sensitized Solar Cells. *Nature* **2013**, 499, 316–319.

Bush, K.A.; Bailie, C.D.; Chen, Y.; Bowring, A.R.; Wang, W.; Ma, W.; Leijtens, T.; Moghadam, F.; McGehee, M.D. Thermal and Environmental Stability of Semi-Transparent Perovskite Solar Cells for Tandems Enabled by a Solution-Processed Nanoparticle Buffer Layer and Sputtered ITO Electrode. *Adv. Mater.*, **2016**, 28, 3937–3943.

Bush, K.A.; Palmstrom, A.F.; Yu, Z.J.; Boccard, M.; Cheacharoen, R.; Mailoa, J.P.; McMeekin, D.P.; Hoye, R.L.Z.; Bailie, C.D.; Leijtens, T.; Peters, I.M.; Minichetti, M.C.; Rolston, N.; Prasanna, R.; Sofia, S.; Harwood, D.; Ma, W.; Moghadam, F.; Snaith, H.J.; Buonassisi, T.; Holman, Z.C.; Bent, S.F.; McGehee, M.D. 23.6%-efficient monolithic perovskite/silicon tandem solar cells with improved stability. *Nat. Energy*, **2017**, 2, 17009.

Bush, K.A.; Rolston, N.; Gold-Parker, A.; Manzoor, S.; Hausele, J.; Yu, Z.J.; Raiford, J.A.; Cheacharoen, R.; Holman, Z.C.; Toney, M.F.; Dauskardt, R.H.; McGehee, M.D. Controlling Thin-Film Stress and Wrinkling during Perovskite Film Formation. *ACS Energy Lett.*, **2018**, 3, 1225–1232.

Bussière, G.; Beaulac, R.; Cardinal-David, B.; Reber, C. Coupled Electronic States in trans-$MCl_2(H_2O)_4^{n+}$ Complexes (M: Ni^{2+}, Co^{2+}, V^{3+}, Cr^{3+}) Probed by Absorption and Luminescence Spectroscopy. *Coord. Chem. Rev.* **2001**, 219–221, 509–543.

Byker, H. J.; Ogburn Jr., P. H.; Vander Griend, D. A.; Winkle, D. D. Ligand Exchange Thermochromic Systems Containing Exchange Metals. US 7,538,931 B2, May 26, 2009.

Byker, H.J; Ogburn Jr, P.H.; Vander Griend, D. A.; Veldkamp, B.S.; Winkle, D.D. Ligand Exchange Thermochromic Systems and High Epsilon Ligands for Same. US 8,182,718 B2, May 22, 2012.

Cariati, F.; Bruni, S.; Martini, M.; Spinolo, G. Raman and Infrared Spectra of $NiI_2 \bullet 6H_2O$. *J. Raman Spectrosc.* **1991**, 22, 397–401.

Castle, J. E.; Chapman-Kpodo, H.; Proctor, A.; Salvi, A. M. Curve-Fitting in XPS Using Extrinsic and Intrinsic Background Structure. *J. Electron Spectrosc. Relat. Phenom.* **2000**, *106*, 65–80.

Celio, H. Interface Designed with Differential Pumping and Built-in Figure of Merit to Monitor Chambers Where Environmentally Sensitive Samples Are Prepared or Transferred for Analysis. 9,945,761 B2, April 17, 2018.

Chae, J.; Dong, Q.; Huang, J.; Centrone, A. Chloride Incorporation Process in $CH_3NH_3PbI_{3-x}Cl_x$ Perovskites via Nanoscale Bandgap Maps. *Nano Lett.* **2015**, 15 (12), 8114–8121.

Chelvanathan, P.; Hossain, M.I.; Amin, N. Performance analysis of copper–indium–gallium–diselenide (CIGS) solar cells with various buffer layers by SCAPS. *Curr. Appl. Phys.*, **2010**, 10, S387–S391.

Chen, A. Z.; Shiu, M.; Deng, X.; Mahmoud, M.; Zhang, D.; Foley, B. J.; Lee, S.-H.; Giri, G.; Choi, J. J. Understanding the Formation of Vertical Orientation in Two-Dimensional Metal Halide Perovskite Thin Films. *Chem. Mater.* **2019**, *31*, 1336-1343.

Chen, A. Z.; Shiu, M.; Ma, J. H.; Alpert, M. R.; Zhang, D.; Foley, B. J.; Smilgies, D.-M.; Lee, S.-H.; Choi, J. J. Origin of Vertical Orientation in Two-Dimensional Metal Halide Perovskites and Its Effect on Photovoltaic Performance. *Nat. Commun.* **2018**, *9*, 1336.

Chen, B.; Bai, Y.; Yu, Z.; Li, T.; Zheng, X.; Dong, Q.; Shen, L.; Boccard, M.; Gruverman, A.; Holman, Z.; Huang, J. Efficient Semitransparent Perovskite Solar Cells for 23.0%-Efficiency Perovskite/Silicon Four-Terminal Tandem Cells. *Adv. Energy Mater.*, **2016**, 6, 1601128.

Chen, C.; Liu, D.; Zhang, B.; Bi, W.; Li, H.; Jin, J.; Chen, X.; Xu, L.; Song, H.; Dai, Q. Carrier Interfacial Engineering by Bismuth Modification for Efficient and Thermoresistant Perovskite Solar Cells. *Adv. Energy Mater.* **2018**, 8, 1703659.

Chen, C.-C.; Bae, S.-H.; Chang, W.-H.; Hong, Z.; Li, G.; Chen, Q.; Zhou, H.; Yang, Y. Perovskite/polymer monolithic hybrid tandem solar cells utilizing a low-temperature, full solution process. *Mater. Horiz.*, **2015**, 2, 203–211.

Chen, J.; Morrow, D. J.; Fu, Y.; Zheng, W.; Zhao, Y.; Dang, L.; Stolt, M. J.; Kohler, D. D.; Wang, X.; Czech, K. J.; Hautzinger, M. P.; Shen, S.; Guo, L.; Pan, A.; Wright, J. C.; Jin, S. Single-Crystal Thin Films of Cesium Lead Bromide Perovskite Epitaxially Grown on Metal Oxide Perovskite ($SrTiO_3$). *J. Am. Chem. Soc.* **2017**, *139*, 13525–13532.

Chen, Q.; Chen, L.; Ye, F.; Zhao, T.; Tang, F.; Rajagopal, A.; Jiang, Z.; Jiang, S.; Jen, A. K.-Y.; Xie, Y.; Cai, J.; Chen, L. Ag-Incorporated Organic–Inorganic Perovskite Films and Planar Heterojunction Solar Cells. *Nano Lett.* **2017**, *17*, 3231–3237.

Chen, W.; Zhang, J.; Xu, G.; Xue, R.; Li, Y.; Zhou, Y.; Hou, J.; Li, Y. A Semitransparent Inorganic Perovskite Film for Overcoming Ultraviolet Light Instability of Organic Solar Cells and Achieving 14.03% Efficiency. *Adv. Mater.*, **2018**, 30, 1800855.

Chen, Y.-S.; Manser, J. S.; Kamat, P. V. All Solution-Processed Lead Halide Perovskite-$BiVO_4$ Tandem Assembly for Photolytic Solar Fuels Production. *J. Am. Chem. Soc.* **2015**, 137, 974–981.

Chiang, C.-H.; Wu, C.-G. A Method for the Preparation of Highly Oriented $MAPbI_3$ Crystallites for High-Efficiency Perovskite Solar Cells to Achieve an 86% Fill Factor. *ACS Nano* **2018**, *12*, 10355–10364.

Cho, H.; Kim, Y.-H.; Wolf, C.; Lee, H.-D.; Lee, T.-W. Improving the Stability of Metal Halide Perovskite Materials and Light-Emitting Diodes. *Adv. Mater.* **2018**, 30, 1704587.

Cho, S. H.; Ghosh, S.; Berkson, Z. J.; Hachtel, J. A.; Shi, J.; Zhao, X.; Reimnitz, L. C.; Dahlman, C. J.; Ho, Y.; Yang, A.; Liu, Y; Idrobo, J.-C.; Chmelka, B. F; Milliron, D. J. Syntheses of Colloidal F:In_2O_3 Cubes: Fluorine-Induced Faceting and Infrared Plasmonic Response. *Chem. Mater.* **2019**, *31*, 2661-2676.

Christian, J. W. *The Theory of Transformations in Metals and Alloys*; Elsevier Science: Kidlington, Oxford, UK, 2002.

Christians, J. A.; Miranda Herrera, P. A.; Kamat, P. V. Transformation of the Excited State and Photovoltaic Efficiency of $CH_3NH_3PbI_3$ Perovskite upon Controlled Exposure to Humidified Air. *J. Am. Chem. Soc.* **2015**, *137*, 1530–1538.

Chung, I.; Lee, B.; He, J.; Chang, R. P. H.; Kanatzidis, M. G. All-Solid-State Dye-Sensitized Solar Cells with High Efficiency. *Nature* **2012**, 485, 486–489.

Chun-Ren Ke, J.; Walton, A. S.; Lewis, D. J.; Tedstone, A.; O'Brien, P.; Thomas, A. G.; Flavell, W. R. In Situ Investigation of Degradation at Organometal Halide Perovskite Surfaces by X-Ray Photoelectron Spectroscopy at Realistic Water Vapour Pressure. *Chem. Commun.* **2017**, 53, 5231–5234.

Ciccioli, A.; Latini, A. Thermodynamics and the Intrinsic Stability of Lead Halide Perovskites $CH_3NH_3PbX_3$. *J. Phys. Chem. Lett.* **2018**, 9, 3756–3765.

Climate Change Threatens National Security Says Pentagon. *United Nations Climate Change*. Washington DC October 14, 2014.

Collins, T. J.; Nichols, T. R.; Uffelman, E. S. A Square-Planar Nickel(III) Complex of an Innocent Ligand System. *J. Am. Chem. Soc.* **1991**, 113, 4708–4709.

Compaan, A.D.; Gupta, A.; Lee, S.; Wang, S.; Drayton, J. High efficiency, magnetron sputtered CdS/CdTe solar cells. *Sol. Energy*, **2004**, 77, 815–822.

Connor, B. A.; Leppert, L.; Smith, M. D.; Neaton, J. B.; Karunadasa, H. I. Layered Halide Double Perovskites: Dimensional Reduction of $Cs_2AgBiBr_6$. *J. Am. Chem. Soc.* **2018**, 140, 5235–5240.

Creutz, S. E.; Crites, E. N.; De Siena, M. C.; Gamelin, D. R. Colloidal Nanocrystals of Lead-Free Double-Perovskite (Elpasolite) Semiconductors: Synthesis and Anion Exchange to Access New Materials. *Nano Lett.* **2018**, 18, 1118–1123.

Day, J. H. Thermochromism of Inorganic Compounds. *Chem. Rev.* **1968**, 68, 649–657.

De Bastiani, M.; Saidaminov, M. I.; Dursun, I.; Sinatra, L.; Peng, W.; Buttner, U.; Mohammed, O. F.; Bakr, O. M. Thermochromic Perovskite Inks for Reversible Smart Window Applications. *Chem. Mater.* **2017**, 29, 3367–3370.

De Santis, G.; Fabbrizzi, L.; Poggi, A.; Taglietti, A. Nickel(III)-Promoted Deprotonation of an Amide Group of Cyclam. Characterization of the Violet Transient through Stopped-Flow Spectrophotometric Techniques and Determination of the pKA Value. *Inorg. Chem.* **1994**, 33, 134–139.

Degans, H. Imec Reports Record Conversion Efficiency of 23.9 Percent on a 4 cm^2 Perovskite/Silicon Solar Module. *IMEC*, **2017**, https://www.imec-int.com/en/articles/imec-reports-record-conversion-efficiency-of-23-9-percent-on-a-4cm2-perovskite-silicon-solar-module

Deng, Z.; Wei, F.; Sun, S.; Kieslich, G.; Cheetham, A. K.; Bristowe, P. D. Exploring the Properties of Lead-Free Hybrid Double Perovskites Using a Combined Computational-Experimental Approach. *J. Mater. Chem. A* **2016**, 4, 12025–12029.

Domanski, K.; Correa-Baena, J.P.; Mine, N.; Nazeeruddin, M.K.; Abate, A.; Saliba, M.; Tress, W.; Hagfeldt, A.; Grätzel, M. Not All That Glitters Is Gold: Metal-Migration-Induced Degradation in Perovskite Solar Cells. *ACS Nano*, **2016**, 10, 6306–6314.

Dou, B.; Whitaker, J. B.; Bruening, K.; Moore, D. T.; Wheeler, L. M.; Ryter, J.; Breslin, N. J.; Berry, J. J.; Garner, S. M.; Barnes, F. S.; Shaheen, S. E.; Tassone, C. J.; van Hest, M. F. A. M. Roll-to-Roll Printing of Perovskite Solar Cells. *ACS Energy Lett.* **2018**, *3*, 2558–2565.

Duong, T.; Lal, N.; Grant, D.; Jacobs, D.; Zheng, P.; Rahman, S.; Shen, H.; Stocks, M.; Blakers, A.; Weber, K.; White, T.P.; Catchpole, K.R. Semitransparent Perovskite Solar Cell With Sputtered Front and Rear Electrodes for a Four-Terminal Tandem. *IEEE J. Photovolt.*, **2016**, 6, 679–687.

Duong, T.; Wu, Y.; Shen, H.; Peng, J.; Fu, X.; Jacobs, D.; Wang, E.-C.; Kho, T.C.; Fong, K.C.; Stocks, M.; Franklin, E.; Blakers, A.; Zin, N.; McIntosh, K.; Li, W.; Cheng, Y.-B.; White, T.P.; Weber, K.; Catchpole, K. Rubidium Multication Perovskite with Optimized Bandgap for Perovskite-Silicon Tandem with over 26% Efficiency. *Adv. Energy Mater.*, **2017**, 7, 1700228.

Durose, K.; Edwards, P.R.; Halliday, D.P. Materials aspects of CdTe/CdS solar cells. *J. Cryst. Growth*, **1999**, 197, 733–742.

Eperon, G.E.; Leijtens, T.; Bush, K.A.; Prasanna, R.; Green, T.; Wang, J.T.-W.; McMeekin, D.P.; Volonakis, G.; Milot, R.L.; May, R.; Palmstrom, A.; Slotcavage, D.J.; Belisle, R.A.; Patel, J.B.; Parrott, E.S.; Sutton, R.J.; Ma, W.; Moghadam, F.; Conings, B.; Babayigit, A.; Boyen, H.-G.; Bent, S.; Giustino, F.; Herz, L.M.; Johnston, M.B.; McGehee, M.D.; Snaith, H.J. Perovskite-perovskite tandem photovoltaics with optimized band gaps. *Science*, **2016**, 354, 861–865.

Eperon, G.E.; Paternò, G.M.; Sutton, R.J.; Zampetti, A.; Haghighirad, A.A.; Cacialli, F.; Snaith, H.J. Inorganic caesium lead iodide perovskite solar cells. *J. Mater. Chem. A*, **2015**, 3, 19688–19695.

Fan, R.; Zhou, N.; Zhang, L.; Yang, R.; Meng, Y.; Li, L.; Guo, T.; Chen, Y.; Xu, Z.; Zheng, G.; Huang, Y.; Li, Liang, Qin, L.; Qiu, X.; Chen, Q.; Zhou, H. Toward Full Solution Processed Perovskite/Si Monolithic Tandem Solar Device with PCE Exceeding 20%. *Sol. RRL*, **2017**, 1, 1700149.

Ferreira da Silva, A.; Veissid, N.; An, C. Y.; Pepe, I.; Barros de Oliveira, N.; Batista da Silva, A. V. Optical Determination of the Direct Bandgap Energy of Lead Iodide Crystals. *Appl. Phys. Lett.* **1996**, 69, 1930–1932.

Foehringer Merchant, E. US Surpasses 2 Million Solar Installations as Industry Looks to "Dominate" the 2020s. *Greentech Media*. May 9, 2019.

Foley, B. J.; Cuthriell, S.; Yazdi, S.; Chen, A. Z.; Guthrie, S. M.; Deng, X.; Giri, G.; Lee, S.-H.; Xiao, K.; Doughty, B.; Ma, Y.-Z.; Choi, J. J. Impact of Crystallographic Orientation Disorders on Electronic Heterogeneities in Metal Halide Perovskite Thin Films. *Nano Lett.* **2018**, *18*, 6271–6278.

Forgács, D.; Gil-Escrig, L.; Pérez-Del-Rey, D.; Momblona, C.; Werner, J.; Niesen, B.; Ballif, C.; Sessolo, M.; Bolink, H.J. Efficient Monolithic Perovskite/Perovskite Tandem Solar Cells. *Adv. Energy Mater.*, **2017**, 7, 1602121.

Forney, C. F.; Brandl, D. G. Control of Humidity in Small Controlled-Environment Chambers Using Glycerol-Water Solutions. *HortTechnology* **1992**, 2, 52–54.

Fransishyn, K. M.; Kundu, S.; Kelly, T. L. Elucidating the Failure Mechanisms of Perovskite Solar Cells in Humid Environments Using In Situ Grazing-Incidence Wide-Angle X-Ray Scattering. *ACS Energy Lett.* **2018**, *3*, 2127–2133.

Frauenhofer ISE. *Photovoltaics Report*; Frauenhofer ISE: Munich, Germany, 2019; pp 1–48.

Fu, F.; Feurer, T.; Jäger, T.; Avancini, E.; Bissig, B.; Yoon, S.; Buecheler, S.; Tiwari, A.N. Low-temperature-processed efficient semi-transparent planar perovskite solar cells for bifacial and tandem applications. *Nat. Commun.*, **2015**, 6, 8932.

Fu, F.; Feurer, T.; Weiss, T.P.; Pisoni, S.; Avancini, E.; Andres, C.; Buecheler, S.; Tiwari, A.N. High-efficiency inverted semi-transparent planar perovskite solar cells in substrate configuration. *Nat. Energy*, **2016**, 2, 16190.

Fu, W.; Wang, J.; Zuo, L.; Gao, K.; Liu, F.; Ginger, D. S.; Jen, A. K.-Y. Two-Dimensional Perovskite Solar Cells with 14.1% Power Conversion Efficiency and 0.68% External Radiative Efficiency. *ACS Energy Lett.* **2018**, *3*, 2086–2093.

Giesbrecht, N.; Schlipf, J.; Grill, I.; Rieder, P.; Dyakonov, V.; Bein, T.; Hartschuh, A.; Müller-Buschbaum, P.; Docampo, P. Single-Crystal-like Optoelectronic-Properties of $MAPbI_3$ Perovskite Polycrystalline Thin Films. *J. Mater. Chem. A* **2018**, *6*, 4822–4828.

Goldie-Scot, L. A Behind the Scenes Take on Lithium-Ion Battery Prices. *BloombergNEF*. March 5, 2019.

Gong, J.; Yang, M.; Rebollar, D.; Rucinski, J.; Liveris, Z.; Zhu, K.; Xu, T. Divalent Anionic Doping in Perovskite Solar Cells for Enhanced Chemical Stability. *Adv. Mater.* **2018**, *30*, 1800973.

Granqvist, C. G.; Lansåker, P. C.; Mlyuka, N. R.; Niklasson, G. A.; Avendaño, E. Progress in Chromogenics: New Results for Electrochromic and Thermochromic Materials and Devices. *Sol. Energy Mater. Sol. Cells* **2009**, 93, 2032–2039.

Green, M.A.; Hishikawa, Y.; Dunlop, E.D.; Levi, D.H.; Hohl-Ebinger, J.; Ho-Baillie, A.W.Y. Solar cell efficiency tables (version 52). *Prog. Photovolt. Res. Appl.*, **2018,** 26, 427–436.

Green, M.A.; Ho-Baillie, A.; Snaith, H.J. The emergence of perovskite solar cells. *Nat. Photonics*, **2014**, 8, 506–514.

Griffin, M. P.; Gearba, R.; Stevenson, K.J.; Vanden Bout, D. A.; Colocan, A. Revealing the Chemistry and Morphology of Buried Donor/Acceptor Interfaces in Organic Photovoltaics. *J. Phys. Chem. Lett.* **2017**. *8*, 2764.

Gu, C.-D.; Tu, J.-P. Thermochromic Behavior of Chloro-Nickel(II) in Deep Eutectic Solvents and Their Application in Thermochromic Composite Films. *RSC Adv.* **2011**, 1, 1220–1227.

Guchhait, A.; Dewi, H.A.; Leow, S.W.; Wang, H.; Han, G.; Suhaimi, F.B.; Mhaisalkar, S.; Wong, L.H.; Mathews, N. Over 20% Efficient CIGS–Perovskite Tandem Solar Cells. *ACS Energy Lett.*, **2017**, 2, 807–812.

Guerrero, A.; You, J.; Aranda, C.; Kang, Y. S.; Garcia-Belmonte, G.; Zhou, H.; Bisquert, J.; Yang, Y. Interfacial Degradation of Planar Lead Halide Perovskite Solar Cells. *ACS Nano* **2016**, *10*, 218–224.

Guillaussier, A.; Yu, Y.; Voggu, V. R.; Aigner, W.; Cabezas, C. S.; Houck, D. W.; Shah, T.; Smilgies, D.-M.; Pereira, R. N.; Stutzmann, M.; Korgel, B.A. Silicon Nanocrystal Superlattice Nucleation and Growth. *Langmuir* **2017**, 33, 13068–13076.

H. Hirsch. The Co-Precipitation of Thallous Thallium in Photographic Emulsions. *J. Photogr. Sci.* **1963**, 11, 321–325.

Halder, A.; Choudhury, D.; Ghosh, S.; Subbiah, A. S.; Sarkar, S. K. Exploring Thermochromic Behavior of Hydrated Hybrid Perovskites in Solar Cells. *J. Phys. Chem. Lett.* **2015**, 6, 3180–3184.

Han, Q.; Hsieh, Y.-T.; Meng, L.; Wu, J.-L.; Sun, P.; Yao, E.-P.; Chang, S.-Y.; Bae, S.-H.; Kato, T.; Bermudez, V.; Yang, Y. High-performance perovskite/Cu(In,Ga)Se_2 monolithic tandem solar cells. *Science*, **2018**, 361, 904-908.

Hao, F.; Stoumpos, C.C.; Cao, D.H.; Chang, R.P.H.; Kanatzidis, M.G. Lead-free solid-state organic–inorganic halide perovskite solar cells. *Nat. Photonics*, **2014**, 8, 489–494.

Hao, F.; Stoumpos, C.C.; Chang, R.P.H.; Kanatzidis, M.G. Anomalous Band Gap Behavior in Mixed Sn and Pb Perovskites Enables Broadening of Absorption Spectrum in Solar Cells. *J. Am. Chem. Soc.*, **2014**, 136, 8094–8099.

He, M.; Pang, X.; Liu, X.; Jiang, B.; He, Y.; Snaith, H.; Lin, Z. Monodisperse Dual-Functional Upconversion Nanoparticles Enabled Near-Infrared Organolead Halide Perovskite Solar Cells. *Angew. Chem. Int. Ed.* **2016**, 55, 4280–4284.

Heidrich, K.; Staude, W.; Treusch, J.; Overhof, H. Optical Properties and Electronic Structure of Polymorphous TlCl and TlBr. *Phys. Rev. Lett.* **1974**, 33, 1220–1223.

Heo, J. H.; Im, S. H. $CH_3NH_3PbBr_3$-$CH_3NH_3PbI_3$ Perovskite-Perovskite Tandem Solar Cells with Exceeding 2.2 V Open Circuit Voltage. *Adv. Mater*. **2016**, 28, 5121–5125.

Heo, J.H.; Song, D. E.; Im, S.H. Planar $CH_3NH_3PbBr_3$ Hybrid Solar Cells with 10.4% Power Conversion Efficiency, Fabricated by Controlled Crystallization in the Spin-Coating Process. *Adv. Mat.* **2104**, *26*, 8179-8183.

Hillebrecht, H.; Ade, M. Trimeric Units $[Ag_3X_8]^{5-}$ with Face-Sharing Polyhedra in the Series Tl_2AgX_3 (*X*=Cl, Br, I): Synthesis, Crystal Structure, and Vibrational Spectra: Trimeric Units $[Ag_3X_8]^{5-}$ with Face-Sharing Polyhedra in the Series Tl_2AgX_3 (*X*=Cl, Br, I): Synthesis, Crystal Structure, and Vibrational Spectra. *Z. Für Anorg. Allg. Chem.* **2018**, 644, 288–292.

Hitomi, K.; Shoji, T.; Ishii, K. Advances in TlBr Detector Development. *J. Cryst. Growth* **2013**, 379, 93–98.

Hoffman, J.B.; Zaiats, G.; Wappes, I.; Kamat, P.V. $CsPbBr_3$ Solar Cells: Controlled Film Growth through Layer-by-Layer Quantum Dot Deposition. *Chem. Mater.*, **2017**, 29, 9767–9774.

Hoke, E.T.; Slotcavage, D.J.; Dohner, E.R.; Bowring, A.R.; Karunadasa, H.I.; McGehee, M.D. Reversible photo-induced trap formation in mixed-halide hybrid perovskites for photovoltaics. *Chem. Sci.*, **2015**, 6, 613–617.

Holmberg, V. C.; Bogart, T. D.; Chockla, A. M.; Hessel, C. M.; Korgel, B. A. Optical Properties of Silicon and Germanium Nanowire Fabric. *J. Phys. Chem. C* **2012**, 116, 22486–22491.

Hu, Y.; Bai, F.; Liu, X.; Ji, Q.; Miao, X.; Qiu, T.; Zhang, S. Bismuth Incorporation Stabilized α-$CsPbI_3$ for Fully Inorganic Perovskite Solar Cells. *ACS Energy Lett.* **2017**, 2, 2219–2227.

Hu, Y.; Qiu, T.; Bai, F.; Miao, X.; Zhang, S. Enhancing Moisture-Tolerance and Photovoltaic Performances of $FAPbI_3$ by Bismuth Incorporation. *J. Mater. Chem. A* **2017**, 5, 25258–25265.

IEA, 2017. Tracking Clean Energy Progress: 2017. IEA, Paris, France.

Ihara, Y.; Fukuda, Y.; Sone, K. Solid-Phase Thermal Square-Planar-to-Octahedral Isomeric Transformation of Nickel(II) Complexes Containing 1,2-Cyclohexanediamines. *Inorg. Chem.* **1987**, 26, 3745–3750.

Im, J.-H.; Chung, J.; Kim, S.-J.; Park, N.-G. Synthesis, Structure, and Photovoltaic Property of a Nanocrystalline 2H Perovskite-Type Novel Sensitizer $(CH_3CH_2NH_3)PbI_3$. *Nanoscale Res. Lett.* **2012**, 7, 353.

IPCC. *Summary for Policymakers.*; Global Warming of 1.5 ºC. An IPCC Special Report on the impacts of Global Warming of 1.5 ºC Above Pre-Industrial Levels and Related Greenhouse Gas Emission Pathways, in the Context of Strengthening the Global Response to the Threat of Climate Change, Sustainable Development, and Efforts to Eradicate Poverty; IPCC, 2018.

Jang, Y.H.; Lee, J.M.; Seo, J.W.; Kim, I.; Lee, D.-K. Monolithic tandem solar cells comprising electrodeposited $CuInSe_2$ and perovskite solar cells with a nanoparticulate ZnO buffer layer. *J. Mater. Chem. A*, **2017**, 5, 19439–19446.

Janssen, D.; De Palma, R.; Verlaak, S.; Heremans, P.; Dehaen, W. Static Solvent Contact Angle Measurements, Surface Free Energy and Wettability Determination of Various Self-Assembled Monolayers on Silicon Dioxide. *Thin Solid Films* **2006**, 515, 1433–1438.

Jaysankar, M.; Filipič, M.; Zielinski, B.; Schmager, R.; Song, W.; Qiu, W.; Paetzold, U. W.; Aernouts, T.; Debucquoy, M.; Gehlhaar, R.; et al. Perovskite–Silicon Tandem Solar Modules with Optimised Light Harvesting. *Energy Environ. Sci.* **2018**, 11, 1489–1498.

Jaysankar, M.; Qiu, W.; van Eerden, M.; Aernouts, T.; Gehlhaar, R.; Debucquoy, M.; Paetzold, U.W.; Poortmans, J. Four-Terminal Perovskite/Silicon Multijunction Solar Modules. *Adv. Energy Mater.*, **2017**, 7, 1602807.

Jena, A. K.; Kulkarni, A.; Sanehira, Y.; Ikegami, M.; Miyasaka, T. Stabilization of α-$CsPbI_3$ in Ambient Room Temperature Conditions by Incorporating Eu into $CsPbI_3$. *Chem. Mater.* **2018**, 30, 6668-6674.

Jesper Jacobsson, T.; Correa-Baena, J.-P.; Pazoki, M.; Saliba, M.; Schenk, K.; Grätzel, M.; Hagfeldt, A. Exploration of the Compositional Space for Mixed Lead Halogen Perovskites for High Efficiency Solar Cells. *Energy Environ. Sci.* **2016**, 9, 1706–1724.

Ji, F.; Pang, S.; Zhang, L.; Zong, Y.; Cui, G.; Padture, N. P.; Zhou, Y. Simultaneous Evolution of Uniaxially Oriented Grains and Ultralow-Density Grain-Boundary Network in $CH_3NH_3PbI_3$ Perovskite Thin Films Mediated by Precursor Phase Metastability. *ACS Energy Lett.* **2017**, *2*, 2727–2733.

Ji, L.; Hsu, H.-Y.; Lee, J. C.; Bard, A. J.; Yu, E. T. Solution-Processed Epitaxial Growth of Hybrid Halide Perovskites and High-Performance Photodetectors. *Nano Lett.* **2018**, *18*, 994-1000.

Jiang, F.; Liu, T.; Luo, B.; Tong, J.; Qin, F.; Xiong, S.; Li, Z.; Zhou, Y. A two-terminal perovskite/perovskite tandem solar cell. *J. Mater. Chem. A*, **2016**, 4, 1208–1213.

Jiang, Q.; Rebollar, D.; Gong, J.; Piacentino, E. L.; Zheng, C.; Xu, T. Pseudohalide-Induced Moisture Tolerance in Perovskite $CH_3NH_3Pb(SCN)_2$ I Thin Films. *Angew. Chem. Int. Ed.* **2015**, 54, 7617–7620.

Jing, L.; Cheng, X.; Yuan, Y.; Du, S.; Ding, J.; Sun, H.; Zhan, X.; Zhou, T-L. Design Growth of Triangular Pyramid $MAPBr_3$ Single Crystal and its Photoelectric Anisotropy between (100) and (111) Facets. *J. Phys. Chem. C* **2019**, *123*, 10826-10830.

Jošt, M.; Albrecht, S.; Lipovšek, B.; Krč, J.; Korte, L.; Rech, B.; Topič, M. Back- and Front-side Texturing for Light-management in Perovskite / Silicon-heterojunction Tandem Solar Cells. *Energy Procedia*, **2016**, 102, 43–48.

Jošt, M.; Bertram, T.; Koushik, D.; Marquez, J. A.; Verheijen, M. A.; Heinemann, M. D.; Köhnen, E.; Al-Ashouri, A.; Braunger, S.; Lang, F.; et al. 21.6%-Efficient Monolithic Perovskite/Cu(In,Ga)Se_2 Tandem Solar Cells with Thin Conformal Hole Transport Layers for Integration on Rough Bottom Cell Surfaces. *ACS Energy Lett.* **2019**, 4, 583–590.

Jung, M.-H. White-Light Emission from the Structural Distortion Induced by Control of Halide Composition of Two-Dimensional Perovskites ($(C_6H_5CH_2NH_3)_2PbBr_{4-x}Cl_x$). *Inorg. Chem.* **2019**, 58, 6748–6757.

Kahani, S. A.; Abdevali, F. Mechanochemical Synthesis and Characterization of a Nickel(II) Complex as a Reversible Thermochromic Nanostructure. *RSC Adv.* **2016**, 6, 5116–5122.

Kamalisarvestani, M.; Saidur, R.; Mekhilef, S.; Javadi, F. S. Performance, Materials and Coating Technologies of Thermochromic Thin Films on Smart Windows. *Renew. Sustain. Energy Rev.* **2013**, 26, 353–364.

Kang, S.-G.; Ryu, K.; Jung, S.-K.; Kim, J. Template Synthesis, Crystal Structure, and Solution Behavior of a Hexaaza Macrocyclic Nickel(II) Complex Containing Two N-Aminoethyl Pendant Arms. *Inorganica Chim. Acta* **1999**, 293, 140–146.

Kapil, G.; Ripolles, T.S.; Hamada, K.; Ogomi, Y.; Bessho, T.; Kinoshita, T.; Chantana, J.; Yoshino, K.; Shen, Q.; Toyoda, T.; Minemoto, T.; Murakami, T.N.; Segawa, H.; Hayase, S. Highly Efficient 17.6% Tin–Lead Mixed Perovskite Solar Cells Realized through Spike Structure. *Nano Lett.*, **2018**, 18, 3600–3607.

Karani, A.; Yang, L.; Bai, S.; Futscher, M. H.; Snaith, H. J.; Ehrler, B.; Greenham, N. C.; Di, D. Perovskite/Colloidal Quantum Dot Tandem Solar Cells: Theoretical Modeling and Monolithic Structure. *ACS Energy Lett.* **2018**, 3, 869–874.

Karmakar, A.; Dodd, M. S.; Agnihotri, S.; Ravera, E.; Michaelis, V. K. Cu(II)-Doped $Cs_2SbAgCl_6$ Double Perovskite: A Lead-Free, Low-Bandgap Material. *Chem. Mater.* **2018**, *30*, 8280–8290.

Katari, J. E. B.; Colvin, V. L.; Alivisatos, A. P. X-Ray Photoelectron Spectroscopy of CdSe Nanocrystals with Applications to Studies of the Nanocrystal Surface. *J. Phys. Chem.* **1994**, *98*, 4109–4117.

Kato, Y.; Ono, L. K.; Lee, M. V.; Wang, S.; Raga, S. R.; Qi, Y. Silver Iodide Formation in Methyl Ammonium Lead Iodide Perovskite Solar Cells with Silver Top Electrodes. *Adv. Mater. Interfaces* **2015**, *2*, 1500195.

Kennaway, E. L.; Hieger, I. Carcinogenic Substances and their Fluorescence Spectra. *BMJ* **1930**, 1, 1044–1046.

Kephart, J.M.; Geisthardt, R.M.; Sampath, W.S. Optimization of CdTe thin-film solar cell efficiency using a sputtered, oxygenated CdS window layer. *Prog. Photovolt. Res. Appl.*, **2015**, 23, 1484–1492.

Kieslich, G.; Skelton, J. M.; Armstrong, J.; Wu, Y.; Wei, F.; Svane, K. L.; Walsh, A.; Butler, K. T. Hydrogen Bonding versus Entropy: Revealing the Underlying Thermodynamics of the Hybrid Organic–Inorganic Perovskite $[CH_3NH_3]PbBr_3$. *Chem. Mater.* **2018**, 30, 8782–8788.

Kim, D. H.; Park, J.; Li, Z.; Yang, M.; Park, J.-S.; Park, I. J.; Kim, J. Y.; Berry, J. J.; Rumbles, G.; Zhu, K. 300% Enhancement of Carrier Mobility in Uniaxial-Oriented Perovskite Films Formed by Topotactic-Oriented Attachment. *Adv. Mater.* **2017**, *29*, 1606831.

Kim, F.; Connor, S.; Song, H.; Kuykendall, T.; Yang, P. Platonic Gold Nanocrystals. *Angew. Chem.* **2004**, *116*, 3759–3763.

Kim, H. N.; Ren, W. X.; Kim, J. S.; Yoon, J. Fluorescent and Colorimetric Sensors for Detection of Lead, Cadmium, and Mercury Ions. *Chem. Soc. Rev.* **2012**, 41, 3210–3244.

Kim, H.-S.; Lee, C.-R.; Im, J.-H.; Lee, K.-B.; Moehl, T.; Marchioro, A.; Moon, S.-J.; Humphry-Baker, R.; Yum, J.-H.; Moser, J. E.; et al. Lead Iodide Perovskite Sensitized All-Solid-State Submicron Thin Film Mesoscopic Solar Cell with Efficiency Exceeding 9%. *Sci. Rep.* **2012**, 2, 591.

Kim, J.; Ouellette, O.; Voznyy, O.; Wei, M.; Choi, J.; Choi, M.-J.; Jo, J.W.; Baek, S.-W.; Fan, J.; Saidaminov, M.I.; Sun, B.; Li, P.; Nam, D.-H.; Hoogland, S.; Lu, Z.-H.; García de Arquer, F.P.; Sargent, E.H. Butylamine-Catalyzed Synthesis of Nanocrystal Inks Enables Efficient Infrared CQD Solar Cells. *Adv. Mater.*, **2018**, 30, 1803830.

Kim, J.; Saidaminov, M.I.; Tan, H.; Zhao, Y.; Kim, Y.; Choi, J.; Jo, J.W.; Fan, J.; Quintero-Bermudez, R.; Yang, Z.; Quan, L.N.; Wei, M.; Voznyy, O.; Sargent, E.H. Amide-Catalyzed Phase-Selective Crystallization Reduces Defect Density in Wide-Bandgap Perovskites. Adv. Mater., **2018**, 30, 1706275.

Kinoshita, T.; Nonomura, K.; Joong Jeon, N.; Giordano, F.; Abate, A.; Uchida, S.; Kubo, T.; Seok, S.I.; Nazeeruddin, M.K.; Hagfeldt, A.; Grätzel, M.; Segawa, H. Spectral splitting photovoltaics using perovskite and wideband dye-sensitized solar cells. *Nat. Commun.*, **2015**, 6, 8834.

Kojima, A.; Teshima, K.; Shirai, Y.; Miyasaka, T. Organometal Halide Perovskites as Visible-Light Sensitizers for Photovoltaic Cells. *J. Am. Chem. Soc.* **2009**, *131*, 6050-6051

Korgel, B. A.; Fullam, S.; Connolly, S.; Fitzmaurice, D. Assembly and Self-Organization of Silver Nanocrystal Superlattices: Ordered "Soft Spheres." *J. Phys. Chem. B* **1998**, 102, 8379–8388.

Kranz, L.; Abate, A.; Feurer, T.; Fu, F.; Avancini, E.; Löckinger, J.; Reinhard, P.; Zakeeruddin, S.M.; Grätzel, M.; Buecheler, S.; Tiwari, A.N. High-Efficiency Polycrystalline Thin Film Tandem Solar Cells. *J. Phys. Chem. Lett.*, **2015**, 6, 2676–2681.

Kranz, L.; Schmitt, R.; Gretener, C.; Perrenoud, J.; Pianezzi, F.; Uhl, A.R.; Keller, D.; Buecheler, S.; Tiwari, A.N. Progress towards 14% efficient CdTe solar cells in substrate configuration. *IEEE Photovoltaics Specialists Conference (PVSC),* **2013**, pp. 1644–1648.

Kubelka, P.; Munk, F. Ein Beitrag zur Optik der Farbenstriche. *Z. Tech. Phys.* **1931**, 12, 593–601.

Kulbak, M.; Gupta, S.; Kedem, N.; Levine, I.; Bendikov, T.; Hodes, G.; Cahen, D. Cesium Enhances Long-Term Stability of Lead Bromide Perovskite-Based Solar Cells. *J. Phys. Chem. Lett.*, **2016**, 7, 167–172.

L. Schellhorn. *Dissertation*; University of Freiburg: Freiburg, 1987.

Lacey, S.; Kann, S. The Deep Decarbonization Draft: Fantasy Sports for Energy Nerds.

Lal, N.N.; Dkhissi, Y.; Li, W.; Hou, Q.; Cheng, Y.-B.; Bach, U. Perovskite Tandem Solar Cells. *Adv. Energy Mater.*, **2017** 7, 1602761.

Lau, C. F. J.; Zhang, M.; Deng, X.; Zheng, J.; Bing, J.; Ma, Q.; Kim, J.; Hu, L.; Green, M. A.; Huang, S.; et al. Strontium-Doped Low-Temperature-Processed $CsPbI_2Br$ Perovskite Solar Cells. *ACS Energy Lett.* **2017**, *2*, 2319–2325.

Lazard Inc. 2018. Lazard's Levelized Cost of Electricity, Version 11.0. Lazard, New York, NY, USA

Lee, C.; Efstathiadis, H.; Raynolds, J.E.; Haldar, P. Two-dimensional computer modeling of single junction a-Si:H solar cells. *IEEE Photovoltaic Specialists Conference (PVSC)*, **2009**, 34, 1118–1122.

Lee, D. S.; Yun, J. S.; Kim, J.; Soufiani, A. M.; Chen, S.; Cho, Y.; Deng, X.; Seidel, J.; Lim, S.; Huang, S.; Ho-Baillie, A. W. Y. Passivation of Grain Boundaries by Phenethylammonium in Formamidinium-Methylammonium Lead Halide Perovskite Solar Cells. *ACS Energy Lett.* **2018**, *3*, 647–654.

Lee, J.-W.; Seol, D.-J.; Cho, A.-N.; Park, N.-G. High-Efficiency Perovskite Solar Cells Based on the Black Polymorph of $HC(NH_2)_2PbI_3$. *Adv. Mater.*, **2014**, 26, 4991–4998.

Lee, M. M.; Teuscher, J.; Miyasaka, T.; Murakami, T. N.; Snaith, H. J. Efficient Hybrid Solar Cells Based on Meso-Superstructured Organometal Halide Perovskites. *Science* **2012**, 338, 643–647.

Lee, S.; Hwang, D.; Jung, S. I.; Kim, D. Electron Transfer from Triplet State of TIPS-Pentacene Generated by Singlet Fission Processes to $CH_3NH_3PbI_3$ Perovskite. *J. Phys. Chem. Lett.* **2017**, 8, 884–888.

Lee, S.; Park, J. H.; Nam, Y. S.; Lee, B. R.; Zhao, B.; Di Nuzzo, D.; Jung, E. D.; Jeon, H.; Kim, J.-Y.; Jeong, H. Y.; Friend, R. H.; Song, M. H. Growth of Nano-Sized Single Crystals for Efficient Perovskite Light-Emitting Diodes. *ACS Nano* **2018**, *12*, 3417-3423.

Leguy, A. M. A.; Hu, Y.; Campoy-Quiles, M.; Alonso, M. I.; Weber, O. J.; Azarhoosh, P.; van Schilfgaarde, M.; Weller, M. T.; Bein, T.; Nelson, J.; et al. Reversible Hydration of $CH_3NH_3PbI_3$ in Films, Single Crystals, and Solar Cells. *Chem. Mater.* **2015**, 27, 3397–3407.

Lehner, A. J.; Fabini, D. H.; Evans, H. A.; Hébert, C.-A.; Smock, S. R.; Hu, J.; Wang, H.; Zwanziger, J. W.; Chabinyc, M. L.; Seshadri, R. Crystal and Electronic Structures of Complex Bismuth Iodides $A_3Bi_2I_9$ (A = K, Rb, Cs) Related to Perovskite: Aiding the Rational Design of Photovoltaics. *Chem. Mater.* **2015**, 27, 7137–7148.

Leijtens, T.; Prasanna, R.; Bush, K.A.; Eperon, G.; Raiford, J.A.; Gold-Parker, A.; Wolf, E.J.; Swifter, S.A.; Boyd, C.C.; Wang, H.-P.; Toney, M.F.; Bent, S.; McGehee, M.D. Tin-lead halide perovskites with improved thermal and air stability for efficient all-perovskite tandem solar cells. *Sustain. Energy Fuels.*, **2018**, 2, 2450-2459

Li, M.; Wang, Z.-K.; Zhuo, M.-P.; Hu, Y.; Hu, K.-H.; Ye, Q.-Q.; Jain, S. M.; Yang, Y.-G.; Gao, X.-Y.; Liao, L.-S. Pb-Sn-Cu Ternary Organometallic Halide Perovskite Solar Cells. *Adv. Mater.* **2018**, *30*, 1800258.

Li, M.; Wang, Z.-K.; Zhuo, M.-P.; Hu, Y.; Hu, K.-H.; Ye, Q.-Q.; Jain, S. M.; Yang, Y.-G.; Gao, X.-Y.; Liao, L.-S. Pb-Sn-Cu Ternary Organometallic Halide Perovskite Solar Cells. *Adv. Mater.* **2018**, 30, 1800258.

Li, M.-H.; Yeh, H.-H.; Chiang, Y.-H.; Jeng, U.-S.; Su, C.-J.; Shiu, H.-W.; Hsu, Y.-J.; Kosugi, N.; Ohigashi, T.; Chen, Y.-A.; Shen, P.-S.; Chen, P.; Guo, T.-F. Highly Efficient 2D/3D Hybrid Perovskite Solar Cells via Low-Pressure Vapor-Assisted Solution Process. *Adv. Mater.* **2018**, *30*, 1801401.

Li, W.-G.; Rao, H.-S.; Chen, B.-X.; Wang, X.-D.; Kuang, D.-B. A Formamidinium–Methylammonium Lead Iodide Perovskite Single Crystal Exhibiting Exceptional Optoelectronic Properties and Long-Term Stability. *J. Mater. Chem. A* **2017**, 5, 19431–19438.

Li, Y.; Hu, H.; Chen, B.; Salim, T.; Zhang, J.; Ding, J.; Yuan, N.; Lam, Y.M. Reflective perovskite solar cells for efficient tandem applications. *J. Mater. Chem. C*, **2017**, 5, 134–139.

Li, Y.; Xu, X.; Wang, C.; Ecker, B.; Yang, J.; Huang, J.; Gao, Y. Light-Induced Degradation of $CH_3NH_3PbI_3$ Hybrid Perovskite Thin Film. *J. Phys. Chem. C* **2017**, 121, 3904–3910.

Li, Z.; Yang, M.; Park, J.-S.; Wei, S.-H.; Berry, J. J.; Zhu, K. Stabilizing Perovskite Structures by Tuning Tolerance Factor: Formation of Formamidinium and Cesium Lead Iodide Solid-State Alloys. *Chem. Mater.* **2016**, 28, 284–292.

Lin, J.; Lai, M.; Dou, L.; Kley, C. S.; Chen, H.; Peng, F.; Sun, J.; Lu, D.; Hawks, S. A.; Xie, C.; Cui, F.; Alivisatos, A. P.; Limmer, D. T.; Yang, P. Thermochromic Halide Perovskite Solar Cells. *Nat. Mater.* **2018**, 17, 261–267.

Lin, Y.; Fang, Y.; Zhao, J.; Shao, Y.; Stuard, S. J.; Nahid, M. M.; Ade, H.; Wang, Q.; Shield, J. E.; Zhou, N.; Moran, A. M.; Huang, J. Unveiling the Operation Mechanism of Layered Perovskite Solar Cells. *Nat. Commun.* **2019**, *10*, 1008.

Liu, M.; Guyot-Sionnest, P. Mechanism of Silver(I)-Assisted Growth of Gold Nanorods and Bipyramids. *J. Phys. Chem. B* **2005**, *109*, 22192-22200.

Liu, M.; Johnston, M.B.; Snaith, H.J. Efficient planar heterojunction perovskite solar cells by vapour deposition. *Nature*, **2013**, 501, 395–398.

Liu, Y.; Renna, L.A.; Bag, M.; Page, Z.A.; Kim, P.; Choi, J.; Emrick, T.; Venkataraman, D.; Russell, T.P. High Efficiency Tandem Thin-Perovskite/Polymer Solar Cells with a Graded Recombination Layer. *ACS Appl. Mater. Interfaces*, **2016**, 8, 7070–7076.

Liu, Z.; Krückemeier, L.; Krogmeier, B.; Klingebiel, B.; Márquez, J. A.; Levcenko, S.; Öz, S.; Mathur, S.; Rau, U.; Unold, T.; Kirchartz, T. Open-Circuit Voltages Exceeding 1.26 V in Planar Methylammonium Lead Iodide Perovskite Solar Cells. *ACS Energy Lett.* **2019**, *4*, 110–117.

Long, M.; Zhang, T.; Liu, M.; Chen, Z.; Wang, C.; Xie, W.; Xie, F.; Chen, J.; Li, G.; Xu, J. Abnormal Synergetic Effect of Organic and Halide Ions on the Stability and Optoelectronic Properties of a Mixed Perovskite via In Situ Characterizations. *Adv. Mater.*, **2018**, 30, 1801562.

Löper, P.; Moon, S.-J.; de Nicolas, S.M.; Niesen, B.; Ledinsky, M.; Nicolay, S.; Bailat, J.; Yum, J.-H.; De Wolf, S.; Ballif, C. Organic–inorganic halide perovskite/crystalline silicon four-terminal tandem solar cells. *Phys. Chem. Chem. Phys.*, **2015**, 17, 1619–1629.

Lozhkina, O. A.; Murashkina, A. A.; Shilovskikh, V. V.; Kapitonov, Y. V.; Ryabchuk, V. K.; Emeline, A. V.; Miyasaka, T. Invalidity of Band-Gap Engineering Concept for Bi^{3+} Heterovalent Doping in $CsPbBr_3$ Halide Perovskite. *J. Phys. Chem. Lett.* **2018**, 9, 5408–5411.

Lu, M.; Zhang, X.; Bai, X.; Wu, H.; Shen, X.; Zhang, Y.; Zhang, W.; Zheng, W.; Song, H.; Yu, W. W.; Rogach, A. L. Spontaneous Silver Doping and Surface Passivation of $CsPbI_3$ Perovskite Active Layer Enable Light-Emitting Devices with an External Quantum Efficiency of 11.2%. *ACS Energy Lett.* **2018**, *3*, 1571–1577.

Lu, M.; Zhang, X.; Zhang, Y.; Guo, J.; Shen, X.; Yu, W. W.; Rogach, A. L. Simultaneous Strontium Doping and Chlorine Surface Passivation Improve Luminescence Intensity and Stability of $CsPbI_3$ Nanocrystals Enabling Efficient Light-Emitting Devices. *Adv. Mater.* **2018**, 30, 1804691.

Luo, J. S.; Merchant, N.; Maroni, V. A.; Riley, G. N.; Carter, W. L. Influence of Silver Cladding on the Formation and Alignment of the $(Bi_{2-x}Pb_x)Sr_2Ca_2Cu_3O_{10+\delta}$ Phase. *Appl. Phys. Lett.* **1993**, *63*, 690–692.

Lv, Q.; He, W.; Lian, Z.; Ding, J.; Li, Q.; Yan, Q. Anisotropic Moisture Erosion of $CH_3NH_3PbI_3$ Single Crystals. *CrystEngComm* **2017**, *19*, 901–904.

MacKintosh, F.C.; Zhu, J.X.; Pine, D.J.; Weitz, D.A. Polarization memory of multiply scattered light. *Phys. Rev. B*, **1989**, 40, 9342–9345.

Maeda, Y.; Nakamura, T.; Ikeda, I. Changes in the Hydration States of Poly(N - Alkylacrylamide)s during Their Phase Transitions in Water Observed by FTIR Spectroscopy. *Macromolecules* **2001**, 34, 1391–1399.

Mahmoudi, T.; Wang, Y.; Hahn, Y.-B. Stability Enhancement in Perovskite Solar Cells with Perovskite/Silver–Graphene Composites in the Active Layer. *ACS Energy Lett.* **2018**, *4*, 235–241.

Mailoa, J.P.; Bailie, C.D.; Johlin, E.C.; Hoke, E.T.; Akey, A.J.; Nguyen, W.H.; McGehee, M.D.; Buonassisi, T. A 2-terminal perovskite/silicon multijunction solar cell enabled by a silicon tunnel junction. *Appl. Phys. Lett.*, **2015**, 106, 121105.

Mailoa, J.P.; Lee, M.; Peters, I.M.; Buonassisi, T.; Panchula, A.; Weiss, D.N. Energy-yield prediction for II–VI-based thin-film tandem solar cells. *Energy Environ. Sci.*, **2016**, 9, 2644–2653.

Majoul, N.; Aouida, S.; Bessaïs, B. Progress of Porous Silicon APTES-Functionalization by FTIR Investigations. *Appl. Surf. Sci.* **2015**, 331, 388–391.

Manser, J. S.; Saidaminov, M. I.; Christians, J. A.; Bakr, O. M.; Kamat, P. V. Making and Breaking of Lead Halide Perovskites. *Acc. Chem. Res.* **2016**, 49, 330–338.

Manshor, N. A.; Wali, Q.; Wong, K. K.; Muzakir, S. K.; Fakharuddin, A.; Schmidt-Mende, L.; Jose, R. Humidity versus Photo-Stability of Metal Halide Perovskite Films in a Polymer Matrix. *PhysChemChemPhys* **2016**, 18, 21629–21639.

Mao, C.; Zhou, L.; Wu, X.; Sun, X. New Understanding of Silver-Induced Texture in Powder-in-Tube Processed Ag/Bi(2223) Tape. *Physica C Supercond.* **1997**, *281*, 159–175.

Mao, L.; Wu, Y.; Stoumpos, C. C.; Traore, B.; Katan, C.; Even, J.; Wasielewski, M. R.; Kanatzidis, M. G. Tunable White-Light Emission in Single-Cation-Templated Three-Layered 2D Perovskites $(CH_3CH_2NH_3)_4Pb_3Br_{10-x}Cl_x$. *J. Am. Chem. Soc.* **2017**, 139, 11956–11963.

Mary Loritz. Oxford PV Raises €36 Million for Its Super-Efficient Solar Cells from Chinese Renewable Giant Goldwind. *EU-Startups News*. April 1, 2019.

Matsui, T.; Yamamoto, T.; Nishihara, T.; Morisawa, R.; Yokoyama, T.; Sekiguchi, T.; Negami, T. Compositional Engineering for Thermally Stable, Highly Efficient Perovskite Solar Cells Exceeding 20% Power Conversion Efficiency with 85 °C/85% 1000 h Stability. *Adv. Mater.* **2019**, *31*, 1806823.

Matteocci, F.; Busby, Y.; Pireaux, J.-J.; Divitini, G.; Cacovich, S.; Ducati, C.; Di Carlo, A. Interface and Composition Analysis on Perovskite Solar Cells. *ACS Appl. Mater. Interfaces* **2015**, *7*, 26176-26183.

Mattick, C.; Williams, E.; Allenby, B. Historical Trends in Global Energy Consumption. *IEEE Technol. Soc. Mag.* **2010**, 29, 22–30.

McCleverty, J.A.; Meyer, T.J. Comprehensive Coordination Chemistry II From Biology to Nanotechnology. Elsivier, Amsterdam, 2003.

McMeekin, D.P.; Sadoughi, G.; Rehman, W.; Eperon, G.E.; Saliba, M.; Hörantner, M.T.; Haghighirad, A.; Sakai, N.; Korte, L.; Rech, B.; Johnston, M.B.; Herz, L.M.; Snaith, H.J. A mixed-cation lead mixed-halide perovskite absorber for tandem solar cells. *Science*, **2016**, 351, 151–155.

McPherson, G. L.; Wall Jr, J. E.; Hermann, A. M. Electrical, Magnetic, and Spectroscopic Properties of $CsNiI_3$. *Inorg. Chem.* **1974**, 13, 2230–2233.

Meek, D. W.; Straub, D. K.; Drago, R. S. Transition Metal Ion Complexes of Dimethyl Sulfoxide. *J. Am. Chem. Soc.* **1960**, 82, 6013–6016.

Meng, L.; Sun, C.; Wang, R.; Huang, W.; Zhao, Z.; Sun, P.; Huang, T.; Xue, J.; Lee, J.-W.; Zhu, C.; Huang, Y.; Li, Y.; Yang, Y. Tailored Phase Conversion under Conjugated Polymer Enables Thermally Stable Perovskite Solar Cells with Efficiency Exceeding 21%. *J. Am. Chem. Soc.* **2018**. *140*, 17255-17262.

Merdasa, A.; Bag, M.; Tian, Y.; Källman, E.; Dobrovolsky, A.; Scheblykin, I. G. Super-Resolution Luminescence Microspectroscopy Reveals the Mechanism of Photoinduced Degradation in $CH_3NH_3PbI_3$ Perovskite Nanocrystals. *J. Phys. Chem. C* **2016**, 120, 10711–10719.

Middlebrook, A. M.; Iraci, L. T.; McNeill, L. S.; Koehler, B. G.; Wilson, M. A.; Saastad, O. W.; Tolbert, M. A.; Hanson, D. R. Fourier Transform-Infrared Studies of Thin H_2SO_4/H_2O Films: Formation, Water Uptake, and Solid-Liquid Phase Changes. *J. Geophys. Res. Atmospheres* **1993**, 98, 20473–20481.

Miller, S. Temperature Controlled Variable Reflectivity Coatings. US 9,422,712 B2, August 23, 2016.

Mir, W. J.; Warankar, A.; Acharya, A.; Das, S.; Mandal, P.; Nag, A. Colloidal Thallium Halide Nanocrystals with Reasonable Luminescence, Carrier Mobility and Diffusion Length. *Chem. Sci.* **2017**, 8, 4602–4611.

Mitzi, D. B.; Wang, S.; Feild, C. A.; Chess, C. A.; Guloy, A. M. Conducting Layered Organic-Inorganic Halides Containing -Oriented Perovskite Sheets. *Science* **1995**, 267, 1473–1476.

Mitzi, D.B.; Field, C.A.; Schlesinger, Z.; Laibowitz, R.B. Transport, Optical, and Magnetic Properties of the Conducting Halide Perovskite $CH_3NH_3SnI_3$. *J. Solid State Chem.* **1995**, 114, 159–163.

Møller, C.K. Crystal Structure and Photoconductivity of Cesium Plumbohalides. *Nature* **1958**, 182, 1436.

Mosconi, E.; Merabet, B.; Meggiolaro, D.; Zaoui, A.; De Angelis, F. First-Principles Modeling of Bismuth Doping in the $MAPbI_3$ Perovskite. *J. Phys. Chem. C* **2018**, *122*, 14107-14112.

Müller, C.; Glaser, T.; Plogmeyer, M.; Sendner, M.; Döring, S.; Bakulin, A. A.; Brzuska, C.; Scheer, R.; Pshenichnikov, M. S.; Kowalsky, W.; et al. Water Infiltration in Methylammonium Lead Iodide Perovskite: Fast and Inconspicuous. *Chem. Mater.* **2015**, 27, 7835–7841.

Munshi, A.H.; Kephart, J.; Abbas, A.; Raguse, J.; Beaudry, J.-N.; Barth, K.; Sites, J.; Walls, J.; Sampath, W. Polycrystalline CdSeTe/CdTe Absorber Cells With 28 mA/cm^2 Short-Circuit Current. *IEEE J. Photovolt.* **2018**, 8, 310–314.

Munsi, A.; Sampath, W.S. CdTe Photovoltaics for Sustainable Electricity Generation. *J. Elect. Mat.* **2016**, 45, 4612-4619.

Murali, B.; Dey, S.; Abdelhady, A. L.; Peng, W.; Alarousu, E.; Kirmani, A. R.; Cho, N.; Sarmah, S. P.; Parida, M. R.; Saidaminov, M. I.; Zhumekenov, A. A.; Sun, J.; Alias, M. S.; Yengel, E.; Ooi, B. S.; Amassian, A.; Bakr, O. M.; Mohammed, O. F. Surface Restructuring of Hybrid Perovskite Crystals. *ACS Energy Lett.* **2016**, *1*, 1119–1126.

Naumkin, A. V.; Kraut-Vass, A.; Gaarenstroom, S. W.; Powell, C. J. NIST X-Ray Photoelectron Spectroscopy Database, NIST Standard Reference Database Number 20. National Institute of Standards and Technology, Gaithersburg, MD, 20899 2000.

Nayak, P. K.; Sendner, M.; Wenger, B.; Wang, Z.; Sharma, K.; Ramadan, A. J.; Lovrinčić, R.; Pucci, A.; Madhu, P. K.; Snaith, H. J. Impact of Bi^{3+} Heterovalent Doping in Organic–Inorganic Metal Halide Perovskite Crystals. *J. Am. Chem. Soc.* **2018**, 140, 574–577.

Nelson, J. *The Physics of Solar Cells*. Imperial College Press: London, UK, 2003.

Nienhaus, L.; Correa-Baena, J.-P.; Wieghold, S.; Einzinger, M.; Lin, T.-A.; Shulenberger, K. E.; Klein, N. D.; Wu, M.; Bulović, V.; Buonassisi, T.; et al. Triplet-Sensitization by Lead Halide Perovskite Thin Films for Near-Infrared-to-Visible Upconversion. *ACS Energy Lett.* **2019**, 4, 888–895.

Noh, J. H.; Im, S. H.; Heo, J. H.; Mandal, T. N.; Seok, S. I. Chemical Management for Colorful, Efficient, and Stable Inorganic–Organic Hybrid Nanostructured Solar Cells. *Nano Lett.* **2013**, 13, 1764–1769.

Notman, R.; den Otter, W. K.; Noro, M. G.; Briels, W. J.; Anwar, J. The Permeability Enhancing Mechanism of DMSO in Ceramide Bilayers Simulated by Molecular Dynamics. *Biophys. J.* **2007**, 93, 2056–2068.

Ohring, M. *Material Science of Thin Films*, 2nd ed.; Academic Press: San Diego, 2002.

Paetzold, U.W.; Jaysankar, M.; Gehlhaar, R.; Ahlswede, E.; Paetel, S.; Qiu, W.; Bastos, J.; Rakocevic, L.; Richards, B.S.; Aernouts, T.; Powalla, M.; Poortmans, J. Scalable perovskite/CIGS thin-film solar module with power conversion efficiency of 17.8%. *J. Mater. Chem. A*, **2017**, 5, 9897–9906.

Pariya, C.; Ghosh, A.; Chaudhuri, N. R. Thermal Studies of N^1-Isopropyl-2-Methyl-1,2-Propanediamine Complexes of Nickel(II)X_2 [X = I^-, CF_3CO^{-2}, $0.5SO_2^{-4}$, and $0.5SeO_2^{-4}$] in the Solid State. *Thermochim. Acta* **1995**, 268, 153–160. https://doi.org/10.1016/0040-6031(95)02436-0.

Park, B.; Kedem, N.; Kulbak, M.; Lee, D. Y.; Yang, W. S.; Jeon, N. J.; Seo, J.; Kim, G.; Kim, K. J.; Shin, T. J.; Hodes, G.; Cahen, D.; Seok, S.I. Understanding How Excess Lead Iodide Precursor Improves Halide Perovskite Solar Cell Performance. *Nat. Commun.* **2018**, *9*, 3301.

Park, J.-S.; Choi, S.; Yan, Y.; Yang, Y.; Luther, J. M.; Wei, S.-H.; Parilla, P.; Zhu, K. Electronic Structure and Optical Properties of α-$CH_3NH_3PbBr_3$ Perovskite Single Crystal, *J. Phys. Chem. Lett.* **2015**, *6*, 4304-4308.

Parrott, E.S.; Green, T.; Milot, R.L.; Johnston, M.B.; Snaith, H.J.; Herz, L.M. Interplay of Structural and Optoelectronic Properties in Formamidinium Mixed Tin-Lead Triiodide Perovskites. *Adv. Funct. Mater*, **2018**, 28, 1802803.

Peng, J.; Duong, T.; Zhou, X.; Shen, H.; Wu, Y.; Mulmudi, H.K.; Wan, Y.; Zhong, D.; Li, J.; Tsuzuki, T.; Weber, K.J.; Catchpole, K.R.; White, T.P. Efficient Indium-Doped TiOx Electron Transport Layers for High-Performance Perovskite Solar Cells and Perovskite-Silicon Tandems. *Adv. Energy Mater.*, **2017**, 7, 1601768.

Peters, S. J.; Ewing, G. E. Water on Salt: An Infrared Study of Adsorbed H_2O on NaCl (100) under Ambient Conditions. *J. Phys. Chem. B* **1997**, 101, 10880–10886.

Pisoni, S.; Fu, F.; Feurer, T.; Makha, M.; Bissig, B.; Nishiwaki, S.; Tiwari, A.N.; Buecheler, S. Flexible NIR-transparent perovskite solar cells for all-thin-film tandem photovoltaic devices. *J. Mater. Chem. A*, **2017**, 5, 13639–13647.

Polman, A.; Knight, M.; Garnett, E. C.; Ehrler, B.; Sinke, W. C. Photovoltaic Materials: Present Efficiencies and Future Challenges. *Science* **2016**, 352, aad4424.

Price, D. This Entrepreneur Plans to Save the World, $1 Trillion at a Time. *Entrepreneur Asia Pacific*. February 17, 2015.

Protesescu, L.; Yakunin, S.; Bodnarchuk, M. I.; Krieg, F.; Caputo, R.; Hendon, C. H.; Yang, R. X.; Walsh, A.; Kovalenko, M. V. Nanocrystals of Cesium Lead Halide Perovskites ($CsPbX_3$, X=Cl, Br, and I): Novel Optoelectronic Materials Showing Bright Emission with Wide Color Gamut. *Nano Lett.* **2015**, 15, 3692–3696.

Protesescu, L.; Yakunin, S.; Kumar, S.; Bär, J.; Bertolotti, F.; Masciocchi, N.; Guagliardi, A.; Grotevent, M.; Shorubalko, I.; Bodnarchuk, M. I.; et al. Dismantling the "Red Wall" of Colloidal Perovskites: Highly Luminescent Formamidinium and Formamidinium–Cesium Lead Iodide Nanocrystals. *ACS Nano* **2017**, *11*, 3119–3134.

Publicover, B. Oxford PV Raises $41m to Commercialize Perovskite Tech. *PV Magazine*. March 20, 2019.

Qiao, H. W.; Yang, S.; Wang, Y.; Chen, X.; Wen, T. Y.; Tang, L. J.; Cheng, Q.; Hou, Y.; Zhao, H.; Yang, H. G. A Gradient Heterostructure Based on Tolerance Factor in High-Performance Perovskite Solar Cells with 0.84 Fill Factor. *Adv. Mater.* **2019**, *31*, 1804217.

Quarti, C.; Grancini, G.; Mosconi, E.; Bruno, P.; Ball, J. M.; Lee, M. M.; Snaith, H. J.; Petrozza, A.; Angelis, F. D. The Raman Spectrum of the $CH_3NH_3PbI_3$ Hybrid Perovskite: Interplay of Theory and Experiment. *J. Phys. Chem. Lett.* **2014**, 5, 279–284.

Rajagopal, A.; Yang, Z.; Jo, S.B.; Braly, I.L.; Liang, P.-W.; Hillhouse, H.W.; Jen, A.K.-Y. Highly Efficient Perovskite-Perovskite Tandem Solar Cells Reaching 80% of the Theoretical Limit in Photovoltage. *Adv. Mater.*, **2017**, 29, 1702140.

Ramírez Quiroz, C.O.; Shen, Y.; Salvador, M.; Forberich, K.; Schrenker, N.; Spyropoulos, G.D.; Heumüller, T.; Wilkinson, B.; Kirchartz, T.; Spiecker, E.; Verlinden, P.J.; Zhang, X.; Green, M.A.; Ho-Baillie, A.; Brabec, C.J. Balancing electrical and optical losses for efficient 4-terminal Si–perovskite solar cells with solution processed percolation electrodes. *J. Mater. Chem. A*, **2018**, 6, 3583–3592.

Raugei, M.; Bargigli, S.; Ulgiati, S. Life cycle assessment and energy pay-back time of advanced photovoltaic modules: CdTe and CIS compared to poly-Si. *Energy.* **2007,** 32, 1310–1318.

Rehman, W.; McMeekin, D.P.; Patel, J.B.; Milot, R.L.; Johnston, M.B.; Snaith, H.J.; Herz, L.M. Photovoltaic mixed-cation lead mixed-halide perovskites: links between crystallinity, photo-stability and electronic properties. *Energy Environ. Sci.*, **2017**, 10, 361–369.

Rehman, W.; Milot, R.L.; Eperon, G.E.; Wehrenfennig, C.; Boland, J.L.; Snaith, H.J.; Johnston, M.B.; Herz, L.M. Charge-Carrier Dynamics and Mobilities in Formamidinium Lead Mixed-Halide Perovskites. *Adv. Mater.*, **2015**, 27, 7938–7944.

Rühle, S. Tabulated values of the Shockley–Queisser limit for single junction solar cells. *Sol. Energy*, **2016**, 130, 139–147.

Rühle, S. The detailed balance limit of perovskite/silicon and perovskite/CdTe tandem solar cells. *Phys. Status Solidi A*, **2017**, 214, 1600955.

Sahli, F.; Kamino, B.A.; Werner, J.; Bräuninger, M.; Paviet-Salomon, B.; Barraud, L.; Monnard, R.; Seif, J.P.; Tomasi, A.; Jeangros, Q.; Hessler-Wyser, A.; De Wolf, S.; Despeisse, M.; Nicolay, S.; Niesen, B.; Ballif, C. Improved Optics in Monolithic Perovskite/Silicon Tandem Solar Cells with a Nanocrystalline Silicon Recombination Junction. *Adv. Energy Mater.*, **2018**, 8, 1701609.

Sahli, F.; Werner, J.; Kamino, B.A.; Bräuninger, M.; Monnard, R.; Paviet-Salomon, B.; Barraud, L.; Ding, L.; Diaz Leon, J.J.; Sacchetto, D.; Cattaneo, G.; Despeisse, M.; Boccard, M.; Nicolay, S.; Jeangros, Q.; Niesen, B.; Ballif, C. Fully textured monolithic perovskite/silicon tandem solar cells with 25.2% power conversion efficiency. *Nat. Mater.*, **2018**, 17, 820-826.

Saliba, M.; Correa-Baena, J.-P.; Grätzel, M.; Hagfeldt, A.; Abate, A. Perovskite Solar Cells: From the Atomic Level to Film Quality and Device Performance. *Angew. Chem. Int. Ed.* **2018**, 57, 2554–2569.

Saliba, M.; Matsui, T.; Seo, J.-Y.; Domanski, K.; Correa-Baena, J.-P.; Nazeeruddin, M. K.; Zakeeruddin, S. M.; Tress, W.; Abate, A.; Hagfeldt, A.; et al. Cesium-Containing Triple Cation Perovskite Solar Cells: Improved Stability, Reproducibility and High Efficiency. *Energy Env. Sci* **2016**, 9, 1989–1997.

Saliba, M.; Tan, K. W.; Sai, H.; Moore, D. T.; Scott, T.; Zhang, W.; Estroff, L. A.; Wiesner, U.; Snaith, H. J. Influence of Thermal Processing Protocol upon the Crystallization and Photovoltaic Performance of Organic–Inorganic Lead Trihalide Perovskites. *J. Phys. Chem. C* **2014**, *118*, 17171–17177.

Sanehira, E. M.; Marshall, A. R.; Christians, J. A.; Harvey, S. P.; Ciesielski, P. N.; Wheeler, L. M.; Schulz, P.; Lin, L. Y.; Beard, M. C.; Luther, J. M. Enhanced Mobility $CsPbI_3$ Quantum Dot Arrays for Record-Efficiency, High-Voltage Photovoltaic Cells. *Sci. Adv.* **2017**, 3, eaao4204.

Sanehira, E. M.; Tremolet de Villers, B. J.; Schulz, P.; Reese, M. O.; Ferrere, S.; Zhu, K.; Lin, L. Y.; Berry, J. J.; Luther, J. M. Influence of Electrode Interfaces on the Stability of Perovskite Solar Cells: Reduced Degradation Using MoO_x/Al for Hole Collection. *ACS Energy Lett.* **2016**, *1*, 38–45.

Scatena, L. F.; Brown, M.G.; Richmond, G.L. Water at Hydrophobic Surfaces: Weak Hydrogen Bonding and Strong Orientation Effects. *Science* **2001**, 292, 908–912.

Schlipf, J.; Bießmann, L.; Oesinghaus, L.; Berger, E.; Metwalli, E.; Lercher, J. A.; Porcar, L.; Müller-Buschbaum, P. In Situ Monitoring the Uptake of Moisture into Hybrid Perovskite Thin Films. *J. Phys. Chem. Lett.* **2018**, 9, 2015–2021.

Schneider, B.W.; Lal, N.N.; Baker-Finch, S.; White, T.P. Pyramidal surface textures for light trapping and antireflection in perovskite-on-silicon tandem solar cells. *Opt. Express*, **2014**, 22, A1422-A1430.

Schumann, H. Synthese Und Spektroskopische Untersuchungen von Nickelkomplexen mit Substituierten Dibenzotetraaza[14] Annulenliganden. *Z. Naturforschung B* **1996**, 51, 989–998.

SEIA and Greentech Media, 2017. Solar Market Insight Report 2016 Year in Review. SEIA, Washington, D.C. USA

Seifert, A.; Vojta, A.; Speck, J. S.; Lange, F. F. Microstructural Instability in Single-Crystal Thin Films. *J. Mater. Res.* **1996**, *11*, 1470–1482.

Shah, K.S.; Lund, J.C.; Olschner, F.; Moy, L.; Squillante, M.R. Thallium Bromide Radiation Detectors. *IEEE Trans. Nucl. Sci.* **1989**, 36, 199–202.

Shannon, R. D. Revised Effective Ionic Radii and Systematic Studies of Interatomic Distances in Halides and Chalcogenides. *Acta Crystallogr. A* **1976**, *32*, 751–767.

Sharma, G. Nepal Scraps $2.5 Bln Hydropower Plant Deal with Chinese Company. *Reuters*. Kathmandu November 13, 2017.

Shen, H.; Duong, T.; Peng, J.; Jacobs, D.; Wu, N.; Gong, J.; Wu, Y.; Karuturi, S.K.; Fu, X.; Weber, K.; Xiao, X.; White, T.P.; Catchpole, K. Mechanically-stacked perovskite/CIGS tandem solar cells with efficiency of 23.9% and reduced oxygen sensitivity. *Energy Environ. Sci.*, **2018**, 11, 394–406.

Sheng, R.; Ho-Baillie, A.W.Y.; Huang, S.; Keevers, M.; Hao, X.; Jiang, L.; Cheng, Y.-B.; Green, M.A. Four-Terminal Tandem Solar Cells Using $CH_3NH_3PbBr_3$ by Spectrum Splitting. *J. Phys. Chem. Lett.*, **2015**, 6, 3931–3934.

Sheng, R.; Hörantner, M.T.; Wang, Z.; Jiang, Y.; Zhang, W.; Agosti, A.; Huang, S.; Hao, X.; Ho-Baillie, A.; Green, M.; Snaith, H.J. Monolithic Wide Band Gap Perovskite/Perovskite Tandem Solar Cells with Organic Recombination Layers. *J. Phys. Chem. C*, **2017**, 121, 27256–27262.

Shi, D.; Zeng, Y.; Shen, W. Perovskite/c-Si tandem solar cell with inverted nanopyramids: realizing high efficiency by controllable light trapping. *Sci. Rep.*, **2015**, 5, 16504.

Shockley, W.; Queisser, H. J. Detailed Balance Limit of Efficiency of P-n Junction Solar Cells. *J. Appl. Phys.* **1961**, 32, 510.

Sigman, M.B.; Korgel, B.A. Strongly Birefringent $Pb_3O_2Cl_2$ Nanobelts. *J. Am. Chem. Soc.*, **2005**, 127, 10089–10095.

Skansa. Skansa and Saule Technologies Commence Revolutionary Solar Panels Test. Warsaw, Poland December 13, 2018.

Slavney, A. H.; Hu, T.; Lindenberg, A. M.; Karunadasa, H. I. A Bismuth-Halide Double Perovskite with Long Carrier Recombination Lifetime for Photovoltaic Applications. *J. Am. Chem. Soc.* **2016**, 138, 2138–2141.

Slavney, A. H.; Leppert, L.; Bartesaghi, D.; Gold-Parker, A.; Toney, M. F.; Savenije, T. J.; Neaton, J. B.; Karunadasa, H. I. Defect-Induced Band-Edge Reconstruction of a Bismuth-Halide Double Perovskite for Visible-Light Absorption. *J. Am. Chem. Soc.* **2017**, 139, 5015–5018.

Slavney, A. H.; Leppert, L.; Saldivar Valdes, A.; Bartesaghi, D.; Savenije, T. J.; Neaton, J. B.; Karunadasa, H. Small-Bandgap Halide Double Perovskites. *Angew. Chem. Int. Ed.* **2018**, 57, 12765–12770.

Smil, V. *Energy Transitions: History, Requirements, Prospects*; Praeger: Santa Barbara, 2010.

Sofia, S. E.; Mailoa, J. P.; Weiss, D. N.; Stanbery, B. J.; Buonassisi, T.; Peters, I. M. Economic Viability of Thin-Film Tandem Solar Modules in the United States. *Nat. Energy* **2018**, 3, 387–394.

Sofia, S.E.; Mailoa, J.P.; Weiss, D.N.; Stanbery, B.J.; Buonassisi, T.; Peters, I.M. Economic viability of thin-film tandem solar modules in the United States. *Nat. Energy*, **2018**, 3, 387–394.

Song, Z.; Watthage, S. C.; Phillips, A. B.; Tompkins, B. L.; Ellingson, R. J.; Heben, M. J. Impact of Processing Temperature and Composition on the Formation of Methylammonium Lead Iodide Perovskites. *Chem. Mater.* **2015**, 27, 4612–4619.

Song, Z.; Werner, J.; Shrestha, N.; Sahli, F.; De Wolf, S.; Niesen, B.; Watthage, S.C.; Phillips, A.B.; Ballif, C.; Ellingson, R.J.; Heben, M.J. Probing Photocurrent Nonuniformities in the Subcells of Monolithic Perovskite/Silicon Tandem Solar Cells. *J. Phys. Chem. Lett.*, **2016**, 7, 5114–5120.

Srimath Kandada, A. R.; Neutzner, S.; D'Innocenzo, V.; Tassone, F.; Gandini, M.; Akkerman, Q. A.; Prato, M.; Manna, L.; Petrozza, A.; Lanzani, G. Nonlinear Carrier Interactions in Lead Halide Perovskites and the Role of Defects. *J. Am. Chem. Soc.* **2016**, *138*, 13604–13611.

Starcoat® T5 High Efficiency and High Output. 2013.

Stewart, R. J.; Grieco, C.; Larsen, A. V.; Doucette, G. S.; Asbury, J. B. Molecular Origins of Defects in Organohalide Perovskites and Their Influence on Charge Carrier Dynamics. *J. Phys. Chem. C* **2016**, *120*, 12392–12402.

Stirrat, C. R.; Newman, P. R.; Cowen, J. A. $NiI_2 \cdot 6H_2O$: A Disordered Linear Chain Magnet. *AIP Conference Proceedings.* **1976**, 34, 199–201.

Stolle, C. J.; Schaller, R. D.; Korgel, B. A. Efficient Carrier Multiplication in Colloidal $CuInSe_2$ Nanocrystals. *J. Phys. Chem. Lett.* **2014**, *5*, 3169–3174.

Sun, T.-W.; Xu, Q.-Y.; Zhang, X.-J.; Wu, Q.; Liu, Z.-S.; Kan, Q.-C.; Sun, C.-Y.; Wang, L. Management of Thallium Poisoning in Patients with Delayed Hospital Admission. *Clin. Toxicol.* **2012**, 50, 65–69.

Sun, X.; Huang, D.; Wu, G. The Current State of Offshore Wind Energy Technology Development. *Energy* **2012**, 41, 298–312.

Sutton, R.J.; Eperon, G.E.; Miranda, L.; Parrott, E.S.; Kamino, B.A.; Patel, J.B.; Hörantner, M.T.; Johnston, M.B.; Haghighirad, A.A.; Moore, D.T.; Snaith, H.J. Bandgap-Tunable Cesium Lead Halide Perovskites with High Thermal Stability for Efficient Solar Cells. *Adv. Energy Mater.*, **2016**, 6, 1502458.

Swanson, D.E.; Reich, C.; Abbas, A.; Shimpi, T.; Liu, H.; Ponce, F.A.; Walls, J.M.; Zhang, Y.-H.; Metzger, W.K.; Sampath, W.S.; Holman, Z.C. $CdCl_2$ passivation of polycrystalline CdMgTe and CdZnTe absorbers for tandem photovoltaic cells. *J. Appl. Phys.*, **2018**, 123, 203101.

Swarnkar, A.; Mir, W. J.; Nag, A. Can B-Site Doping or Alloying Improve Thermal- and Phase-Stability of All-Inorganic $CsPbX_3$ (X = Cl, Br, I) Perovskites? *ACS Energy Lett.* **2018**, 3, 286–289.

Tai, Q.; You, P.; Sang, H.; Liu, Z.; Hu, C.; Chan, H. L. W.; Yan, F. Efficient and Stable Perovskite Solar Cells Prepared in Ambient Air Irrespective of the Humidity. *Nature Commun.* **2016**, 7, 11105.

Tao, A. R.; Habas, S.; Yang, P. Shape Control of Colloidal Metal Nanocrystals. *Small* **2008**, *4*, 310–325.

Thomas A Germer; Joanne C Zwinkels; Benjamin K Tsai. *Spectrophotometry: Accurate Measurement of Optical Properties of Materials*; Experimental Methods in the Physical Sciences; Elsevier Science: Waltham, MA, USA, 2014; Vol. 46.

Thompson, C. V. Structure Evolution During Processing of Polycrystalline Films. *Annu. Rev. Mater. Sci.* **2000**, *30*, 159–190.

Todorov, T.; Gershon, T.; Gunawan, O.; Lee, Y.S.; Sturdevant, C.; Chang, L.-Y.; Guha, S. Monolithic Perovskite-CIGS Tandem Solar Cells via In Situ Band Gap Engineering. *Adv. Energy Mater.*, **2015**, 5, 1500799.

Todorov, T.; Gershon, T.; Gunawan, O.; Sturdevant, C.; Guha, S. Perovskite-kesterite monolithic tandem solar cells with high open-circuit voltage. *Appl. Phys. Lett.*, **2014**, 105, 173902.

Todorov, T.K.; Gunawan, O.; Guha, S. In *Halide Perovskites: Photovoltaics, Light Emitting Diodes, and Beyond*; T.C. Sum, N. Mathews, Eds.; Wiley: Weinheim, Germany, 2018; Chapter 2.5 pp 83-99

Tong, J.; Song, Z.; Kim, D. H.; Chen, X.; Chen, C.; Palmstrom, A. F.; Ndione, P. F.; Reese, M. O.; Dunfield, S. P.; Reid, O. G.; et al. Carrier Lifetimes of >1 μs in Sn-Pb Perovskites Enable Efficient All-Perovskite Tandem Solar Cells. **2019**, 364, 475-479.

Uhl, A. R.; Yang, Z.; Jen, A. K.-Y.; Hillhouse, H. W. Solution-Processed Chalcopyrite–Perovskite Tandem Solar Cells in Bandgap-Matched Two- and Four-Terminal Architectures. *J. Mater. Chem. A* **2017**, 5, 3214–3220.

Unger, E. L.; Kegelmann, L.; Suchan, K.; Sörell, D.; Korte, L.; Albrecht, S. Roadmap and Roadblocks for the Band Gap Tunability of Metal Halide Perovskites. *J. Mater. Chem. A* **2017**, 5, 11401–11409.

Uzu, H.; Ichikawa, M.; Hino, M.; Nakano, K.; Meguro, T.; Hernández, J.L.; Kim, H.-S.; Park, N.-G.; Yamamoto, K. High efficiency solar cells combining a perovskite and a silicon heterojunction solar cells via an optical splitting system. *Appl. Phys. Lett.*, **2015**, 106, 013506.

Vashishtha, P.; Metin, D. Z.; Cryer, M. E.; Chen, K.; Hodgkiss, J. M.; Gaston, N.; Halpert, J. E. Shape-, Size-, and Composition-Controlled Thallium Lead Halide Perovskite Nanowires and Nanocrystals with Tunable Band Gaps. *Chem. Mater.* **2018**, 30, 2973–2982.

Veldhuis, S. A.; Boix, P. P.; Yantara, N.; Li, M.; Sum, T. C.; Mathews, N.; Mhaisalkar, S. G. Perovskite Materials for Light-Emitting Diodes and Lasers. *Adv. Mater.* **2016**, 28, 6804–6834.

Venkatesan, N. R.; Labram, J. G.; Chabinyc, M. L. Charge-Carrier Dynamics and Crystalline Texture of Layered Ruddlesden–Popper Hybrid Lead Iodide Perovskite Thin Films. *ACS Energy Lett.* **2018**, *3*, 380–386.

Voggu, V. R.; Sham, J.; Pfeffer, S.; Pate, J.; Fillip, L.; Harvey, T. B.; Brown, R. M.; Korgel, B. A. Flexible $CuInSe_2$ Nanocrystal Solar Cells on Paper. *ACS Energy Lett.* **2017**, 2, 574–581.

Vos, A.D. Detailed balance limit of the efficiency of tandem solar cells. *J. Phys. D: Appl. Phys.*, **1980**, 13, 839–846.

Wang, J. T.-W.; Wang, Z.; Pathak, S.; Zhang, W.; deQuilettes, D. W.; Wisnivesky-Rocca-Rivarola, F.; Huang, J.; Nayak, P. K.; Patel, J. B.; Mohd Yusof, H. A.; et al. Efficient Perovskite Solar Cells by Metal Ion Doping. *Energy Env. Sci* **2016**, 9, 2892–2901.

Wang, J.; Fu, W.; Jariwala, S.; Sinha, I.; Jen, A. K.-Y.; Ginger, D. S. Reducing Surface Recombination Velocities at the Electrical Contacts Will Improve Perovskite Photovoltaics. *ACS Energy Lett.* **2019**, *4*, 222–227.

Wang, Y.; Fu, W.; Yan, J.; Chen, J.; Yang, W.; Chen, H. Low-bandgap mixed tin–lead iodide perovskite with large grains for high performance solar cells. *J. Mater. Chem. A*, **2018**, 6, 13090–13095.

Wang, Y.; Sun, X.; Chen, Z.; Sun, Y.-Y.; Zhang, S.; Lu, T.-M.; Wertz, E.; Shi, J. High-Temperature Ionic Epitaxy of Halide Perovskite Thin Film and the Hidden Carrier Dynamics. *Adv. Mater.* **2017**, *29*, 1702643.

Wang, Z.; Jin, K.; Zhang, Y.; Wang, F.; Zhu, Z. ToF-SIMS Depth Profiling of Insulating Samples, Interlaced Mode or Non-Interlaced Mode? *Surf. Interface Anal.* **2014**, *46*, 257–260.

Wang, Z.; Lin, Q.; Chmiel, F. P.; Sakai, N.; Herz, L. M.; Snaith, H. J. Efficient Ambient-Air-Stable Solar Cells with 2D–3D Heterostructured Butylammonium-Caesium-Formamidinium Lead Halide Perovskites. *Nat. Energy* **2017**, *2*, 17135.

Wang, Z.-K.; Li, M.; Yang, Y.-G.; Hu, Y.; Ma, H.; Gao, X.-Y.; Liao, L.-S. High Efficiency Pb-In Binary Metal Perovskite Solar Cells. *Adv. Mater.* **2016**, *28*, 6695-6703.

Weber, D. $CH_3NH_3PbX_3$, ein Pb(II)-System mit kubischer Perowskitstruktur/$CH_3NH_3PbX_3$, a Pb(II)-System with Cubic Perovskite Structure. *Z. Für Naturforschung B* **1978**, 33, 1443–1445.

Weber, D. $CH_3NH_3SnBr_xI_{3-x}$ (x=0-3), ein Sn(II)-System mit kubischer Perowskitstruktur. *Z. Für Naturforschung B* **1978**, 33, 4.

Weissbuch, I.; Guo, S.; Edgar, R.; Cohen, S.; Howes, P.; Kjaer, K.; Als-Nielsen, J.; Lahav, M.; Leiserowitz, L. Oriented Crystalline Thin Films of Tetracosanedioic Acid and Its Metal Salts at the Air-Aqueous Solution Interface. *Adv. Mater.* **1998**, *10*, 117–121.

Wells, H.L. Über die Cäsium- und Kalium-Bleihalogenide. *Z. Für Anorg. Chem.* **1893**, 3, 195–210.

Werner, J.; Barraud, L.; Walter, A.; Bräuninger, M.; Sahli, F.; Sacchetto, D.; Tétreault, N.; Paviet-Salomon, B.; Moon, S.-J.; Allebé, C.; Despeisse, M.; Nicolay, S.; De Wolf, S.; Niesen, B.; Ballif, C. Efficient Near-Infrared-Transparent Perovskite Solar Cells Enabling Direct Comparison of 4-Terminal and Monolithic Perovskite/Silicon Tandem Cells. *ACS Energy Lett.*, **2016**, 1, 474–480.

Werner, J.; Dubuis, G.; Walter, A.; Löper, P.; Moon, S.-J.; Nicolay, S.; Morales-Masis, M.; De Wolf, S.; Niesen, B.; Ballif, C. Sputtered rear electrode with broadband transparency for perovskite solar cells. *Sol. Energy Mater. Sol. Cells*, **2015**, 141, 407–413.

Werner, J.; Niesen, B.; Ballif, C. Perovskite/Silicon Tandem Solar Cells: Marriage of Convenience or True Love Story? - An Overview. *Adv. Mater. Interfaces*. **2018,** 5, 1700731.

Werner, J.; Sahli, F.; Fu, F.; Diaz Leon, J. J.; Walter, A.; Kamino, B. A.; Niesen, B.; Nicolay, S.; Jeangros, Q.; Ballif, C. Perovskite/Perovskite/Silicon Monolithic Triple-Junction Solar Cells with a Fully Textured Design. *ACS Energy Lett.* **2018**, 3, 2052–2058.

Werner, J.; Walter, A.; Rucavado, E.; Moon, S.-J.; Sacchetto, D.; Rienaecker, M.; Peibst, R.; Brendel, R.; Niquille, X.; De Wolf, S.; Löper, P.; Morales-Masis, M.; Nicolay, S.; Niesen, B.; Ballif, C. Zinc tin oxide as high-temperature stable recombination layer for mesoscopic perovskite/silicon monolithic tandem solar cells. *Appl. Phys. Lett.*, **2016**, 109, 233902.

Werner, J.; Weng, C.-H.; Walter, A.; Fesquet, L.; Seif, J. P.; De Wolf, S.; Niesen, B.; Ballif, C. Efficient Monolithic Perovskite/Silicon Tandem Solar Cell with Cell Area >1 cm ^{2}. *J. Phys. Chem. Lett.* **2016**, 7, 161–166.

Wheeler, L. M.; Sanehira, E. M.; Marshall, A. R.; Schulz, P.; Suri, M.; Anderson, N. C.; Christians, J. A.; Nordlund, D.; Sokaras, D.; Kroll, T.; Harvey, S.P; Berry, J.J; Lin, L.Y; Luther, J.M. Targeted Ligand-Exchange Chemistry on Cesium Lead Halide Perovskite Quantum Dots for High-Efficiency Photovoltaics. *J. Am. Chem. Soc.* **2018**, 140, 10504–10513.

Wheeler, L.M., Moore, D.T., Ihly, R., Stanton, N.J., Miller, E.M., Tenent, R.C., Blackburn, J.L., Neale, N.R. Switchable Photovoltaic Windows Enabled by Reversible Photothermal Complex Dissociation from Methylammonium Lead Iodide. *Nature Commun.* **2017**, 8, 1722.

Winemiller, K. O.; McIntyre, P. B.; Castello, L.; Fluet-Chouinard, E.; Giarrizzo, T.; Nam, S.; Baird, I. G.; Darwall, W.; Lujan, N. K.; Harrison, I.; et al. Balancing Hydropower and Biodiversity in the Amazon, Congo, and Mekong. *Science* **2016**, 351, 128–129.

Winterbottom, W. L. Equilibrium Shape of a Small Particle in Contact with a Foreign Substrate. *Acta Metall.* **1967**, *15*, 303–310.

Woodhouse, M.; Jones-Albertus, R.; Feldman, D.; Fu, R.; Horowitz, K.; Chung, D.; Jordan, D.; Kurtz, S. *On the Path to SunShot: The Role of Advancements in Solar Photovoltaic Efficiency, Reliablity, and Cost*; NREL/TP-6A20-65872; National Renewable Energy Laboratory, 2016.

Wrigley, E. A. Energy and the English Industrial Revolution. *Philos. Trans. R. Soc. Math. Phys. Eng. Sci.* **2013**, 371, 20110568–20110568.

Wu, B.; Yuan, H.; Xu, Q.; Steele, J. A.; Giovanni, D.; Puech, P.; Fu, J.; Ng, Y. F.; Jamaludin, N. F.; Solanki, A.; Mhaisalkar, S.; Mathews, N.; Roeffaers, M. B. J.; Grätzel, M.; Hofkens, J.; Sum, T. C. Indirect Tail States Formation by Thermal-Induced Polar Fluctuations in Halide Perovskites. *Nat. Commun.* **2019**, *10*, 484.

Wu, Y.; Yan, D.; Peng, J.; Duong, T.; Wan, Y.; Phang, S.P.; Shen, H.; Wu, N.; Barugkin, C.; Fu, X.; Surve, S.; Grant, D.; Walter, D.; White, T.P.; Catchpole, K.R.; Weber, K.J. Monolithic perovskite/silicon-homojunction tandem solar cell with over 22% efficiency. *Energy Environ. Sci.*, **2017**, 10, 2472–2479.

Wu, Z.; Liu, Z.; Hu, Z.; Hawash, Z.; Qiu, L.; Jiang, Y.; Ono, L. K.; Qi, Y. Highly Efficient and Stable Perovskite Solar Cells via Modification of Energy Levels at the Perovskite/Carbon Electrode Interface. *Adv. Mater.* **2019**, 31, 1804284.

Xiao, Z.; Yan, Y.; Hosono, H.; Kamiya, T. Roles of Pseudo-Closed s^2 Orbitals for Different Intrinsic Hole Generation between Tl–Bi and In–Bi Bromide Double Perovskites. *J. Phys. Chem. Lett.* **2018**, 9, 258–262.

Xu, W.; Liu, L.; Yang, L.; Shen, P.; Sun, B.; McLeod, J. A. Dissociation of Methylammonium Cations in Hybrid Organic–Inorganic Perovskite Solar Cells. *Nano Lett.* **2016**, 16, 4720–4725.

Xu, W.; Zheng, L.; Zhang, X.; Cao, Y.; Meng, T.; Wu, D.; Liu, L.; Hu, W.; Gong, X. Efficient Perovskite Solar Cells Fabricated by Co Partially Substituted Hybrid Perovskite. *Adv. Energy Mater.* **2018**, 8, 1703178.

Yakunin, S.; Dirin, D. N.; Shynkarenko, Y.; Morad, V.; Cherniukh, I.; Nazarenko, O.; Kreil, D.; Nauser, T.; Kovalenko, M. V. Detection of Gamma Photons Using Solution-Grown Single Crystals of Hybrid Lead Halide Perovskites. *Nat. Photonics* **2016**, 10, 585–589.

Yamada, Y.; Hoyano, M.; Akashi, R.; Oto, K.; Kanemitsu, Y. Impact of Chemical Doping on Optical Responses in Bismuth-Doped $CH_3NH_3PbBr_3$ Single Crystals: Carrier Lifetime and Photon Recycling. *J. Phys. Chem. Lett.* **2017**, 8, 5798–5803.

Yamamoto, K.; Iikubo, S.; Yamasaki, J.; Ogomi, Y.; Hayase, S. Structural Stability of Iodide Perovskite: A Combined Cluster Expansion Method and First-Principles Study. *J. Phys. Chem. C* **2017**, 121, 27797–27804.

Yang, W. S.; Noh, J. H.; Jeon, N. J.; Kim, Y. C.; Ryu, S.; Seo, J.; Seok, S. I. High-Performance Photovoltaic Perovskite Layers Fabricated through Intramolecular Exchange. *Science* **2015**, 348, 1234–1237.

Yang, Y. (Michael), Chen, Q.; Hsieh, Y.-T.; Song, T.-B.; Marco, N.D.; Zhou, H.; Yang, Y. Multilayer Transparent Top Electrode for Solution Processed Perovskite/$Cu(In,Ga)(Se,S)_2$ Four Terminal Tandem Solar Cells. *ACS Nano*, **2015**, 9, 7714–7721.

Yang, Z.; Rajagopal, A.; Chueh, C.-C.; Jo, S.B.; Liu, B.; Zhao, T.; Jen, A.K.-Y. Stable Low-Bandgap Pb-Sn Binary Perovskites for Tandem Solar Cells. *Adv. Mater.*, **2016**, 28, 8990–8997.

Yoshimura, K.; Bao, S. Color-Neutral Reflective Control Switchable Thin Film Material. US 7,414,772 B2, August 19, 2008.

Zhang, J.; Shang, M.; Wang, P.; Huang, X.; Xu, J.; Hu, Z.; Zhu, Y.; Han, L. N-Type Doping and Energy States Tuning in $CH_3NH_3Pb_{1-x}Sb_{2x/3}I_3$ Perovskite Solar Cells. *ACS Energy Lett.* **2016**, 1, 535–541.

Zhang, M.; Zheng, Z.; Fu, Q.; Guo, P.; Zhang, S.; Chen, C.; Chen, H.; Wang, M.; Luo, W.; Tian, Y. Determination of Defect Levels in Melt-Grown All-Inorganic Perovskite $CsPbBr_3$ Crystals by Thermally Stimulated Current Spectra. *J. Phys. Chem. C* **2018**, *122*, 10309–10315.

Zhang, Q.; Su, R.; Du, W.; Liu, X.; Zhao, L.; Ha, S. T.; Xiong, Q. Advances in Small Perovskite-Based Lasers. *Small Methods* **2017**, 1, 1700163.

Zhang, Y.; Liang, Y.; Wang, Y.; Guo, F.; Sun, L.; Xu, D. Planar $FAPbBr_3$ Solar Cells with Power Conversion Efficiency above 10%. ACS Energy Lett., **2018**, 3, 1808–1814.

Zhang, Y.; Wu, Z.; Li, P.; Ono, L. K.; Qi, Y.; Zhou, J.; Shen, H.; Surya, C.; Zheng, Z. Fully Solution-Processed TCO-Free Semitransparent Perovskite Solar Cells for Tandem and Flexible Applications. *Adv. Energy Mater.* **2018**, 8,

Zhang, Yaokang, Wu, Z.; Li, P.; Ono, L.K.; Qi, Y.; Zhou, J.; Shen, H.; Surya, C.; Zheng, Z. Fully Solution-Processed TCO-Free Semitransparent Perovskite Solar Cells for Tandem and Flexible Applications. *Adv. Energy Mater.*, **2018**, 8, 1701569.

Zhang, Z.; Ren, L.; Yan, H.; Guo, S.; Wang, S.; Wang, M.; Jin, K. Bandgap Narrowing in Bi-Doped $CH_3NH_3PbCl_3$ Perovskite Single Crystals and Thin Films. *J. Phys. Chem. C* **2017**, 121, 17436–17441.

Zhao, D.; Wang, C.; Song, Z.; Yu, Y.; Chen, C.; Zhao, X.; Zhu, K.; Yan, Y. Four-Terminal All-Perovskite Tandem Solar Cells Achieving Power Conversion Efficiencies Exceeding 23%. *ACS Energy Lett.*, **2018**, 3, 305–306.

Zhao, D.; Yu, Y.; Wang, C.; Liao, W.; Shrestha, N.; Grice, C.R.; Cimaroli, A.J.; Guan, L.; Ellingson, R.J.; Zhu, K.; Zhao, X.; Xiong, R.-G.; Yan, Y. Low-bandgap mixed tin–lead iodide perovskite absorbers with long carrier lifetimes for all-perovskite tandem solar cells. *Nat. Energy*, **2017**, 2, 17018.

Zhao, T.; Liu, H.; Ziffer, M. E.; Rajagopal, A.; Zuo, L.; Ginger, D. S.; Li, X.; Jen, A. K. Y. Realization of a Highly Oriented $MAPbBr_3$ Perovskite Thin Film via Ion Exchange for Ultrahigh Color Purity Green Light Emission. *ACS Energy Lett.* **2018**, *3*, 1662–1669.

Zhao, Y.; Tan, H.; Yuan, H.; Yang, Z.; Fan, J. Z.; Kim, J.; Voznyy, O.; Gong, X.; Quan, L. N.; Tan, C. S.; Hofkens, J.; Yu, D.; Zhao, Q.; Sargent, E. H. Perovskite Seeding Growth of Formamidinium-Lead-Iodide-Based Perovskites for Efficient and Stable Solar Cells. *Nat. Commun.* **2018**, *9*, 1607.

Zheng, G.; Zhu, C.; Ma, J.; Zhang, X.; Tang, G.; Li, R.; Chen, Y.; Li, L.; Hu, J.; Hong, J.; Chi, Q.; Gao, X.; Zhou, H. Manipulation of Facet Orientation in Hybrid Perovskite Polycrystalline Films by Cation Cascade. *Nat. Commun.* **2018**, *9*, 2793.

Zheng, J.; Lau, C.F.J.; Mehrvarz, H.; Ma, F.-J.; Jiang, Y.; Deng, X.; Soeriyadi, A.; Kim, J.; Zhang, M.; Hu, L.; Cui, X.; Lee, D.S.; Bing, J.; Cho, Y.; Chen, C.; Green, M.A.; Huang, S.; Ho-Baillie, A.W.Y. Large area efficient interface layer free monolithic perovskite/homo-junction-silicon tandem solar cell with over 20% efficiency. *Energy Environ. Sci.*, **2018**, 11, 2432–2443.

Zheng, X.; Chen, B.; Wu, C.; Priya, S. Room temperature fabrication of $CH_3NH_3PbBr_3$ by anti-solvent assisted crystallization approach for perovskite solar cells with fast response and small J–V hysteresis. *Nano Energy*, **2015**, 17, 269–278.

Zhou, D.; Liu, D.; Jin, J.; Chen, X.; Xu, W.; Yin, Z.; Pan, G.; Li, D.; Song, H. Semiconductor Plasmon-Sensitized Broadband Upconversion and Its Enhancement Effect on the Power Conversion Efficiency of Perovskite Solar Cells. *J. Mater. Chem. A* **2017**, 5, 16559–16567.

Zhou, S.; Ma, Y.; Zhou, G.; Xu, X.; Qin, M.; Li, Y.; Hsu, Y.-J.; Hu, H.; Li, G.; Zhao, N.; Xu, J.; Lu, X. Ag-Doped Halide Perovskite Nanocrystals for Tunable Band Structure and Efficient Charge Transport. *ACS Energy Lett.* **2019**, *4*534–541.

Zhou, Y.; Kwun, J.; Garces, H. F.; Pang, S.; Padture, N. P. Observation of Phase-Retention Behavior of the $HC(NH_2)_2PbI_3$ Black Perovskite Polymorph upon Mesoporous TiO_2 Scaffolds. *Chem. Commun.* **2016**, 52, 7273–7275.

Zhou, Y.; Yong, Z.-J.; Zhang, K.-C.; Liu, B.-M.; Wang, Z.-W.; Hou, J.-S.; Fang, Y.-Z.; Zhou, Y.; Sun, H.-T.; Song, B. Ultrabroad Photoluminescence and Electroluminescence at New Wavelengths from Doped Organometal Halide Perovskites. *J. Phys. Chem. Lett.* **2016**, 7, 2735–2741.

Zhou, Y.; Yong, Z.-J.; Zhang, W.; Ma, J.-P.; Sadhanala, A.; Chen, Y.-M.; Liu, B.-M.; Zhou, Y.; Song, B.; Sun, H.-T. Ultra-Broadband Optical Amplification at Telecommunication Wavelengths Achieved by Bismuth-Activated Lead Iodide Perovskites. *J Mater. Chem. C* **2017**, 5, 2591–2596.

Zhou, Y.; Zhao, Y. Chemical Stability and Instability of Inorganic Halide Perovskites. *Energy Environ. Sci.* **2019**, 12, 1495–1511.

Zhou, Y.; Zhu, K. Perovskite Solar Cells Shine in the "Valley of the Sun." *ACS Energy Lett.* **2016**, 1, 64–67.

Zhu, J.; Huang, A.; Ma, H.; Ma, Y.; Tong, K.; Ji, S.; Bao, S.; Cao, X.; Jin, P. Composite Film of Vanadium Dioxide Nanoparticles and Ionic Liquid–Nickel–Chlorine Complexes with Excellent Visible Thermochromic Performance. *ACS Appl. Mater. Interfaces* **2016**, 8, 29742–29748.

Zimmermann, K.; Thiele, G. Polymorphie von $Cs_3Tl_2Br_9$. *Z. Naturforsch. B* **1987**, 42, 818–824.

Vita

Timothy D. Siegler was born in New Berlin, WI in 1992, and lived in Wisconsin throughout his childhood. He graduated valedictorian of Catholic Memorial High School in 2010, and went on to attend the University of Notre Dame from 2010-2014. At Notre Dame, he performed research in the labs of Prof. Prashant Kamat and Prof. Thomas Bein at the University of Munich, graduating *magna cum laude* in 2014 with a senior thesis entitled "Device Architecture Optimization Towards the Development of Idealized Quantum Dot Solar Cells". He went on to begin his graduate studies in the lab of Prof. Brian A Korgel at the University of Texas at Austin in 2014, working on perovskite solar cell materials.

Permanent email: tsiegler@alumni.nd.edu

This dissertation was typed by Timothy D. Siegler